Small Animal 4D SPECT Imaging - Assessment of Respiratory Motion and Iodide Biodistribution -

Marine Breuilly

UNIVERSITE DE NICE - SOPHIA ANTIPOLIS
ECOLE DOCTORALE STIC
SCIENCES ET TECHNOLOGIES DE L'INFORMATION
ET DE LA COMMUNICATION

T H E S E

pour l'obtention du grade de

Docteur en Sciences

de l'Université de Nice - Sophia Antipolis

Mention : Automatique, Traitement du Signal et des Images

Présentée et soutenue par

Marine Breuilly

Imagerie TEMP 4D du petit animal

- Estimation du Mouvement Respiratoire et de la Biodistribution de l'Iode -

Thèse dirigée par Grégoire Malandain et Jacques Darcourt

préparée conjointement à INRIA Sophia Antipolis - Méditerranée, projet Asclepios
et à l'Université de Nice - Sophia Antipolis, équipe TIRO

soutenue le 21 Novembre 2013

Jury :

Rapporteurs :	David Sarrut	-	CNRS Lyon - CREATIS
	Régine Trebossen	-	CEA Orsay
Directeurs :	Grégoire Malandain	-	INRIA Sophia-Antipolis
	Jacques Darcourt	-	UNS / CAL - TIRO
Président :	Laure Blanc-Féraud	-	CNRS Sophia - I3S
Examinateurs :	Catherine Ghezzi	-	INSERM Grenoble
	Mauricio Reyes Aguirre	-	University of Bern
Invités :	Philippe Franken	-	UNS -TIRO

UNIVERSITY OF NICE - SOPHIA ANTIPOLIS

DOCTORAL SCHOOL STIC

SCIENCES, INFORMATION TECHNOLOGIES AND COMMUNICATION

P H D T H E S I S

to obtain the title of

PhD of Science

from the University of Nice - Sophia Antipolis

Speciality : Control Systems, Signal and Image Processing

Defended by

Marine Breuilly

Small Animal 4D SPECT Imaging

- Assessment of Respiratory Motion and Iodide Biodistribution -

Thesis Advisors: Grégoire Malandain and Jacques Darcourt

prepared at INRIA Sophia Antipolis - Méditerranée, Asclepios research group
and at the University of Nice - Sophia Antipolis, TIRO research group

defended on November 21, 2013

Jury :

Reviewers :	David Sarrut	-	CNRS Lyon - CREATIS
	Régine Trebossen	-	CEA Orsay
Advisors :	Grégoire Malandain	-	INRIA Sophia-Antipolis
	Jacques Darcourt	-	UNS / CAL - TIRO
President :	Laure Blanc-Féraud	-	CNRS Sophia - I3S
Examiners :	Catherine Ghezzi	-	INSERM Grenoble
	Mauricio Reyes Aguirre	-	University of Bern
Invited :	Philippe Franken	-	UNS -TIRO

Imagerie TEMP 4D du petit animal - Estimation du Mouvement Respiratoire et de la Biodistribution de l'Iode

Résumé: L'objectif de cette thèse est d'étudier temporellement des phénomènes évolutifs à l'aide de la tomographie d'émission monophotonique (TEMP). La première partie de cette thèse traite le problème du mouvement respiratoire dans les images TEMP de souris. Nous présentons ici une méthode permettant de détecter ce mouvement respiratoire dans les images TEMP 4D, d'extraire un signal respiratoire intrinsèque, et de déterminer la phase du cycle respiratoire sans mouvement la plus large possible. Les données enregistrées durant ces phases sans mouvement sont alors utilisées pour reconstruire une seule image TEMP 3D sans artefact de mouvement par acquisition. Les images ainsi reconstruites présentent un bon compromis en terme de statistiques et de précision des mesures par rapport aux images TEMP 3D de base et TEMP 4D. Dans la deuxième partie, nous étudions la cinétique d'accumulation de l'iode dans l'estomac de souris par le biais de l'étude de la biodistribution du pertechnetate de technetium (^{99m}Tc-pertechnetate) avec des images TEMP 4D. Afin de comprendre le rôle biologique de cette accumulation dans l'estomac, nous avons modélisé le phénomène par une approche d'analyse compartimentale avec un modèle simplifiée à deux compartiments (paroi et cavité stomacale) et une entrée (sang). Les courbes temps - activité (TAC) de chaque compartiment sont déduites des observations et une première estimation des paramètres a été obtenue.

Mots-clés: TEMP du petit animal; Images dynamiques; Mouvement respiratoire; Synchronisation respiratoire; ^{99m}Tc-pertechnetate biodistribution; Analyse compartimentale

Small Animal 4D SPECT Imaging - Assessment of Respiratory Motion and Iodide Biodistribution

Abstract: The aim of this thesis is to investigate temporally evolving phenomena with the use of single photon emission computed tomography (SPECT).

The first part of this thesis addresses the problem of respiratory motion in SPECT images of mice. The presented method permits us to detect the respiratory motion in 4D SPECT images, to extract an intrinsic respiratory signal and to determine the widest possible phase of the respiratory cycle without movement. The data recorded during these motionless phases are then used to reconstruct a single 3D SPECT image without motion artefacts per acquisition. Reconstructed motionless SPECT images present a good compromise in terms of statistics and accuracy of the measurements with respect to basic 3D SPECT and 4D SPECT images.

In the second part, we study the iodide uptake kinetics in the stomach of mice through the study of ^{99m}Tc-pertechnetate biodistribution with the use of 4D SPECT images. To understand the biological role of the iodide accumulation in the stomach, we modelled the phenomenon with a compartmental analysis approach using a simplified two-compartment (stomach wall and cavity) model with one input (blood). Time activity curves (TAC) of each compartment are deduced from observations and a first estimation of the parameters was obtained.

Keywords: Small animal SPECT; Dynamic images; Respiratory motion; Respiratory gating; ^{99m}Tc-pertechnetate biodistribution; Compartmental analysis

Acknowledgments

Un docteur en France est appelé “PhD” dans les pays anglophones. Ces trois lettres signifient “docteur en philosophie”. Ainsi qu'un ami me l'a rappelé récemment, ce titre reconnait non seulement un apport scientifique mais surtout l'aboutissement d'un cheminement personnel. Le côté scientifique est celui qui est mis en avant mais ce qui nous permet d'atteindre ce résultat c'est le côté personnel, le fait d'avoir surmonté les difficultés et de s'être dépassé, les nombreuses discussions passionnées et les rencontres avec d'autres personnes qui nous font évoluer.

J'aimerai commencer ces remerciements en les adressant aux personnes qui m'ont offert la chance d'effectuer cette thèse: Grégoire Malandain, Jacques Darcourt, Nicholas Ayache et Thierry Pourcher. Merci Grégoire d'avoir dirigé cette thèse, de m'avoir guidée, soutenue et encouragée tout au long de cette thèse, sans relâche, malgré certaines incompréhensions et remises en question. Merci de m'avoir accordé ta confiance, d'avoir partagé ton expérience, de m'avoir poussée à étudier un problème sous tous les angles possibles, de m'avoir enseigné ton perfectionnisme. Merci Jacques d'avoir accepté de co-encadrer ce travail, malgré ton emploi du temps très chargé, d'avoir partagé ton expérience et ton savoir en imagerie nucléaire, et bien sûr d'avoir pris le temps de (re)lire ce mes articles et manuscrit.

Ces travaux n'auraient pas pu être menés à bien si je n'avais pas disposé d'un cadre idéal de travail. Je souhaite donc remercier Nicholas pour m'avoir accueillie dans le projet - ou plutôt la famille - Asclepios durant toute la durée de ma thèse. Merci Nicholas de toujours nous encourager à être à la pointe et visionnaire dans nos travaux. Je souhaite aussi remercier Thierry Pourcher pour m'avoir accueillie et intégrée à l'équipe de biologistes TIRO, pour m'avoir enseigné sa curiosité insatiable pour la recherche, pour m'avoir enseignée une quantité astronomique de notions biologiques me permettant de comprendre les enjeux de mon travail en termes de biologie.

Je remercie vivement mes rapporteurs David Sarrut et Régine Trébossen qui ont lu avec beaucoup d'attention ce manuscrit, pour leur remarques et questions, très intéressantes et constructives. Je remercie aussi Laure Blanc-Féraud, Catherine Ghezzi et Mauricio Reyes Aguirre d'avoir accepté de faire partie de mon jury.

Je voudrais remercier un autre acteur très important dans mon travail de thèse, Philippe Franken, pour m'avoir enseigné l'utilisation de la caméra petit animal avec toujours autant de diponibilité, de motivation et d'émerveillement mais aussi pour m'avoir guidée et soutenue. J'ai beaucoup apprecié nos discussions et j'admire tes qualités de conteur d'histoire.

Je voudrais remercier sincèrement mes collègues de l'équipe TIRO, Julien Guglielmi, Audrey Lamit et Philippe Pognonec pour leur soutien et leur disponibilité sans faille dans la mise en place de protocoles expérimentaux, la gestion et manutention des souris, et les nombreuses sessions d'acquisitions d'images.

Je ne me serais pas lancée dans cette aventure si je n'avais pas rencontré et travaillé avec Aymeric, Frédéric et Bogdan que je remercie profondément pour avoir partagé leur passion, pour m'avoir donné le goût de la recherche, et toujours encouragé à poursuivre dans cette voie.

Je voudrais remercier toutes les personnes avec qui j'ai passé de si bon moments au cours des 4 dernières années, et je m'excuse si j'en ai oublié quelques uns au moment d'écrire ces mots. Merci aux membres du groupe "Xtreme Salad" pour ces instants musicaux: Marco, Wassim, François et Grégoire. Merci à tous mes co-bureaux du légendaire *bureau des filles*: Florence pour les nombreuses discussions philosophiques de début de thèse, Liliane pour son soutien et son amitié, Krissy pour son amitié et son insatiable énergie qui m'ont donné du courage au moment de l'écriture du manuscrit mais aussi pour ces nombreuses corrections en langue anglaise, ainsi que Rocio, Sonia, et Nina (la petite "dernière") pour leur soutien et encouragements. Merci aussi aux quelques garçons qui ont séjourné dans ce bureau pour la bonne ambiance qui y régnait, Thomas et Hervé (expert en construction éco-coca-cola). Merci à tous les amateurs de thés pour les 2kg de thés que nous avons bus ensemble: Vincent, Benoît, Kristin et Brina. Un grand merci à toute la famille Asclepios. I just wanted to thank all of you for attending my defense, and for the 4 past years in your company. Thank you for all the talks, (tea) breaks, hiking, climbing, camping, snowshoeing, board game playing, music playing, for your friendship and for all these moments that made these years so specials to me: Fatih, Chloé, Loïc, Olivier, Nicolas, Hervé, Thomas, Stanley, Romain, Alan (merci pour toute ces discussions et tes conseils), Ezequiel, Pascal, Vikash, Mehdi, Tobias, Bishesh, Michael, Muriel, Hans, Hakim, Matthieu, Arnaud, Loïc, Yonni, Siyamalan, Tommasso, Stéphanie, Jan Margeta, Bjoern, Julien, Xavier, Jean-Marc, Adityo, Islem, Jatin, Stephan, Maxime, Federico, John, Erin, Andrew, Hugo, Nicolas, Viateur, Clair, Florian, Irina et Ken. Sans oublier l'indispensable Isabelle Strobant qui veille comme une mère sur chacun d'entre nous.

Je voudrais aussi remercier mes co-bureaux de l'équipe TIRO pour leur amitié et leur soutien: Jérôme (merci toutes les discussions politico-environnementales qui ont rythmé nos pauses déjeuner), Malick, Eleonora,

Elodie mais ausi Béatrice, Lydie, Carole. Merci aussi pour leur accueil à tous les membres de TIRO, permanents et stagiaires que j'ai eu le plaisir de cottoyer pendant ces 4 années: Elisabeth, Nelly, Fanny, Renaud, Sabine, Dider, Robert, Charles, Philippe, Peggy, Colette, Tijana et Georges.

Au cours de la dernière année, j'ai enseigné en tant qu'ATER dans deux départements de l'IUT de Nice et je voudrais remercier tous mes collègues avec lesquels j'ai eu le plaisir de travailler. Merci à eux pour leur accueil, leur sympathie, les discussions sur la pédagogie et la confiance qu'ils m'ont accordée: Frédéric, Pierre, Claire, Marie-Claude, Aline, Philippe, Sandrine, Aliou et Olivier.

Je voudrais aussi faire une dédicace á tous les anciens et actuels collocataires du Catrusoutrane pour leur amitié et tous les moments passés ensemble: Max et Krobb, Céline, Olivier, Fab et Franck, Max "le bricoleur" et Rachou "l'acrobate", NicoDey et Morgane.

Durant ces quatre années, j'ai eu le plaisir d'explorer une grande partie de la région que ce soit en marchant, en courant, en escaladant, en ski ou en raquettes à neige. Je voudrais remercier les sportifs en tous genres et autres mutants qui ont croisé mon chemin: Virgile, Semifamily, Pascafamily, Mélaine, Cyril, Misha et Janna, Jon et Sheila, Seb et Caro, Sarah, et tous les autres de la section escalade du COV.

Je voudrais aussi remercier pour leur amitié: Sophie, Bartek, Diana Yifan the "crazy chinese girl", toute la clique du "club Spec"' - Marie, Leila et Antoine, Léti et Flo, Sethphane, Nico D -, Bertrand, Catherine, Eléonore, Erik, Aurélie et Florence.

Je voudrais remercier toute ma famille pour leur soutien infaillible malgré la distance, Jean-Louis et Evelyne pour leur accueil dans la région, mes grandparents de Normandie, Mamie de Blois dont le courage face à la difficulté m'a toujours inspiré, mon grand-père pour avoir fait tout ce trajet pour assister à ma soutenance, mes frères et soeur Vincent, Gwenaëlle et Léo d'être tout simplement géniaux, mes parents pour m'avoir encouragé à faire ce que nous aimons mais surtout d'avoir toujours été là pour me soutenir et m'encourager.

Enfin, pour les 1000 kilomètres horizontaux et 100 km de D+ parcourus ensemble (Yepeeh!), et pour tous ceux à venir, pour m'avoir soutenu sans relâche, pour m'avoir aidé à me relever dans les périodes difficiles, pour m'avoir remotivée pendant la longue phase d'écriture, pour avoir relu l'ensemble du manuscrit plusieurs fois, pour avoir été mon "coach" sportif, culinaire, en jeux de sociétés, pour sa patience infinie et son amour, merci Ludo!

Merci aux Anis de Flavigny pour avoir ajouté de la douceur et de la convivialité!

Contents

INTRODUCTION

Chapter 1

Introduction

Contents

1.1 Context and Motivations: Longitudinal studies and applications to small animal imaging

The context of this thesis is the study of longitudinal phenomena. Our aim is to use imaging in order to understand the evolution of biological processes. The objective is to provide tools to perform longitudinal studies of these processes.

In order to follow a phenomenon over time, we need to gather enough information, but also we need this information to be as accurate as possible. That is why, our objective in this thesis is to provide to biologists tools to extract as many information as possible from the imaging data at their disposal. Image processing techniques already provide solutions to difficult problems. Our approach consists here in developing simple methods based on some of the image processing techniques. These methods are dedicated to the resolution of precise biological problems.

The context of this thesis is also a collaborative work between two research teams: the ASCLEPIOS team at INRIA that focuses on biomedical image analysis and physiological systems modelling among others, and the

TIRO team at Commissariat à l'Energie Atomique et aux énergies alternatives (CEA) / Université de Nice Sophia Antipolis (UNS) / Centre de lutte contre le cancer Antoine Lacassagne (CAL) that focuses on iodide metabolism: thyroid function, radiotoxicology, reporter gene imaging and treatments in oncology. This collaboration was materialised by the purchase of an innovative small animal camera as part of the *contrat de projet État-Région* (CPER), application file Telius proposed by INRIA and its collaborators.

Consequently, the biological problems we address in this thesis are related to the in vivo tracking of iodide uptake in cells with small animal single photon emission computed tomography (SPECT) imaging, and in particular mice imaging. It is of particular interest to remind that longitudinal imaging is really important for longitudinal studies comparing to the animal sacrifices that would be required otherwise.

To summarise, the direct impact of this thesis is to provide tools to precisely characterise the studied longitudinal phenomena, observed on mice, through imaging. Most problems we encountered are related to the movement of the anaesthetized small animal. Getting accurate measures from images in the presence of such movement is among the main challenges addressed in this thesis.

In this thesis we illustrate how to deal with evolution problem with two different contributions:

- A method that address respiratory motion for imaging of tumours. We propose a procedure to reconstruct SPECT motionless images with a good signal-to-noise ratio.

- A representation of the stomach tolerant to its deformations and to animal motion in order to understand its iodide uptake. We propose a way to measure this uptake in the stomach with a layer-based approach that is much more tolerant to stomach contraction and relaxation than a classical voxel-based approach.

1.2 Material and experiments

The pre-clinical camera used in this thesis allows for 4D SPECT images acquisition. The four dimensions refer to the three spatial dimensions plus a fourth temporal dimension. This temporal dimension is characterized by the fact that several acquisitions are processed in a row, at regular temporal intervals (minutes, days or weeks). SPECT images allow the observation of the evolution of biological phenomena with respect to the biodistribution of radiopharmaceutical injection.

In the case of temporal interval on a daily or weekly scale, SPECT is dedicated to the study of processes such as tumour growth. For example, the

tumour uptake sites can be localized and quantified, and by extension, their growth can be estimated.

In the case of short temporal interval on a minute or hour scale, SPECT allows the observation of radiopharmaceutical biodistribution variations after injection.

1.3 Respiratory motion

The first challenge addressed in this thesis is the reconstruction of high contrasted and quantitatively reliable SPECT images of peritoneal tumours of anaesthetized mice. Among the different physical artefacts, respiratory motion is the most important one [HFGH08].

Respiratory motion may affect the tomographic reconstruction of positron emission tomography (PET) or SPECT images, which subsequently impair quantitative measurements, e.g. in the upper abdomen area. Respiratory signal phase-based gated reconstruction addresses this problem, but deteriorates the signal-to-noise ratio (SNR) ratio and other intensity-based quality measures. In this thesis, we propose a method for the reconstruction of 3D images that are not impaired by the respiratory motion and keep a high SNR.

The expected impact of this work is to provide a method that guarantees motionless image reconstruction and that allows accurate measurement and understanding tumour growth. The biological objective here is to be able to track, to model and ideally to predict the evolution of tumours in order to treat them more efficiently.

1.4 Dynamic distribution of iodide in stomach

The second study is incorporated in the framework of the study of iodide metabolism in the murine stomach. The idea is to understand the gastric cycle of iodide. The first objective is to automatically segment an organ in layers in a set of successive three (spatial) dimensions (3D) SPECT images, where the organ is animated by a random movement. The second objective is to model the dynamic distribution of iodide with the use of compartmental analysis, where each compartment is a functional compartment at the cellular scale.

In order to understand the physiological role of iodide, we first study the process of iodide uptake. Then we elaborate a model of the stomach using compartmental analysis. Our contribution concerning this phenomenon is more a study of feasibility and a methodology than the exact characterisation of the process. Our results can be summarised as follows.

- We realise a regional decomposition of the (3D) stomach in layers in order to be tolerant to its contraction and relaxation, and to the animal movement.
- We elaborate a compartmental model for the iodide transport in the stomach.
- We define mixing coefficients that allow us to compute the activity in each compartment from the measured activity in each layer.
- We design a combination of analytical and numerical resolution steps allowing the full characterisation of the iodide uptake.
- Finally, we compute the transfer coefficients for our compartmental model; those coefficients are the parameters of the compartmental model. The results are reliable enough for a first study.

1.5 Manuscript organisation

This manuscript revolves around two parts demonstrating the two main contributions:

1. The first part deals with the respiratory motion and motionless reconstruction of small animal SPECT images.
2. The second part describes the modelling of the iodide biodistribution in the murine stomach.

Chapter 2 gives a background on the biological and technical context of this thesis. It also describes the inherent material and animal model constraints.

Part I focuses on respiratory motion and consists of two chapters. Chapter 3 presents a state of the art about respiratory motion correction methods. Chapter 4 presents in its entirety the journal paper [BMG+13], we where we propose a dedicated method for optimal motionless reconstruction of 3D SPECT images.

Part II focuses on the iodide biodistribution in the murine stomach and consists of two chapters. In Chapter 5, we describe qualitatively the biodistribution of the iodide analog ^{99m}Tc-pertechnetate in the stomach based on the observations of dynamic SPECT images. In Chapter 6, we characterise the iodide uptake phenomenon with a simplified compartmental model.

Lastly, Chapter 7 concludes this thesis with the list of contributions and directs us towards the feasible perspectives to this work. A list of publications is provided page 141.

The most useful appendices of this thesis are the following. Appendix A gives additional results for the motionless reconstruction method. Appendix B describes the principles of compartmental analysis.

Chapter 2

Technical context for the experimental protocol elaboration

Contents

2.1 Introduction

During this thesis, a great deal of effort has been done in order to work on common subjects with a team of biologists. From the definition of the subject to the interpretation of the results, a permanent dialog has been maintained between the researchers of the two domains. On the one side, biologists shared their experience, knowledge, and working constraints related to the study of the small animal. The advantage of this dialog and experience sharing was to define and to set up a custom-made experimental protocol that would allow us to answer the questions that are of real interest for the biologists. On the other side, we also investigated the material at disposal - a SPECT/CT camera - in order to determine the material constraints.

In this chapter, the idea is to describe at best the tools, material, and techniques that were used in the presented works, and to define their limits. First, the small animal imaging camera will be described in order to determine the material constraints that have to be considered in the protocol elaboration

(Section 2.2). These constraints are to inject the smallest dose (radioactivity or X-rays) to the animal, to use the shortest acquisition sequence, and to acquire image without artefacts that could lead to wrong analysis and interpretation. Second, the creation of an appropriate animal model is also a complex task for biologists (Section 2.3). The constraints are numerous and mainly concern how to successfully elaborate an animal model with tumour growth and how to maintain this animal alive over several weeks with repetitive acquisitions so that it is possible to image the tumours along the time.

The knowledge of both material and animal constraints were taken into account for the definition of the final experimental protocol.

2.2 Material constraints: Pre-clinical imaging system [1]

The imaging system used for this work is a coupled SPECT/CT camera dedicated to small animal (eXplore speCZT- CT 120, GE Healthcare/Gamma Medica (London, ON, Canada)). This camera consists of three distinctive parts: a small animal table, the SPECT module, and the CT scanner (see Figure 2.1(a)). The first module, the animal table, is used for the animal preparation. The table is the place where the anaesthetised animals are prepared and installed for acquisitions. The animal preparation and monitoring steps are described in Section 2.3 below.

The two imaging modalities are presented separately in this section in order to understand the functioning of each modality, and to identify the constraints of their use in an imaging protocol. A SPECT/CT camera permits to image two different types of information from the same subject. The idea for using such a multimodal camera is to combine both modalities in order to have more detailed information and images of the studied phenomenon. However, in this camera, the SPECT module is located in front of the other module CT scanner, and therefore they are not localised on the same gantry. The acquisition of each modality can not be processed simultaneously and images of each modality can only be acquired one after another. Nevertheless, SPECT and CT images corresponding to the same acquisition sequence can be mapped together afterwards, after registration using the global rigid transform between the two gantries. This rigid transform is established from preliminary test acquisitions.

[1] A big thank you to Philippe Franken for is help at all time for camera understanding and handling, and support during acquisitions.

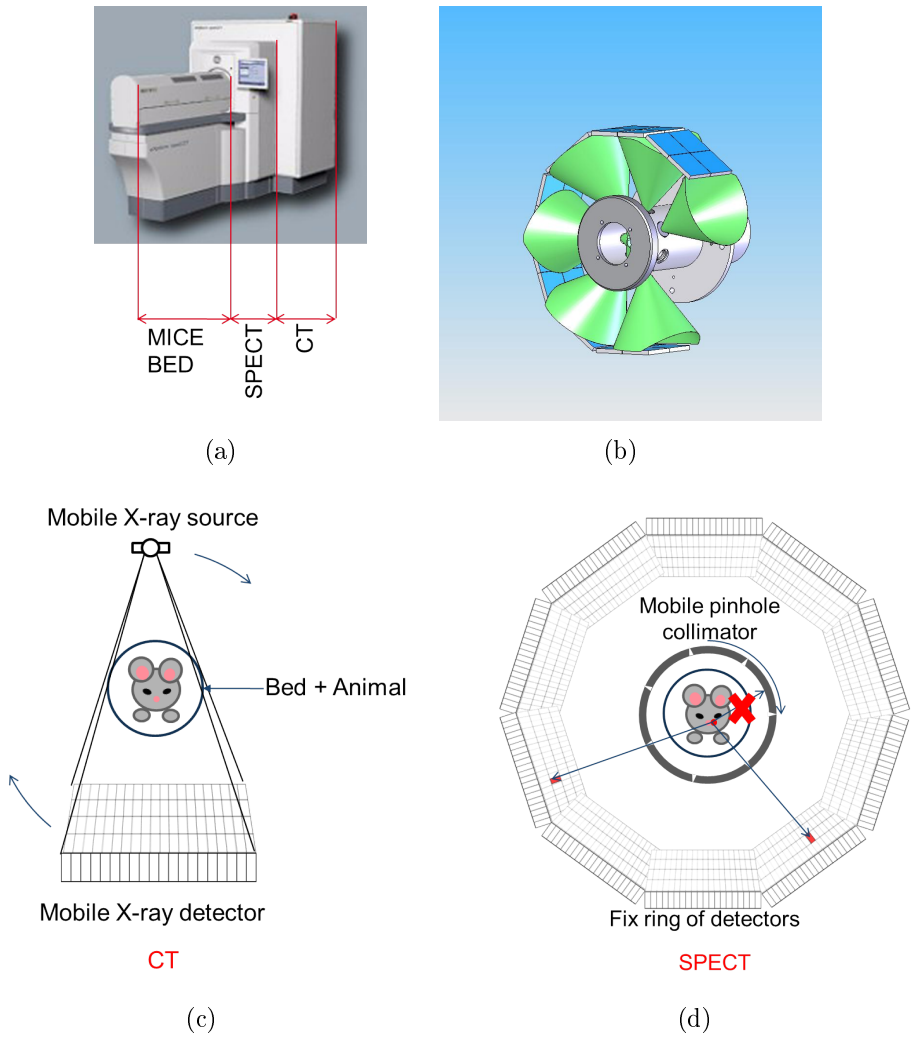

Figure 2.1: **Presentation of pre-clinical imaging system eXplore speCZT CT 120**: (a) Description of the assembly of animal table SPECT and CT imaging systems, (b) Description of the pinhole collimator operating, (c) Schema describing CT acquisition process, (d) Description of SPECT acquisition process (pinhole collimation).

2.2.1 Single photon emission computed tomography (SPECT)

Camera description The SPECT module allows for imaging the biodistribution of radiopharmaceutical. The resulting SPECT images exhibit physiological and functional information about biological processes. This information is related to radiopharmaceutical distribution and accumulation through the subject body.

In order to acquire biodistribution images, the camera is equipped with a rotating seven-pinhole collimator (Figure 2.1(b)) and a stationary gantry of gamma photon detectors. The ring of detectors (Figure 2.1(d)), made of ten panels of four semi-conductor CZT modules, will record all events with a one-ms sampling.

The CZT modules serve for the detection of the gamma photons, also called scintillation. Usually, the scintillation phenomenon describes the gamma photon absorption by the NaI(T1) crystals in the camera [BDF09]. The crystal scintillates in response to incident gamma radiation. When a gamma photon is emitted by the animal and hits the crystal, it induces an electron loose from an iodine atom in the crystal, and a flash of light is produced when the electron again finds a minimal energy state. Then, the flash of light (called event) is detected by photomultiplier tubes (PMTs) behind the crystal and recorded. In our case, the scintillation process with the CZT modules is different from the one with scintillating classical NaI(T1) crystals. The energy of the detected photons is directly converted into electrical energy. The detection information is recorded with a one-ms sampling under the form of a list, called listmode, that contains the characteristics (time, detection location, energy, gating trigger) of each detected photons.

Then, in order to reconstruct an image from the listmode, we need to know the direction of each detected photons and the location of their emission in the animal. The direction can be deduced with the use of a collimator. The collimator is a lead tube with slits or pinholes, inside which one the animal is positioned. In our case, the collimator is a seven-pinhole collimator. The principle of collimation with a pinhole (or cone-beam) collimator is simple. Gamma photons will be emitted in each directions from the animal but only the ones that will go through the collimators pinholes will hit the detectors. The direction of the detected photon is thus determined from the position of the detection and the pinhole. The collimator selects the gamma photons according to their direction. The other photons will be stopped by the lead collimator in order to specifically detect photons emitted according to a cone-beam geometry. Since the collimator is going to select photons according to a certain direction with respect to each pinhole, the collimator is rotating in order to acquire data from each angle around the animal projections. In the case of the seven-pinhole collimator, the system acquires 51 projections for a single field of view (FOV). One FOV measures 32 mm with mice collimator.

In addition to the photon direction selection, a selection of the detected photons according to their energy (spectrometry) is processed in order to discard the photons that were Compton scattered. This selection is done by choosing an energy window around the energy of the emitted photons. For this work, the radiopharmaceutical that has been chosen is the ^{99m}Tc-pertechnetate, and the gamma photons are emitted with a 140 keV energy. The width of the energy window of ^{99m}Tc ranges from 126 to 154 keV with

this camera.

Consequently, SPECT acquisition with the eXplore speCZT camera consists in recording information about gamma photons that are emitted during an user-defined time over the 360°around the animal and detected on the CZT detectors. The SPECT images are reconstructed with a block-iterative process, the ordered subset expectation maximization algorithm [HL94], that has been proved to be fast. From seven to nine subsets and from six to nine iterations were used for the algorithm, the number of EM equivalent updates ranged from 54 to 56.

However, a certain number of physical phenomena affect the SPECT imaging [BDF09], and thus degrade the quality of the obtained image, such as attenuation, scatter, partial volume effect, as well as by motion artefacts. Attenuation is characterised by a diminution of the energy of the photons. Scatter is characterised by the deviation of the emitted photons. The two steps of cone-beam collimation and spectrometry take care of the attenuation and scatter effects. Therefore, respiratory motion compensation is one of the main obstacles of accurate quantification in micro-SPECT (μ-SPECT).

Radiopharmaceuticals Different factors have to be taken into account in order to choose the radiopharmaceutical:

- the cells or molecules that are targeted;
- the half life of the radioisotope;
- the ease of supply.

For this work, the radiopharmaceutical that has been chosen is the ^{99m}Tc-pertechnetate. Considering its chemical properties, ^{99m}Tc-pertechnetate is considered as an iodine analog. That makes of it the perfect radiopharmaceutical for our purpose, which is tracking tumourous cells that express sodium/iodide symporter (NIS) protein (see Section 2.3). Indeed, as an iodine analog, ^{99m}Tc-pertechnetate is transported into the body through the same paths, it is mediated by NIS protein, and it accumulates in these tissue. ^{99m}Tc has a short half life (around 6 hours), which is perfect for frequent animal imaging and radioactive waste management. As the radioactivity will decay quickly, it can be considered as null after only a few days. Injected animals can then be safely considered not having radiopharmaceutical anymore within a week. This short half life make the storage of radioactive contents easier: the radioactive waste (syringe, paper towel or even dead animal) have to be put in quarantine for only a short period of time (typically a week).

Gating or not? During SPECT acquisition, data are recorded continuously. If the region imaged is animated by a motion, one can desire to reconstruct

images without motion artefact in order to to study the biodistribution of the radiopharmaceutical. When the motion is cyclic, motionless images can be reconstructed by using only a fraction of data at a specific motionless period of time of gated acquisition.

Retrospective gated reconstruction is possible when the acquisition has been triggered by an external monitoring system. External monitoring systems which are used to record a signal can be associated with a physiological motion (see Section 2.3.2 for further details on physiological signal extraction).

Gated SPECT images are then reconstructed within a specific time window of the periodic motion. The shorter the window of reconstruction, the less the motion artefacts in the image, and the smaller the signal to noise ratio. In order to prevent from a too high noise level, a compromise has to be done between the window of reconstruction and the motion artefacts in the image. For further details on motions that can affect SPECT imaging and the method for reconstructing free of motion image, see Chapter 3.

2.2.2 Computed Tomography (CT)

Camera description The CT scanner allows for anatomical imaging of small animals. The CT imaging part of this scanner consists of a rotating system made of one X-ray tube and one flat panel of detectors as presented in Figure 2.1(c). 3D images are reconstructed from a set of X-ray projections that are acquired at different angles around the subject. Image units are expressed in Hounsfield units (HU) as for clinical CT scanners. This means that each kind of tissue has a different radiodensity with respect to water according to the expression:

$$\mathrm{HU} = 1000 * \frac{\mu_X - \mu_{\mathrm{water}}}{\mu_{\mathrm{water}}}$$

where μ_X is the average linear attenuation coefficient in the image voxel X. Thus water has a zero HU. Air, that is not attenuating the X-rays has a radiodensity of -1000 HU. While bones which is attenuating X-rays, has a high radiodensity from 700 HU to 3000 HU. The distinction between soft tissue and organs is harder since they all contains water in similar proportion. They have radiodensity ranged from 15 to 300 HU. In our case, we are not interested in bones, so we would like to favor soft tissue contrast with:

- fast acquisition;
- low dose.

Acquisition settings There are several predefined acquisition settings for the CT scanner. Each setting allows for either faster acquisition, better image resolution, lower noise (HU), or lower dose (mGy). Thus a compromise

between information, image resolution, acquisition time, and dose (X-rays radiation) has to be done (see the Appendix D for more details on each available setting).

The fastest sequences are the ones done only over 180°, with 220 projections, while other sequences acquire between 360 and 1200 projections over the 360°. These are numbers of projections required for a single FOV. If the region of interest is larger than one FOV, the number of projections required for the reconstruction is increased. In our case, the CT FOV is around 80 mm-length, it is large enough to image both lungs and abdomen.

Besides the number of projections required for CT image reconstruction, the properties of the X-rays tube (voltage and current) can also be adjusted. The tube current controls the dose that is received by the subject, while the voltage only controls the energy of the emitted X-rays and does not affect the dose. A lower voltage means less penetrating photons and a better contrast in soft tissues. A higher voltage means more penetrating photons and the resulting image with a better contrast in bone. The dose is proportionate to the tube current by the acquisition time. The acquisition time is a multiple of the number of X-rays shoot by the duration of one shoot. Thus, for lower dose and better contrast in soft tissue, the setting with the lowest tube current and tube voltage would be the best. For the three constraints mentioned previously, the best setting is the "Fast Scan" setting (less than 2 min, tube current: 32 mA, tube voltage: 70 kV, and low dose: 36 mGy).

Gating or not? However, "Fast Scan" setting does not take into account motion information during the acquisition and reconstructed lungs images will be impaired with a blurred peri-diaphragmatic area. It is possible to obtain gated CT images with another CT acquisition setting, called "Cardiac" setting. This setting presents many advantages but in the scope of our study, the duration of a 4D is too long and increases incidence of animal mortality. This setting is not further detailed here since we did not investigate motion correction method based on dynamic CT.

For the protocol, we had the choice of acquiring either a high resolution CT image in order to extract some information about the lesion growth, or a lower resolution and faster image that will be used only for rough anatomical information. In our context, the benefit from CT image is low since the lesions that are studied are located in the abdomen, among soft tissues, and are not visible with a basic CT image. As a consequence, only a "Fast Scan" setting has been planned in the protocol for longitudinal studies.

2.3 Animal model constraints [2]

For this interdisciplinary work, the presence of biologists is required and needed at all steps of the process, from the protocol elaboration to image acquisitions via the animal preparation. The protocol elaboration from the biologist side consists in defining everything that is related to the animal model preparation and the special care for it, before, during, and after imaging. This is also required for regulatory reasons.

2.3.1 Animal preparation

Animal model elaboration Elaborate the animal model consists in associating a specific mice lineage with a tumourous cell lineage that has been introduced in its body in order to generate life like tumours. The tumourous cell lineage is the result of in vitro development and studies beforehand. Cell lineage that are considered here have been modified in order to express a specific protein, the NIS. This protein is naturally expressed in thyroid cells and it is responsible for the uptake of iodine into these cells. The idea with this modification is to use radiopharmaceuticals based on radioisotopes (such as ^{99m}Tc or ^{123}I) in order to localise these cells wherever it goes, fixes and grows in the body. This is called reporter gene imaging.

Then, the lineage of the mice that will receive these cells has to be carefully chosen in order to allow the development of the tumour. Preliminary biological investigation on different mice lineage showed that syngenic tumourous cells expressing NIS protein caused a violent immune response at early stage of the development of the tumour. This reaction seems to be due to the Natural Killer (NK) lymphocytes that are able to distinguish altered cells from normal by recognising changes of a surface molecule. These NK lymphocytes are known to prevent proliferation of tumours and infected cells by destroying both of them. Thus, if we want to study the growth of tumours, we need to select a lineage with impaired immunodeficient NK lymphocytes. Table 2.1 presents a list of mice lineage with its immune system characteristics. According to the constraints on immune characteristics, the most eligible mice lineage are Fox-chase SCID (®) Beige and NOD SCID. For the following, the mice lineage that has been chosen by biologist is NOD SCID mice.

Next, the tumourous developing site depends on the type of injection of the tumourous cells into the animals. Lesions will develop in the peritoneal cavity when cells are injected intraperitoneally. If injected intravenously, tumourous cells are distributed through all the body, and tumour might be developing in the lungs. When subcutaneous or orthotopic injection are done, tumourous

[2] A big thank you to Julien Guglielmi and Audrey Lamit for their support and help at all time before and during acquisitions.

Lymphocyte type	T	B	NK
Balb/c	=	=	=
Balb/c nude	↘	=	=
Athymic nude	↘	=	↗
Fox-chase SCID (®)	↘	↘	=
Fox-chase SCID (®) Beige	↘	↘	↘
NOD SCID	↘	↘	↘

Table 2.1: Different mice lineage with its immune system characteristics compared to the ones of wild type mice (healthy lineage). = stands for a lymphocyte activity equivalent to wild type, ↘ (respectively ↗) for a reduced (respectively increased) activity of lymphocytes compared to wild type.

cells are trapped, and orthotopic tumour are going to develop. For biological interest and also because it is easier to proceed without surgeon intervention, an intraperitoneal injection has been chosen and peritoneal tumours are going to be studied.

Animal daily care Once the animal model has been set up, biologists have to take care of the animals in order to prevent from death and to ensure that the animals can be imaged according to the protocol until the end. Longitudinal study of animal requires the animal to be under daily surveillance. The daily surveillance can be completed by additional palpation in order to detect any disorder in the animal that could be linked with the tumourous cells injection and that could affect the future acquisitions. Acquisition time and frequency are determined according to the knowledge of biologists based on preliminary studies. Acquisition protocols are planned in order to minimise the side effects of an early imaging or frequent imaging. Biologist surveillance also aims to determine when the subject has to be sacrificed in order to prevent the animal pain.

Animal preparation for imaging When an imaging session is planned, biologists are here to deal with the animal preparation before the acquisition. The preparation is divided into three steps:

- radiopharmaceutical injection;
- animal anaesthesia;
- animal positioning on the bed with motion and control sensors (anaesthesia, temperature).

2.3.2 Animal monitoring during acquisition

After the animal preparation section, this section is about the animal monitoring during acquisition. The more difficult part is to be able to control the anaesthesia and the breathing rhythm at all times of the acquisition, with the less side effects possible. The respiratory rhythm is particularly important since it indicates the state of the mice: deeply asleep, lightly asleep or almost awake. The respiratory motion is also important since the studied specimens point of interest are located in the area of the diaphragm (tumorous lesions in the lungs or abdomen). Therefore, this physiological periodic motion has to be studied and controlled, and eventually corrected.

Free breathing anaesthesia vs ventilation Contrary to adult humans, animals cannot stand still in a specific position for a certain period of time (acquisition), except died or asleep. When imaging alive subjects, anaesthesia is used for artificially send animals to sleep. It avoids animal motion and allows to control the breathing rhythm. Awake healthy wild type mice breathing rate ranges from 84 to 230 breath per min (equivalent to 0.26 to 0.71 seconds per cycle) while for immuno-depressed strains, respiratory rate ranges from 177 to 420 breath per min (equivalent to respiratory cycle length ranges from 0.14 to 0.34 sec) [SZI00]. Martiniova et al. [MSL+10] distinguished different anaesthetic alternatives: intra-peritoneal or intra-muscular injection of mixture of ketamine and other drug, or isoflurane inhalation. When animal are anaesthetised, their respiratory rhythm generally slows down.

An heaviest anaesthesia can be used but it affects the animal ventilation. These kind of anaesthesia consists of intra-peritoneal or intra-muscular injection of ketamine mixture. The mixture is injected only once before surgery or acquisition, sends animals to deep sleep, but the duration of sleep is not controlled and recovery is long. However, the animal can be placed in any position which allows better imaging or surgery without additional anaesthesic control [DCMW+04]. In order to keep animal alive with a regular respiratory rate, mechanical ventilation can also be required. Ventilation is mainly used for a fully controlled respiratory rhythm but it is heavy and invasive (deterioration of airways with tubes). This does not allow for repeated acquisitions. Thus, heavy anaesthesia (especially when coupled with ventilation) is not recommended on a regular basis as planned for longitudinal studies.

With superficial anaesthesia (gas inhalation such as isoflurane), the sleep is light and free breathing acquisition can be done with continuous anaesthetic gas supply. In that case, animal will recover fast, and repeated and longer acquisitions can be planned.

For the animal care, superficial anaesthesia is preferred.

Anaesthetic gas effect on breathing rhythm Although less invasive, to use anaesthesic gas also induce side effects on the respiratory behaviour. Cavanaugh et al. [CJP+04], one of the first in literature to mention respiratory gated acquisition in small animals, highlighted a side effect. Especially under isoflurane anaesthesia, specimens breathe convulsively in such a way that the respiratory cycle is not sinusoidal. The cycle can be divided into two main phases: a motion phase (breathing in and out) during around a third of the cycle and a still phase during around two third of the cycle. This still phase is suitable for motionless gating acquisition. Moreover, as anaesthesic gas, isoflurane is less invasive, and allows longer acquisition and fast recovery of the specimen. Thus, it is perfect for longitudinal studies. In this work, isoflurane anaesthesia has been chosen for the animal care.

Respiratory motion sensors Once the animal has been anaesthetised and placed in the camera, acquisitions can be set up and launched. However, the animal is not visible from outside the camera and it is not possible to check if the animal is still asleep and regularly breathing, if it woke up and moved from its initial position, or worse case if it died.

Several systems have been developed and used to record respiratory-like signals from external sensors. Most of the systems have been set up for humans [CVS+08].

The respiratory-like signal can be deduced from various physiological information that can be observed with a range of tools: the deformation of the ribs and thorax with a video-based system, the alteration of the heart electrical activity with ECG, the variation of pressure applied to a pressure sensor attached to the chest or the abdomen, the variation of the air volume in the lungs measured with a spirometer, or the temperature variation of the air that is going through the lungs. Once extracted this respiratory signals are used for two things. First, it is used as an information about the breathing rhythm of the animal, according to which the anaesthetic gas ratio is adjusted in the air that the animal breathes. It is also used for triggering image acquisition.

In the coming paragraphs, different respiratory motion sensors that can be used to monitor the mice are described.

Opto-electronic or video-based system These systems [BB11, BRG+08, GRS+09, MDB+11, NHAQ+11, SOM11, WLKV11] consist in tracking the movements of several markers positioned on the chest or on the abdomen of the subject with camera. In the case of a system called real-time position management (RPM), they use infrared light to track the infrared reflective markers set up on the subject abdomen during an acquisition. In that case, the respiratory like signal is extracted from the spatial position variation of the markers.

ECG electrocardiogram (ECG) consists in recording and interpreting the electrical activity of the heart over a specified period of time with the use of electrodes attached to the surface of the skin across the thorax and chest. It has been shown that the electrical activity signal can also be interpreted in order to extract a respiratory like signal [MMZM85, TLDF98]. Indeed, the heart is also submitted to respiratory motion and the heart electrical activity is impaired by respiratory disturbances. However the respiratory signal extracted through this method, only tested on human subject, is only representative of tidal volume changes. It does not contain the whole respiratory motion information.

Pressure sensors The pressure sensor (or chest belt) is frequently used both for human and animal acquisition [BB11, CCP+10, DFBM09, GJQ+11, KIK+07, LRS+06, vHJ+11]. It consists in recording the change of pressure inside a cushion that is fixed with a belt on the chest or abdomen of the subject. The cushion contains a sensor that detects and measures this pressure variation. A higher pressure applied to the cushion is associated to an increased volume in the lung and thus to the inspiration phase while a lower pressure is associated to the expiration phase.

Spirometer The spirometer [CJP+04, GJQ+11, JPK+08] is another tool that records the volume of air exchanged by the lungs (inspiration and expiration) over a specified period. This information can be exploited in order to obtain a signal representative of the respiration motion. The signal is resulting from the measurement of the flow rates through a sensor in the tool that is fixed to the head. Positive flow rates are then associated to expiration while negative ones are associated to inspiration.

Temperature This is another method that can be linked with the spirometer. Instead of measuring the flow rate, it consists in recording the temperature of the air incoming and outgoing from the nose during breathing [NE08, BPD+10]. The temperature is compared to the air temperature in the room. A lower temperature is associated with the inspiration (air going from the room into the lungs) while higher temperature is associated with expiration. These method is used both for human and for animal imaging.

For all methods, the obtained respiratory-like signal can be used online (while recording) in order to control gated acquisition. Triggers can be generated at specific time of the respiratory cycle thanks to an external signal monitoring software. Those triggers are used for prospective gating acquisition of dynamic images in the case of CT. In the case of emission tomography (ET), the triggers are used for retrospective gated reconstruction.

Among all these systems, a few have been adapted for small animal, but all systems require specific tools. For the following, the respiration motion sensor that has been chosen is the pressure sensor, although this is probably not the most accurate. It has been chosen since it is a part of a mice monitoring set that is already on disposal, and that the biologist already know how to use for the control of the well-being of the animal during the acquisition (temperature, breathing rhythm). The signal that is obtained from this pressure sensor associated with the monitoring system can also be used for the detection of the respiratory phases. Indeed, the respiratory signal can be split into different temporal phases according to the amplitude variation associated with the motion phases. An ideal phase splitting would be that these phases were defined in such a way that the organ can be considered as motionless during each phase.

Additionally, we will see in Chapter 4 that the precision of the sensor is not necessarily as crucial here as in other works. Indeed, in our work, we only use the signal for SPECT imaging for a preliminary listmode gating step: the delimitation of each consecutive respiratory cycle based on an amplitude motion thresholding. The suppression of the motion artefacts themselves will be done by a specific method that we will detail in Chapter 4.

2.4 Conclusion

One of the strong points of this work is its interdisciplinary nature, between image analysis and biology. The material presented in this chapter is the link between those two research domains. In this chapter, we focused on the material and biological aspects, and presented many related constraints. We summarise below the constraints, the decisions we took for this study and their consequences.

Animal model First, our objective is to study tumour growth, and in order to do this, we chose to observe cells expressing the protein NIS. For this, we have seen that the animal lineage had to be highly immuno-depressed (NK lymphocytes); we chose the lineage NOD-SCID.

We chose to inject the cells intra-peritoneally inducing tumour growth in the peritoneal area, subject to significant movements.

Anaesthesia We chose isoflurane as anaesthetic gas which is the most flexible anaesthesic technique since we want to maximise the duration of the experimental period and to optimise the quality of acquisitions during this period. The chosen anaesthesia is the less invasive and allows fast recovery for the health of the mouse.

Frequency of acquisition Here a compromise has to be made: frequent acquisitions gather more longitudinal information, but may interfere with the tumour growth. We chose to acquire images once a week.

Motion Due to the fact that imaged tumours are in the peritoneal area, the acquisition will be impaired by respiratory induced movements of the imaged area. Also the chosen anaesthesia, isoflurane, induces a change in the respiratory pattern. Consequently, the movement will have to be studied, monitored, and taken into account to improve the accuracy of our acquisitions.

Motion signal detection To monitor the animal motion, a pressure cushion has been chosen. Due to the particular respiratory motion pattern and the importance of the induced movement, we only use this sensor for detecting breathing cycles.

The following constraints depend on the imaging modality chosen.

For SPECT imaging, the problem here is to choose the adequate radiopharmaceutical product. It has to be adapted to the camera and to the cells we want to observe. Among the available products, we chose ^{99m}Tc-pertechnetate. Since ^{99m}Tc half life is relatively short (6 hours), a compromise has to be done between the dose of injected radioactivity and the duration of the acquisition. If the dose is too low, the acquisition will have to be longer in order to obtain an image with a good signal-to-noise ratio. If the dose is too high, this could interfere with the tumour growth.

For CT imaging, the only constraints concern the camera settings that must be chosen carefully to ensure a good contrast and accuracy in the region of interest. The setting that has been chosen is "Fast Scan", corresponding to a dose of 36 mGy for one FOV, a tube current of 32 mA, and a tube voltage of 70 kV. It has a good compromise between acquisition duration and irradiation of the animal.

Some works consider the joint use of CT and SPECT imaging, the main advantage is that CT image could be used for anatomical registration while SPECT provides biodistribution information [SDP+03]. However, the anatomical information included in the CT is not sufficient. If more detail on abdominal area is needed, the use of CT contrast agent could be considered, but this will also increase the difficulties in preparing the animal (multiple injection with unknown side effects). Thus, we directed our investigations toward a method dedicated to SPECT, neglecting CT image information.

All the constraints and resulting choices presented in this chapter will have an impact on the methods that will be considered for the motion correction as we will see in the following chapter.

Part I

RESPIRATORY MOTION

Chapter 3

State of the art about respiratory motion correction methods

Contents

3.1 Introduction

To acquire static images from a moving target is a real challenge. It depends on the relative speed between the observed motion and the imaging modality. The difficulty lies in the determination of a type of acquisition that is adapted to both the motion of the organ of interest and the modality.

In clinical and pre-clinical imaging, different types of motion have been identified [MAB94]: involuntary subject motion with only one occurrence, physiological cyclic motion such as cardiac and respiratory motions, and physiological non cyclic motion induced by digestion for example. Involuntary subject motion cannot be predicted in advance but one can prevent the subject from moving by using anaesthesia and mold especially for infants, elderly, or animals. If the acquisition duration is longer than the motion duration, as it is the case in small animal single photon emission computed tomography (SPECT) imaging, specific methods have to be developed. Cardiac and respiratory motion have been frequently studied since there are cyclic and the duration of a cycle is shorter than some acquisition sequence.

Two types of acquisition approaches have been developed. The motion can be considered as soon as the image acquisition with gating approaches, or a posteriori during the image reconstruction. The choice is done according to the modality characteristics and the type of observed physical phenomenon: X-rays for computed tomography (CT), gamma photons for SPECT, radio-frequency waves for magnetic resonance imaging (MRI).

Generally gated acquisitions are frequently used for CT since images are reconstructed from a set of X-rays projections. Each projection is obtained from a short time X-ray shoot at different angular views around the subject, and the X-ray shoots can be gated according to the signal (gated acquisition).

Concerning emission tomography (ET) images, the acquisition process is usually longer than the respiratory motion and motion is taking into account more frequently at the reconstruction step. In SPECT imaging, the observed phenomenon is one single gamma photon emitted by radioactive decay. In positron emission tomography (PET), the observed phenomenon are two 511 keV gamma photons being emitted at almost 180 degrees to each other by annihilation of one positron emitted by decay. The reconstructed tomography images will then give the biodistribution of the radioisotope, and as a consequence the distribution of the targeted cells. Radioactive decay is a continuous process and not controllable, so there are emission of gamma rays at any time of movement if one. Thus, the acquisition and reconstruction processes have to take into account the motion of the organ of interest at the time of acquisition.

As in this thesis we work with a pre-clinical SPECT/CT camera, we will focus this chapter on motion correction methods dedicated to these two modalities. First, we detail the motion effects in ET that justify the necessity to find an appropriate motion correction method. Then, we go through different solutions for ET that have been developed and proposed in the literature. Finally, we discuss the advantages and drawbacks with respect to our subject in order to introduce the method that we present in Chapter 4 "Amplitude-based data selection for optimal retrospective reconstruction in micro-SPECT".

3.2 Motion effects in emission tomography (ET) images

ET give images of radiopharmaceutical biodistribution in the subject. This modality permits to localise group of cells by their ability to accumulate radiopharmaceuticals.

As previously mentioned, the acquisition is done during a continuous period of time dependent on the activity of the injected radiopharmaceutical. Thus, when there is a radiopharmaceutical uptake in a region submitted to

motion, the source is moving and the emitted photons coming from the same source will hit the detector at different locations. The reconstruction will lead to a blurred image and quantification will underestimate the real target uptake.

In the context of our work, we wanted to be able to detect small intra peritoneal lesions as soon and as small as possible, and to follow quantitatively their growth along the time. Chapter 4 will describe our approach for motion detection in this context. If the lesion is submitted to motion, the emitted gamma photons will be spread around in a wider region of the image and the average activity in that region will then be reduced. As a consequence, the lesion can either be not detected or wrongly quantified. The first case is frequently met when the average activity is too low and the hotspot cannot be distinguished from the noise.

When the average activity is still above the noise (second case), it is still possible to detect the lesion but the location is less accurate, the definition of the size will lead to a larger lesion volume and quantification will be biased.

Since a longitudinal study based on ET will consist in comparing lesion size, the quantification measure have to be reproducible especially for a group study. If the motion was identical for all subjects and at all times, the impairment will be the same and the measures would be comparable. However, respiratory motion is cyclic but not very reproducible, motion correction methods have to be developed in order to avoid the reduce the bias on the size measurement.

3.3 Methods for image acquisition and reconstruction of moving subjects

This section provides a more detailed state of the art to complement the Section 4.1.

3.3.1 How to get rid of motion effect in emission tomography imaging?

We identified two main techniques to prevent motion from affecting image acquisition and reconstruction:

- motion gating, which consists in acquiring or reconstructing images when the subject is not moving or when there is momentarily no motion (at the time of the acquisition) [NER+03, VLB+07];
- motion compensation, which consists in incorporating a motion model in the image reconstruction algorithm [RMK+07].

A variant of the motion gating approaches, called motion correction, has been characterised as a third technique. Motion correction works on dynamic or three spatial + 1 temporal dimensionss (4Ds) image. It consists in registering each three (spatial) dimensions (3D) image of a sequence to the first image [BB09], and adding up all registered images to a single 3D image [BB11]. In this section, we present motion gating approaches first, then motion compensation methods, and finally one major variant of the motion correction methods.

For human, a trivial solution is to stop the considered motion at the time of acquisition, this is the purpose of breath-holding and this assumes that the duration of acquisition is short enough. The drawbacks of their approach is that it only works for short-time acquisition, basically CT, and cannot obviously be applied to animals.

For small animals, an other cheap method is to constrain the respiratory motion by banding the chest [DCMW+04]. However chest banding changes the geometry of thorax, and affects the respiratory motion. So the motion might be reduced enough for the lesion detection from the operator point of view (no dorso-ventral or ribs enlargement). Indeed, the motion is just constrained and it might enlarge the inside motion in the craniocaudal axis. That is why more sophisticated methods such as gating appear to be necessary for accurate quantitative study.

3.3.2 Motion-gated and dynamic acquisition

3.3.2.1 Definition

Motion gating methods consist in conducting data acquisition and image reconstruction at a time when the object of interest is considered as still. To detect the time when the object is still, we use an additional signal representative of the motion, such a signal is called the physiological signal. This time is determined according to this physiological signal: usually we consider the physiological signal as cyclic modulo amplitude, i.e. still and moving phases appear cyclically potentially with a different movement amplitude in each cycle. The physiological signal can be divided into a number of time or amplitude slots called gates or bins. In each gate, the imaged object is assumed to be static. It is then possible to acquire data at one (or several) time(s) corresponding to these gates. When several gates are defined, the set of gated data is reconstructed into a sequence of gated images. In the resulting gated image or sequence of gated images, the subject of interest can be considered as still at all times. The sequence of gated images is also called dynamic image or 4D image.

The number of gates has to be adapted to the respiratory motion pattern and the statistical noise [BRG09]. Bettinardi et al. showed that this number is

a function of the lesion size and displacement. However, the method proposed by Bettinardi et al. relies on a breathing training adapted to the patient in order to acquire the most regular breathing signal possible. In the context of small animal, a breathing training is out of context. The alternative would be to ventilate the animal but, as explained previously, ventilation is invasive, requires additional hardware and animal settings. It also prevents from longitudinal imaging (daily or weekly frequency) because it may harm or kill the animal.

Gating methods are also used for therapy planning [MDB+11]. Mancosu et al. proposed a semiautomatic method to determine the best phase of the respiratory cycle for gated radiotherapy (RT) in lung region with extrinsically prospectively gated 4D-PET/CT acquisitions. Such gated approach helps in determining the best and most accurate segmentation of the lesion to avoid other organs during RT. In this example, both dynamic PET and CT were used to determine intrinsically the motion of the lesion geometric center with a combination of image processing: maximum intensity projection, segmentation and thresholding.

3.3.2.2 Types of gating methods

Among all the motion gating methods [BPD+10], it is possible to distinguish:

- prospective [VLB+07] from retrospective [DLJS06] acquisition gating;
- intrinsic [BDS+09] from extrinsic [vHJ+11] retrospective gating;
- amplitude-based [BB11, BPD+10, BDS+09, BED+10, CCP+10, DFBM09, NHAQ+11, SOM11, vHJ+11] from phase-based gating [BPD+10, BMME+08, DFBM09, GRS+09, LRS+06, MDB+11].

Prospective gating methods consists in acquiring data at specific gates. These gates are determined before or simultaneously to the acquisition itself. Simultaneity is possible thanks to the synchronisation between the camera and the external physiological signal. This signal has to be analysed in real time. In a prospective mode, acquired data are directly assigned to one of the bins. Usually, prospective mode is used for 4D-CT and the gates correspond to time slots.

Retrospective gating consists in sorting imaging data into different gates after the acquisition. Data are acquired first, and then sorted into gates. Retrospective gating mode is frequently used for ET since data are recorded in mode list (continuous acquisition) with triggers as gate markers. Then, triggers can be taken into account for the reconstruction.

Physiological signals are normally recorded simultaneously to the data acquisition from external sensor. When it is used for gated acquisition, it is called extrinsic gating. Physiological signals can also be extracted from the

data itself. In that case, gating mode is called intrinsic gating. The only way of acquiring the cardiac signal with external sensor is the electrocardiogram (ECG) in which characteristic phases can be clearly identified such as end of systole or diastole. For the respiratory motion, signals can be recorded by different means using Real-time position management, pressure sensor (chest belt) or optical fiber among others. Only two characteristic phases can be identified, the end of inspiration and expiration.

The advantage of extrinsic gating is that it is frequently used since a wide set of sensors and external monitoring systems have been developed. It is also interesting since it gives an external observation of the motion. Moreover, it is frequent to observe the extrinsic signal for a small period of time before the acquisition in order to define the parameters of gating in advance. On the contrary, intrinsic gating advantages are that the intrinsic signal does not rely on external monitoring systems. However, intrinsic gating requires additional step after the acquisition itself, which means that the gated image are not reconstructed directly after acquisition.

Both phase-based (or time-based) and amplitude-based gating mode refers to the distribution of data in a set of gates, with the assumption that the motion can be neglected within each gate. In the case of a phase-based gating, the bins are distributed with respect to the length of physiological cycles. Phase-based 3D reconstructed images may still exhibit some residual motion artefacts, and quantitative measurements are generally performed in 'most still' phases, typically at the end of expiration [MSL+10] or inspiration [FWHD07] for respiratory motion. While in the case of an amplitude-based gating, the bins are distributed with respect to the amplitude of physiological signal. The amplitude variation of this physiological signal can usually be associated with specific characteristics of the observed physiological motion. For example, with pressure sensor, lowest pressure amplitudes correspond to expiration and highest amplitudes correspond to inspiration. It is then possible to select the range of amplitude to select data for amplitude-based gated reconstruction. Thus, images at end of expiration or inspiration can be reconstructed by selecting either the lowest or the highest amplitude values. More examples of such parallels between the observed signal and the motion are given in the Section 2.3.2, in the paragraph about respiratory motion sensors.

In theory, any combination of gating methods is possible but according to the imaging modalities, some are preferred to others. Table 3.1 summarises different combination of gating methods described in the literature.

Extrinsic prospective gating Usually, prospective gating mode is combined with extrinsic gating. This approach has been explored both for human and small animal. In [BDS+09], cardiac signal is obtained from electrocardiogram (ECG). In [MDB+11], respiratory signal is obtained from real-time position management (RPM). These signals have been all used for

Table 3.1: Number of gates in literature for motion gated reconstruction. **pro.**: prospective, **retro.**: retrospective, **intr.**:intrinsic, **extr.**: extrinsic, **phas.**: phase-based, **ampl.**: amplitude-based

Reference	Modality	Physiological signal	Organ	Gating mode and mode	Number of gates
Nehmeh [NER+03]	PET	respiratory	lung tumour	pro. extr. phas./ampl.	5
Nehmeh [NER+03]	PET	respiratory	lung tumour	retro. intr. phas./ampl.	1 (?) 5 (?)
Cavanaugh [CJP+04]	μ-CT (muCT)	respiratory	lung	pro. extr. phas.	1
Dawood [DLJS06]	PET	respiratory	lung	retro. phas.	8
Visvikis [VLB+07]	PET	respiratory		extr./intr. phas.	8-10
Bettinardi [BPD+10]	CT			pro. phas.	1 or 2 (end-exhalation / end-inspiration)
Bettinardi [BPD+10]	CT			retro. phas.	10
Buther [BDS+09]	PET	respiratory + cardiac	heart	retro. intr. ampl.	8
Buther [BED+10]	PET	respiratory	lung/liver tumours	retro. extr. ampl.	3; 8
Mancosu [MDB+11]	CT	respiratory	lung tumours	retro. phas.	10
Mancosu [MDB+11]	PET	respiratory	lung tumours	retro. phas.	6
Van Elmpt [vHJ+11]	PET	respiratory	lung tumours	retro. extr. ampl.	1

extrinsic prospective gating acquisition mode.

In human SPECT imaging, some gating approaches take into account several physiological signals (cardiac and respiratory signals). In [BRG+08], Bitarafan el al. present an amplitude-based extrinsic prospective gating approach for cardiac imaging with respect to respiratory signal. A preliminary step consists in dividing respiratory signal into three parts with respect to the amplitude range of motion. The lowest part corresponds to the appropriate time for gating. Afterwards, synchronised cardiac and respiratory signal are analysed in real time (while acquiring data). Data are then acquired on the third lowest amplitude bin. At the end, a dynamic cardiac SPECT is obtained where the cardiac motion is divided into 8 time gates. This method is adaptable to each patient breathing pattern upon condition that the pattern remains identical during the whole acquisition.

In small animal imaging, approaches have been developed mainly for CT imaging. However almost no work mentioned any method for SPECT. Cavanaugh et al. [CJP+04] are among the first to mention respiratory gating in small animal CT in order to study lung tumours. Animals were ventilated and an extrinsic prospective gating was used with lung ventilation signal as physiological data. The aim was to study and to measure the largest lung lesions after several weeks of growth, and to compare them with the ground truth. The major drawbacks of the presented method were that the intubation harms the animal and the sacrifice of animals that ruled out the long term studies. Later, longitudinal study of lung tumours was performed with CT. Pulmonary tumors growth was quantified from a sequence of respiratory-gated 3D-CT [HTM+08]. However, early lesions could not be detected and the reconstruction process was sensitive to motion.

Extrinsic retrospective gating In ET imaging, it is sometime wiser to determine the gates after the whole acquisition is finished. Extrinsic retrospective gating requires both imaging data and synchronised physiological signal acquired simultaneously to the imaging data. Van Elmpt et al. [vHJ+11] propose a retrospective amplitude-based extrinsic gating method for human PET image. The respiratory signal was acquired simultaneously to the list-mode PET acquisition and was analysed after the acquisition. The method consists in determining the best motion amplitude range from the analysis of this signal. The optimal amplitude slot was defined as the narrowest amplitude range containing 35% of the respiratory signal. Then, the gated reconstruction was done with all the data corresponding to this amplitude range. The advantage of this approach is that it allows the consideration of all variabilities in the extrinsic signal, such as changes over the time in the amplitude range of motion or motion rhythm. On the contrary, prospective gating are usually based on predetermined non-adaptive thresholds. For example, it is frequent that anaesthetised animal have time when they breath faster or more

deeply for a few periods of time. That is why retrospective gating approaches are interesting. However, this kind of approaches requires additional work after the acquisition in order to adapt the gating in order to optimise the reconstruction.

Intrinsic internal gating Instead of using an external sensor, respiratory and cardiac motion signals can be extracted directly from the acquired data. Methods dedicated to human ET [BDS+09] as well as small animal CT [Bar, KDZ+10] have been developed.

In [Bar], Bartling et al. focus on thoracic small-animal CT imaging which is affected by respiratory motion. Authors present a method for generating respiratory gated images from the X-ray projections. First, spatial features from the numerous 2D projections are extracted: the z-axis of the centre of mass (COM) of region of interest (ROI). The variation of z-value depicts a respiratory-like signal along the time of acquisition. Then, the projections are sorted into several gates that correspond to the different phases of the respiratory cycle. Finally, gated 4D image can be reconstructed from this set of gates. The advantages of this method are that it is independent of external gating system and it can be extended to other motions such as cardiac motion [BKS10]. The process has been improved and automated later in [KDZ+10], in such a way that both physiological signals (respiratory and cardiac) are now extracted from the X-ray projections. Moreover, the ROI delineation is now automatic and based on the diaphragm position. The projections are sorted accorded to their angle position. The diaphragm motion is detected for every angle set and permits to position the ROI for the following step. The advantage is that the method is fully automatic while the drawback concerns the ability to acquire many X-ray projections: 500 projections per rotation angle, with a rate of 100 projections per second. This means that each X-rays projection has to be shorter than 10 ms. At the end, only few projections are finally used for reconstruction. Furthermore, the animal have to breath with a particularly low respiratory rate (ranged from 18 to 35 cycles per min that is 1.71 to 3.33 sec per cycle). In comparison, with the camera at our disposal, X-ray projections last at least 16 ms, and with isoflurane anaesthesia, mice were maintained with a respiratory rate range from 60 to 100 cycle per min (see Section 2.3.2). Another drawback of this approach is the irradiation of the animal induced by the large number of X-ray shoots.

Concerning ET, Büther et al. presented two methods [BDS+09, BED+10] to obtain respiratory and cardiac motion signals intrinsically from PET list-mode. The features that they used are the COM and sensitivity of the field of view (FOV). Then, both amplitude-based and phase-based gating method can be used. Some work highlighted that amplitude-based gating is more accurate than phase-based gating [DBL+07]. Thus, amplitude-based gating method has been used for sorting listmode data into 8 bins according to both

cardiac and respiratory motion signals. This method has been applied to both cardiac [BDS+09], and, with additional image segmentation step, tumour motion [BED+10]. The best results were obtained for signal extracted from COM features.

Intrinsic external gating Usually, intrinsic gating is combined with retrospective gating approaches [KDZ+10]. Nehmeh et al. [NER+03] are among the first to propose this kind of method: retrospective gated PET reconstruction based on intrinsic motion information. The intrinsic information comes from an additional source fixed to the body surface and imaged in the FOV. A dynamic PET (set of 200 3D PET images with one millisecond time window) is performed, assuming one-ms is a short time with respect to the respiratory cycle. Then post-reconstruction analysis on this dynamic PET permits the tracking the source motion. The position variation is assumed to be synchronous to respiratory motion. This data is then assimilated to respiratory signal. Gates or bins are then determined as previously described and data corresponding to specific position of this source during the respiratory cycle were used for retrospective reconstruction.

The advantage of this approach is indeed that it works for imaging without anatomical reference. It is also the best solution when one extracts the information from the imaging data, since it is harder to analyse in real time the imaging data in order to determine the gating. It is compatible with imaging without external monitoring system whether it be a choice or a constraint. The drawback for most of retrospective gating method is then to acquire enough data in order to make sure that the amount of data that will be kept for gated reconstruction will be sufficient to not affect the quality of the resulting image.

3.3.3 Motion compensation

Correction for respiratory motion can also be applied directly into the image reconstruction process. This is called motion compensation [RMK+07, Rey05, LLC+07, BB11]. These approaches distinguish from gating-based methods since they include a respiratory motion model into the reconstruction algorithm. It does not require any external signal representative of physiological motion, but a prior model for this motion. The motion model can be estimated from the study of dynamic image (typically MRI) and various other physiological measures. Different level of complexity in model building can be achieved, with more or less phases.

For example, Lamare et al. propose respiratory motion compensation methods based on affine [LCS+07] and elastic [LLC+07] transformations of PET raw data. These method are tested on human phantom, with respect to an extrinsic respiratory motion signal. The elastic-transformation method

may also be improved by incorporating attenuation correction from corresponding CT. The best results are obtained with the improved method, given uniform improvement for different size lung lesions. The corrected listmode is then used for the reconstruction of a single motionless image. Bundschuh et al. [BMME+08] estimate intrinsically to the list-mode the local motion of an organ. The deformation is then directly applied to the data. The reconstruction is performed on the corrected listmode.

In fine, the motion model consists of a deformation step which corrects for the organs motion between each consecutive phases of the motion. Once the model is set up and validated, it can be incorporated into the reconstruction process for other imaging modalities. Motion compensation methods aims at using all the data that is available.

The advantage of such approaches is the accuracy of the resulting image as well as the fact that all acquired data are used. However, it requires a motion model that matches with the observed motion in the subject. For example, if a subject has lung lesions, the endured pain can induce changes in the breathing motion pattern. The same goes for subject (animal) that have the chest banded, or that lying on the back or on the abdomen during the acquisition, since this might constrain the motion in other than natural motion. In these cases, the model should be adjustable in order to match with the motion variabilities.

3.3.4 Motion correction

A variant for motion gating is the motion correction. Motion correction approaches are based on registration of prior prospectively motion gated acquisitions.

An overview of techniques concerning the respiratory motion correction in ET is given in [VLB+07]. The motion correction can be done either on the reconstructed 4D images or on the raw data. Basically, the idea is always to find the best deformation description between two images at two different motion phases, to realign the images with respect to a reference phase and then to sum all realigned images into an average image. The aim for respiratory motion correction in PET/CT is the same as for motion compensation or motion gating techniques: maximise the signal-to-noise ratio (SNR), improve the accuracy of quantification, and minimise the motion artefacts.

When working on 4D images, one phase is selected and used as reference, and then all others are registered to the reference one. In that case, motion correction for 4D image consists of image or frame registration followed by summation of the registered images or frames. The registration techniques are numerous: from simple linear transformation including rotation, scaling, translation, and other affine transformation to nonrigid transformation algorithms (elastic, demons, B-splines or optical flow). It slightly

differs according to the registered data: with ET images, methods are generally based on optical flow [DLJS06, DBJS08, DKF+08] or on B-splines deformation [BB09, BB11] while elastic registration is used with multimodal acquisitions such as PET/CT images. The transformation parameters are usually estimated iteratively from image-derived features by analysing how a source volume should be translated and rotated in order to better align with the reference volume.

For example, Bai et al. [BB09] proposed a deformable registration method based on regularised B-spline dedicated to respiratory motion correction in PET images. Improvements for this method have been later presented in [BB11]. This improvement concerns the attenuation correction. An extension to B-splines 4D image registration is to improve the image resolution. Authors in [WLKV11, HMW+12] describe a method which combines the spatio-temporal information from the registration of 4D PET images with maximum a posteriori (MAP) algorithm. MAP algorithm produces a higher-resolution 4D PET image. The higher resolution motion corrected 3D PET image is the result of the summation of the registration of this higher-resolution 4D-PET image. Then, after registration of all 3D image to the first image of the higher-resolution 4D PET image, all registered 3D image are summed up to a higher resolution motion corrected 3D PET image.

A third alternative motion correction approach consists of motion blur reduction. Xu et al. [XYY11] consider that the motion blur can be modelled as a point spread function (PSF). The 2D PSF is estimated directly from the reconstructed PET image. PSF parameters are estimated from image intensity derivation along different angular directions. Then the motion blur is corrected with a deconvolution algorithm using the resulting 2D PSF and wavelets.

As a conclusion, motion correction approaches advantages are that they aim at using all data available for reconstruction, even though the motion itself is not well known, thanks to a wide range of registration methods (both for raw data or images of a sequence). However, for ET, these approaches often require additional correction steps for making sure that final reconstructed image is correct in term of estimated activity in lesions.

3.4 Discussion

Remembering that our study is a preliminary work for lesion study, we want to find the best approach that is also as simple and fast as possible with respect to the tools and constraints that we have. For ET, the ideal method would be a motion compensation method since this kind of approaches uses all the data available and the reconstructed image activity is closer to what we should have without motion artefacts. However, there are drawbacks that

prevent us to consider it. First, we don't have a motion model for the mice respiratory motion. But still, if we needed to build such a motion model, it would have required additional time, tools and experiments. Moreover, the uptake of the motion model into the reconstruction process also requires either knowledge and modification of that process, or development of a new process. The complexity for elaborating the motion model encouraged us to look for a simpler method.

Motion correction methods also tend to use all the data. First registration step is usually done on anatomical modality images (e.g. CT): either on the data that will be used for the following, or on synchronised data with the other modality acquired simultaneously. This is then perfect when both coupled modality can be acquired simultaneously. However, in our case, the dynamic CT cannot be acquired at the same time as SPECT. Then, the registration and following sum up steps have to be processed directly on the dynamic SPECT, without the anatomical reference. All together this might degrade the main information that needs to be preserved: the activity. As a consequence, an additional interpolation step has to be considered and carefully chosen [HSO+95]. The approach that is developed for gated images could be considered in our case at the condition that the gating information is reliable, and that all data used for the reconstruction of each phase correspond exactly to the same motion phase.

In our case the gating information is not as reliable as expected: a time shift between respiratory-like signal recorded thanks to the pressure sensor and the motion measured on data itself was observed. This suggests that pressure variation and the intrinsic motion information are not synchronous. The question is then which motion information to believe. As the motion is impairing data, one decided to find an approach that takes into account the intrinsic motion information.

This led us then to consider the motion gated techniques. Although the advantage is that gating approaches are rather simple, the difficulty lies in the determination of the gates. If not well defined, the gated acquisition might not correspond exactly to the same motion phase for each cycle. Then, the reconstructed image will be impaired by motion. This problem can occur when the physiological signal is not perfectly cyclic (both with respect to amplitude or phase) and when acquisition are done in a prospective gating mode. This might be often the case in CT. In the case of retrospective gating reconstruction methods (for ET), only a small fraction of the available data is used for each gate. The reconstructed images will have a low SNR that is inappropriate for activity quantification. However regarding our technical constraints (see previous Chapter 2) and the nature of the animal respiratory signal (gasps), a method using gating approaches is the best choice. The main drawback is that gating in SPECT means using a fraction of available data. What we decided is then to elaborate a gating method that will maximise

the fraction of available data used with respect to the physiological signal and without a complex registration step.

In the next chapter, we will describe our method, based on well defined gating parameters. Among others, our method achieves in using around 65% of available data for the motionless reconstruction of small animal 3D SPECT image.

Chapter 4

Amplitude-based data selection for optimal retrospective reconstruction in micro-SPECT

Contents

This chapter presents in its entirety the following journal paper: M. Breuilly, G. Malandain, J. Guglielmi, R. Marsault, T. Pourcher, P.R. Franken and J. Darcourt. *Amplitude-based data selection for optimal retrospective reconstruction in micro-SPECT*. Physics in Medicine and Biology, 2013.

Respiratory motion can blur the tomographic reconstruction of PET or SPECT images, which subsequently impair quantitative measurements, e.g. in the upper abdomen area. Respiratory signal phase-based gated reconstruction addresses this problem, but deteriorates the signal-to-noise ratio and other intensity-based quality measures. This article proposes a 3D reconstruction method dedicated to micro-SPECT imaging of mice. From a 4D acquisition, the phase images exhibiting motion are identified and the associated list-mode data are discarded, which enables the reconstruction of a 3D image without respiratory artefacts. The proposed method allows a motion-free reconstruction exhibiting both satisfactory count statistics and accuracy of measures. With respect to standard 3D reconstruction (NG3D) without breathing motion correction, an increase of 14.6% of the mean SUV has been observed, while, with respect to a gated 4D reconstruction (G4D), up to 60% less noise and an increase of up to 124% of the SNR have been demonstrated.

4.1 Introduction

Molecular pre-clinical imaging is a major research tool which provides non-invasive *in vivo* information on cellular processes and allows longitudinal studies [PGW10, FAMH08, KC08]. In oncology, obtaining measurements of tumour characteristics is mandatory. Emission tomography (ET) quantification is hampered by physically induced biases such as attenuation, scatter and partial volume effect, as well as by motion artefacts. In clinical imaging, the physical biases can be corrected in Positron Emission Tomography (PET) as well as in Single-Photon Emission Computed Tomography (SPECT) [RVHK11]. However, there are few studies addressing specifically the quantification issues in pre-clinical imaging. Concerning physical biases, Hwang et al. [HFGH08] showed that for technetium-99m (^{99m}Tc), attenuation and scatter errors are reduced in small animal SPECT compared to clinical SPECT. Therefore, respiratory motion compensation is one of the main obstacles of accurate quantification in micro-SPECT (μ-SPECT).

Computed Tomography (CT), PET or SPECT images are produced by a tomographic reconstruction from the projections of the object of interest, with the implicit assumption that the imaged object remains still during the projection acquisition. Motivated by the respiratory and cardiac motion observed in clinical practice, a number of motion handling methods have been developed, with the goal of reconstructing images free of motion artefacts. A trivial approach consists in controlling the considered motion during the acquisition, by breath-holding, for example. This is only valid for human imaging and short-time acquisition techniques such as CT or Magnetic Resonance (MR).

Motion artefacts can also be handled by gating protocols. An additional signal, which is considered representative of the motion of interest, is recorded and synchronised with the data acquisition. Reconstruction is then based on a selection of the acquired data. Such signals can be acquired by an external device and include electrocardiogram [LRS+06], Real-time Position Management [GRS+09] or Multidimensional Respiratory Gating [NHAQ+11], pressure sensor (chest belt) [CCP+10, vHJ+11], and optical fiber [BLW+12]. These signals can also be extracted directly from the data itself, by looking for time variation in raw projections in CT [KM11] or in ET [BMME+08, SOBM09].

For periodic signals, phase-based gating consists in dividing the period into several phases of equal duration, with the assumption that the motion can be neglected within each phase. This method is used for both cardiac [BED+10] and respiratory [BPD+10, BMME+08, GRS+09, LRS+06] gating for human imaging and allows the reconstruction of dynamic or 4D (3D+t) images. Using only a fraction of the acquired data deteriorates the signal-to-noise ratio (SNR) of each 3D image. Therefore, Dawood et al. propose to co-register each 3D image and then to sum them up [DLJS06]. With this method, obtained 3D images have minimal motion artefacts and improved SNR.

Furthermore, amplitude-based gating assumes that the signal amplitude is representative of the motion of interest. A range of amplitude values is selected, and the associated acquired data are used for reconstruction. For instance, images at end of exhalation or inhalation can be reconstructed by selecting either the lowest or the highest amplitude values. In human imaging, such a method has been used for cardiac motion in SPECT [KIK+07] and for respiratory motion in PET [BPD+10, CCP+10, NHAQ+11, SOBM09, vHJ+11].

When a motion model is available, some authors proposed to incorporate it into the tomographic reconstruction procedure in order to take into account all the acquired data to reconstruct a 3D still image. In human imaging, cardiac [BVMA04] and respiratory [LLC+07, RMK+07] motion models have been developed. In addition to the difficulty in defining an accurate motion model, such methods also imply a huge computational cost.

In human imaging, motion compensation has been studied in CT or PET [NE08, Luc09]. In pre-clinical imaging, the methods are similar. For instance, Kuntz et al. used phase-based gating [KDZ+10]. However the literature is less abundant than in the clinical field and mostly concerns μ-CT [GJQ+11, MSL+10].

In this article, we propose an amplitude-based gating reconstruction method in mice μ-SPECT. The signal obtained from an external pressure sensor is filtered and allows the reconstruction of an initial 4D image, which is then analysed to detect the respiratory induced motion. We take advantage

of the particular breathing pattern of anaesthetized mice to detect motion-corrupted phases, and subsequently use all raw data corresponding to the motionless phases to reconstruct a single motionless 3D image.

4.2 Materials and methods

4.2.1 Animal model

The different methods were tested on data obtained on 3 female mice of a mouse model. The mouse model consisted of NOD-SCID mice with intra-peritoneally injection of 1.5 million cells of rat colonic adenocarcinoma expressing the Natrium Iodide Symporter (PROb-mNIS) in 50μL of Phosphate Buffered Saline. SPECT/CT acquisitions were performed after 1, 2, and 3 weeks of growth, and PROb-mNIS peritoneal nodules of NIS-transfected cells were observed. However, we considered only 8 acquisitions out of the 9 for our study, since the Biovet pressure signal failed for one acquisition.

Animal housing and procedures were conducted according to the guidelines of the French Agriculture Ministry and were approved by the local ethics committee.

4.2.2 Imaging protocol

We acquired experimental animal images using a dedicated small animal SPECT/CT scanner (eXplore speCZT CT 120, GE Healthcare Bioscience, London ON, CA).

The SPECT imaging part of this camera consists of a fixed full-ring of detectors coupled to a rotating 7-pinhole collimator for mice. The ring of detectors is composed of 10 panels of 4 CZT detectors. SPECT acquisitions lasted around 18 min. The output of the camera is a list-mode record of all CZT detected events : each event consists of the detection time (ms), the gating indices, and the properties of the detected photon. SPECT reconstructions used data from the list-mode in the energy window from 125 to 150 keV, according to the energy of 99mTc.

Mice were injected intra-peritoneally 180 MBq in 400 μL of ^{99m}Tc-pertechnetate. Five minutes later, the animals were anaesthetized with isoflurane (1.3% v/v) (Baxter, France). The animals were placed prone and freely breathing (without mechanical ventilation) on the bed and kept sedated during the whole imaging protocol, using inhaled anaesthetic.

A monitoring system (BioVet, m2m Imaging Corporation, Newark, USA) was used with a pneumatic pressure sensor. The pressure sensor was placed under the animal abdomen. The pressure signal was recorded (1 ms-sampled rate) and used to monitor the animal anaesthesia.

Body temperature was maintained at 37°Celsius and anaesthetized gas rate was regularly controlled to keep the respiratory rate between 60 and 100 breaths per minute. Once a stabilized respiratory rate was reached, the SPECT acquisition started.

At the beginning of each acquisition, an amplitude threshold was arbitrarily fixed in order to detect the falling edge of the pressure signal variation. Each time the signal passed this threshold, a trigger was recorded in the list-mode SPECT acquisition data to be used for reconstruction. We assumed that this trigger corresponded to the same time in the cycle for each respiratory cycle. A respiratory cycle is then defined by the interval between two consecutive triggers.

4.2.3 Reconstruction algorithm

SPECT reconstruction was done using the Ordered Subset Expectation Maximization (OSEM) algorithm [HL94]. We used from 7 to 9 subsets and from 6 to 9 iterations, the number of EM equivalent updates ranged from 54 to 56. For a given set of data, the number of subsets and iterations were kept constant for all the reconstruction methods.

4.2.4 "Standard" reconstruction methods

In this section, we describe the different kinds of SPECT reconstruction methods for the list-mode, resulting in either 3D or 4D images. We start with the reconstruction that are provided by the camera and then we introduce the improvements which lead to our final reconstruction scheme: a breath-hold like 3D image.

4.2.4.1 Non-gated 3D reconstruction

Non-gated 3D reconstruction (NG3D) consists in reconstructing a single 3D image using all data recorded in the list-mode within the range of energy corresponding to the radiopharmaceutical used.

4.2.4.2 Gated 4D reconstruction

Gated 4D reconstruction (G4D) consists in reconstructing a temporal sequence of N 3D images. The number of phases N is set to 15 in the experiments. Using the trigger set in pressure signal, we compute the respiratory cycle average duration, denoted by $\overline{C}$, over the whole acquisition. The duration of each reconstruction window is then $D = \overline{C}/N$. Therefore the n^{th} gating window of the i^{th} cycle is defined by the temporal interval $[t_i + (n-1)D, t_i + nD[$ where t_i is the time of the i^{th} trigger and $n \in [1, N]$. A 3D image for each gating

window is then reconstructed from the data of the corresponding window. The raw data (list-mode) used is the same as for NG3D reconstruction.

4.2.5 Proposed Method

The proposed method is a combination of three main steps that are described here: a cycle filtering which consists in cycle pre-selection according to duration, a cycle resampling, and an image-based motionless phase detection. This method denoted by breath-hold like 3D reconstruction (BH3D) gives 3D images without motion artefact.

Cycle selection

Figure 4.1: **Histogram of cycle duration** This figure presents the distribution of cycle duration for a pressure signal record, with its Gaussian curve fit. Vertical red dotted lines indicate the average cycle duration $\overline{C}$ (middle) and the two limits $\overline{C} - 3\sigma$ and $\overline{C} + 3\sigma$ that have been defined for the cycle selection. Cycle with a duration outside the limits are discarded for following reconstruction.

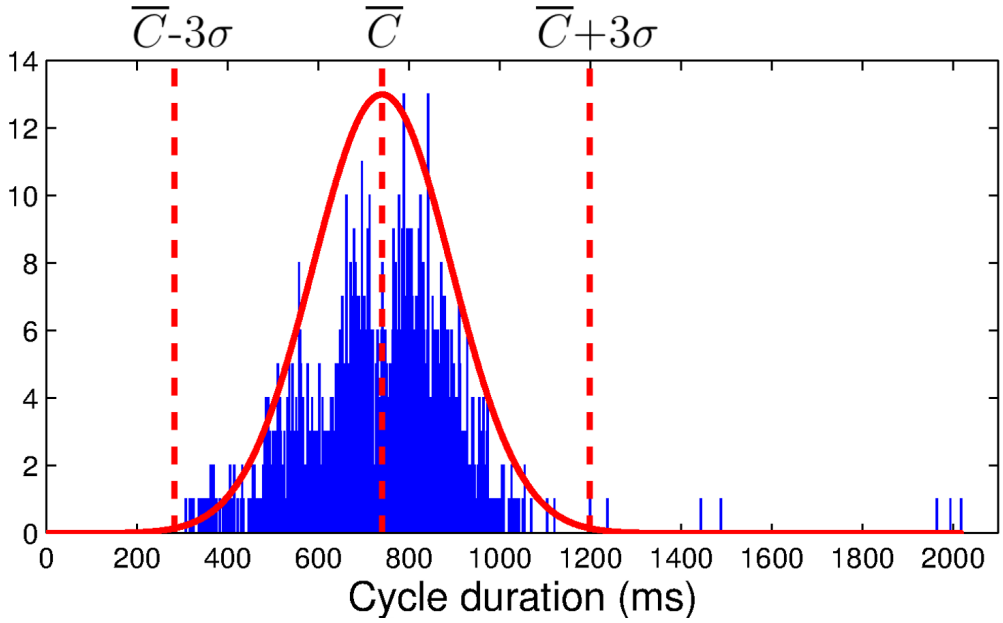

As the acquisitions are done on free-breathing mice, the respiratory rate is linked to the level of isoflurane. Even once the steady state of narcosis is reached, some extreme cycles lengths are observed. These outlier cycles may impair the reconstruction by inducing a non coherent motion in images: moving structures appear blurred. Consequently, we discarded the outlier cycles from the list-mode. The study of the pressure signal gives the distribution of

respiratory cycle duration and allows the identification of the outlier cycles. A new list-mode data set is generated where the corresponding outlier cycles are discarded. We experimentally set the acceptance cycle duration window to the mean cycle duration +/- 3 standard deviations $[\overline{C}\text{-}3\sigma;\overline{C}\text{+}3\sigma]$.

Figure 4.1 presents a typical example of the distribution of cycle durations for an acquisition. The acceptance set to $[\overline{C}\text{-}3\sigma;\overline{C}\text{+}3\sigma]$ will guarantee to keep around 99.7% of the cycle if the distribution is Gaussian, while it will discard the outlier cycles.

After rejection of the outlier cycles, a new respiratory cycle average duration $\overline{C}_s$ is calculated and leads to a new duration of gating window $D_s = \overline{C}_s/N$. The n^{th} gating window of the i^{th} cycle is defined by $[t_i + (n-1)D_s, t_i + nD_s[$ where t_i is the time of the i^{th} trigger.

Cycle resampling

Obviously, even after the cycle selection step, the remaining respiratory cycles still exhibit some length variations.

About half of the cycles are longer than $\overline{C}_s$ and their trigger time t_j satisfies $t_{j+1} - t_j > \overline{C}_s$. As a consequence, the counts after the last gating window of this cycle and before the next trigger signal (*i.e.* in the interval $[t_j + \overline{C}_s, t_{j+1}[$) will not be used at all in the reconstruction process. This is illustrated by figure 4.2(b).

Conversely, the other half of the cycles are shorter than the average cycle duration $\overline{C}_s$ and their trigger time t_k satisfies $t_{k+1} - t_k < \overline{C}_s$. As a consequence, the counts of the last gating windows defined for this cycle (in the interval $[t_{k+1}, t_k + \overline{C}_s[$) also belong to the first gating windows of the next cycle, meaning that those counts will be used twice in the reconstruction process for different phase images. This is illustrated by figure 4.2(a).

These observations motivate a temporal resampling of the counts so that the interval between two trigger signals is equal to the cycle average duration $\overline{C}_s$ .This ensures that each event will be used once and only once in the reconstruction process. Therefore the detection time t of an event located between the trigger signals t_i and t_{i+1} will be changed to

$$t' = (i-1)\overline{C}_s + (t - t_i)\frac{\overline{C}_s}{t_{i+1} - t_i}$$

while the trigger signals become $t'_i = (i-1)\overline{C}_s$. This temporal normalisation results in a new list-mode data set that enables the reconstruction of a gated 4D image, denoted G4DSR.

Image-based motionless phase detection

Anaesthetised mice exhibited a particular breathing rhythm characterized by long intervals (around 2/3 of the cycle) without respiratory motion separated

Figure 4.2: **Reconstruction windows for G4D reconstruction** The two graphs represent two samples of the same pressure signal. Vertical lines delimit the reconstruction windows for each phase of the G4D image. Sample of pressure signal with cycles shorter than the average duration $\overline{C}_f$ highlights the overlapping of phases from consecutive cycles **(a)**; Sample of pressure signal with cycles longer than $\overline{C}_f$ highlights the fact that data at the end of some cycle are not used for reconstruction **(b)**. Moreover, to reconstruct a phase of the G4D image (for example phase 15), G4D reconstruction use data that does not correspond to the same time in the respiratory cycle. Sometimes it corresponds to the end of exhalation **(a)**, sometimes it corresponds to the end of inhalation **(b)**.

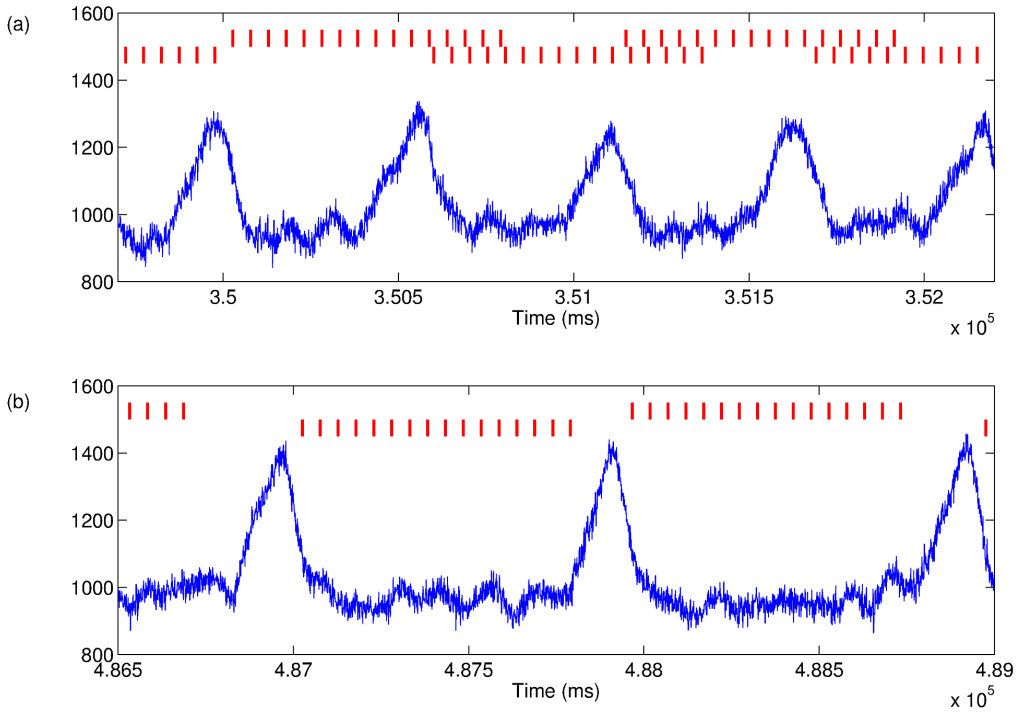

by gasping breaths, as mentioned in [CJP+04] and exemplified in the pressure signal in figure 4.3(a). Extracting the list-mode data corresponding to the rest intervals will allow then to reconstruct a breath-hold like image. However, the visual inspection of the 4D images (either G4D or G4DSR) reveals that the observed motion is temporally shifted with respect to the observed variations of the respiratory signal. Therefore, the latter can not be used directly for motion detection and motivates the design of a dedicated image-based motion detection method from a 4D sequence with 15 phases (here the G4DSR images, i.e. the 4D image after cycle selection and temporal resampling).

This method is based on the observation that, around the borders of high

Figure 4.3: **Singularity of anaesthetized mice pressure signal with motion phase detection** Pressure signal recorded with the monitoring system **(a)**; and normalized average pressure signal (continuous curve) and normalized histogram resulting from the image-based motion phase detection (dashed curve), the horizontal line depicts the threshold determined by the Otsu method **(b)**. The phases getting more votes (above the threshold) are associated with the motion phase and the ones with less votes (below the threshold) are associated with the motionless phase.

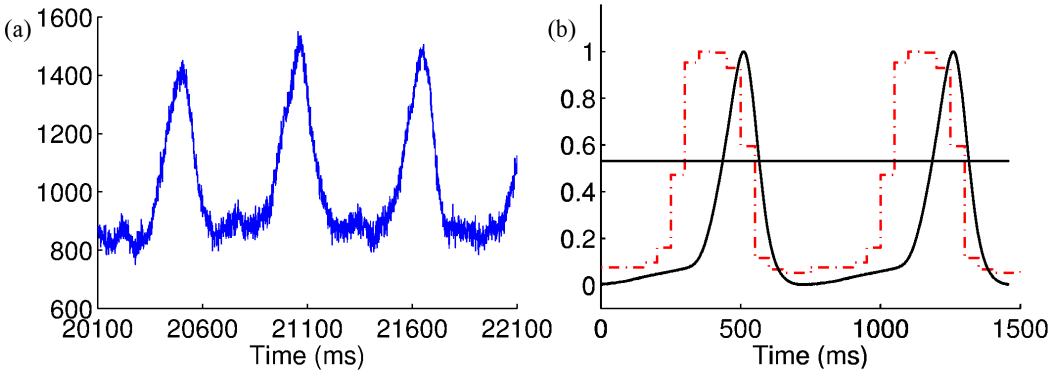

contrasted areas, the time-course uptake value of a given voxel may exhibit a large variation due to spatial displacement. It consists in the study of time-course uptake values of voxels in the abdominal region - assuming that a spatial position in an image should always refer to the same object along time if there is no motion.

The workflow for detecting motionless phases can be described as followed:

1. *Intensity normalisation* of the 3D images $I_n, n \in [1, N]$ resulting from the 4D reconstruction according to the proportion of available counts that has been used for reconstruction.

$$\forall x : \hat{I}_n(x) = I_n(x) \frac{\text{total number of counts}}{\text{number of counts used to reconstruct } I_n}$$

2. *Spatial regularization* with a 3D Gaussian filter ($\sigma = 1.00$) of the normalised images $\hat{I}_n$ yielding $\tilde{I}_n$.

3. *Volume of interest definition.* Since we are interested in abdominal lesions, we restrict the above analysis to a sub-volume containing only the abdominal area.

4. *Generation of an amplitude image.* A 3D image of intensity variation is generated from the images $\tilde{I}_n$. For a given voxel x, the uptake amplitude

can be simply computed by subtracting the minimal uptake value from the maximal one, resulting in an amplitude image A.

$$\forall x : A(x) = \max\{\tilde{I}_n(x)\}_{n\in[1,N]} - \min\{\tilde{I}_n(x)\}_{n\in[1,N]}$$

5. *Generation of a mask M of regions of potential motion.* This mask aims at isolating voxels with large variations of time-course uptake values. This mask is obtained by thresholding the amplitude image A at 15% of its maximum value, yielding segmented regions with potential spatial displacement.

6. *Detection of the gasping breaths.* We observe that around 2/3 of the respiratory cycle do not exhibit significant motion. Since N phases are reconstructed, with $N = 15$, this correspond to around 10 phases without motion while the motion-induced large uptake variations are then mostly due to the other 5 phases. Therefore, for each voxel x, we compute the amplitude after discarding every possible sequence of 5 consecutive phases. We define S_m as a sequence of 5 consecutive phases:

$$S_m = \{k \in [1, N] | \exists j \in [0, 4] : k - m \equiv j[N]\}$$

The discarded sequence yielding the smallest amplitude is associated to a possible motion under the considered voxel. This sequence is defined by its first phase $\hat{m}(x)$ computed by:

$$\hat{m}(x) = \arg\min_{m\in[1,N]} \left(\max\{\tilde{I}_n(x)\}_{n\in[1,N]\setminus S_m} - \min\{\tilde{I}_n(x)\}_{n\in[1,N]\setminus S_m}\right)$$

We cumulate the obtained sequences $S_{\hat{m}(x)}$ into a histogram h.

$$\forall n \in [1, N],\ h(n) = \text{card}\{x \in M / n \in S_{\hat{m}(x)}\}$$

The resulting histogram is automatically thresholded using the Otsu method [Ots79], yielding two groups of phases. The smallest group (typ. 5 to 6 phases) is associated with motion state and the largest group (typ. 10 or 9 phases) is associated with the motionless state. The first phase of the latter group is denoted by $\hat{p}$ and the number of phase is denoted L. The results of the histogram thresholding (table 4.1) confirms the visual inspection illustrated by figure 4.3(b) : the phases associated with the motion state are shifted with respect to the pressure signal peak.

Breath-hold like 3D reconstruction

Breath-hold like 3D reconstruction consists in reconstructing a single 3D image using all data belonging to motionless phases. More precisely this reconstruction method considers counts that lie in intervals of length LD_s beginning at phase $\hat{p}$, *i.e.* $[t'_i + (\hat{p} - 1)D_s, t'_i + (\hat{p} - 1)D_s + LD_s[$ in the list-mode data set (after the temporal resampling).

Table 4.1: Respiratory signal analysis for G4D (15 phases) reconstructions.

Acquisition	Cycle $\mu \pm \sigma$ (ms)	Motion duration (ms/nb phases)	Time shift (ms/nb phases)
0182	762.8 ± 112.9	255 (5)	153 (-3)
0183	740.5 ± 152.7	294 (6)	147 (-3)
0185	751.0 ± 48.9	250 (5)	200 (-4)
0186	765.6 ± 43.6	255 (5)	204 (-4)
0187	712.5 ± 44.6	240 (5)	192 (-4)
0189	702.9 ± 100.4	282 (6)	188 (-4)
0190	658.5 ± 52.1	220 (5)	220 (-5)
0191	713.8 ± 59.1	240 (5)	192 (-4)

4.2.6 Image value normalisation

Reconstructed images were converted into Standardized Uptake Values (SUV) for comparison purpose. The conversion is divided in two steps.

First, all the reconstructed images (3D images, as BH3D, or 3D phase images from 4D images, as G4D, G4DSR) were normalised to NG3D. The values of the reconstructed voxels depend directly on the number of counts used in the reconstruction process. NG3D is the 3D image reconstructed with all the available counts, while all other images only uses a fraction of them. Let us denote by $Nc(I)$ the number of counts used for the reconstruction of image I. By mutiplying the values of image I after reconstruction by the ratio $Nc(NG3D)/Nc(I)$, the resulting values are comparable with the ones of NG3D.

Second, the values are converted into Standardized Uptake Values (SUV). Thanks to the previous normalisation, values of all reconstructed images are comparable and the conversion into SUV is the same for all images. Image values are first converted into uptake values by calibration using an external known 99mTc source acquired simultaneously with the image. SUV values are obtained by normalising the uptake values by the total injected activity divided by the animal weight.

4.2.7 Image measurements

A number of measures, either image-based or lesion-based, were performed for each reconstructed image.

A volume of interest was manually delineated in the liver with the help of both anatomical (CT) and SPECT (NG3D) images avoiding any abnormal lesion, yielding a volume of homogeneous SUV. Calculating the standard deviation (SD) over this region allow the noise of the reconstructed image to be estimated.

Peritoneal metastases were localized by three experts with the help of maximum of intensity projections (MIP), and a VOI was delineated around every identified lesion. The maximal SUV value, SUV_{max}, is calculated, but was not directly used for comparison purposes since it is sensitive to noise, especially for small lesions. The following measurements are then made within every VOI:

- SUV_{peak}: the mean SUV of the 5% of highest values;
- SUV_{mean}: the mean SUV of values over 40% of SUV_{max};
- lesion volume: volume at 40% of the SUV_{max} (given in mm^3);
- lesion SNR: ratio of lesion SUV_{mean} to the liver VOI SD.

VOI were drawn using AMIDE software [LG03]. No correction for partial volume effect were performed.

4.2.8 Statistical tools

Paired variables were compared using t-tests (Matlab R2009b; Mathworks, Natick, MA). Image-based measures (i.e. noise), which can be considered as intrinsic, were compared using paired t-tests. Lesion-based measures (SNR, SUV_{peak}, SUV_{mean}, and volume) were not directly comparable since they vary from lesion to lesion. Therefore they were compared using ratio paired t-tests that correspond to paired t-tests on their logarithms (base 10).

4.3 Results

4.3.1 Lesions distribution

Figure 4.4 presents the volume rendering of fused CT and SPECT (NG3D) images of peritoneal carcinoma lesions after 3 weeks of growth. Figure 4.4 illustrates both biological and imaging challenges as there are numerous small peritoneal carcinoma lesions, distributed throughout the abdomen.

A total of 76 foci of ^{99m}Tc-uptake were detected on the 8 acquisitions (3 to 14 lesions per acquisition). They were located in the abdomen, showing NIS-expressing tumour tissue, and corresponded to peritoneal carcinoma nodules. These nodules were small, their size (equivalent spherical diameter) ranged from 1.09 to 2.34 mm (average 1.55 ± 0.28 mm). Twenty-seven lesions were located in the upper abdominal area (above the stomach), 31 were located in the middle abdominal area (at stomach level), and 18 were located in the lower abdominal area (below the stomach).

Figure 4.4: **CT/SPECT volume rendering highlighting peritoneal carcinoma lesions.** Volume rendering of fused CT and SPECT (NG3D) highlighting peritoneal carcinoma lesions after three weeks of growth, salivary glands and stomach (S).

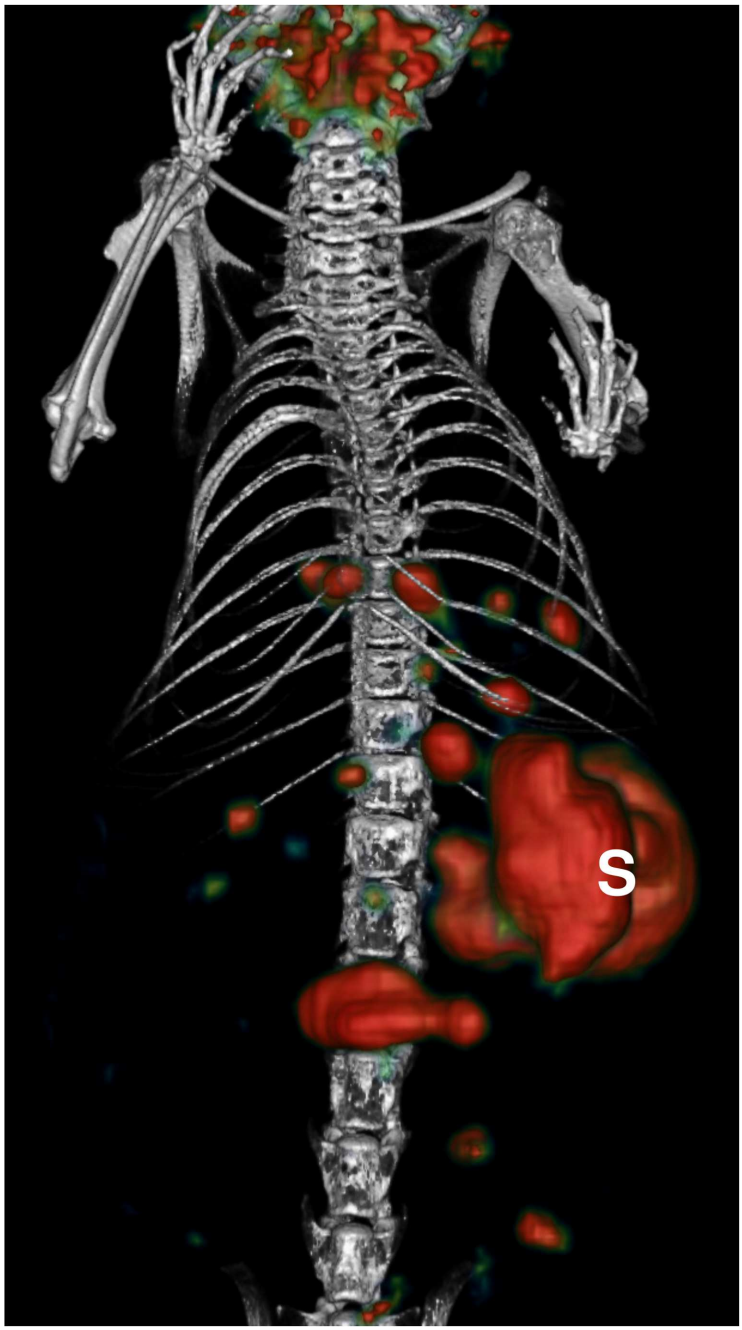

Figure 4.5: **Comparison between pressure signal and image-based measures computed on 4D SPECT and 4D CT.** normalized average pressure signal (continuous curve); normalized histogram $h_{4DSPECT}(n)$ computed on the 4D SPECT image (staircase); normalized histogram $h_{4DCT}(n)$ of motion phase computed on the 4D CT image (gray curve with cross-shaped markers); and lung volume (mL) measured on the 4D CT image (dotted curve with circle-shaped markers).

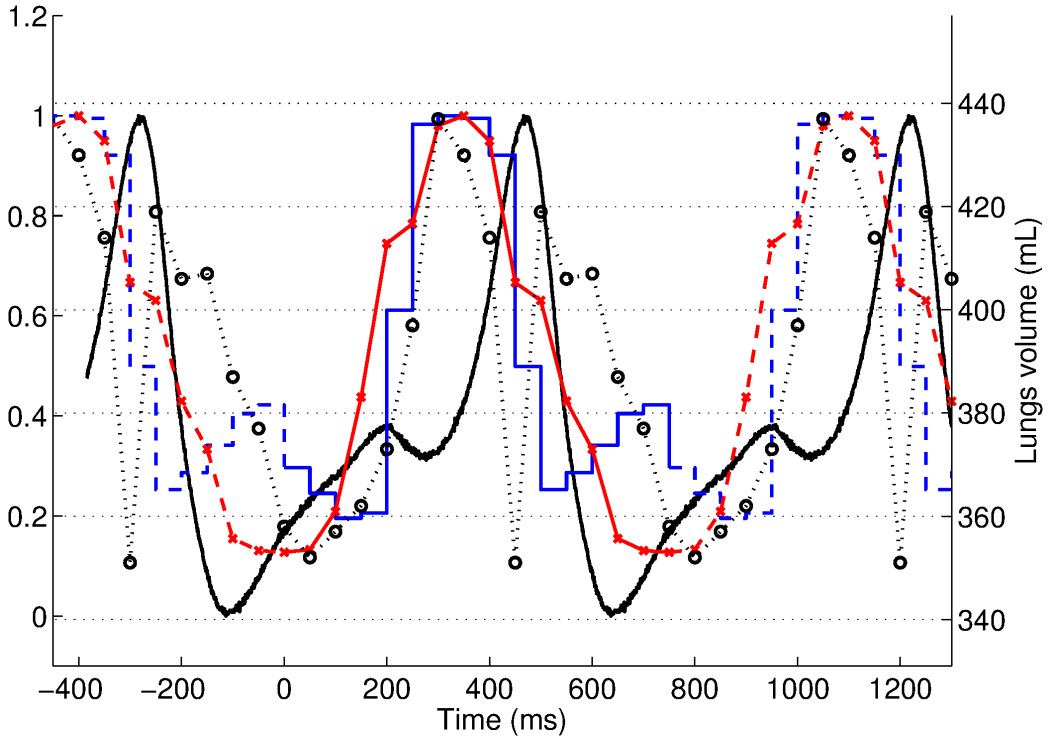

4.3.2 Respiratory signal analysis

Figure 4.3 (a) presents a sample of pressure signal of free-breathing mice. Table 4.1 presents the results of the pressure signal analysis on the 8 acquisitions. The average duration of the respiratory cycle varies from 658 ms to 766 ms while its standard deviation ranges from 44 to 153 ms.

This signal is characterised by a still phase at the end of exhalation. The image-based motionless phase detection demonstrated that the shorter phase associated with motion state lasts 5 or 6 phases out of 15 (see table 4.1) which corroborates our initial observation of a duration of around 1/3 of the respiratory cycle. Moreover, it has been detected that the motion state is time-shifted away from the pressure signal. According to the image-based motionless phase detection, the time shift varies from 3 to 5 phases.

Figure 4.3 (b) presents the normalised average respiratory cycle (continuous curve) for one acquisition, after the cycle selection and the cycle resam-

pling steps, with the result of the image-based motionless phase detection (dashed curve). A horizontal line represents the threshold computed by the Otsu method. This threshold separates the phases in two groups, the ones above the threshold are associated with the motion phase, the others (below the threshold) are associated with the motionless phase.

We did further experiments on the observed time shift between the image-based detected motion and the pressure signal. For this purpose, one mouse has undergone several 4D SPECT acquisitions (with different gating triggers) and one 4D CT acquisition. The proposed image-based method has been used on all the 4D SPECT acquisitions and on the 4D CT acquisition. Changing the trigger parameters on the pressure signal (rising/falling edge, with/without delay) for the consecutive SPECT acquisitions of the same animal did not change the location of the peak (data not presented here). The peak of the motion detected in the 4D CT appeared at the same location as in SPECT, with a temporal shift with respect to the pressure signal (figure 4.5). Last, we computed the lung volume from the CT images along the phases with an ad-hoc and simple method (Gaussian smoothing, threshold between -650 HU and -250 HU, and morphological closing). Again, the peak of volume change appeared at the same location. There is a discontinuity in the lung volume variations (at phase #10): the corresponding reconstructed CT image appears to exhibit different characteristics which explained the lung segmentation differences.

4.3.3 Sensitivity of the image-based motion detection with respect to noise

We investigated the ability of the proposed method to detect the motion in noisy images. To that end, we extracted from one 4D SPECT sequence a series of 3D images containing a moving lesion. This lesion has been thresholded, and different (white and gaussian) noise levels have been added to the binary images. It appears from our experiments that the image-based motion detection method is always successful in detecting the motion phases for SNRs above 2.5.

4.3.4 Image statistics

The number of counts used for each reconstruction method were compared to the total number of acquired counts. Table 4.2 presents the figures concerning the average percentages on the set of 8 acquisitions. By definition, the 3D reconstruction method NG3D used 100% of the counts.

15 3D phase images were reconstructed by the G4D method. The average percentage of counts used for the reconstruction of each 3D phase image is then around 1/15th of the counts (6.65%). However, because of the variation

of respiratory cycle duration, 3.64% of the counts are not taken in account while 3.51% of them are used twice (i.e. for the reconstruction of two different phases). If the total number of used counts is defined as the sum of the number of counts used for each phase reconstruction, it appears that this total number may exceed 100% if the number of counts used twice is larger than the number of omitted counts. As a consequence, the average total of counts used for the reconstruction of the 15 phases is 99.76% with a standard deviation of 2.88%. The twice used counts were not evenly distributed among phases, and are more likely to occur in the first phases: an average of 31.44% (resp. 9.67%) of counts used for phase 1 (resp. phase 2) were already used in a preceding phase. Twice used counts appeared up to the 9th phase.

The cycle selection step discarded an average of 3.25% of the counts. After the update of the average respiratory cycle duration, there were still 3.74% of omitted counts and 2.73% of twice used counts in a 4D reconstruction without cycle resampling. The trends in the repartition of the twice used counts among the phases were similar to those observed for G4D: e.g. an average of 26.86% (resp. 7.61%) of counts used for phase 1 (resp. phase 2) were already used in a preceding phase.

After cycle resampling, all the retained counts are used once and only once in the 4D reconstruction G4DSR. Each reconstructed phase of G4DSR used around 6.45% of counts per reconstructed phase, which corresponded to a total of 96.75% counts over the 15 phases.

For the BH3D reconstruction, the counts from the equivalent of 9 or 10 phases have been used. On average 64% of the total number of counts have been used for the reconstruction of one 3D image.

4.3.5 Qualitative comparison

Each acquisition was reconstructed using the three methods NG3D, G4D and BH3D, that have been described in section 4.2.

The first comparison was a visual comparison of the lesions in images reconstructed with the different methods. Figure 4.6 illustrates these reconstructions with sagittal views showing 2 peritoneal lesions. The peritoneal location can be visualised with the CT image (a). NG3D image (b) shows the underestimation of the lesion uptake and the overestimation of size compared to G4D images, with a significantly improved signal-to-noise ratio. The zoomed-in images of the G4D end-of-exhalation (c) and end-of-inhalation (d) images show the high lesion uptake and the respiratory induced lesion displacement, but are corrupted by a high noise level. On the BH3D reconstructed image (e), the obtained result is a trade-off between the previous methods: the outlines of the lesions are less blurred and the volumes are smaller than in NG3D image and closer to G4D end-of-exhalation image, while the lesion uptake is higher than in NG3D image with an equivalent noise level.

Table 4.2: Percentages of counts used for the different SPECT images reconstruction schemes: NG3D, G4D (15 phases) and BH3D. Values are presented as mean ± SD.

		Number of counts used (%)
NG3D	Total	100.00
G4D	Used counts / phase	6.65 ± 0.19
	Total	99.76 ± 2.88
	Omitted counts	3.64 ± 3.14
	Counts used twice	3.51 ± 1.55
	Percentages of counts used twice per phase	
	Phase 1	31.44 ± 7.11
	Phase 2	9.67 ± 7.94
	Phase 3	5.29 ± 7.02
	Phase 4	3.60 ± 4.87
	Phase 5	1.79 ± 2.48
	Phase 6	0.46 ± 0.68
	Phase 7	0.22 ± 0.47
	Phase 8	0.10 ± 0.26
	Phase 9	0.01 ± 0.04
	Phases 10 to 15	0
G4DSR	Used counts / phase	6.45 ± 0.29
	Total	96.75 ± 4.36
BH3D	Total	63.99 ± 4.58

4.3.6 Quantitative comparison

NG3D, G4D and BH3D reconstruction methods were compared with respect to image-based and lesion-based quantitative measurements. The average values of the lesions' SUV_{peak}, SUV_{mean} and volumes, noise estimation in homogeneous liver area and signal-to-noise ratio (SNR) are presented in table 4.3. Here, G4D images are reconstructed with both 6 phases and 15 phases.

Image noise, measured in a homogeneous liver area, for BH3D method (see figure 4.7 (d)) was significantly reduced (-60.83% and -38.25%) in comparison to 15 phases-G4D and 6 phases-G4D ($p < 0.001$) and closer to NG3D measured noise, although it was still significantly higher (increase of +21.37%, $p = 0.0012$).

The SUV_{peak} and SUV_{mean} for the BH3D method (see figure 4.7 (a)) show an increase of respectively +9.67% and +14.59% with respect to NG3D reconstruction ($p < 0.001$), but remained significantly lower (respectively -5.29% and -11.99%) than those obtained by 15 phases-G4D reconstruction ($p < 0.001$).However, SUV_{peak} and SUV_{mean} were not significantly different to the ones for 6 phases-G4D reconstruction (slight decrease of respectively

Figure 4.6: **Sagittal views from sub-diaphragmatic peritoneal lesions comparing NG3D, G4D (15 phases), BH3D SPECT reconstruction methods.** Top row: anatomical reference CT image **(a)**, NG3D reconstruction **(b)**, end-of-exhalation phase from G4D reconstruction **(c)**, end-of-inhalation phase from G4D reconstruction **(d)**, BH3D reconstruction **(e)**; bottom row: zoomed-in on lesions of interest of the SPECT images. The SUV colour map has been set up on SUV_{max} values in G4D images for the selected lesion.

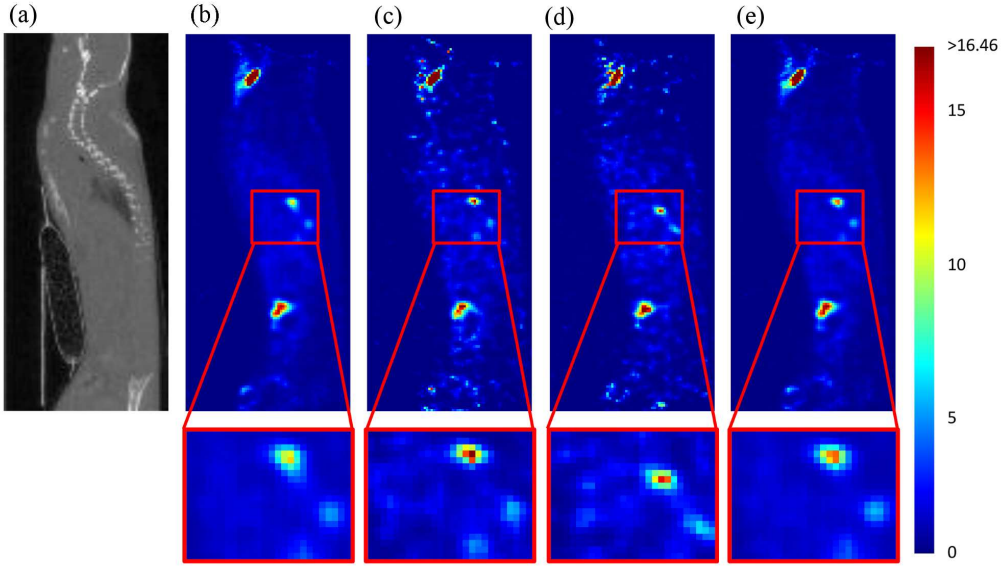

-0.64% and -1.2%) ($p = 0.9873$ and $p = 0.5608$). Volumes measured with BH3D method (see figure 4.7 (b)) were significantly lower (-14.41%) than with NG3D ($p < 0.001$) and significantly higher (+12.04%) than with G4D ($p < 0.001$), but were not significantly different (-1.3%) to 6 phases-G4D ($p = 0.655$).

Lesion SNR on BH3D images was significantly higher (+124% and +55%) (see figure 4.7 (c)) than on both 15 phases- and 6 phases-G4D images ($p < 0.001$) and closer to NG3D lesion SNR, while it was still significantly smaller than on NG3D (-5.40%) ($p = .0035$).

Table 4.3: Quantitative results for NG3D, G4D and BH3D reconstruction methods: SUV_{peak}, SUV_{mean}, lesion volume (threshold at 40% of the SUV_{max} value), noise estimation in homogeneous liver area and SNR. Values are presented as mean ± SD.

Parameters	NG3D	G4D [a]		BH3D
		(15 phases)	(6 phases)	
Noise[b]	0.15 ± 0.04	0.47 ± 0.14	0.30 ± 0.08	0.18 ± 0.05
SUV_{peak}	7.26 ± 5.32	8.18 ± 5.56	7.87 ± 5.46	7.87 ± 5.47
SUV_{mean}	6.90 ± 5.26	8.63 ± 6.00	7.85 ± 5.67	7.80 ± 5.65
Volume (mm^3)	2.14 ± 1.29	1.60 ± 0.87	1.84 ± 1.00	1.79 ± 1.02
SNR (SUV_{mean}/Noise)	48.85 ± 40.02	19.81 ± 14.98	31.82 ± 22.50	45.61 ± 35.86

[a] G4D values are the average values of end-of-exhalation images corresponding to the motionless phases - i.e. nine or ten phases (respectively four) in the case of G4D with 15 phases (respectively 6 phases).

[b] Noise measure refers to the SD in a homogeneous liver area.

4.4 Discussion

The motivation of this work is tumour detection and quantification in oncology small animal SPECT imaging. Respiratory motion is a major source of impairment not only for lung lesions but also for abdominal lesions as in our peritoneal carcinosis model. The gating reconstruction method was able to reconstruct motionless images but at the cost of a degraded SNR. Therefore we proposed a retrospective amplitude-based data selection that aimed to maximise the data available for reconstruction, hence keeping a high SNR, while suppressing respiratory motion artefacts.

The proposed method was possible thanks to the breathing rhythm particular to anaesthetised mice, which is characterised by gasping breaths separated by long intervals without respiratory motion. Cavanaugh et al. [CJP+04] previously reported that this pattern, which is also depicted in [BLW+12], was induced by isoflurane anaesthesia.

The average duration of the motionless baseline is 9.75 phases (for a 15-phases reconstruction), which corresponds to 65% of the respiratory cycle, which indicates that the same percentage of acquired counts may be used for the reconstruction of a motion free image.

We observed that the true motion, as observed in the CT or SPECT respiratory gated reconstruction (3D+t images), is not synchronised with the pressure signal, but appeared temporally shifted. This shift represents around a fourth of the cycle length (around 187 ms). It has been identified as a

Figure 4.7: **Quantitative results for lesions and image characteristics** Quantitative results for lesions SUV_{mean} **(a)**, lesions volumes **(b)**, SNR **(c)**, and noise **(d)**. Box plots show the median, upper and lower quartiles and range; + indicate outliers. Statistical significance: ** for $p < 0.01$, *** for $p < 0.001$, p-value is given when non significant ($p > 0.05$).

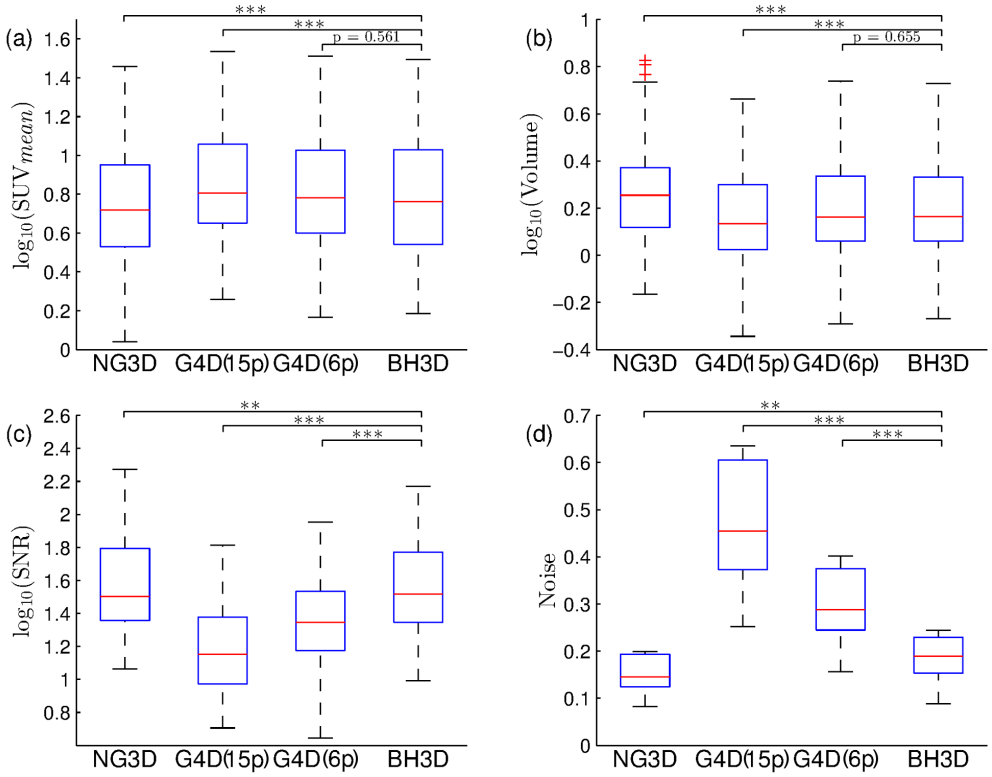

consequence of the external pneumatic sensor system and might then depend on the length ot the air pipe. This asynchronism motivated a dedicated image-based motion detection method that allowed to identify the respiratory phases associated with the motionless baseline.

The proposed image-based motion detection method is simpler than those proposed in e.g. [BMME+08] or [SOBM09]. Indeed, both approaches aimed at reconstructing a respiratory representative signal from the images while we only focused on the detection of the phases exhibiting a motion with respect to baseline. More precisely, [BMME+08] followed the centre of mass of a (manually specified) tumour in a 4D series and then used the measured displacement as a trigger signal. This approach required some manual interaction and is dedicated to the reconstruction of one single tumour. The proposed method is closer to [SOBM09] since we study the variation of counts induced by an object motion. They proposed to integrate this variation in the sinogram to get a respiratory-like signal while we simply identified the largest variations

at the voxel level. As with theirs, our method is versatile and can deal either with emission tomography or CT data. The proposed method appears to be quite robust with respect to noise, and is still able to detect the motion in noisy challenging images (SNR of 2.5), noisier than the pre-clinical images (see the SNRs in Table 4.3).

The average time shift between the image-based detected motion and the amplitude peak in the pressure signal was -3.875 phases (for 15 phases-G4D), which corresponds to 25% of the respiratory cycle. Rather than using a 4D CT image for the motion detection, that would imply a large acquisition time and a subsequent radiation dose, we rely on a 4D SPECT image. Although the operator tried to stabilize the respiratory cycle of the anaesthetised mice, some variation still occurred (Table 4.1). As a consequence, some counts may be skipped from the reconstruction of gated images and others will be used twice, mostly in the first phases to be reconstructed. This motivated the equalization (done by resampling) of all respiratory cycles before reconstruction.

The proposed data selection allowed to retain 64% of all detected counts to reconstruct one single 3D image (BH3D). These counts correspond to the motionless baseline, hence the proposed reconstruction method simulated a breath-hold acquisition.

Using all acquired counts in the reconstruction would have required to either co-register all 3D phase image and then average them (e.g. [DLJS06]), or to incorporate a motion model into the reconstruction process (e.g. [RMK+07]). This would then either rely on some non-linear registration method, whose validation for such noisy data is challenging, or on the calculation of a personalized respiratory motion model. 4D CT may offer a means for such computation, but will still depends on the used registration algorithm and at the cost of a high radiation dose of the mice. Therefore, the proposed method offers a means toward the reconstruction of a still image, while not requiring the validation of any registration method.

Measures of image noise (figure 4.7d) and lesion signal-to-noise ratio (figure 4.7c) demonstrated that BH3D is of better quality than a 3D phase image extracted from a 4D reconstruction (G4D, 6 and 15 phases reconstruction have been tested), and even suggested that it is of similar quality to the 3D image reconstructed with all the available counts (NG3D). Measures of SUV_{mean} are significantly larger in BH3D than in NG3D, and close to the ones from the phase image (G4D). Similarly, volume measures are smaller in BH3D than in NG3D, and close to G4D. These figures suggested that the blurring effect due to the respiratory motion has been compensated for. As expected, using less phases in G4D reconstruction yielded better quality images. The advantage of the proposed method is to discard prospectively the motion impaired data before reconstruction, while one has to identify retrospectively (possibly with a monitoring system) the motionless phases in G4D reconstruction. Last, the "optimal" G4D will reconstruct 2 phases, each of them from 50% of the data,

assuming only one of them is impaired with motion, while our method used 64% of the data.

More thorough validation could be conducted with simulations. First, one would have to animate a numerical mouse phantom with the same particular respiratory pattern that has been observed (gasps followed by a rest period). Such a model has not been identified. The MOBY phantom [STF+04] implemented a respiratory motion similar to humans, and would not be adequate. Moreover, we have no indication whether such a model may produce the same time shift as we observe between the pressure signal and the abdominal motion. Second the acquisition can be simulated (e.g. with the GATE software [SRK+06]), but this will also require to model our camera. Such a considerable amount of work is certainly worthwhile for a finer characterization of the benefits of the proposed method. However, the presented figures already suggest there is an the overall benefit.

4.5 Conclusion

We developed a reconstruction method dedicated to anaesthetised free-breathing mice. It enabled the reconstruction of a breath-hold like acquisition that is comparable to a non-gated reconstruction in terms of noise measure and signal-to-noise ratio, and intermediary between gated and non-gated reconstruction for lesion-based measurements (SUV_{peak}, SUV_{mean} and lesion volume).

Overall, the proposed method improves the quality of pre-clinical images, and the precision of the quantitative measurements they provide. This method is promising for more challenging studies concerning organs or tumour affected by motion using the emission tomography modalities in the pre-clinical research.

In addition to the results presented in this chapter, we provide complementary results in Appendix A. This appendix illustrates different reasons that led us to the approach presented in this chapter, and illustrates with additional tests the efficiency of our approach.

Acknowledgements

We thank Audrey Lamit for the supply of biological material, the planning of experimentation, the manipulation of animals, and the support during acquisition.

Part II

IODIDE DYNAMIC DISTRIBUTION IN STOMACH

Chapter 5

Dynamic SPECT analysis of ^{99m}Tc-pertechnetate uptake in stomach: biodistribution study

Contents

5.1 Introduction

In this second part of the thesis, we study the biodistribution of ^{99m}Tc-pertechnetate in murine stomach. The idea is to automatically segment an organ in a temporal sequence of three (spatial) dimensions (3D) images. Then, a layer-based decomposition of the segmented organ will get rid of the animal motion. In the information provided by the layer decomposition, we try to integrate notions of functional compartment.

5.1.1 Objectives

The main objective of this work is to demonstrate the feasibility of the modelling of the ^{99m}Tc-pertechnetate biodistribution with a very simple model. For this purpose, we first study the ^{99m}Tc-pertechnetate uptake kinetic with three spatial + 1 temporal dimensions (4D) single photon emission computed tomography (SPECT), and then we propose a simplified compartmental model that describes this progressive uptake. The compartments of the model corresponds to real compartment that are biological functional units: the sodium/iodide symporter (NIS) expressing cell in the glandular wall and the mucus secreted in the stomach cavity. The model will help biologists to complement their knowledge about the role of ^{99m}Tc-pertechnetate in extrathyroidal tissues.

By studying ^{99m}Tc-pertechnetate uptake kinetic, we mean to analyse spatially and temporally the 4D SPECT images. This requires the acquisition of dynamic SPECT, then extraction of information from the sequence. The first objective is achieved in this chapter while the modelling aspect is addressed in Chapter 6.

5.1.2 Dynamic SPECT acquisition and analysis

Dynamic SPECT or 4D SPECT consists of a sequence of 3D images. The four dimensions refer here to the three spatial dimensions plus the time of image acquisition with respect to the time of the iodide analog ^{99m}Tc-pertechnetate injection. During the acquisition sequence, the animals are maintained under anaesthesia at all time. Indeed, the length of acquisition could not exceed 140 min in order to prevent animal from premature death.

The temporal and spatial study of iodide uptake is a biodistribution study. Biodistribution refers to both static and dynamic distribution of compounds within a biological system or within an organism. In this work, it is not the iodide biodistribution that is studied but the ^{99m}Tc-pertechnetate biodistribution. As ^{99m}Tc-pertechnetate is a substitute of iodide with respect to the NIS protein, we assume that ^{99m}Tc-pertechnetate biodistribution reflects the iodide transport mechanism. ^{99m}Tc-pertechnetate is transported like iodide but it is not incorporated like iodide. ^{99m}Tc-pertechnetate is thus privileged for the study of iodide dynamic distribution. Moreover, we assume that the transformation of iodide into organic compound does not occur in this gastric biodistribution. At first sight, it consists of a voxel-based analysis: the activity measure in the different regions of the stomach along the time. This task could be done easily if the stomach was not deforming and if there was an anatomical reference at all times, given by computed tomography (CT) imaging. However, as previously mentioned in the first part of this thesis, the abdominal organs are not distinguishable in non contrasted CT images.

Contrast agent could be used in order to see the stomach but this would require to alternate SPECT and CT acquisitions in order to have a 4D image for each modality. Such 4D CT images would have allowed the longitudinal registration of the 4D SPECT on the anatomical information. However, this kind of protocol makes more complex the acquisition and image analysis process. That is why, in a first phase, we investigate only 4D SPECT images to study the biodistribution, without any anatomical reference for the position or shape of the stomach.

5.1.3 Challenges

The challenges here are to identify the two functional compartments of the stomach in the images, and to understand what is going on between these two compartments. In others words, the first challenge of this study is to find an appropriate segmentation method for organs in movement. The second challenge is to obtain qualitative data from this segmentation that allow the compartmental analysis.

The difficulties that arise are that the stomach is moving according to the animal movement, respiration, and deformation induced by digestion. Although the animal is under anaesthesia, it can still slightly move. Thus, an appropriate automatic segmentation method should be able to integrate all of that.

5.1.4 Region-based analysis of the ^{99m}Tc-pertechnetate biodistribution

The task consists in developing an appropriate method for stomach segmentation and activity tracking dedicated to 4D SPECT. The ideal approach would be a voxel-based tracking approach as the animals are not moving under anaesthesia during the whole acquisition. Such a voxel-based approach could be done without any additional registration for static object. However, as the stomach is subject to deformation along the time, images should be registered in order to compensate for the organ deformation. The problem with registration is that it is usually based on intensity. As no anatomical CT image for each frame of the dynamic SPECT was provided, the registration algorithm should be proceed directly on the SPECT images. In the case of a activity progressive uptake in the organ of interest, the voxel intensities in SPECT images change over the time and this might bias the outcome of the registration. Therefore, voxel-based tracking approach might not be appropriate. For example, a particular voxel that corresponds to the stomach wall in the first image of the sequence might not correspond to the stomach wall for the next images. Figure 5.10 illustrates clearly this problem.

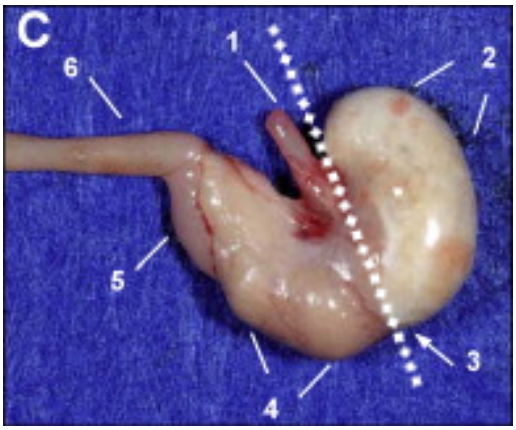

Figure 5.1: Anatomy of a murine stomach [KRK11]. 1 = distal esophagus, 2 = forestomach, 3 = margo plicatus, 4 = pars fundica, 5 = pars pylorica, 6 = proximal duodenum. The dotted line highlight the position of the margo plicatus.

From this point of view, we considered a region-based approach for the extraction of the time activity curves. A set of time activity curve will be obtained with each curve associated to one region. In a first time, the activity will be the average activity in the each region.

5.2 Biological context

The biologists study the iodide uptake and elimination processes in the body. Iodide accumulates in different organs of the body, not only the thyroid but also salivary glands, or stomach. NIS protein mediates all this accumulation in these tissues. In this context, biologists from TIRO team focus their study on the role of iodide uptake in the extrathyroidal tissue.

Here, we focus on the murine stomach. Biologists conducted ex vivo investigations with immunohistochemistry (IHC) image. From these investigations, they identified NIS protein in glandular cells of the gastric wall. Since, NIS protein mediates the iodide uptake, biologists expect that iodide has a specific function in the stomach. However this hypothesis has to be confirmed by kinetic studies. These studies have to be conducted in vivo and SPECT imaging was proved to be the appropriate tool.

5.2.1 Biological objectives

The motivations for this study are biological. The main biological goal is the understanding of the iodide gastric cycle.

^{99m}Tc-pertechnetate is a substitute of iodide with respect to NIS protein. In the sense that NIS mediates ^{99m}Tc-pertechnetate like iodide. This mediation by NIS protein allow the observation and the study in vivo with SPECT imaging of mice using the ^{99m}Tc-pertechnetate. The ^{99m}Tc-pertechnetate biodistribution study will help to understand the iodide uptake. More precisely, biologists are interested in the NIS properties and role in the context of

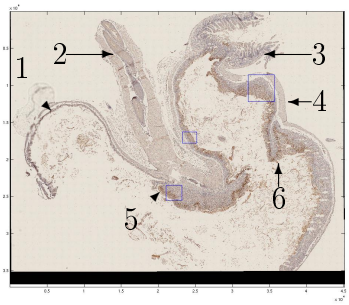

(a) IHC image of a section of murine stomach

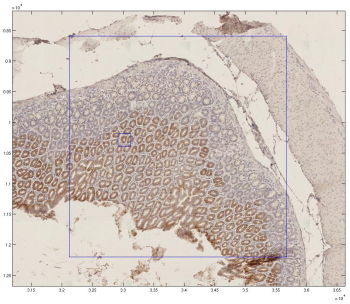

(b) Zoomed-in on the mucosa of the glandular stomach corresponding to the upper right square of (a)

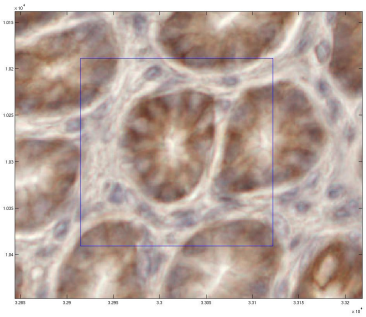

(c) Zoomed-in of the glandular stomach mucosa centered on a follicle

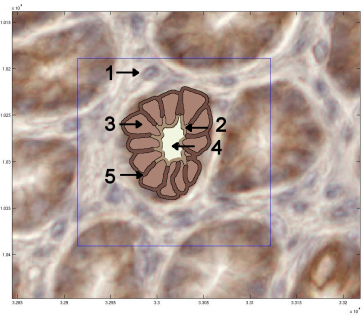

(d) Description of the follicle constitution

Figure 5.2: **IHC image of murine stomach**. Figure (a) shows a section of the stomach with nucleus (blue) and NIS protein (brown) marking. Arrows indicate the forestomach (1), the esophagus (2), the duodenum (3), the glandular stomach (4) and the margo plicatus (5,6). Figure (b) shows a zoomed-in image on the mucosa. Figure (c) shows a zoomed-in on a transverse section of a follicle of the glandular stomach mucosa. Figure (d) describes the follicle made of 13 epithelial cells: extracellular space (1), apical region (2), cellular space (3), stomach cavity (4), NIS protein marking on basolateral region (5)

iodide metabolism in the gastrointestinal tract. Here, we focus on the stomach since NIS protein are expressed by cells in the gastric mucosa, yielding to iodide accumulation.

Starting with the anatomical knowledge of the stomach, we want to help biologists to understand the physiology, to answer the following questions, to validate or to correct their assumptions.

How, where and why does iodide accumulate in the stomach wall? Based on

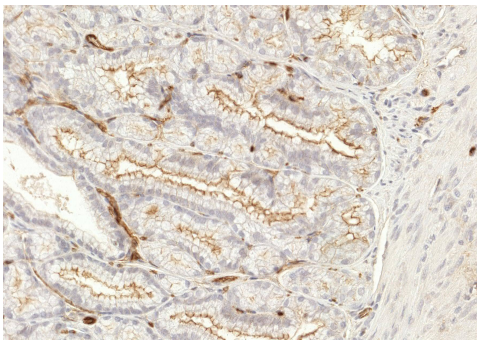

Figure 5.3: **IHC image of murine stomach centered on the pars pylorica.** The NIS protein can be identified by the slight brown marking on the apical membrane of pars pylorica cells.

biological observations, iodide uptake is due to NIS expressing cells of the glandular stomach epithelium. One of the biologists assumptions is that iodide accumulates in the glandular cells in order to play the role of an antioxidant and that only a fraction of the iodide will diffuse in the cavity.

Is there a iodide concentration regulation process in the cavity? If yes, why and what are the limiting steps? Another assumption is that iodide play an antiseptic role under the condition a specific gradient is maintained between NIS expressing cells and stomach cavity. If this is confirmed, we expect the iodide concentration in the cavity to be abundant.

Is the iodide regulated by a reabsoption into blood and where? Experimental data shows a slight expression of NIS on the apical membrane of cells located in the pars pylorica (see Figure 5.3). Two biological assumptions can be done on the role of this NIS expression. This NIS expression could be done in order to either maintain a low concentration of iodide in the stomach cavity, or to reabsorb iodide that leave the stomach cavity with the alimentary bolus.

5.2.2 Biological knowledge

5.2.2.1 Sodium-iodide symporter - NIS

The sodium/iodide symporter (NIS) is a protein that mediates the iodide transport by coupling the entry of iodide anion (I^-) with two sodium cations (Na^+) [DDlVP+03]. In human, NIS is highly expressed in the thyroid, in salivary glands, and in the gastric mucosa, and in the mammary glands during lactation. In the thyroid, NIS protein is present in the basolateral membrane

of thyroid follicular cells. Iodide is accumulated in the thyroid for the synthesis of thyroid hormones. The thyroid hormones containing iodide are vital. Free iodide in blood is eliminated from the body through urine.

5.2.2.2 Murine stomach anatomy

The murine stomach divides into two main regions [Coo65, Kar95, TVD12]. Figure 5.1 show an ex vivo stomach where we can identify each parts. The nonglandular forestomach has a thin wall and is transparent. The glandular stomach has instead a a thicker wall as shown on the IHC images Figure 5.2(a). These two regions are separated by a limiting ridge or margo plicatus. The glandular stomach does present a thick epithelium. It is divided into three parts: the small cardia adjacent to the limiting ridge (margo plicatus); the fundus, where the mucosa is folded with rugae; and the antrum or pars pylorica, which has relatively smooth mucosa. On Figure 5.1, the limiting ridge is emphasized by the white dotted line but it is clearly visible by the difference of tissue color. On Figure 5.2(a), the limiting ridge is the visible, slightly raised division at the left hand side junction with esophagus.

The wall of the gastric stomach, the gastric mucosa, is the mucous membrane layer of the stomach which contains the glands and the gastric pits. The gastric epithelium is responsible for most digestive, absorptive and secretory processes. In human, gastric glands are organized in order to secrete a mucus, enzyme or acids that all contribute to the digestive process. The secreted mucus contains among other iodide secreted by NIS expressing cells in its epithelium. In comparison, the forestomach does not present NIS expressing cells in its epithelium and is used for food storage and digestion process. Biological investigations with murine IHC imaging highlight the fact that NIS proteins are expressed by cells from the innermost layer of glandular stomach called epithelium as we can see on Figure 5.2. This can be characterized by an important iodide uptake observed with the SPECT imaging.

5.2.2.3 Stomach SPECT imaging with ^{99m}Tc-pertechnetate

The iodide biodistribution can be observed and studied in vivo with SPECT imaging of mice using the ^{99m}Tc-pertechnetate that is an iodide substitute. In this sense, it is transported by same routes than iodide. First, it is mediated by NIS proteins and thus is accumulated and diffused in the whole cellular space. Then, in the case of stomach, the glandular cells that accumulate ^{99m}Tc-pertechnetate also secrete it in the gastric mucus. This ^{99m}Tc-pertechnetate also diffuses in the whole stomach cavity.

High resolution SPECT imaging with ^{99m}Tc-pertechnetate allows now the observation of ^{99m}Tc-pertechnetate distribution and allow the identification of both tissue and mucus as well as the quantification of the iodide uptake

capacity in tissue.

5.3 Material

5.3.1 Animal model

No specific mouse lineages were required for this work. Two common laboratory inbred strains (i.e. with pure genotype), C57Bl/6 and Balb/c, have been used. A set of fourteen 4D SPECT images were acquired with six to 24 frames. The description of these acquisitions is detailed in Table 5.1. Five animals were injected intra-peritoneally between 110 MBq and 180 MBq in 400 μL of ^{99m}Tc-pertechnetate. The other nine animals were injected subcutaneously between 90 MBq and 110 MBq in 400 μL of ^{99m}Tc-pertechnetate. The radioactivity was obtained from a freshly eluted 99Mo/99mTc generator. Then the animals anaesthetized with isoflurane (2-chloro-2-(difluoromethoxy)-1,1,1-trifluoro-ethane)(1.3% v/v) (Baxter, France) and maintained asleep during the whole imaging protocol, using inhaled anaesthetic.

Animal housing and procedures were conducted according to the guidelines of the French Agriculture Ministry and were approved by the local ethics committee.

5.3.2 Dynamic SPECT imaging protocol

The acquisition process of dynamic SPECT images is very similar to the acquisition process described in Section 4.2. However, the temporal dimension is not at the respiratory cycle scale but at the scale of several dozen of minutes. Thus, we set up a sequence of six to 24 acquisitions distributed along 80 min to 145 min. As we are not initially interested in respiratory gated acquisitions, images are reconstructed using the basic non-gated 3D reconstruction scheme (see Section 4.2).

During the whole protocol, animals were maintained asleep and their breathing rhythm was controlled with the respiratory monitoring system.

Besides the temporal setting of the protocol, the field of view were carefully chosen in order to see the whole stomach. In most acquisitions (11 out of 14), the field of view also contains the heart. However, the larger the field of view, the longer the acquisition. The three dynamic acquisition with 24 frames were acquired without the heart. All protocols also include a CT image for anatomical reference, although it is not helping much with the stomach localization without contrast agent. It is principally used to localize the left ventricle. Indeed the heart and in particular the left ventricle is acquired to measure the blood activity function. This function is essential for the

Table 5.1: Description of data used for the study of iodide uptake in the stomach. ^{99m}Tc-pertechnetate injection were done intraperitoneally (IP), or subcutaneously (SC).

Mice	Animal weight (g)	^{99m}Tc Injection	Injected Activity (MBq)	Diet (time before injection)	SPECT Protocol: Time/angle (sec)	Nb of SPECT acq.	Nb of SPECT acq. after barium sulphate absorption	Acquisition duration (min)	field of view (FOV) with heart
0366	26.5	IP	111.08	none	5	24	1	139.500	n
0370	23.6	SC	111.08	none	5	24	1	144.500	n
0371	26.5	SC	107.43	none	5	24	1	130.500	n
0395	17.8	SC	99.61	none	5	6	0	101.000	Y
0396	19.7	SC	99.07	none	5	6	0	90.000	Y
0397	23.4	SC	118.29	none	5	6	0	105.000	Y
0398	23.0	SC	84.59	none	5	6	0	92.000	Y
0402	19.4	SC	90.71	none	5	6	0	84.000	Y
0420	20.4	SC	99.13	none	5	6	0	82.000	Y
0530	21.0	SC	102.61	empty stomach (7h)	5	19	0	134.917	Y
0544	18.6	IP	156.59	empty stomach (3h)	5	10	0	100.000	Y
0545	19.4	IP	156.00	empty stomach (5h30)	5	10	0	102.000	Y
0544	18.6	IP	167.02	empty stomach (4h30)	5	10	0	101.500	Y
0545	18.6	IP	176.43	empty stomach (8h15)	5	10	0	106.500	Y

biodistribution analysis. Although biodistribution are done on whole-body images, here we will only consider the cardiac and abdominal regions.

Three sequences include an additional SPECT image and a CT images acquired after contrast agent absorption. Food mixed with barium sulphate was given to mice after the dynamic SPECT imaging. This required to remove the mice from the bed, fill them with the barium food, to re-anaesthetized and to replace in the cradle. This step was done only after the radioactivity dynamic observation since the barium sulphate can affect the iodide uptake kinetic in stomach. These additional images were acquired to investigate the feasibility of stomach imaging combining both modalities SPECT and CT. However, the impact of this barium sulphate ingestion is not further studied in this thesis since the images acquired afterwards exhibited large changes. These changes would have required additional registration that has not been performed.

5.4 Method and qualitative results

In this section, we describe the method that we used to analyse the dynamic SPECT images in order to observe qualitatively the iodide biodistribution in the stomach. There are two challenges for this method that we had to consider:

1. the progressive uptake in the stomach wall coupled with a progressive diffusion of the activity in the stomach cavity, and
2. the progressive deformation of the stomach due to the combination of digestion, air bubble displacement, and respiration.

Despite these difficulties, the method is kept as simple as possible with several assumptions. The assumptions that have been done are:

- The stomach has a bean shape. It can be decomposed into layers.
- In a sequence of images, layers can be associated with respect to the distance to the border.

These assumptions are debatable and will be discussed in Section 5.5.

5.4.1 Segmentation of dynamic SPECT images of stomach

SUV conversion All images were converted into SUV. Image values were first converted into uptake values by calibration using an external known ^{99m}Tc source acquired simultaneously with the image. SUV values are obtained by normalising the uptake values by the total injected activity divided by the animal weight.

Visual assessment Due to the variations in the protocol for the acquisition of dynamic images, the sequences were observed and analysed with respect to:

- presence of the heart and the stomach in the field of view;
- definition of a bounding box that contains only the stomach;
- eventual incident such as the wake up of the animal inducing animal movement;
- presence of activity close by the stomach that remains from subcutaneous injection trace that could affect the stomach segmentation.

0	0	1	0	0
0	1	1	1	0
1	1	1	1	1
0	1	1	1	0
0	0	1	0	0

Figure 5.4: **Structuring element for the 2D morphological closing in order to segment both stomach wall and cavity**, the 3D structuring element can be easily deduced: each voxel at an Euclidean distance less or equal to 2 voxels is associated with the value 1.

Stomach segmentation An intermediary dynamic image is obtained after applying a Gaussian filtering with $\sigma = 1.00$ to the original image. This step is done in order to smooth irregularities that might affect the intensity-based segmentation. This filtered image will be used only for the stomach segmentation. Then the stomach is segmented by thresholding the intensity at the level determined by the Otsu method [Ots79]. The level is the threshold that minimises the standard deviation in each group. This level is computed independently for each image of the sequence. For each, a mask of the higher intensity is obtained. The largest connected component is kept. The mask corresponds to the stomach wall at early times. For later times, because of the diffusion phenomenon in the cavity, the mask includes also the stomach cavity. In order to segment both wall and cavity, we apply a 3D morphological closing with the 3D extension of the 5x5 structuring element in Figure 5.4.

5.4.2 Layer-based decomposition of the stomach

For the temporal observation of the stomach activity a region-based analysis has been chosen. This approach can be also designated as a layer-based approach. The stomach is divided in to layers modelled on onion layers. Each

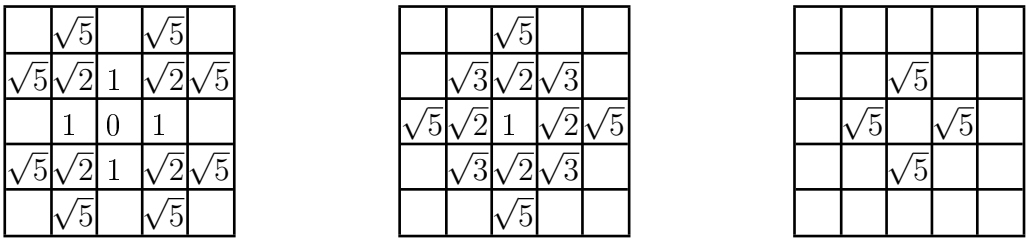

(a) Euclidean distance (in voxel) (plane 0, 1 and 2)

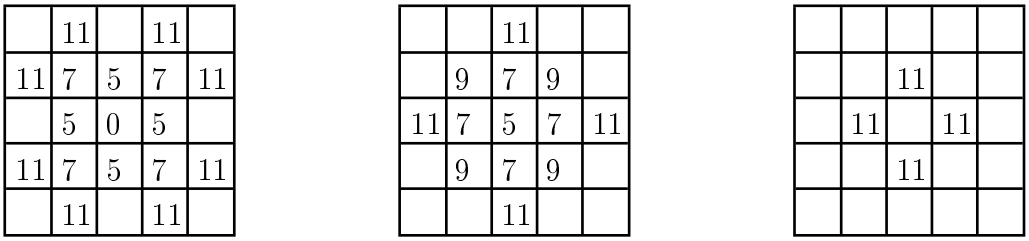

(b) 5-7-11 Chamfer distance (in voxel): extension to 3D (plane 0, 1 and 2)

Figure 5.5: **Distance transformation in 3D in a 5x5x5 neighbourhood.** These figures illustrate the distance computation in a 5x5x5 neighbourhood. The distance is given with respect to the inner voxel at level 0. Values are given for the planes at level 0, +1 and +2. Distance in planes -1 and -2 are obtained by symmetry. (a) presents the Euclidean distance transformation from the inner voxel. (b) presents the 5-7-11 Chamfer distance transformation which is the a 3D integer approximation for the Euclidean distance before division by 5.

stomach region or layer consists of the set of voxels that are equidistant to the outside of the stomach (background). Then, the idea is to associate each layer along the time, starting from the outer layer, and then to observe the temporal activity variation for each layer.

The distance transformations of the segmented stomach was computed with a 3D neighbourhood mask. According to [Bor86], the optimal distances in 2D digital images compared to the Euclidean distance are obtained with a 5x5 neighbourhood mask denoted Chamfer 5-7-11. We used the 3D extension for the Chamfer 5-7-11 illustrated by Figure 5.5. Only level 0, 1, and 2 are given. The others can be deduce from symmetry transform (reflection with respect to plane at level 0). The empty value are not given since they can be obtained from the combination of three first values.

After the distance transformation step, all distance are divided by the smallest distance value calculated by Chamfer distance transform (5 in this case). The first layer (the outer layer) is affected to a distance of 1 voxel

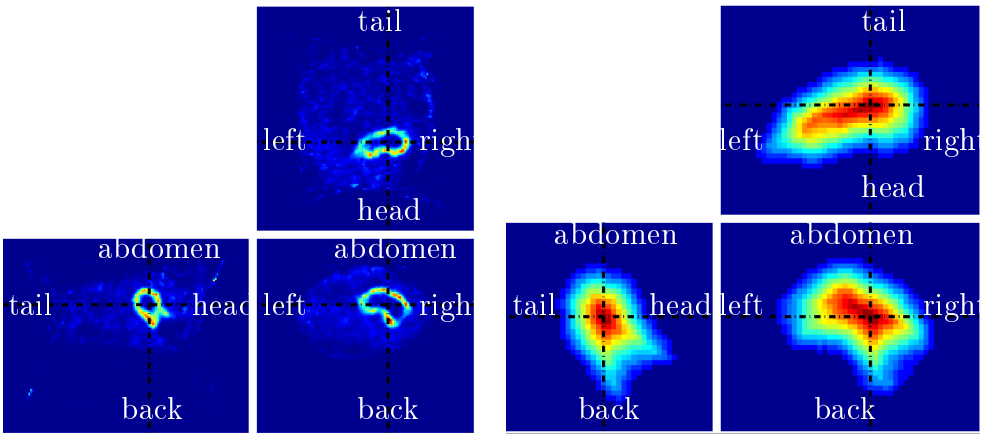

(a) Cross sections of the stomach in the three planes

(b) Chamfer distance transform 5-7-11

Figure 5.6: Stomach for the subject 0371 at early time after ^{99m}Tc-pertechnetate injection (a), and the resulting distance transform (b). Background (outside of the stomach) has a zero distance value. Foreground (stomach) distance increase with the distance to the background.

with respect to the background. The following layers (toward the inside of the stomach) are located at a distance that is an optimal approximation to the Euclidean distance according to [Bor86]. Indeed, after normalisation, the 2^{nd} layer is located at the distance $7/5 = 1.4$ from the stomach border which is a good estimate for $\sqrt{2} \simeq 1.41$. The 3^{rd} layer is located at the distance $9/5 = 1.8$ from the stomach border which is a good estimate for $\sqrt{3} \simeq 1.73$. The 4^{th} layer is located at the distance $11/5 = 2.2$ from the stomach border which is a good estimate for $\sqrt{5} \simeq 2.24$. The distances can thus be expressed in voxel unit, that represent the distance between voxel centers.

An example for the Chamfer distance transformation is given in Figure 5.6. Figure 5.6(a) shows the image at the first time point, 11.5 min after ^{99m}Tc-pertechnetate injection, of the 4D image for subject #0371 centered in the cavity of the stomach. The stomach can be distinguished by the layer of activity that surrounds the cavity without acivity at that time. After segmentation of the wall and a morphological closing step, the Chamfer distance transformation is computed. Figure 5.6(b) shows the resulting distance 3D map. The distance zero is attributed to all voxel from the outside of the stomach (background) and starting from the outer layer of the segmented stomach, the distance increases according to the Chamfer distance transformation.

5.4.3 Kinetic evolution of activity in stomach layers

The spatial and temporal evolution of the stomach activity uptake are simply observed with respect to the layers defined by the Chamfer distance transformation previously described.

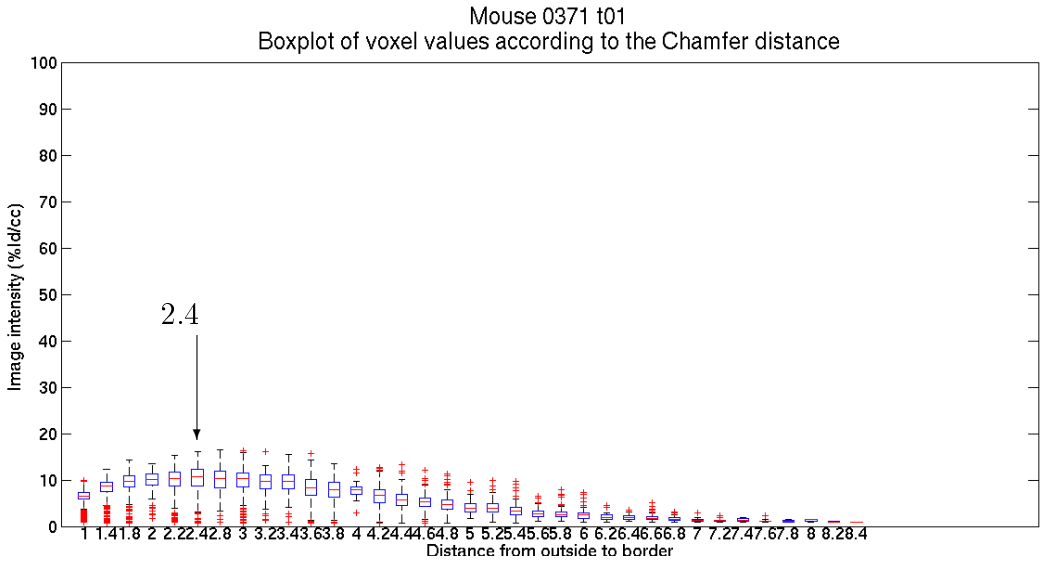

Figure 5.7: **Spatial-activity boxplot at first time acquisition observations for subject #0371:** T0 + 12.5 min. Axes: Distance from stomach border (left) to inner stomach (right) in abscissa, image intensity in (%Id/cc) in ordinate.

Distance-activity curves The spatial activity curves are observed for each time point of the dynamic images. Each layer that has been segmented, either in the stomach wall or cavity, is considered. An example is given for the subject 0371 in Figure 5.7. The spatial variation confirms the visual assessment: the activity increases from the border up to small distances (around 2.4 voxels) and then decrease up to a nearly zero activity in the cavity. (See Section 5.4.2 for details on the distance computation.) According to the Chamfer distance transformation Figure 5.5, distances larger than 4.5 voxels should all be gathered in a single thick layer associated to stomach cavity. This question will be discussed in Section 5.5.

Time-activity curves Time activity curves are observed for each layer. Layers are associated with respect to their distance to the background. An example is given for a layer that corresponds to the inner layer of the stomach

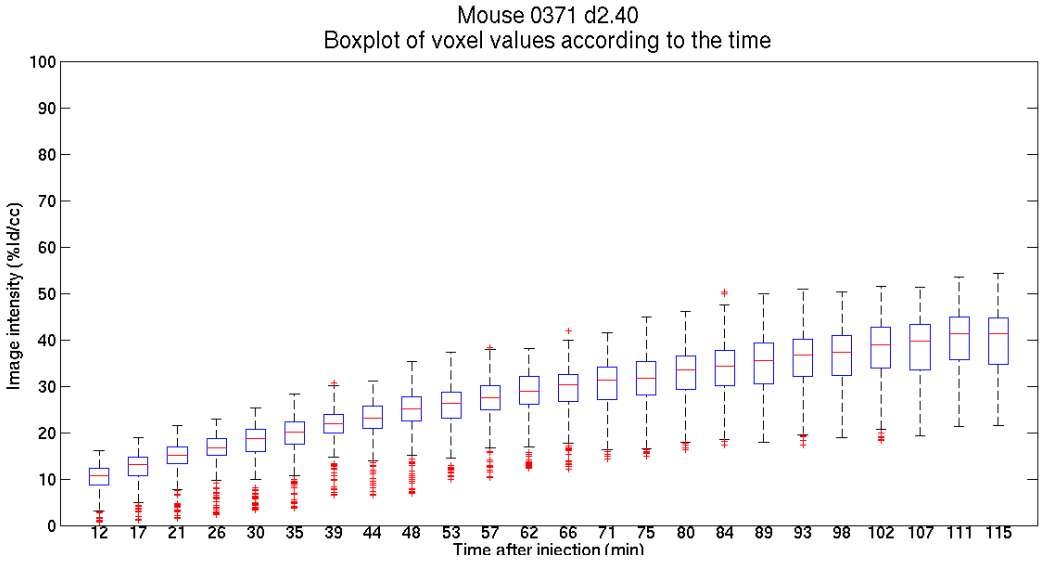

Figure 5.8: **Time activity boxplot for layer at distance 2.4 from stomach border.** Axes: Time after injection (min) in abscissa, image intensity in (%Id/cc) in ordinate.

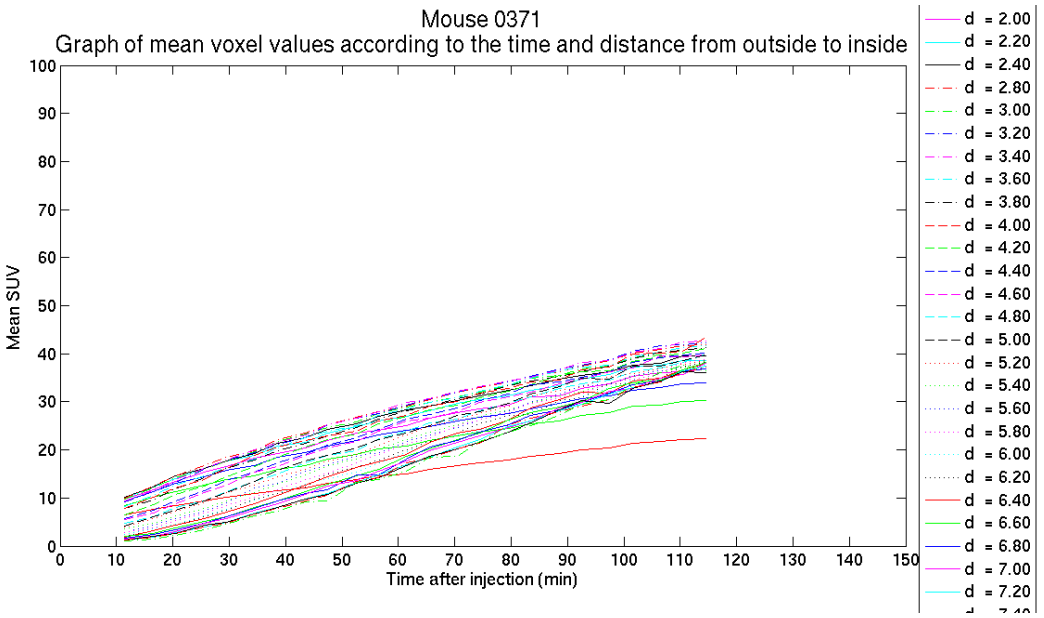

Figure 5.9: **Time activity curves for each layer for subject #0371.** Axes: Time after injection (min) in abscissa, average SUV in ordinate.

wall at distance 2.4 in Figure 5.8. The assumption that are made concerning the layer matching will also be discussed in the in Section 5.5.

Then, it is possible to compare all time-activity curves of all layers in order to observe some trends that could suggest some specific kinetic according to the distance. Figure 5.9 shows an example for the same subject. The analysis is difficult since there are too many layers. However, it seems that the activity corresponding to stomach wall increases faster at the beginning but then slower, while the activity in the stomach cavity layers is almost nonexistent but then increases faster up to an equivalent or greater average activity than in the wall.

5.4.4 Results

5.4.4.1 Stomach segmentation

Here, we present the results for the segmentation process for some interesting cases. For each case, we present one transverse slice centered in the stomach cavity where the original image in gray level is superimposed by the resulting segmentation (green line). Generally, the segmentation performed well for all subjects, segmenting what was expected. However, we notice some interesting results.

The segmentation for subject #0366 performed well as presented in Figure 5.10. This acquisition present clearly both challenges: a large stomach deformation and a progressive radioactivity uptake along the time. This large deformation results in a large variation in stomach size.

Figure 5.11 shows the resulting segmentation for the subject #0370 performed well. The process went well although at T22, 111.5 min after injection the stomach shape abruptly changed. This was due by the fact that the mouse woke up during the acquisition sequence and moved. This induced a spatial shift but the stomach was still segmented and the stomach volume remained coherent. In the end, the method is effective in the slices where the stomach appear like a balloon.

Figure 5.12 exhibit the interesting segmentation for the subject #0371. This shows a progressive activity uptake in the cavity that filled up to the margo plicatus (opening on the upper right corner). In the end, the method is less effective in the slices where the stomach appear like a “bucket”.

Despite the numerous segmentations that performed well, the process failed for some images acquired at early time after injection (less than 10 min). The activity uptake in the stomach was not high enough to compete with the low signal to noise ratio, or with the presence of the site of subcutaneous injection in the stomach field of view. However, after several minutes, the activity uptake in the stomach wall increased while it decreased in the site of subcutaneous injection, and the stomach was segmented again. This difficulty occurs with all subjects #0396, #0397, #0398, #0402, #0420 that were injected subcutaneously and imaged at short after the injection. As an

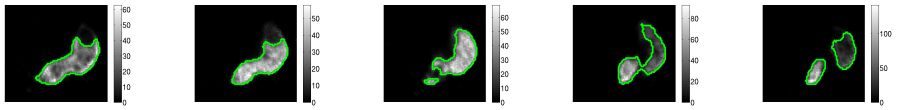

(a) T01: T0 + 18.5 min (b) T06: T0 + 40.5 min (c) T09: T0 + 54.5 min (d) T12: T0 + 67.5 min (e) T20: T0 + 103.5 min

Figure 5.10: Stomach segmentation for subject #0366 at several time point, same transverse slice

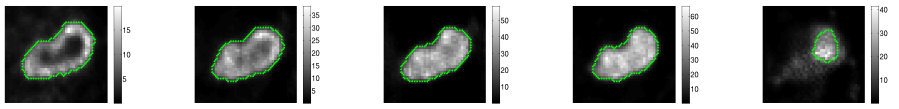

(a) T01: T0 + 16.5 min (b) T07: T0 + 43.5 min (c) T14: T0 + 74.5 min (d) T21: T0 + 106.5 min (e) T22: T0 + 111.5 min

Figure 5.11: Stomach segmentation for subject #0370 at several time point, same transverse slice

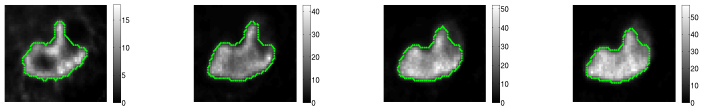

(a) T01: T0 + 11.5 min (b) T08: T0 + 43.5 min (c) T16: T0 + 79.5 min (d) T24: T0 + 114.5 min

Figure 5.12: Stomach segmentation for subject #0371 at several time point, same transverse slice

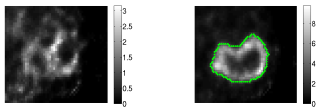

(a) T01: T0 + 5 min (b) T02: T0 + 20 min

Figure 5.13: Stomach segmentation for subject #0396 at several time point, same transverse slice

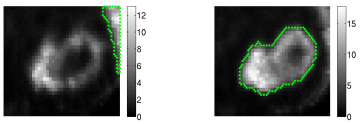

(a) T02: T0 + 18 min (b) T03: T0 + 31 min

Figure 5.14: Stomach segmentation for subject #0402 at several time point, same transverse slice

example, in Figure 5.13, the stomach wall can be distinguished at any on the selected slice by adjusting the intensity window but for the first instant, it was not segmented. In Figure 5.14, it is clear that the presence of remaining activity in the site of injection affects the segmentation as it defined.

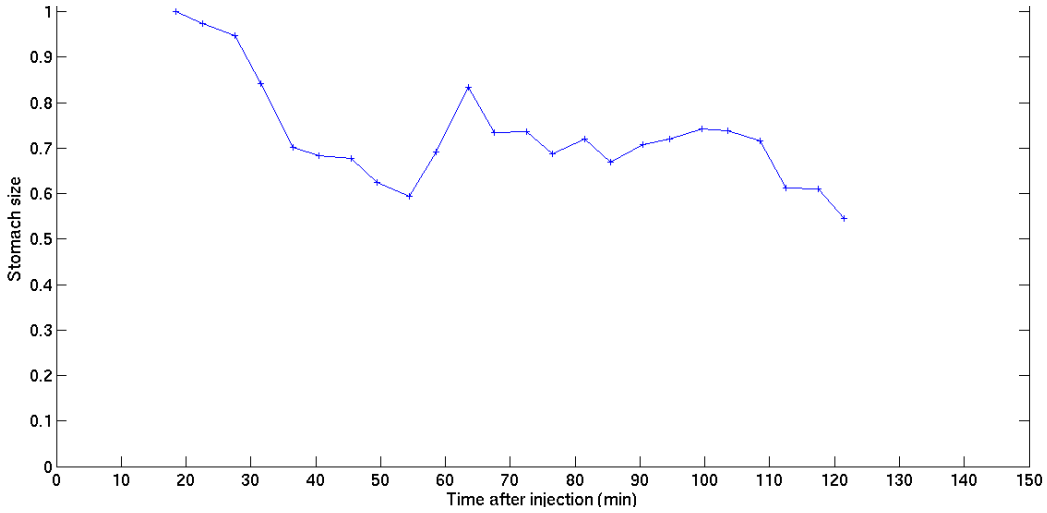

Figure 5.15: **Volume variation for the segmented stomach wall and cavity for subject #0366.** Volume are normalised to the largest volume. Axes: Time after injection (min) in abscissa, normalised stomach volume in ordinate.

Finally, Figure 5.15, Figure 5.16, Figure 5.17, Figure 5.18, and Figure 5.19 show the temporal variation of the stomach volume for some cases that have been described. As expected, for the subject #0366 (see Figure 5.15), the large variation in the stomach segmentation yields to a large variation in the volume as well. Figure 5.16 shows that the stomach volume slowly but regularly decreases with respect to the time. Only the third to last volume measures presents a small discrepancy comparing to the other, but it corresponds to the time when the mouse woke up and moved. Figure 5.17 is similar to the previous one, except for a small variation in the first instants that occurs very early. However, the rest of the variation shows a slow decrease of the volume. Figure 5.18 shows that the stomach volume is much bigger for the first acquisition than after. Actually, this is due to the fact that the volume corresponds here to the volume of the segmented activity. And the segmented activity for the first time point was the subcutaneous injection site instead of the stomach itself. The same goes for the two first instants for the subject #0402 Figure 5.19, although this time the wrong segmented region was smaller. This first volume (resp. two first volumes) is (are) then not relevant and should not be considered for the following steps. For the next

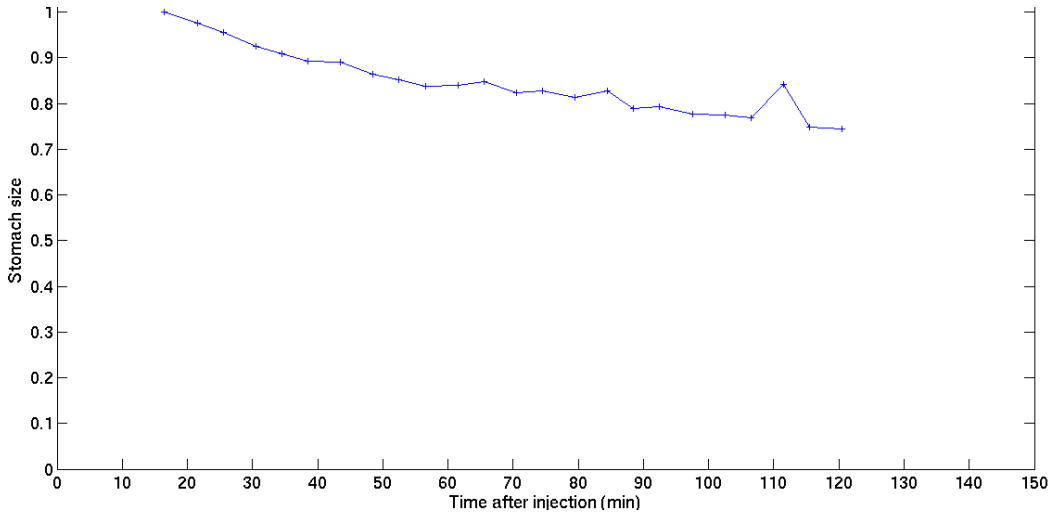

Figure 5.16: **Volume variation for the segmented stomach wall and cavity for subject #0370.** Volume are normalised to the largest volume. Axes: Time after injection (min) in abscissa, normalised stomach volume in ordinate.

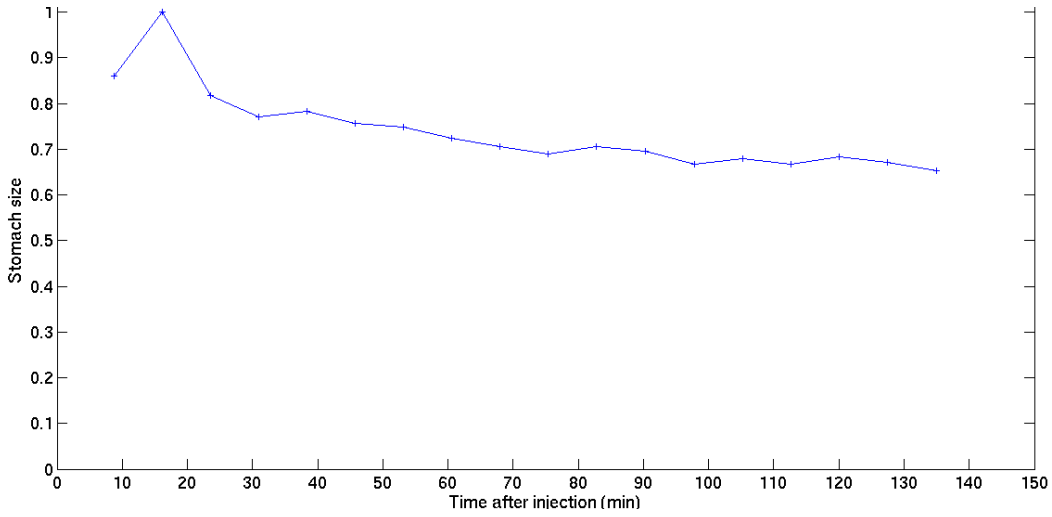

Figure 5.17: **Volume variation for the segmented stomach wall and cavity for subject #0530.** Volume are normalised to the largest volume. Axes: Time after injection (min) in abscissa, normalised stomach volume in ordinate.

volume measurements, volume slowly but regularly decreases with respect to the time, as it is shown in Figure 5.16.

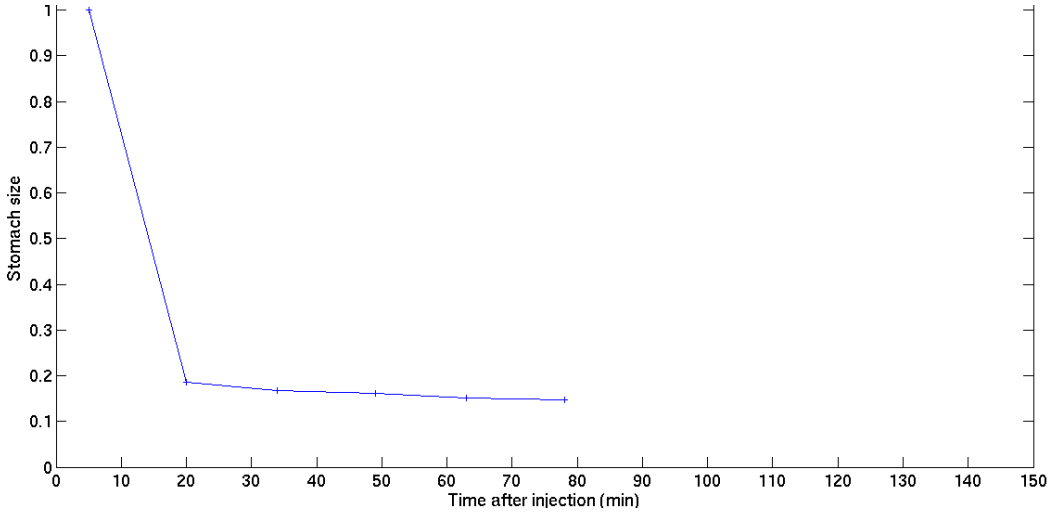

Figure 5.18: **Volume variation for the segmented stomach wall and cavity for subject #0396.** Volume are normalised to the largest volume. Axes: Time after injection (min) in abscissa, normalised stomach volume in ordinate.

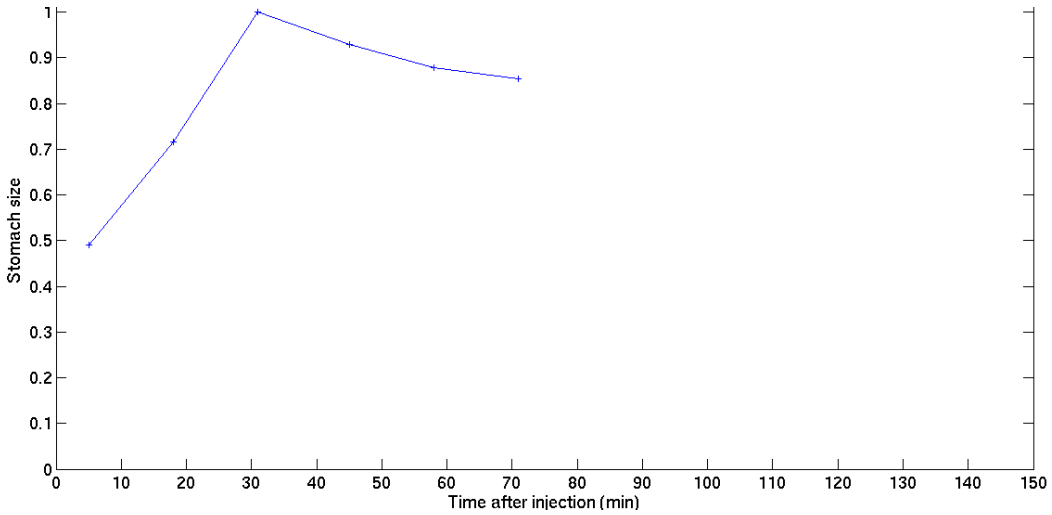

Figure 5.19: **Volume variation for the segmented stomach wall and cavity for subject #0402.** Volume are normalised to the largest volume. Axes: Time after injection (min) in abscissa, normalised stomach volume in ordinate.

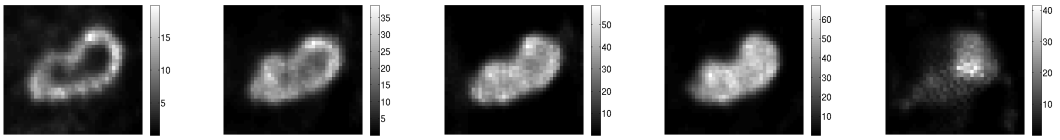

(a) Original transverse slice

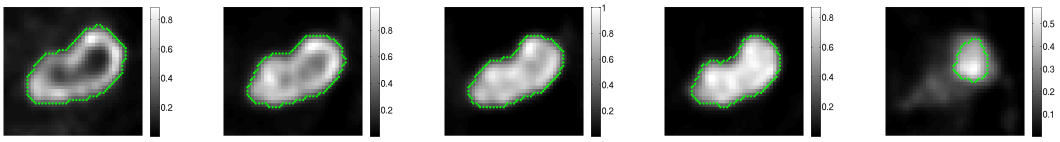

(b) Result of the segmentation superimposed over the normalised image after Gaussian filtering ($\sigma = 1.00$)

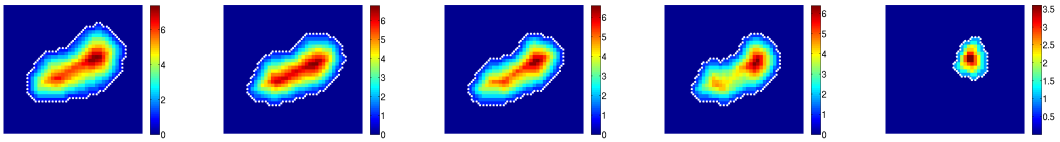

(c) Result of the Chamfer distance transformation

Figure 5.20: **Temporal evolution of iodide uptake after intraperitoneal injection of ^{99m}Tc of subject 0370**. From left to right: T01: T0 + 16.5 min, T07: T0 + 43.5 min, T14: T0 + 74.5 min, T21: T0 + 106.5 min, T22: T0 + 111.5 min.

5.4.4.2 Stomach segmentation and Chamfer distance transformation

Figure 5.20 presents the result of the Chamfer distance transformation with respect to the stomach original image and its segmentation for the subject #0370. On the original image slices presented in Figure 5.20(a), we can see that the intensity window enlarge with the time, suggesting that the stomach activity uptake increases proportionally. At the same time, it seems that the stomach is slightly shrinking as suggested by the Chamfer distance 3D map presented in Figure 5.20(c). To be mentioned, the 5th image corresponding to an acquisition 111.5 min after injection of ^{99m}Tc-pertechnetate reveals that the animal motion during the sequence of acquisition. Still, despite the animal motion, the layer-based decomposition allows the tracking of the progressive ^{99m}Tc-pertechnetate uptake in the stomach cavity.

5.4.4.3 Temporal and spatial activity curve

Spatial activity curves Figure 5.21, Figure 5.22, Figure 5.23, Figure 5.24 and Figure 5.25 show activity curves at different times. Each figure shows the activity depending on the distance from the border of the stomach. More

precisely, each point of the curve corresponds to the average activity observed on the layer defined by its distance to the border. Boxplots represent the range of activity in the layer, they show maximum and minimum, and first and third quartile. We first observe that the activity is more and more important along the acquisition but also that the activity does not evolve in the same way in all the layers.

In Figure 5.21, at 8.73 min, the activity is quite low in all the layers. However, the external layers (approximately between 0 and 4.5 voxels) expose a higher activity, we assume that these layers correspond to the stomach wall. The internal layers that have a lower activity correspond to the stomach cavity.

The Figure 5.22 and Figure 5.23 show the activity after 45.73 min and 82.75 min. At these instants, the activity is constantly growing, and the stomach wall still has more activity than the stomach cavity. Note that the point where the activity decreases is always around 4.5 voxels, this corroborates our hypothesis that the frontier between stomach wall and cavity is around this position.

In Figure 5.24 and Figure 5.25, at 112.62 and 134.92 min, the growth of the activity slows down, and the activity of the stomach wall stabilizes. However, the activity of the stomach cavity still slowly increases and finally reaches approximately the same activity as the inside of the stomach wall.

To summarize, along time the activity shown by the stomach increases: at the beginning this activity is accumulated mostly in the stomach wall, and then, after a delay, the activity diffuses towards the stomach cavity.

Temporal activity curves In Figure 5.26, the sub-figure (a) shows superimposition of all average temporal activity curves, for every layer of the stomach of subject #530. It suggests that all layer activity uptakes follow a similar trend. Only the curves corresponding to the outer layer seem to have a stabilized activity at some point in time. On sub-figure (b), we show the global activity of the whole stomach, that has the same global trend. This corroborates the precise analysis that we made in the previous paragraph.

Figure 5.27 shows the variation of the threshold that was automatically computed for segmenting the whole stomach. The sub-figure on the left shows that the threshold grows along time, similarly to the global activity. The sub-figure on the right confirms the trend that appears on the left hand side: the variation of the automatic threshold grows more or less at the same rate as the maximum intensity. The conclusion is that some of the external layers may be lost along time, because the global activity grows. The external layers that always have a small activity may be lost in the segmentation after some time. However, we showed in Figure 5.17, Section 5.4.4.1, that for this same mouse, the variation of the stomach volume was very low, but decreasing. The conclusion is that the automatic threshold detection is not perfect and most probably looses some of the external layers of the stomach along time.

However, we consider in the following that, as the volume variation is quite low, the quality of the automatic segmentation is sufficient enough for our study.

5.4.4.4 Plasma temporal activity curve

In addition to time activity curves for stomach layers, we extracted the blood time activity curves for all acquisitions that have the heart in the field of view. This time activity curve will be used to estimate the input function in the compartmental analysis that we will present in the next Chapter. They were obtained by measuring the average activity in a 3x3x3 mm^3 sphere located in the left ventricule. Figure 5.28 shows the time-activity curve (TAC) for all subjects, for each type of injection: subcutaneous (subfigure (a)) and intraperitoneal (subfigure (b)). As the injection can be considered as an impulse, the blood TAC is expected to be a bolus. As we can see for the subject #0530, in the subcutaneous case, the activity increases quickly, reaches its maximum around 20 min after injection and then decreases slowly. This shape can be considered as closed to a bolus. In the intraperitoneal case, the curve is only decreasing and if there was a peak it was in the first instants, before the first measure. We would probably need more data right after the injection in order to observe a peak and use this kind of injection method.

We choose to perform our compartmental analysis on the subject #0530 and with the subcutaneous injection because we have a very precise sampling in this case, and the blood temporal activity curve has the expected shape, i.e., it is closed to a bolus.

5.5 Discussion

The main contribution in this chapter is a region-based analysis for the study of iodide biodistribution in SPECT images of mice stomach. This simple approach allows the observation and the description of the progressive ^{99m}Tc-pertechnetate uptake in the stomach. We also described the challenges that had to be addressed in our analysis: progressive radioactive uptake and stomach deformation. The region-based approach has been chosen instead of a voxel-based. Voxel-based analysis would have allowed a much more precise study if the stomach was not deforming, but the movement of the stomach and the evolution of the activity makes this approach impossible. Our region-based approach is based on layers, it relies on the following observations:

- The stomach has a bean shape. It can be decomposed into layers.
- In a sequence of images, layers can be associated with respect to the distance to the border.

The strengths of this layer-based approach are the following:

- Our approach is adapted to stomach deformation.
- The Chamfer distance transform is simple, efficient, and provides the best approximate for Euclidean distance.
- The layer-based approach makes up for the irregularities of the stomach shape.

However, the region-based approach has some weaknesses induced by some assumptions and choices that were done. In the following of this section, we review these weaknesses, explain them, and describe how we could improve the method in the future.

Stomach segmentation short after the injection Intensity thresholding with Otsu method finds the optimal threshold that divides the data into two groups of voxel by minimising the standard deviation in both groups. As it is only based on the intensity, the process failed when the intensity in the object (e.g. the stomach wall) was too low compared to the noise or the site of injection. In practice, in these first instants, it is often the injection site that is segmented. The consequence of this wrong segmentation is that all the activity measured in the layer will lead to wrong interpretation and affect further work such as the extraction of the time activity curves for the compartmental analysis that will be presented in Chapter 6. A solution for this would be to guide and constrain the segmentation in early acquisition using the result of the segmentation at later instants. This way, the region segmented in the first instants would be more precise and lead to a better analysis.

Approximation due to the Gaussian filtering The fact that we apply a Gaussian filter smooths the irregularities of the stomach but it also tends to enlarge the segmented area for the stomach, especially when the activity is low (i.e., short after the injection). However, we consider that the benefits of the filtering are more important than this slight imprecision.

Stomach volume decrease As mentioned in Section 5.4.4.3, when the activity increases, the size of the stomach decreases because the external layers of the stomach may be lost in the automatic segmentation process. The main consequence is a slight layer mismatch in our analysis: the first layer at a given instant might disappear in the next instant. However, we have shown that the decrease of the stomach volume is quite low, and we consider that this layer mismatch is negligible for our study. In the future, more complex segmentation techniques might be considered in order to limit the layer mismatch.

Morphological closing is not adapted to the shape of the stomach.
The stomach of the mouse is in fact made of two parts: the glandular wall and the cavity. The margo plicatus forms the limit between the two areas; it behaves a bit like a valve which prevent the food to go back to the forestomach. In the forestomach and in the margo plicatus, there is few or no NIS expressing cells. Consequently, the shape of the area of the stomach is not fully closed by the stomach wall. Indeed the region corresponding to the margo plicatus is very thin, and the layer approach will consider the margo plicatus and the part of the stomach cavity nearby as part of the stomach wall. However, this region of the stomach is quite small and we consider that the imprecision induced by this wrong classification as negligible. Detecting more precisely this area would be very complex and would probably not improve the quality of our study.

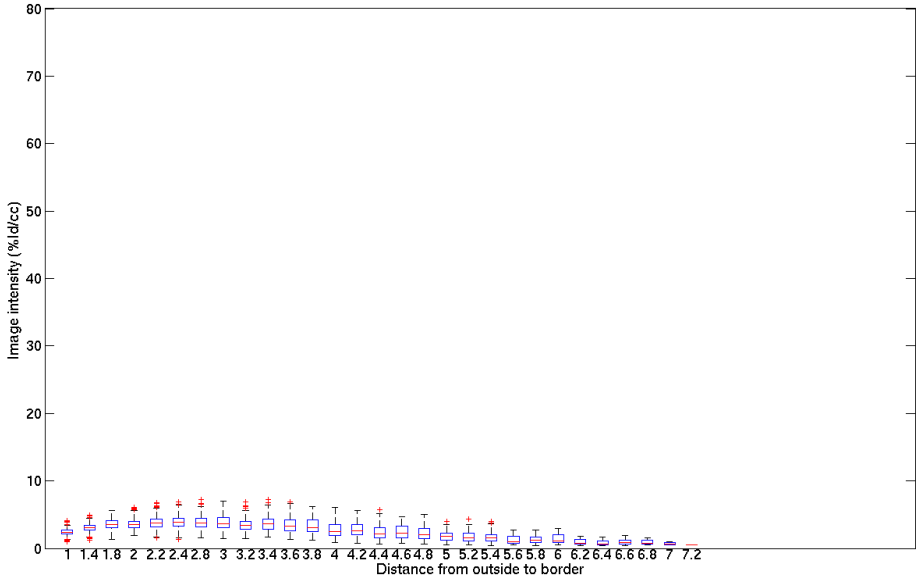

Figure 5.21: **Activity boxplots with respect to the distance from stomach wall to stomach cavity for mouse #0530 (T0 + 8.73 min).** Axes: Distance from stomach border (left) to inner stomach (right) in abscissa, image intensity in (%Id/cc) in ordinate.

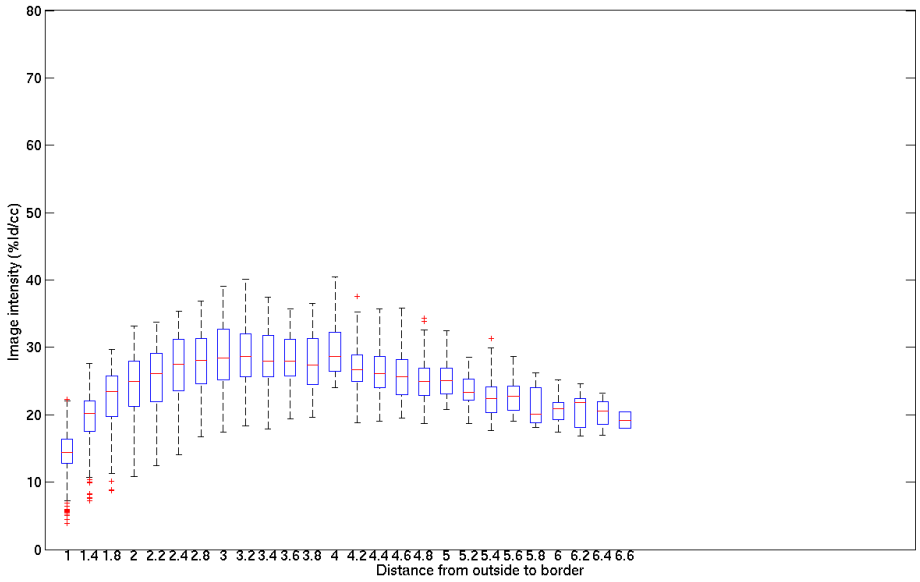

Figure 5.22: **Activity boxplots with respect to the distance from stomach wall to stomach cavity for mouse #0530 (T0 + 45.73 min).** Axes: Distance from stomach border (left) to inner stomach (right) in abscissa, image intensity in (%Id/cc) in ordinate.

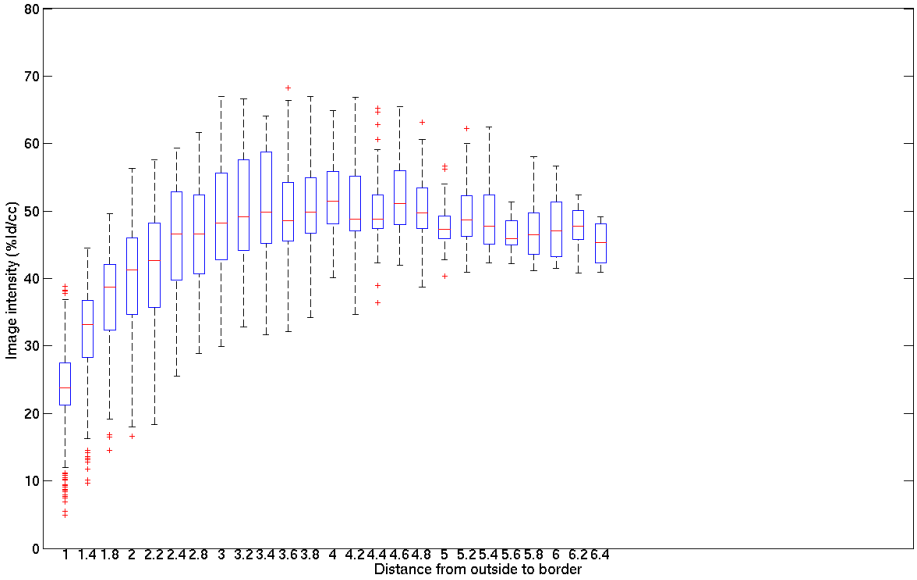

Figure 5.23: **Activity boxplots with respect to the distance from stomach wall to stomach cavity for mouse #0530 (T0 + 82.75 min).** Axes: Distance from stomach border (left) to inner stomach (right) in abscissa, image intensity in (%Id/cc) in ordinate.

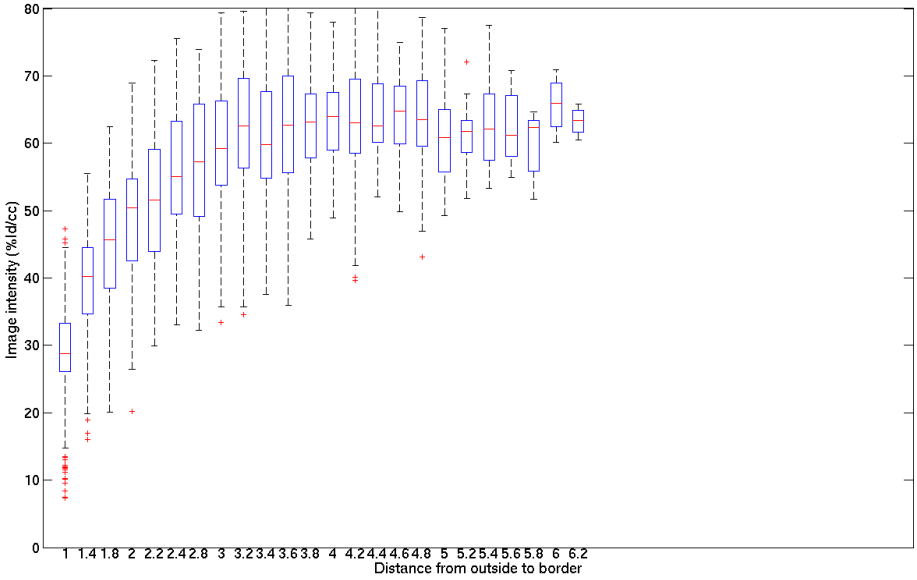

Figure 5.24: **Activity boxplots with respect to the distance from stomach wall to stomach cavity for mouse #0530 (T0 + 112.62 min).** Axes: Distance from stomach border (left) to inner stomach (right) in abscissa, image intensity in (%Id/cc) in ordinate.

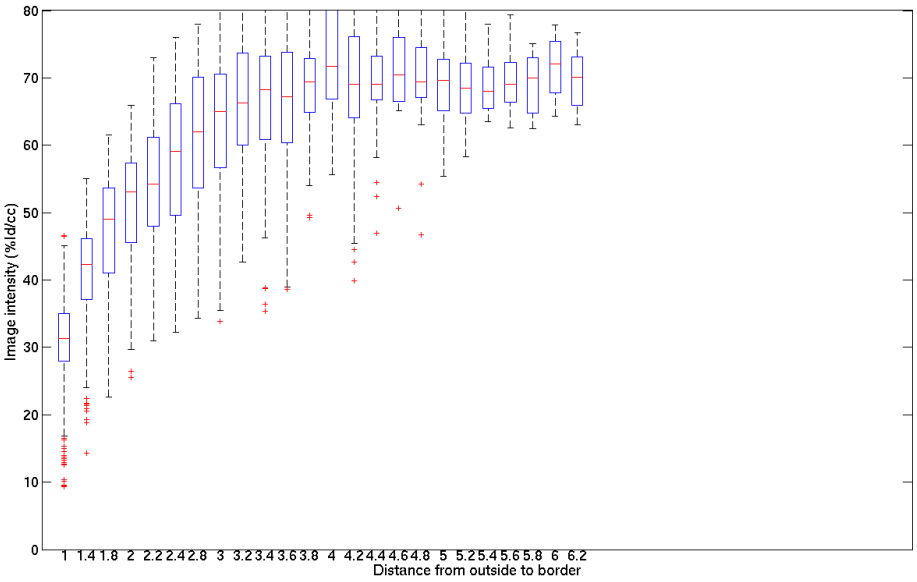

Figure 5.25: **Activity boxplots with respect to the distance from stomach wall to stomach cavity for mouse #0530 (T0 + 134.92 min).** Axes: Distance from stomach border (left) to inner stomach (right) in abscissa, image intensity in (%Id/cc) in ordinate.

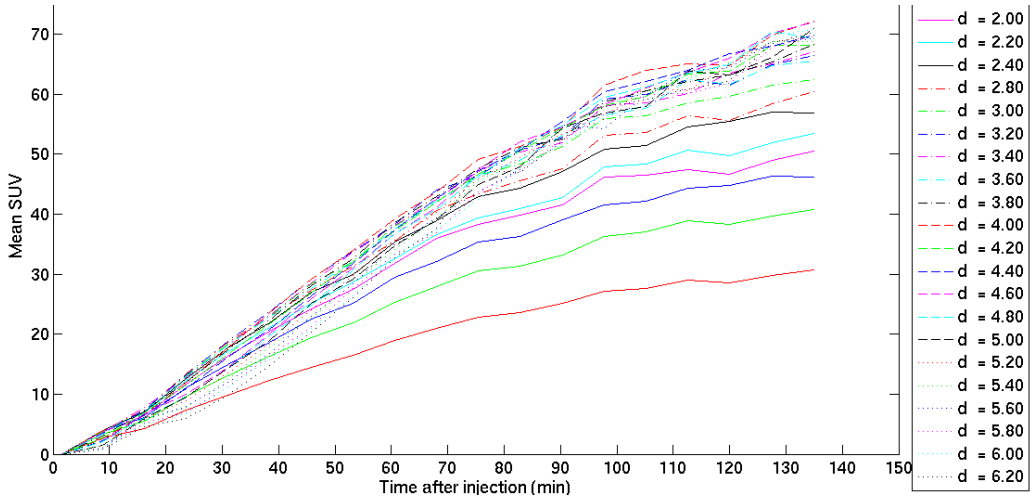

(a) Superimposition of all time-activity curves for each layer. Axes: Time after activity injection (min) in abscissa, average SUV in ordinate.

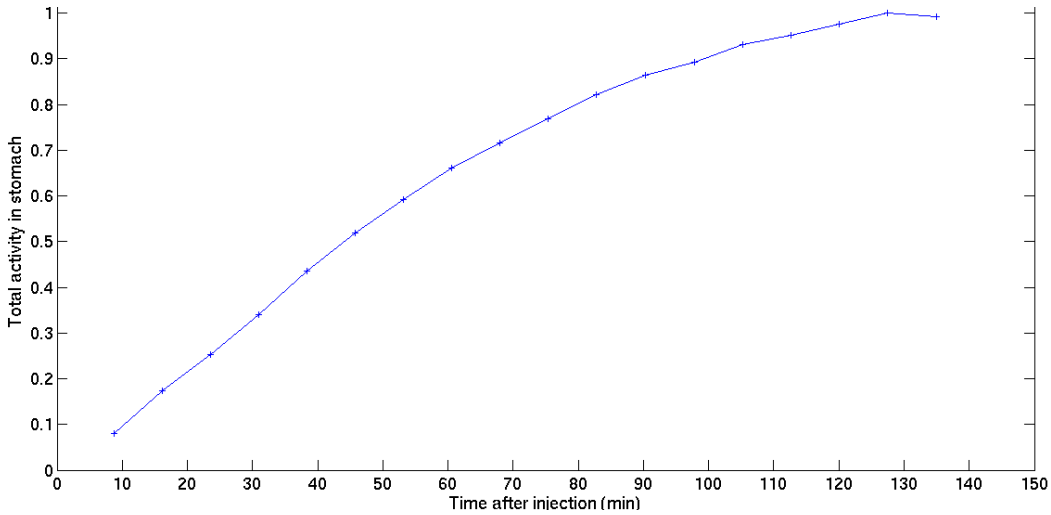

(b) Variation of total activity in the stomach with respect to the time. Axes: Time after activity injection (min) in abscissa, total activity in stomach normalised to maximum activity measured in ordinate.

Figure 5.26: Mouse #0530: time activity curves per layer and in the whole stomach

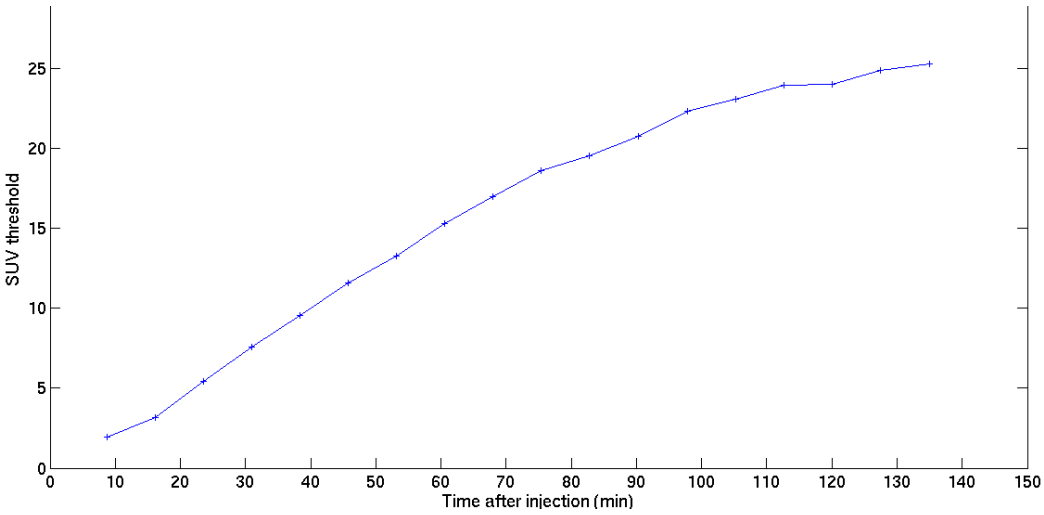

(a) Variation of automatic activity threshold for stomach segmentation with respect to the time. Axes: Time after activity injection (min) in abscissa, SUV in ordinate.

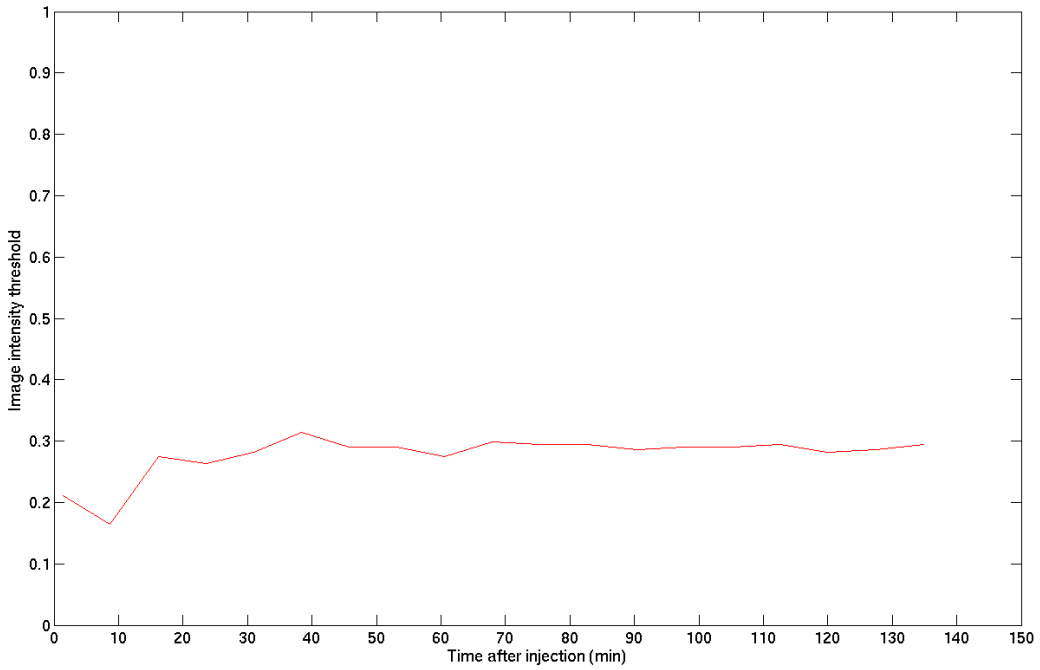

(b) Variation of automatic activity threshold normalised to the maximum intensity for stomach segmentation with respect to the time. Axes: Time after activity injection (min) in abscissa, SUV normalised to the maximum SUV at each time point in ordinate.

Figure 5.27: Mouse #0530: segmentation threshold variation through the time.

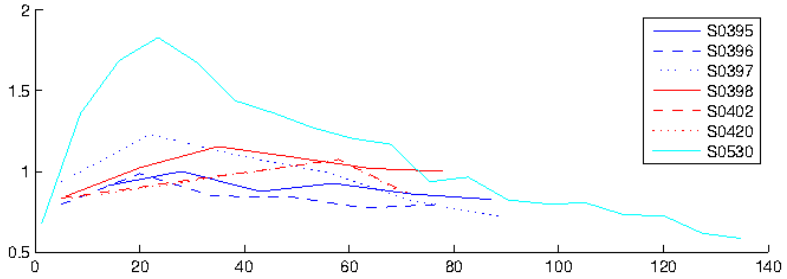

(a) Plasmatic temporal activity curves for subcutaneous injection of ^{99m}Tc-pertechnetate

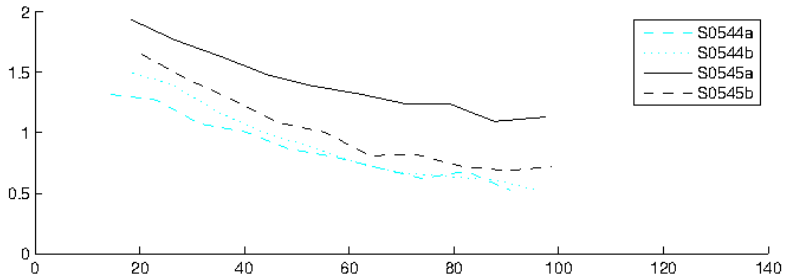

(b) Plasmatic temporal activity curves for intraperitoneal injection of ^{99m}Tc-pertechnetate

Figure 5.28: Plasma temporal activity curves. Axes: Time after activity injection (min) in abscissa, average SUV in ordinate.

Chapter 6

Dynamic SPECT analysis of ^{99m}Tc-pertechnetate uptake in stomach: biodistribution modelling

Contents

6.1 Introduction

In the previous chapter, we defined the biological context of this study and we showed that it is possible to quantify the ^{99m}Tc-pertechnetate uptake in the murine stomach with dynamic single photon emission computed tomography (SPECT). The working hypotheses in terms of biology are:

- the ^{99m}Tc-pertechnetate uptake in stomach is cyclic with a reabsoption phenomenon in the pars pylorica region of the stomach (see Figure 5.3)
- there is a ^{99m}Tc-pertechnetate retention in the glandular cells of the gastric mucosa (see Figure 5.2)

These hypotheses are done according to observations done on stomach immunohistochemistry (IHC) images. Knowing all of this, we do want to investigate further the mechanisms of this uptake. We would like to set up a model that explains these observed ^{99m}Tc-pertechnetate dynamic uptake in the stomach. Then, we would like to estimate the model parameters that best fit the observations. Among others, with this descriptive model, we would like to confirm that the sodium/iodide symporter (NIS) expression in the apical membrane of pars piloric cells contribute to the cyclic ^{99m}Tc-pertechnetate uptake mechanism. Moreover, we would like to answer the biologists main question: *Is the ^{99m}Tc-pertechnetate accumulation in the gastric glandular cells superior to the secretion into the stomach cavity? and if yes, what is the limiting step?* We remind that the role of gastric cells expressing NIS on their basolateral membrane is the accumulate and the secretion of ^{99m}Tc-pertechnetate. However, the functional role of gastric cells expressing NIS on their apical membrane has to be confirmed: *Does it maintain or control the ^{99m}Tc-pertechnetate concentration in the cavity?*

Observations Indeed, the ^{99m}Tc-pertechnetate uptake from the blood to the stomach wall is clearly associated to the expression of NIS proteins in the glandular cells. Then, it is also known that the ^{99m}Tc-pertechnetate is also secreted by these glandular cells in the stomach cavity. Both of these observations have been assessed by SPECT imaging. However, since there is no NIS protein expression in the apical regions of some stomach wall cells, there is no proof of reabsoption of ^{99m}Tc-pertechnetate by the stomach. Still, dynamic SPECT analysis showed that, after some time, the activity in both stomach wall and cavity tends to stabilise (i.e. the speed of activity uptake is slightly reduced). This observation suggested that there might be a ^{99m}Tc-pertechnetate reabsoption phenomenon by the stomach wall.

Objectives Consequently, the objective of this chapter is first to define a descriptive model of the ^{99m}Tc-pertechnetate uptake in the stomach, then to

identify the parameters of this model using the observations and finally to confirm the existence of this reabsoption according to the parameters that have been observed.

Different types of modelling The general objective of modelling is to find some general laws that will describe a phenomenon. The model is good if it the real behaviour exactly follows the laws that have been discovered. However, reality is often too complex, then simplified models provide a precise enough approximation of the phenomenon under certain assumptions. One could classify modelling in two main categories according to their objectives:

- the descriptive modelling that aims at describing a phenomenon according to some observations. It is used to explain how and why the studied phenomenon occurs. The field of application of such models is wide, they are frequently used for understanding consequences or behaviour of some new products (pharmaceuticals).
- the predictive modelling goes a step further. It aims at deducing laws that not only describe the present but also predict what will happen in new situations according to a wide set of data.

In this study, our primary objective is to confirm the existence of a phenomenon. This should be addressed by descriptive modelling, based on the data we presented in the previous chapter. The data we currently have and the current status of our analysis prevents us from doing any predictive analysis at this point. However, a possible follow-up of our work could be to use the model we design in order to predict the value of the parameters of the phenomenon for a new subject, or in a different context.

Compartmental analysis In this chapter, a mathematical model based on compartmental analysis approach is proposed. Compartmental analysis is frequently used in pharmacology to estimate drug exchanges in organs, or in biomedical emission tomography (ET) to study dynamically the biodistribution of markers. So far, most biodistribution studies considered organs as a whole but only a few of them considered organs as a set of different functional subunits (subregions or tissues). Here both the size of the stomach and the camera resolution were suitable for the distinction between of the stomach wall and the stomach cavity.

More generally, compartmental analysis consists in describing phenomena as compound exchanges between compartments. Each compartment is supposed to have a homogeneous concentration of the studied compound but they distinguishes from each other from the uptake kinetic. Exchanges of compound between compartments are described by transfer functions. The ordinary differential equations that describe the transfer functions are linear

functions with time-invariant parameters. The bases of compartmental analysis are summarised in Appendix B. We also remind the major definitions and principles that can be found in the literature (ref. to [God83, Jac96] for further information). The reading of this appendix might be useful for the understanding of the mathematical description of the compartmental analysis.

The compartment analysis used for the characterisation of a biodistribution model can be considered in two ways. Either by solving a direct problem that consists in simulating the kinetic evolution from the knowledge of the transfer functions of a theoretical model. Or, as it is the case here, by solving an inverse problem that consists in estimating the transfer functions from longitudinal observations and characterise the model parameters [BÅ70, RW71]. This inverse problem can be solved in two different ways: a direct approach that uses a semi-analytic resolution, or an indirect approach that estimate the set of transfer parameters with optimisation approaches.

The purposes and applications for compartmental analysis are multiple. In the literature, a few biodistribution works have been conducted with compartmental analysis approaches on other organs than stomach using ET imaging and different radiopharmaceuticals: on the thyroid [Hay78, DCH$^+$08, FGV$^+$10], on the heart [RGH98, HRZG98, RGH00, KG01, RGH02, GRS$^+$10, ZGK10, NYK12] and on the brain [JST$^+$12, NSG$^+$13].

Our approach In this work, we will focus on the study of the kinetics of one substance, the iodide analog ^{99m}Tc-pertechnetate, and in one single organ - the stomach - since the general idea is to design a model for iodide uptake kinetic in the stomach.

This chapter presents the following contributions:

- A compartmental model of the stomach (Section 6.2) that distinguishes the stomach wall from the stomach cavity;
- An analytic and numerical resolution methodology for determining the time-activity curves (TACs) for each compartment of the stomach (Section 6.3) based on the activity of each layer obtained as described in the previous chapter;
- The results: the parameters that characterise ^{99m}Tc-pertechnetate uptake in the stomach such that those parameters fit with the observations made in the previous chapter (Section 6.4).

6.2 Compartmental model of the stomach

A few works have been conducted that only focus on compartmental analysis in the stomach. Several studies addresses the question of ^{99m}Tc-pertechnetate

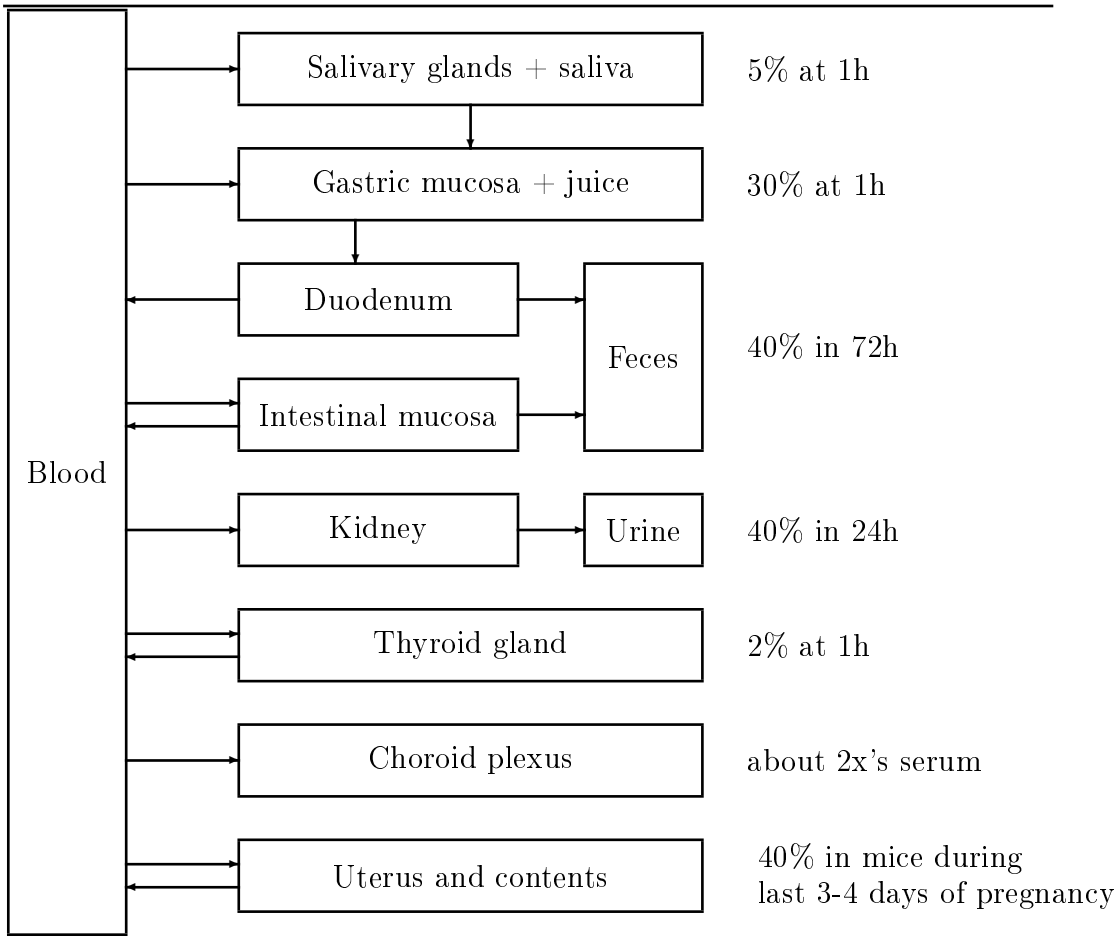

Figure 6.1: ^{99m}Tc-pertechnetate biodistribution in mice, proposed in [LH72]

biodistribution in mice. For example, Figure 6.1 shows a schematic representation of the ^{99m}Tc-pertechnetate biodistribution proposed in [LH72]. This representation also gives temporal estimation of uptake or secretion of ^{99m}Tc-pertechnetate after an intravenous injection. However ^{99m}Tc-pertechnetate uptake and kinetic in stomach has been mentioned in a few papers [Hof67]. The difficulty with the stomach is that it is a soft organ, with non predictable deformation due to alimentary bolus combined with respiratory motion and subject movement.

In this section, we will a schematic representation of the ^{99m}Tc-pertechnetate biodistribution in the stomach that corresponds to the block "gastric mucosa + juice" in Figure 6.1. The gastric juice is a digestive fluid that is secreted by the gastric mucosa, i.e. various glands in the mucous membrane of the stomach (i.e. the gastric mucosa). This representation will be used for the kinetic study with compartmental analysis.

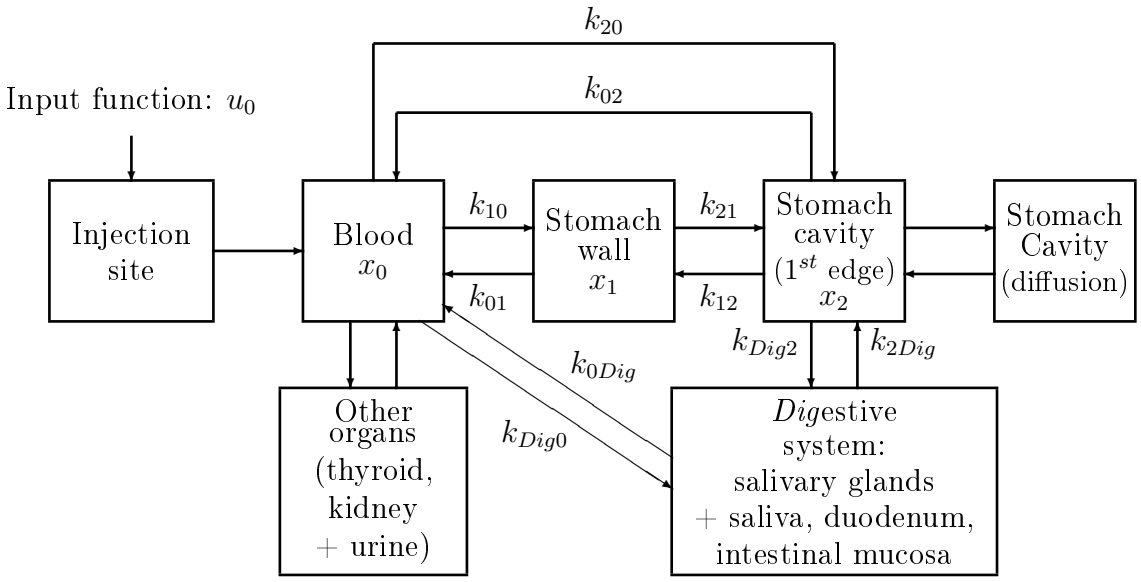

Figure 6.2: Complete compartmental model describing the studied problem: kinetic of iodide uptake in the murine stomach.

6.2.1 Complete model

Figure 6.2 presents a first proposition for the compartmental system that describes the dynamic distribution of ^{99m}Tc-pertechnetate in the murine body. It is focused on the organ of interest: the stomach. Each box refers to a compartment, i.e. an organ or a set of organs, which is a macroscopic subunit containing a concentration x_i of ^{99m}Tc-pertechnetate. The observations (or measures) of this activity are the system outputs of the model, and are denoted y_i. Arrows between boxes represent the transport of ^{99m}Tc-pertechnetate between compartments, they are labeled with transfer parameters k_{ij}; some arrows have no label because they will not be used in the simplified model that we will describe in the next section.

The input function $u_0(t)$ refers to the ^{99m}Tc-pertechnetate injection in the mouse. Two types of injection can be performed: an impulse (bolus) that is a one-time injection of all the activity in the site of injection before the imaging sequence, or a continuous injection that is a permanent injection during the imaging sequence. In this study, the ^{99m}Tc-pertechnetate injection was always an impulse. It is formally defined by $u_0(t) = D_0\delta(t)$.

Then, according to the site of injection, the blood activity function $x_0(t)$ is different. This blood activity function is experimentally measured in the left ventricle of the heart. In the case of an intravenous injection, all the activity is directly injected into the blood system, which generally induces the blood activity function to be of the form $x_0(t) = D_0e^{-kt}$. However, intravenous injection are difficult to perform. There are two other possible sites for injection: in the peritoneum (intraperitoneal injection), or under the skin (subcutaneous

injection). For these two cases, the blood activity function can be modelled as of a sum of two exponential functions such as: $x_0(t) = \phi_1 e^{-\theta_1 t} + \phi_2 e^{-\theta_2 t}$. The first term represents the slow activity uptake in the blood system and the second term represents an even slower distribution of the activity through all the body. However, the kinetic is slightly different, since in the case of intraperitoneal injection, there is an activity diffusion phenomenon in the peritoneum simultaneously to the progressive activity uptake by the blood system.

Once in the blood system, ^{99m}Tc-pertechnetate is carried through all the body and is going to accumulate in several glandular organs such as the thyroid, salivary glands, stomach, or to be eliminated by kidneys.

As we focus on the interaction at the stomach level, Figure 6.2 details the exchange between the blood, the stomach wall, and the stomach cavity. From the stomach wall point of view, ^{99m}Tc-pertechnetate can be exchanged only either with the blood or with the stomach cavity. From the stomach cavity point of view, ^{99m}Tc-pertechnetate is mainly secreted by the stomach wall, but exchanges might exist with the rest of the digestive track. Indeed, there is a progressive diffusion of ^{99m}Tc-pertechnetate in the cavity up to the forestomach cavity. Some ^{99m}Tc-pertechnetate might be transported from the salivary glands to the stomach cavity in the saliva of from the stomach cavity to the duodenum at the same time as the alimentary bolus.

6.2.2 Simplified compartmental model

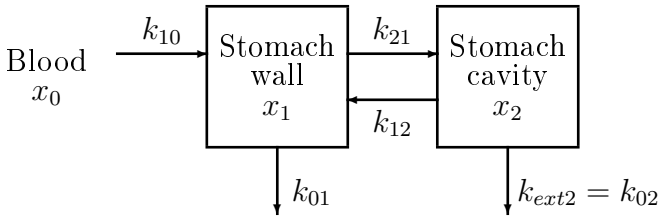

Figure 6.3: Compartmental system after second simplifications: two-compartment catenary system

Figure 6.3 presents the model after simplification. This simplified model is a general linear, time-invariant catenary system with only two compartments and one input (x_0) on the first compartment. We explain below the different simplifications we made relatively to the original model.

Blood input function Blood activity is now considered as the input of the system instead of the former input function u_0, and is only applied to the first compartment: the stomach wall. The injection of ^{99m}Tc-pertechnetate from the input into the first compartment is characterised by the parameter k_{10}. Blood cannot be considered as a compartment

since the space that is occupied by blood is not a closed space and is hard to define. As a consequence, the blood activity function cannot be deduced from the knowledge of the type of ^{99m}Tc-pertechnetate injection in the body since the bioavailability fraction of activity in the blood is not known beforehand. Fortunately, the blood activity function can be easily measured in the left ventricle in SPECT images. Thus, we simplify our model by removing the two first blocks: input function u_0 and the injection site. *We now consider the input function of our compartmental model as equal to the blood activity* x_0 as shown on the left of Figure 6.3. This is not an impulse function anymore. It can be approximated by sum of two exponential functions, as we will show in Section 6.3.

Diffusion in the stomach cavity In the previous chapter, it has been observed that ^{99m}Tc-pertechnetate is diffusing in the stomach cavity from the stomach wall toward the middle of the cavity. Here, we first put aside the diffusion phenomenon inside the cavity, it might be studied in later improvements of the model. Consequently, in this first study, *we won't consider the diffusion phenomenon in the cavity, but we will consider the stomach cavity as a whole.*

^{99m}Tc-pertechnetate in other organs and in digestive system We assume that the blood is carrying ^{99m}Tc-pertechnetate through the whole body and that ^{99m}Tc-pertechnetate can accumulate in organs that are deserved by blood. If it is accumulated in those organs, we assume that it cannot leave them, it is trapped like the model of the "thyroid trap"([Hay78]).

Then, the only glandular organ of the digestive system located before the stomach is the salivary glands, however according to Figure 6.1 (and [LH72]), these glands only contribute to 5% of the activity after one hour. Additionally, in our case the mouse is sleeping, thus is assumed to produce less saliva that would go to the stomach. We thus consider that the ^{99m}Tc-pertechnetate transport from the digestive system directly into the stomach is negligible.

In other words, from the stomach point of view, the ^{99m}Tc-pertechnetate uptake can be considered as an autonomous cyclic phenomenon. As a consequence, *we assume that there is no* ^{99m}Tc*-pertechnetate transport parameters from the other organs into the blood.* Additionally, *we assume that there is no transport from the digestive system to the stomach cavity, and also that there might be leaks from stomach wall and cavity to the outside of the system, with transport parameters denoted* k_{01} *and* k_{02}.

Transport between blood and stomach cavity As there is no direct blood injection into the stomach cavity, we remove from the model the

transfer parameter k_{20} of ^{99m}Tc-pertechnetate from blood to the stomach cavity. However, we still consider there is a ^{99m}Tc-pertechnetate transport k_{ext2} from the cavity to the outside, until it is re-transfered into blood. It is a non direct transport to the blood. In the next, by abuse of notation, we will denote it k_{02}.

6.2.3 Mathematical representation of the model

The final simplified model presented in Figure 6.3 can be studied using compartmental analysis similarly to the two-compartment model of Section B.3 in Appendix B. Let us adapt the equations to our current model. As mentioned in the previous section, the input blood activity function $x_0(t)$ is obtained from the measure of activity in the left ventricle. It is frequent to assume that the input function of the compartmental model are particular functions such as impulse or continuous function. In our study, this input function is neither an impulse nor a continuous function. However it can be approximated by a sum of two exponential functions, this will be shown in Section 6.3.

$$\begin{cases} \dot{x_1}(t) &= -(k_{21}+k_{01})x_1(t) &+ k_{12}x_2(t) &+ k_{10}x_0(t) \\ \dot{x_2}(t) &= k_{21}x_1(t) &- (k_{12}+k_{02})x_2(t) & \\ y_1(t) &= x_1(t) & & \\ y_2(t) &= x_2(t) & & \\ x_0(t) &= \phi_1 e^{-\theta_1 t} &+ \phi_2 e^{-\theta_2 t} & \end{cases} \tag{6.1}$$

In the Laplace equations, the input matrix $\mathbf{U}(s)$ is now expressed as follows:

$$\mathbf{U}(s) = \begin{bmatrix} X_0(s) \\ 0 \end{bmatrix} = \begin{bmatrix} \frac{\phi_1}{s+\theta_1} + \frac{\phi_2}{s+\theta_2} \\ 0 \end{bmatrix} \tag{6.2}$$

The transfer matrix $\mathbf{G}(s)$ remains unchanged (see Section B.3) but not the observation matrix $\mathbf{Y}(s)$ which depends on $\mathbf{U}(s)$.

$$\begin{aligned} \mathbf{Y}(s) &= \mathbf{G}(s)\mathbf{U}(s) \\ &= \begin{bmatrix} \frac{(s+(k_{12}+k_{02}))k_{10}}{(s-\lambda_1)(s-\lambda_2)} X_0(s) \\ \frac{k_{21}k_{10}}{(s-\lambda_1)(s-\lambda_2)} X_0(s) \end{bmatrix} \\ &= \begin{bmatrix} \frac{(s+(k_{12}+k_{02}))k_{10}}{(s-\lambda_1)(s-\lambda_2)} (\frac{\phi_1}{s+\theta_1} + \frac{\phi_2}{s+\theta_2}) \\ \frac{k_{21}k_{10}}{(s-\lambda_1)(s-\lambda_2)} (\frac{\phi_1}{s+\theta_1} + \frac{\phi_2}{s+\theta_2}) \end{bmatrix} \end{aligned} \tag{6.3}$$

The denominator of the two terms of the observation matrix $\mathbf{Y}(s)$ are polynomials of degree 4 in s. Thus, each term can be decomposed in a sum of four rational fraction with denominator of degree 1 in s. Then, the inverse

Laplace transform ($\mathcal{L}^{-1}$) of each term results in a sum of four exponential functions such as:

$$y_1(t) = \alpha_{1,1}e^{-\beta_{1,1}t} + \alpha_{1,2}e^{-\beta_{1,2}t} + \alpha_{1,3}e^{-\beta_{1,3}t} + \alpha_{1,4}e^{-\beta_{1,4}t}$$

$$y_2(t) = \alpha_{2,1}e^{-\beta_{2,1}t} + \alpha_{2,2}e^{-\beta_{2,2}t} + \alpha_{2,3}e^{-\beta_{2,3}t} + \alpha_{2,4}e^{-\beta_{2,4}t}$$

where each coefficient α_i and β_i is a combination of k_{01}, k_{02}, k_{21}, k_{12}, k_{10}, ϕ_1, ϕ_2, θ_1, θ_2. Conversely, the transfer parameters k_{01}, k_{10}, k_{02}, k_{21}, k_{12} can be expressed and computed as combination of the α_i, β_i, ϕ_1, ϕ_2, θ_1, θ_2. However, the analytic equations are too complex to be shown here. In practice, the system is solved both analytically and numerically with a mathematical software such as Maple.

6.2.4 Hypotheses according to the available data

The simplified model is a two compartmental model, with one compartment for the stomach wall and one for the stomach cavity. Our compartmental analysis relies on the following hypotheses:

- **Each SPECT image voxel contributes to each compartment with a percentage that can be calculated** The first challenge is to extract TACs for each compartment: the two compartments are physically close, the stomach wall is surrounding the stomach cavity. Thus the extraction of TAC for each compartment is hard since each voxel is a mix of each compartments and blood. Indeed, a SPECT image voxel measures $0.33\times0.33\times0.33$ mm^3 which is more or less the same scale as the thickness of the stomach wall, thus most voxels contribute partly to the stomach wall and partly to the stomach cavity. The challenge here is to discover what percentage of each voxel corresponds to the wall and to the cavity, we call this percentage the *mixing coefficient*. These coefficients allows for transforming the layer-based activity measure into TACs for each compartment.

- **We can consider that the activity inside a compartment is homogeneous** One of the hypotheses of compartmental analysis is that each compartment is homogeneous. Unfortunately, neither the stomach cavity nor the stomach wall is homogeneous. There are a progressive activity uptake in stomach wall coupled with secretion in the mucus and then a diffusion phenomenon and all of these happen along the different layers. Consequently, the simplification hypothesis we do here is the homogeneity of each compartment; we consider the activity of the wall as the sum of the activities of the layers forming the wall.

- **The input is approximated by the activity of the left ventricle, expressed as a sum of two exponential functions** We approximate the input function by a sum of two exponential functions; the TAC for this input function is estimated from the measure of the average activity in the left ventricle (see Section 5.4.4.4).

- **Each TAC can be approximated by a multiexponential function** We suppose also that each TAC can be approximated by a sum of exponential functions.

6.2.5 Problem statement

We described in Section 6.2.2 the compartmental model that describes the ^{99m}Tc-pertechnetate uptake kinetics in the murine stomach. The objective now is to determine the transfer parameters k_{ij} of the model. These transfer parameters k_{ij} represent the speed at which the substance flows from compartment j to compartment i, or from the outside ($j = 0$) to compartment i. In our case, these parameters are the two transfer parameters k_{21} and k_{12} between the two compartments, stomach wall and stomach cavity, the two transfer parameters k_{01} and k_{02} from each compartment to the outside, and k_{10} the transfer parameter from the input to the first compartment.

Knowing the TAC in the left ventricle, we will see in the next section that it is possible to fit the input function with a sum of two exponential functions. In that case, we have shown in the previous section that the observations of each compartments should be of the form of a sum of four exponential functions.

There are two different ways to determine these parameters. Both ways consists in determining the kinetic model (i.e. the k_{ij} constants) of a compartmental system from its observations (y).

A first way consists in solving the inverse problem analytically [RW71, GRS+10]. As we already have the input function expressed as a sum of two exponential functions, if we can approximate the output functions as a sum of four exponential functions, then the transfer parameters will be given by the analytic solution to the inverse problem.

A second way consists in solving the inverse problem numerically. Knowing the input functions, we test different sets of values for the transfer parameters, then we obtain the output functions of the system, i.e. compartment functions, as sum of (four) exponential functions. Finally, we compare these computed functions to the compartment observation and we optimise iteratively the transfer parameter in order to minimise the differences between the computed and the observed compartment activities.

In the next sections, we will build the TACs for the different observations and try both the analytic and the numerical resolution methods to characterise the parameters of the system.

6.3 Time-activity curve (TAC) acquisitions

First of all, before any other work, we now need to obtain the time-activity curves (TACs) for each of the involved compartments, i.e., the blood, the stomach wall, and the stomach cavity. These TACs are obtained by measuring the activity in volume of interests (VOIs) of dynamic SPECT images. In our case, we work with dynamic images that have been corrected for the radioactive decay and the cylinder factor, normalised with respect to both the animal weight and the injected radioactivity. Therefore the values of the image after conversion have no unit. By abuse of notation, we express these activity value in standardized uptake value (SUV) as it is usually done for positron emission tomography (PET) imaging.

6.3.1 Blood: model input function

First the blood time-activity curve is the measure of the activity variation in the left ventricle of the dynamic SPECT images. This curve is easily obtained. Then, for the analytic resolution of the compartmental system, it is better to provide not only a time-activity curve but its approximation by functions such as impulse or exponential functions. However, the measured time-activity curve is neither a simple impulse nor a single exponential function. Though, it can be approximated easily by a sum of two exponential functions.

6.3.1.1 Approximation with sum of exponential functions

One assumes that the observations y of compartmental systems can be approached by continuous functions, that are sum of exponential functions [Fos70, FJ86]. Here we shortly describe how to approximate the set of observations, e.g. the blood time-activity curve u_0, with a sum of two exponential functions $y_0(t)$ such as:

$$y_0(t) = \phi_1 e^{-\theta_1 t} + \phi_2 e^{-\theta_2 t}$$

The idea is first to differentiate the theoretical expression of $y_0(t)$ twice and then re-integrate twice in order to obtain a formal representation such as:

$$y_0(t_n) = a + bt_n + cF(t_n) + dG(t_n)$$

where

$$\begin{cases} a &= \phi_1 + \phi_2 \\ b &= \phi_2\theta_1 + \phi_1\theta_2 \\ c &= -(\theta_1 + \theta_2) \\ d &= -(\theta_1 * \theta_2) \\ F(t_n) &= \int_0^{t_n} y_0(\lambda)d\lambda \\ G(t_n) &= \int_0^{t_n}\int_0^{\lambda} y_0(\xi)d\xi d\lambda = \int_0^{t_n} F(\lambda)d\lambda \end{cases}$$

Then, it is possible to estimate $F(t_n)$, $G(t_n)$, and $y_0(t_n)$ by integrating by parts on each segment delimited by the observations. The integration on each segment can be done according to the trapezoidal rule. This results in the following expressions.

$$\begin{cases} \hat{F}(t_n) &= \frac{1}{2}\sum_{k=0}^{n-1}(t_{k+1} - t_k)(y_0(t_{k+1}) + y_0(t_k)) \\ \hat{G}(t_n) &= \frac{1}{2}\sum_{k=0}^{n-1}(t_{k+1} - t_k)(F(t_{k+1}) + F(t_k)) \\ \hat{y}_0(t_n) &= a + bt_n + c\hat{F}(t_n) + d\hat{G}(t_n) \end{cases}$$

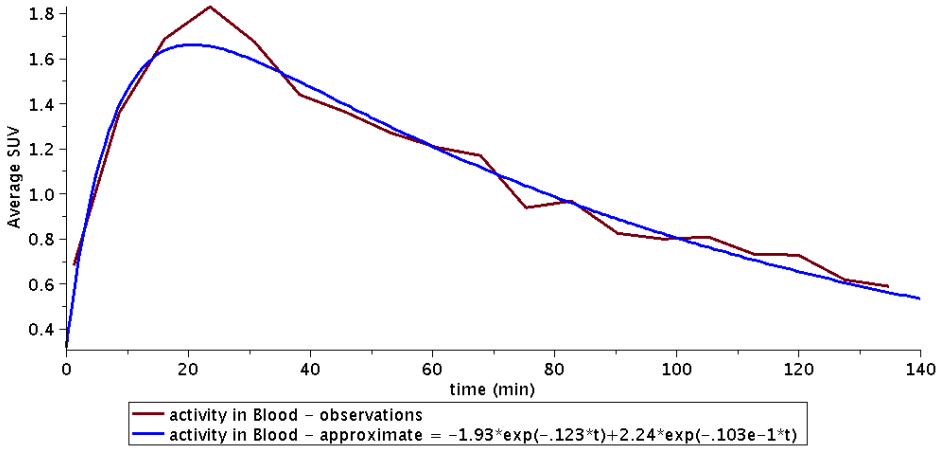

Figure 6.4: Blood time-activity curve (red continuous line) and its approximate function (blue dotted line) for subject #0530.

The next step is the determination of the unknown constants a, b, c, and d with least square minimisation algorithm between the observation y_0 and its estimate $\hat{y}_0$. Finally, it is possible to retrospectively determine the unknown constants ϕ_1, ϕ_2, θ_1, and θ_2 that are combinations of the previously determined constants a, b, c and d.

Figure 6.4 presents the observed blood time-activity curve for the subject #0530 (cf Table 5.1), and its multiexponential approximate function. The resulting coefficients are $\phi_1 \approx -1.93$, $\phi_2 \approx 2.24$, $\theta_1 \approx 0.123$, and $\theta_2 \approx 0.0103$. The squared residuals between the observations and the estimate function at the observed time is approximately equal to 0.0826. The root mean square (RMS) is equal to $RMS = \sqrt{\frac{SSD}{19}} = 0.0659$.

6.3.2 Stomach wall and cavity: model output

As mentioned in Section 6.2, if our TAC input model can be approximated by a sum of two exponential functions, we expect the observations in the two compartments of our model to be the sum of four exponential functions. In this section, we explain how we obtain the TAC for each compartment. These TACs are expected to be approximated by a sum of four exponential functions using a similar approach to the one used for the blood function, but adapted to four-exponential functions.

6.3.2.1 Principles

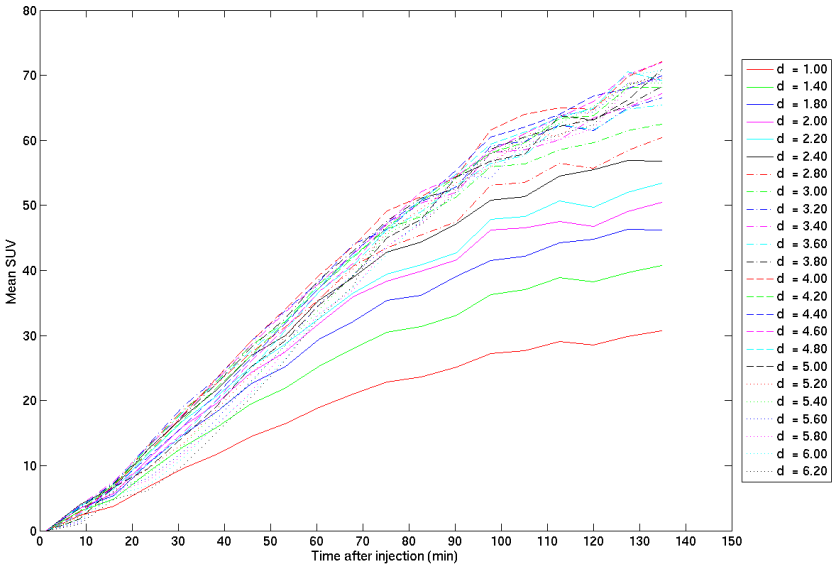

Figure 6.5: Stomach layer TAC for all the distances from the outer layer of the segmented stomach ($d = 1.00$) to the inner layer for subject #0530.

The first goal is to obtain the TAC of the two compartments of the stomach from the activity in stomach layers. We have at our disposal the TAC for each layer of the stomach as presented in Figure 6.5. Finding TACs for the two compartments from these observations is challenging. On the one hand, compartmental analysis requires one TAC per studied compartment. On the other hand, we have a set of TACs, one per layer of the segmented stomach. However, each layer is not homogeneous but a mix of compartment. It is assumed that each layer composition is time invariant. The question is then: how much each compartment contribute to each layer?

Then, we assume that the activity concentration in each layer can be expressed as a linear combination of the activity concentration in the two compartments. Consequently, in order to build the TAC of the two compartments

of the stomach, we need to determine which percentage of each layer belongs to the stomach wall, or the stomach cavity. We call these percentages *mixing coefficients*. Those mixing coefficient are defined as follows. Let m be the number of layers of the stomach model considered, and n the number of time frames. We suppose that the activity follows the rule:

$$L = K \cdot C$$

where

- L denotes the activity concentration in layers, expressed as a $m \times n$ matrix;
- K denotes the time-invariant mixing coefficients, is it as $m \times 2$ matrix and
- C denotes the activity concentration, expressed as a $2 \times n$ matrix in compartments.

In other terms, we have:

$$\begin{pmatrix} a_{l,1}(t) & a_{l,1}(t_2) & \cdots & a_{l,1}(t_n) \\ a_{l,2}(t) & a_{l,2}(t_2) & \cdots & a_{l,2}(t_n) \\ \vdots & & & \\ a_{l,m}(t) & a_{l,m}(t_2) & \cdots & a_{l,m}(t_n) \end{pmatrix} = \begin{pmatrix} \kappa_{1,1} & \kappa_{1,2} \\ \kappa_{2,1} & \kappa_{2,2} \\ \vdots & \vdots \\ \kappa_{m,1} & \kappa_{m,2} \end{pmatrix} \cdot \begin{pmatrix} a_{c,1}(t) & a_{c,1}(t_2) & \cdots & a_{c,1}(t_n) \\ a_{c,2}(t) & a_{c,2}(t_2) & \cdots & a_{c,2}(t_n) \end{pmatrix}$$

Assuming K is known, we can deduce the TAC for the two compartments by computing the pseudo-inverse of K [Pen55, Son86]:

$$C = ({}^tK \cdot K)^{-1} \cdot {}^tK \cdot L$$

The pseudo-inverse computes the best solution to a system of linear equations. Here, we compute the concentration in each compartment that produces activity curves in each layer as close as possible to the observed ones[1]. The best fit produced by the pseudo-inverse is in terms of least-squares minimisation. This solution will provide us the TACs for the two compartments of the stomach.

6.3.2.2 Identification of mixing coefficients

The idea described above is pretty simple, however in practice, the difficulty lies in the determination of the mixing coefficient $\kappa_{i,j}$.

First, we assume that the whole **S**tomach (S) is a combination of four different compartments identified by their ^{99m}Tc-pertechnetate uptake properties:

[1] The solution cannot be exact as we have m equations for only two parameters.

the gastric mucosa or NIS expressing cells, the gastric juice, the extra-cellular matrix, and the non diffusible. The gastric mucosa is mainly composed by NIS expressing cells. By abuse of language, this compartment will be called stomach **W**all (W). The gastric juice result from the secretion of the glandular cells. By abuse of language, it will be called stomach **C**avity (C). The extra-cellular matrix is assumed to be of the same scale of magnitude in terms of activity than the blood. By abuse of language, this compartment will be called **B**lood (B). The **N**on **D**iffusible is composed by everything that does not uptake ^{99m}Tc-pertechnetate such as non glandular gastric wall and alimentary bolus. This compartment occupies most of the space, but as it does not uptake ^{99m}Tc-pertechnetate, the contribution in terms of activity is null. This can be represented analytically with:

$$\mathrm{S} = \mathrm{W} \cup \mathrm{C} \cup \mathrm{B} \cup \mathrm{ND}$$

In a first time, we assume that the volume ratio of each compartment composing the layer can be used as the activity ratio for each compartment that contributes. In other words, we suppose that the activity in the layer is the combination of the activity of each compartment multiplied by a ratio that is the proportion of the volume of the layer that belongs to the compartment. More formally, denoting V_W, V_C, V_B, and V_{ND} the volume of the compartments and V_l the volume of the layer, the activity of the layer l is:

$$\begin{aligned} TAC_l &= \frac{TAC_W \times V_W + TAC_C \times V_C + TAC_B \times V_B + TAC_{ND} \times V_{ND}}{V_l} \\ &= TAC_W \times \frac{V_W}{V_l} + TAC_C \times \frac{V_C}{V_l} + TAC_B \times \frac{V_B}{V_l} + TAC_{ND} \times \frac{V_{ND}}{V_l} \end{aligned}$$

Note that we only need the fraction of the volume layer that is occupied by each compartment, not the volume itself.

For example, supposing that

$$V_W = \frac{10}{100}V_l; \quad V_C = \frac{5}{100}V_l; \quad V_B = \frac{1}{100}V_l; \quad V_{ND} = \frac{84}{100}V_l$$

We have

$$TAC_l = \frac{10}{100}TAC_W + \frac{5}{100}TAC_C + \frac{1}{100}TAC_B + \frac{84}{100}TAC_{ND}$$

Consequently, in order to estimate the mixing coefficients, we need to estimate the percentage of volume of each layer that is a part of each compartment (wall, cavity, blood, or non diffusible).

Table 6.1: Estimated compartment volume contribution (in % of layer volume) of each compartment to each layer for subject #0530. These ratio were first estimated from the observation of a chosen stomach IHC image. Then, the ratio for the first 14 layers were manually optimised.

Layer Nb	**W**	**C**	**B**	**ND**
L1	15	0	1	84
	20	0	1	79
	22	0	1	77
	23	0	1	76
	24	0	1	75
L6	25	0	1	74
	25	15	1	59
	20	25	1	54
	20	35	1	44
	15	45	1	39
L11	12	55	1	32
	10	65	1	24
	10	75	1	14
L14	5	85	1	9
	0	*95*	*0*	*5*
L16	*0*	*95*	*0*	*5*
	0	*80*	*0*	*20*
	0	*75*	*0*	*25*
	0	*70*	*0*	*30*
	0	*65*	*0*	*35*
L21	*0*	*60*	*0*	*40*
	0	*55*	*0*	*45*
	0	*50*	*0*	*50*
	0	*45*	*0*	*55*

6.3.2.3 TACs for the stomach wall and cavity

Now, we propose an estimation of the mixing coefficient matrix K, where each coefficient has been chosen according to the estimated volume ratio of each compartment in each layer.

In order to obtain the approximation of the stomach wall and cavity TACs ($\hat{\text{TAC}}_{\mathbf{W}}$ and $\hat{\text{TAC}}_{\mathbf{C}}$), the mixing coefficient matrix K has been set up. As previously explained, one assume that the mixing coefficients are equal to the volume ratio of each compartment in each layer. A first rough estimation of these ratio (see Table 6.1), expressed in %, has been done according to the

anatomical spatial distribution of each compartment in a chosen stomach IHC image (see Figure 5.2(a)). In practice, this rough estimation of the ratio was done by measuring the space occupied by each compartment in a 1250x1250 pixel^2 neighbourhood at different position in the stomach wall and cavity, in the 2D IHC slice. For example, with this manual method we estimated that the six first layers are composed by around 10% of NIS expressing cells and no cavity, the rest being the non diffusible space and the extra-cellular matrix. Then, from the seventh to the tenth layers, around 25% of the space is occupied by NIS expressing cells with around 20% of cavity. Next, from the eleventh to the fourteenth layers, we estimated that around 5% of the space was occupied by NIS expressing cells and 80% of the space by the cavity. Then, in the inner layers, only cavity and non diffusible material remain. The proportion is more variable since in the stomach cavity, the non diffusible material corresponds to the alimentary bolus and it is hard to quantify its occupation on IHC slices.

Then the mixing coefficient matrix consists of only the ratio of the three compartments (Wall, Cavity and Blood) that contribute in term of activity to each of the first 14 layers. K is of size 14×3.

Then the approximated compartment TACs, $\hat{C}$, is computed according to the relation: $\hat{C} = ({}^tK \cdot K)^{-1} \cdot {}^tK \cdot L$ The accuracy of the mixing coefficient matrix K is checked by recomputing $\hat{L} = K \cdot \hat{C}$. The mixing coefficient of the first 14 layers were adjusted in order to minimise the sum of squared differences (SSD) between L and $\hat{L}$. Table 6.1 presents the final volume estimated contribution, in %, from which K was extracted. K was then used for all the following steps.

In practice, we chose to only consider the first 14 layers of the stomach. The 10 last layers are ignored on all the following of this chapter. The reason for this simplification is that the inner part of the stomach cavity is subject to the diffusion phenomenon, that we do not study here. As we decided in Section 6.2.2 to neglect this phenomenon, we decided to ignore the last layers of the stomach cavity. The mixing coefficient matrix that has been used is composed by the first 14 rows (from L1 to L14) and the first 3 columns (**W**, **C** and **B**).

The mixing coefficient matrix has been used to obtain the TACs of the stomach compartments. Figure 6.6(a) presents the resulting TACs for the two compartments: stomach wall $\tilde{\text{TAC}}_{\mathbf{W}}$ and stomach cavity $\hat{\text{TAC}}_{\mathbf{C}}$ compared to the blood $\text{TAC}_{\mathbf{B}}$. Figure 6.6(b) presents the observed TACs for each layer in order to give a reference for the amplitude of activity variation. Figure 6.6(c) and Figure 6.6(d) present respectively present the matrix of difference (signed error) between "L - $\hat{L}$", and the matrix of relative error "$\frac{|L-\hat{L}|}{L}$", per layer and per time frame. We can see that the signed error does not exceed 4 in absolute value for the latest time frame. The relative error is maintained under 10%

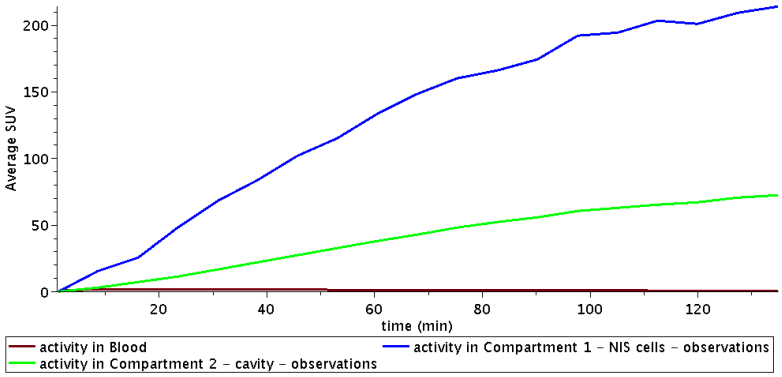

(a) Stomach wall (blue), cavity (green) and blood (red) TACs

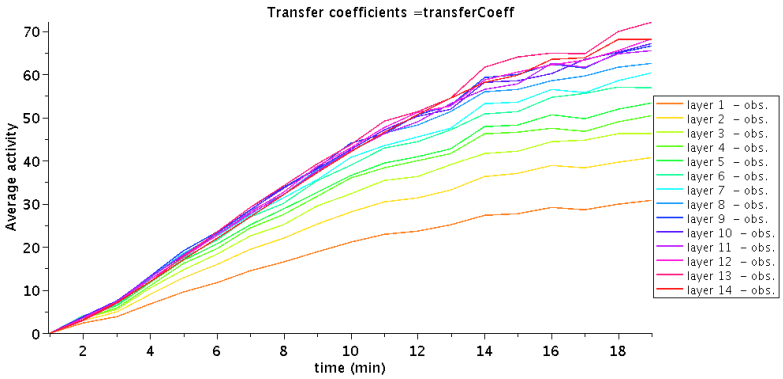

(b) TACs for the first 14 layers

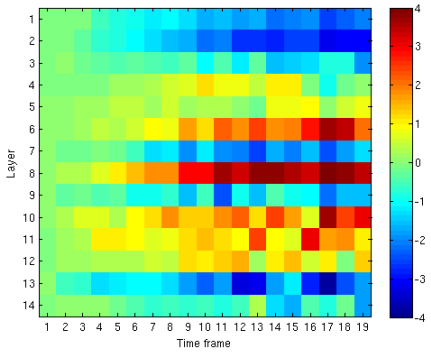

(c) Difference (signed error) in SUV between the observed L and the approximated $\hat{L}$ TACs of the first 14 layers for each time frame, color axis scaling range from -4 SUV (blue) to +4 SUV (red)

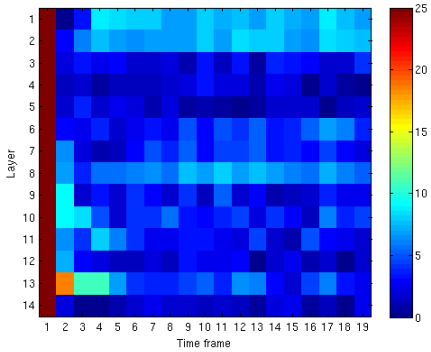

(d) Relative error (in %) between the observed L and the approximated $\hat{L}$ TACs of the first 14 layers for each time frame, color axis scaling range from 0% (blue) to +25% (red)

Figure 6.6: Stomach wall and cavity TACs for subject #0530.

for most time points (after time point 2) and for all layers. Only the first

instant present a relative error above 25% but the activity measured in the layers is really low (smaller than 5 SUV) with an absolute error between 0.5 and 1 SUV.

Overall, the final *SSD* summed over all the layer and all the time frames is 633.09, and the root mean square (*RMS*) per layer and per time frame is 1.54, which represents around 2% of error for the latest time frames. We can thus consider that the approximated activity found by this method fits well with the observations, and as a result, the mixing coefficient matrix is satisfying for this first approach.

6.4 Results

In this section, we describe the different steps that conducted to a the first estimation of the five transfer parameters (k_{01}, k_{02}, k_{12}, k_{21}, and k_{10}) that best describe the ^{99m}Tc-pertechnetate uptake phenomenon.

First, we present the analytic resolution of the inverse problem. The inverse problem approach is a straightforward as soon as we are able to approximate all observations with simple functions such as sum of negative exponential functions. If the input functions and compartment observations are known, we fit these with multiexponential functions and we find analytically the k_{ij}. However, the estimation of $\mathrm{TAC}_{\mathbf{W}}$ and $\mathrm{TAC}_{\mathbf{C}}$ with multiexponential functions failed. This is partially due to the fact that there are not enough observations along the time. The acquisition sequence stopped 140 min after activity injection, before any activity equilibrium has been reach. Besides, we have no confirmation of the existence of any equilibrium. Thus, we can not make any assumption about the evolution of the uptake after 140 min, such an assumption could lead to the convergence of a solution. As a consequence, it was not possible to estimate the transfer parameters of our compartmental model by this analytic way.

That is why, in a second time, we decided to solve numerically the inverse problem. This approach consists in determining numerically the transfer parameters. Here, a large set of values for the k_{ij} is tested. For each set, the resulting estimated $\tilde{\mathrm{TAC}}_{\mathbf{W}}$ and $\tilde{\mathrm{TAC}}_{\mathbf{C}}$ were compared with the observed TACs $\hat{\mathrm{TAC}}_{\mathbf{W}}$ and $\hat{\mathrm{TAC}}_{\mathbf{C}}$. The sum of squared differences (*SSD*) and the *RMS* are computed between the observation and estimation of each compartment TAC. The accuracy of each set of parameters was quantified by the *SSD* and *RMS* between observed and estimated compartment TAC. To improve the result of the first parameter exploration, two steps of optimisation with Nelder-Mead (downhill) simplex algorithm [NM65, PTVF92, LRWW98] have been performed. The final set of parameters is the one that led to the smallest *SSD* and *RMS* computed on the sum: $SSD_{\mathbf{W}} + SSD_{\mathbf{C}}$.

6.4.1 Analytic resolution

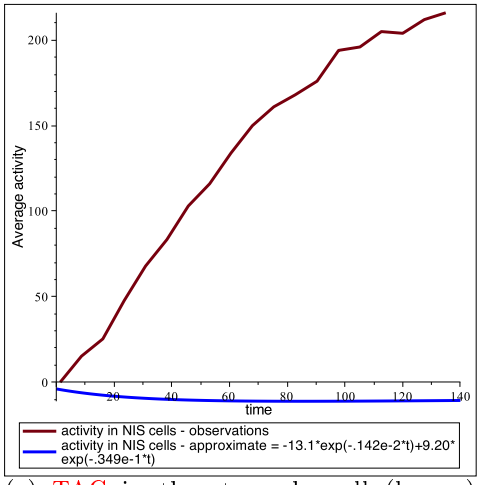

(a) TAC in the stomach wall (brown) and its multiexponential approximation(blue) – Fresen method

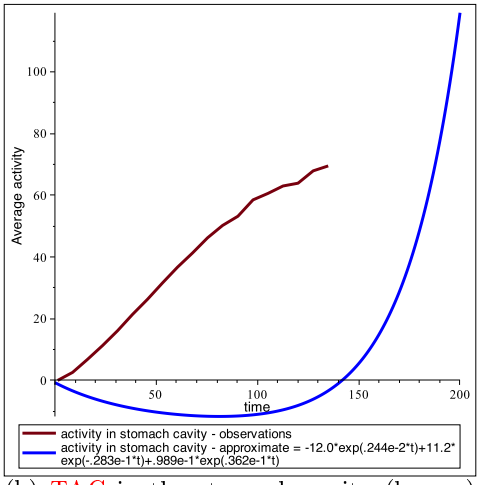

(b) TAC in the stomach cavity (brown) and its multiexponential approximation(blue) – Fresen method

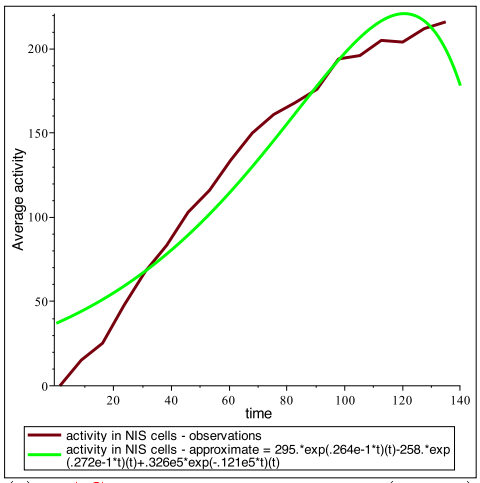

(c) TAC in the stomach wall (brown) and its multiexponential approximation(green) – Maple method (`Fit` function)

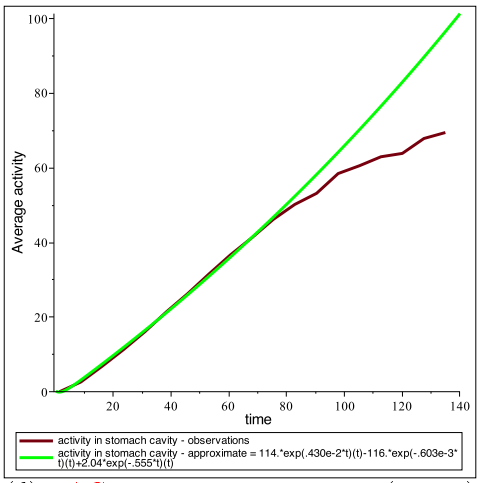

(d) TAC in the stomach cavity (brown) and its multiexponential approximation(green) – Maple method (`Fit` function)

Figure 6.7: Stomach wall and cavity TACs multiexponential approximation.

In order to solve the inverse problem, we first need to approximate the TACs by sums of four exponential functions. The analytic solution we presented in Section 6.2.3 will then allow us to compute the transfer coefficients.

To approximate the TACs, we first tried the method proposed by Fresen and Juritz [FJ86]. The result is shown on the two sub-figures at the top of Figure 6.7(a) and (b). The results is clearly very far from the original curves.

This is due to the fact that the computed TACs do not contain enough data; in particular it is impossible to know when the activity will stop growing, or if it decreases, only from the TACs data. If we try to add a point further, e.g. an activity curve closed to zero after a long period of time, the result is slightly better but still unsatisfactory.

To verify that this failure was not only due to the method used, we briefly experimented with Maple `Fit` function in order to try to fit the TACs with multiexponential functions. Here again, the software has difficulties to find an approximation, and the approximation found is still unsatisfactory as shown by the two approximation on the bottom of Figure 6.7(c) and (d).

In both cases, not only the approximated curves are far from the original ones, but also the method is not robust and the approximated function varies a lot for a small change in the TACs, e.g. a small change in the mixing coefficients.

The problem of fitting a function with a multiexponential approximation is known to be a difficult one (see for example [Act90] p. 253). Here, additionally to the basic complexity of the problem, we also have to face another difficulty: there is not enough data to compute a good approximated multiexponential function. Indeed, from the TACs computed by the previous step, it is impossible to predict the evolution of the activity (i.e., whether and when it decreases). Consequently, we did not investigate further the resolution of the problem with analytic resolution.

6.4.2 Numerical resolution

6.4.2.1 Exploration of transfer parameters space

As a first step, we tested a large number of combination for the set of transfer parameters. Instead of a regular sampling, we try a sampling at a logarithmic scale in order to determine the rough size of the parameters. We choose the following sampling for k_{ij}: $\{5 \times 10^{-3}, 10^{-2}, 5 \times 10^{-1}, 1, 5\}$. The number of possible values in this set are $n = 5$ and the number of parameters to estimate is $z = 5$. The number of combination of set of transfer parameter values that were tested is thus $n^z = 3125$.

These sets of parameters were evaluated with respect to the sum of squared differences (SSD) in the stomach wall TAC ($SSD_{\mathbf{W}}$), in the stomach cavity ($SSD_{\mathbf{C}}$), and in both compartments (sum of the two). In order to find the best candidate for each transfer parameter, the evaluation function that is minimised is the sum: $SSD_{\mathbf{W}}+SSD_{\mathbf{C}}$. Thus, the sets of parameters were sorted with respect to this sum. We additionally computed the RMS error in SUV.

Then, to further evaluate the precision of our approximation for transfer parameters, we consider the matrix C of TACs computed from the approxi-

mated transfer parameters for both stomach wall and cavity. This matrix is multiplied by the mixing coefficient matrix K in order to obtain the estimated TACs for all layers $\tilde{L}$. We compare $\tilde{L}$ and L, the matrix for observed TAC in each layer. To make this comparison, we compute $SSD_{\mathbf{L}}$, the sum of squared differences on the first 14 layers (between L and $\tilde{L}$) and its RMS error.

The first lines of Table 6.2 presents the six combinations of parameters that performed the best with respect to $SSD_{\mathbf{W}} + SSD_{\mathbf{C}}$ (case (A)), as well as the sets of parameters that performed the best with respect to $SSD_{\mathbf{W}}$ (case(B)) and with respect to $SSD_{\mathbf{C}}$ (case (C)). This parameter space exploration step has been performed in order to determine initial set of values for the transfer parameters that would permit to fit the compartment TACs with sums of four exponential functions.

Case (A): The six sets of parameters are slightly different however the RMS error on the TAC, around 60.00, is almost the same for all six sets. This suggests that these sets of parameters could be good candidates as initialisation of an optimisation process.

For the first set, the RMS error on the compartment TACs is below 60 that represents around 30% of error for the latest time frame for $\text{TAC}_{\mathbf{W}}$ and 85% of error for the latest time frame for $\text{TAC}_{\mathbf{C}}$. Moreover, the RMS error on the layer TACs is around 40 that represents around 57% of error for the latest time frame. The estimated $\tilde{\text{TAC}}_{\mathbf{W}}$ and $\tilde{\text{TAC}}_{\mathbf{C}}$ are also qualitatively compared to the approximated ones. As shown on Figure 6.8(a), the estimated $\tilde{\text{TAC}}_{\mathbf{W}}$ and $\tilde{\text{TAC}}_{\mathbf{C}}$ obtained with the first set of parameters of case (A) does not fit very well the approximated $\hat{\text{TAC}}_{\mathbf{W}}$ and $\hat{\text{TAC}}_{\mathbf{C}}$.

Case (B): The set of parameters gives a better estimation for $\tilde{\text{TAC}}_{\mathbf{W}}$ than the sets of cases (A). However, the RMS error on the wall and cavity TACs is around 145 that represents around 73% of error for the $\text{TAC}_{\mathbf{W}}$ and around 207% of error for the $\text{TAC}_{\mathbf{C}}$. This is not satisfying.

Case (C): The set of parameters gives a better estimation for $\tilde{\text{TAC}}_{\mathbf{C}}$ than any other set of cases (A) and case (B). The RMS error on the $\text{TAC}_{\mathbf{W}}$ and $\text{TAC}_{\mathbf{C}}$ is around 85 that represents around 43% of error for the $\tilde{\text{TAC}}_{\mathbf{W}}$ and around 120% of error for the $\tilde{\text{TAC}}_{\mathbf{C}}$. This is better than case (B) but still not satisfying. Surprisingly, the RMS error on the layer TACs is smaller than for the best case (A).

Indeed, the relatively good results for case (B) and for case (C) with respect to $SSD_{\mathbf{W}}$ or $SSD_{\mathbf{C}}$ reveal that when the priority is given to the one or the other compartment, the general results on the sum over the two compartment SSD are worse. However, the two compartments are linked together with the parameters k_{12} and k_{21}. Thus it is not relevant to just compare with respect to one or the other.

One desires to find a set of parameters that results in a best fitting of both wall and cavity TAC. Therefore, one chooses to select the best parameters with respect to the sum $SSD_{\mathbf{W}} + SSD_{\mathbf{C}}$. This sum will be used as the

evaluation function for the fitness of the approximated solution.

6.4.2.2 Optimisation of transfer parameters with Nelder-Mead simplex algorithm

In order to optimise the set of transfer parameters, we use the Nelder-Mead (or downhill) simplex algorithm [NM65, PTVF92]. This downhill simplex algorithm is an iterative process that allows the determination of a local optimum for a multidimensional point which minimises a specified evaluation function. The space dimension is equal to the number of parameter to estimate $z = 5$. A simplex is composed by $z + 1 = 6$ points, that is one point more than the number of parameters to estimate.

This algorithm is executed twice. A first execution is done with a simplex composed by six points determined by another mean (here, the parameter space exploration). Then a second execution is performed using as initialisation a simplex composed by six random perturbations of the final point obtained at the end of the first execution of the algorithm. As suggested in the previous paragraph, the chosen evaluation function is the sum of *SSD* of the two compartments TACs.

First execution of simplex algorithm The simplex was initialised according to the result of the parameter space exploration. The six sets of parameters that yield to the smallest $SSD_{\mathbf{W}} + SSD_{\mathbf{C}}$ have been chosen to initiate the first execution of the downhill simplex algorithm. As some of the parameters (k_{10} and k_{01}) were of the same scale for all sets, we perturbed randomly all parameter values between $+/-50\%$ of their initial value. The main reason for this perturbation is that it allows the algorithm to also investigate the possible variations on k_{10}, this would not be the case if the value of k_{10} were identical for all the initial points. As this is an iterative process, the stopping condition was the difference between the result of the evaluation function at the centroid of the simplex and each point of the simplex. When the difference was lower than ε, the process stopped. We choose $\varepsilon = 1000$ for this first execution since it is a hundredth of the scale of the result for $SSD_{\mathbf{W}} + SSD_{\mathbf{C}}$ in case (A). The set of parameters after stopping condition that led to the smallest result of the evaluation function is presented in Table 6.2 (case (D)). The resulting estimated TACs are also compared visually to the approximated ones in Figure 6.8(b). Qualitatively, the estimated $\tilde{\text{TAC}}_{\mathbf{W}}$ (blue dashed line) is somehow closer to the approximated $\hat{\text{TAC}}_{\mathbf{W}}$ than it is the case for the $\hat{\text{TAC}}_{\mathbf{W}}$ (green continuous line). This is probably due to the fact that $\hat{\text{TAC}}_{\mathbf{W}}$ is around 2.5 greater than $\hat{\text{TAC}}_{\mathbf{W}}$ and the resulting error has more weight in the evaluation function.

Quantitatively, the process stopped after 32 iterations and the set of parameters results in an *RMS* error on the compartment TACs around 32, that

Table 6.2: **Quantitative results of the parameter space exploration (see Section 6.4.2.1) and after downhill optimisation with the simplex algorithm (see Section 6.4.2.2) for subject #0530.** This table presents several sets of transfer parameters and the errors measured between the observations ($\hat{C}$ and L), and the estimations ($\tilde{C}$ and $\tilde{L}$). The errors are presented in columns (1) to (6). Columns (1): $SSD_{\mathbf{W}}$ between $\hat{\text{TAC}}_{\mathbf{W}}$ and $\tilde{\text{TAC}}_{\mathbf{W}}$; (2): $SSD_{\mathbf{C}}$ between $\hat{\text{TAC}}_{\mathbf{C}}$ and $\tilde{\text{TAC}}_{\mathbf{C}}$; (3): $SSD_{\mathbf{W}} + SSD_{\mathbf{C}}$; (4): $RMS_{\mathbf{W,C}} = \sqrt{\frac{(3)}{2\times\text{nb of frames}}}$ = equivalent SUV error/compartment/time frame; (5): $SSD_{\mathbf{L}}$ between $\text{TAC}_{\mathbf{L}}$ and $\text{TAC}_{\tilde{\mathbf{L}}}$; (6): $RMS_{\mathbf{L}} = \sqrt{\frac{(4)}{\text{nb of layers}\times\text{nb of frames}}}$ = equivalent SUV error/layer/time frame. The results of the parameter space exploration are presented in cases (A), (B) and (C). The results of the optimisation with downhill simplex algorithm are presented in cases (D) and (E). (A1-A6): The results for the best six sets of transfer parameters with respect to column (3) are presented since these six sets will be used as initialisation of the downhill simplex algorithm that requires an initialisation with a number of sets equal to the number of parameters + 1. Figure 6.8 (a) presents the graphic for case (A1); (B): Best transfer parameters with respect to column (1) and results; (C): Best transfer parameters with respect to column (2) and results. (D): Best parameters and results with respect to column (3) after the first execution of the downhill simplex algorithm ($\varepsilon = 1000$) (see Figure 6.8(b)); (E): Best parameters and results with respect to column (3) after the second execution of the downhill simplex algorithm ($\varepsilon = 10$)(see Figure 6.8(c)).

	Transfer parameters					Error					
						on compartment TACs				on layer TACs	
Case	k_{01}	k_{02}	k_{12}	k_{21}	k_{10}	(1)	(2)	(3)	(4)	(5)	(6)
A1	0.010	0.010	1.000	0.500	5.0	$7.201\ 10^4$	$5.793\ 10^4$	$\mathbf{1.299\ 10^5}$	**58.48**	$4.347\ 10^5$	**40.43**
A2	0.005	0.5	5.0	0.5	5.0	$1.035\ 10^5$	$2.829\ 10^4$	$1.318\ 10^5$	58.90		
A3	0.005	0.005	5.0	0.005	1.0	$9.678\ 10^4$	$4.025\ 10^4$	$1.370\ 10^5$	60.05		
A4	0.005	0.01	5.0	0.005	1.0	$9.683\ 10^4$	$4.025\ 10^4$	$1.371\ 10^5$	60.06		
A5	0.005	0.005	5.0	0.01	1.0	$9.698\ 10^4$	$4.012\ 10^4$	$1.371\ 10^5$	60.07		
A6	0.005	0.01	5.0	0.01	1.0	$9.708\ 10^4$	$4.012\ 10^4$	$1.372\ 10^5$	60.09		
B	0.005	0.005	0.500	1.000	5.0	$\mathbf{8.886\ 10^3}$	$7.899\ 10^5$	$7.988\ 10^5$	144.99	$5.340\ 10^6$	141.70
C	0.010	0.010	0.010	0.005	5.0	$2.719\ 10^5$	$\mathbf{2.546\ 10^2}$	$2.722\ 10^5$	84.63	$1.720\ 10^5$	**25.43**
D	0.0059168	0.079148	4.4649	0.11882	2.2448	$5.145\ 10^3$	$3.416\ 10^4$	$\mathbf{3.931\ 10^4}$	**32.16**	$4.111\ 10^5$	**39.31**
E	-0.0036095	0.012502	0.38636	0.12773	1.9911	312.46	94.225	**406.68**	**3.26**	$4.039\ 10^4$	**12.32**

SSD stands for Sum of Squared Differences.

RMS stands for Root Mean Square.

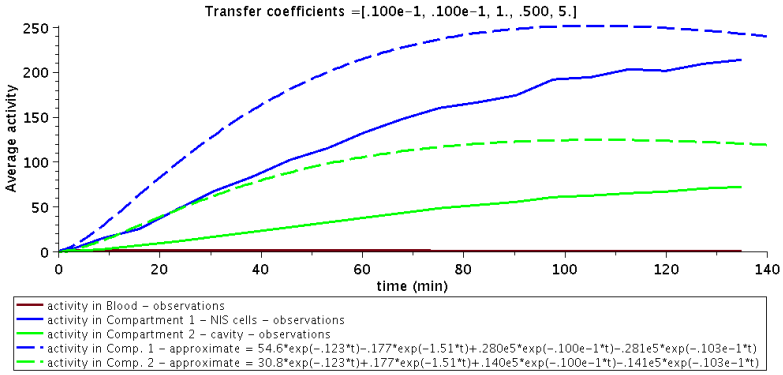

(a) Best result among the 3125 combinations tested for the parameter space exploration, case (A1) in Table 6.2

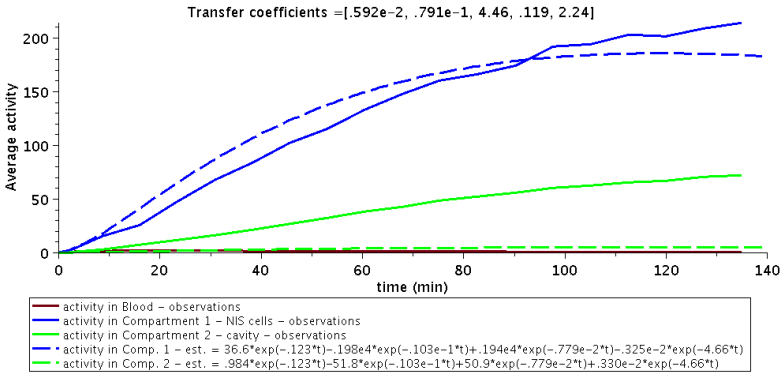

(b) Best result after the first execution of the downhill simplex algorithm, ε=1000, case (D) in Table 6.2

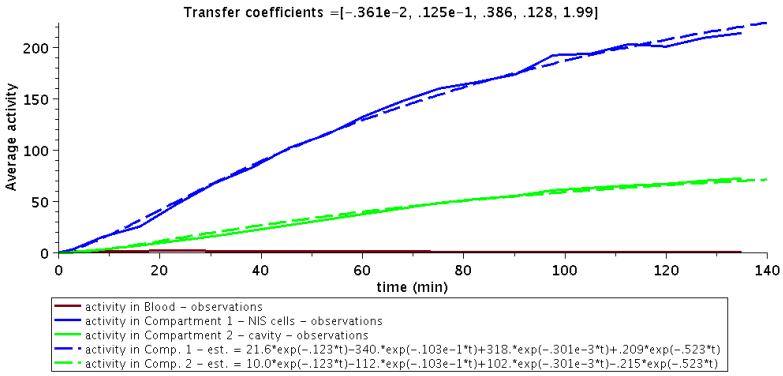

(c) Best result after the second execution of the downhill simplex algorithm, ε=10, case (E) in Table 6.2

Figure 6.8: **Compartments TACs and their approximates functions.** These figures present the compartment TACs: $\hat{\text{TAC}}_{\mathbf{W}}$ for the wall (blue continuous line) and $\hat{\text{TAC}}_{\mathbf{C}}$ for the cavity (green continuous line), and their approximate functions $\tilde{\text{TAC}}_{\mathbf{W}}$ (blue dashed line) and $\tilde{\text{TAC}}_{\mathbf{C}}$ (green dashed line). The given transfer parameters correspond to k_{01}, k_{02}, k_{12}, k_{21}, and k_{10} (from left to right).

is equivalent to the half of *RMS* for the best case of (A). This is equivalent to around 16% error on the $\hat{\text{TAC}}_{\mathbf{W}}$ for the latest time and around 45% error on the $\hat{\text{TAC}}_{\mathbf{C}}$.

Second execution of simplex algorithm The first execution of the simplex algorithm did not result in a satisfying estimation of the transfer parameters according to the resulting estimated TAC. Thus, a second execution of the simplex algorithm has been performed. This time, the stopping condition has been divided by 100 to reach $\varepsilon = 10$, and the simplex has been reinitialised with a set of six perturbations of the resulting set of parameters of case (D). The perturbation was randomly chosen between $-50/+200\%$ of the parameter values.

The set of parameters after stopping condition that led to the smallest result of the evaluation function is given in Table 6.2 (case (E)). The resulting estimated TACs are also visualised and compared with the approximated ones in Figure 6.8(c).

Qualitatively, the estimated $\tilde{\text{TAC}}_{\mathbf{W}}$ (blue dashed line) fits well the approximated $\hat{\text{TAC}}_{\mathbf{W}}$ and so does the estimated $\tilde{\text{TAC}}_{\mathbf{C}}$ (green dashed line) with $\hat{\text{TAC}}_{\mathbf{C}}$. Thus, from a qualitatively point of view, the estimation of the transfer parameters is satisfying.

Quantitatively, the process stopped after 83 iterations and the set of parameters results in a *RMS* error on the compartment TACs around 3.3, that is equivalent to the tenth of the *RMS* error in case (D). This is also equivalent to around 1.6% error on the $\hat{\text{TAC}}_{\mathbf{W}}$ for the latest time and around 4.7% error on the $\tilde{\text{TAC}}_{\mathbf{C}}$.

Finally, the *RMS* error on the layer TACs, 12.32, is equivalent to around 30% less than the *RMS* error in case (A). In order to visualise the distribution of the error, we present respectively on Figure 6.9(a) and Figure 6.9(b) the signed error in SUV between the observed layer TACs and the estimated layer TACs "$L - \tilde{L}$", and the relative error "$\frac{|L-\hat{L}|}{L}$", at each time frame and for the first 14 layers. One can see that for most of the time frames and layers, the error does not exceed 4 SUV in absolute. The error is larger for the three last time frames (17 to 19) and for the seven inner layers (layer 8 to 14). Indeed, this is confirmed by the relative error that is greater to 10% for these instants and layers. On the other hand, expected for the first time point, the relative error does not exceed 10%-15% for most of layers and time points. At this step, one can conclude that the proposed approach is excellent.

Biological interpretation of the transfer parameter values The resulting transfer parameters are: k_{01}=-0.0036, k_{02} $\simeq$=0.013, k_{12} $\simeq$0.39, k_{21} $\simeq$=0.13 and k_{10} $\simeq$2. k_{01} and k_{02} are very small comparing to the others. The fact that k_{10} is larger than the others is not surprising in terms of

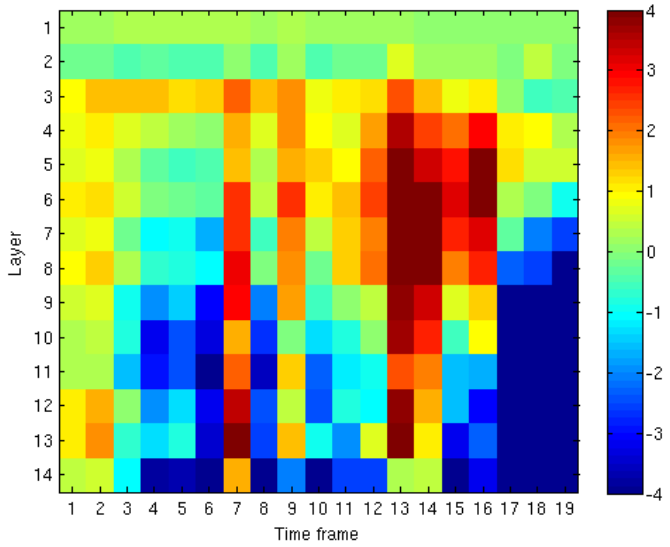

(a) Difference (signed error) in SUV, color axis scaling range from -4 SUV (blue) to +4 SUV (red)

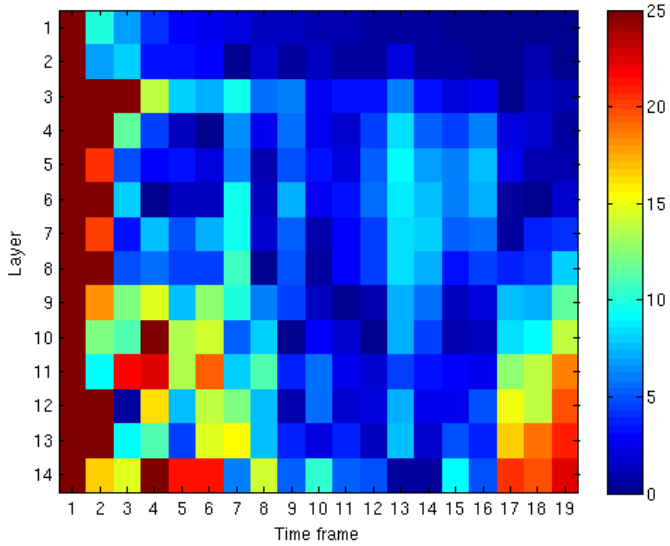

(b) Relative error (in %), color axis scaling range from 0% (blue) to +25% (red)

Figure 6.9: Difference (signed error) and relative error between observed and estimated layer TAC for the first 14 layers and for all time frame for subject #0530.

biology. As $k_{01} < 0$, one can assume that $k_{01} = 0$, this will mean that no ^{99m}Tc-pertechnetate is secreted by the NIS expressing cells outside the con-

sidered system. This is a reasonable hypothesis according to the biologists. However, the three other parameter values pose a problem in terms of biology. According to the biologists knowledge, k_{12} should be small comparing to the others and it is not the case. The overestimation of k_{12} might be a consequence of the short circuit of both k_{02} and k_{10}. This has to be confirm by additional experiments and a refined model of the system. Consequently, we cannot claim yet that the results are biologically relevant.

6.5 Discussion and Future works

In this chapter, we established a methodological approach based on compartment analysis for the modelling of the ^{99m}Tc-pertechnetate uptake in the murine stomach. Our objective was also to study the feasibility of this approach. In order to simplify the model and reduce the number of parameters of the model, several assumptions have been made. The results (transfer parameters) that have been obtained at the end are satisfying knowing all the assumptions.

From this feasibility study, one can conclude that our modelling, together with the methodology proposed in this chapter, allows the estimation of parameters, here the transfer parameters between compartments.

The originality of this feasibility study is to take into account information that was available on some functional units such as the presence of NIS expressing cells in the glandular part of the stomach wall.

In this section we review each choice and assumption done in this work and discuss them. We conclude this section by proposing future works; these research directions present the limitations of our approach and how we could improve it, the next steps that should be undertaken to exploit the methodology we developed, and the alternative directions and choices that should be investigated.

6.5.1 General approach

Our objective in this work is to study the iodide uptake in the murine. For this study, we first provided, in Chapter 5 qualitative results on this evolution. The data available, and the experimental conditions conducted us to a first choice concerning our approach.

Region-based approach (Choice 1) Iodide is mainly accumulated in two regions of the stomach, the wall and the cavity. Thus, one would like to consider only two regions for the uptake study. However, these two spatial regions are not homogeneous. Then, the regions should be spatialised in order to take into account the diffusion phenomenon in the cavity. A voxel-based approach is not possible to study iodide uptake

in the murine stomach because of the movement and deformation of the stomach (see Chapter 5). Thus we considered an approach that permits us to gather the voxels in homogeneous regions. Once the regions defined for each image, we associate each layer along the time. We made the assumption that the layers also refer to the same anatomical region. This kind of approach was already advocated by Zang et al. for functional MRI [ZJL+04], where voxels are gathered into homogeneous regions.

> Regional Homogeneity (ReHo) is a voxel-based measure of brain activity which evaluates the similarity or synchronization between the time series of a given voxel and its nearest neighbors (Zang et al., 2004).

The difficulty here, that differs from parcel-based approaches with parceling/regional homogeneity in functional MRI [ZJL+04], is that our regions are interlocked layers: we base our analysis on a measure of the activity inside each layer of the stomach, each layer being composed of a mix of the different stomach regions.

6.5.2 Model proposal: compartmental modelling

To provide a model for the phenomenon observed and presented in Chapter 5, we proposed a first model of the stomach based on compartmental analysis, and then two steps of simplification. Those simplifications were needed in order to deal with the equations of the model both analytically and numerically. The general assumptions we made are related to compartmental analysis.

The system follows compartment modelling prerequisites (Assumption 1) This assumption can be split into two hypotheses.

Temporal invariance of transfer functions The transfer functions between any two compartments are constants.

Nature of transfer equations We supposed that the transfer equations between compartments are ordinary differential equations (ODEs), which are linear and of first order.

The fact that our analysis concludes with relatively stable results shows that these two hypotheses were reasonable, at least in a first time.

Observability (Assumption 2) We can observe the concentration of ^{99m}Tc-pertechnetate in each compartment, and use these observation as system outputs. This hypothesis is somehow justified by the observations of Chapter 5 and **Choice 1**, but building the activity in each compartment from the layered observation is not trivial, as explained below.

In this work, we decided to study our subject with compartmental analysis but other approaches could have been considered. For example, another kind of approach used in medical imaging is the factor analysis of dynamic structures [FBDP89]. Its aim is to estimate the kinetic of different physiological mechanisms.

6.5.3 Computing TACs

To build the system input and outputs, we need to construct time-activity curves (TACs) for the input function, i.e. the activity in the blood, and each of the observed output, i.e., the activity in the stomach wall and cavity. The activity in the blood could be observed from the activity variation in the left ventricle of the dynamic SPECT images. For obtaining the TAC in the two other compartments, we make the following assumptions.

Time dependency of composition of each layer (Assumption 3) We made the assumption that the composition of each layer, in terms of the volume occupied by each compartment, does not change with respect to the time. This assumption does not take into account that, although the animal is anaesthetized, its stomach might be subject to local deformation, such as contraction or relaxation. More precisely, we made the assumption that the n^{th} layer had the same composition over the time, but if the stomach contracts the layer number n will get closer to the stomach cavity and have a different composition. To summarise, the composition of each layer might slightly vary over the time but we neglected this variation in a first time. In the future more complex segmentation techniques might be considered in order to limit the layer mismatch.

From these assumption and from an estimation of the mixing coefficients that express the activity in each layer depending on the activity in each compartment, we approximated the TAC of each compartment. Then, we verified that the TACs of all the layers reconstructed from the TAC in the compartment was precise enough.

At the moment, the mixing coefficients have been estimated from a simple observation of the IHC images, but a more precise estimation of these coefficient could be performed (see Section 6.5.6 below).

6.5.4 Computation of the transfer parameters

Once the TACs and the compartmental model are known, the objective is to find the transfer parameters in order to fully characterise the system. This characterisation can be done by solving the inverse problem. The inverse

problem consists in estimating the transfer functions from longitudinal observations. This inverse problem can be solved in two different ways: a direct approach that uses a semi-analytic resolution, or an indirect approach that estimate the set of transfer parameters with optimisation approaches. Here, we tested both ways but the chosen resolution is the numerical one with optimisation steps.

Numerical resolution (Choice 2) The attempt of determination of the compartment TACs with a sum of four exponential functions failed with a mixed analytic/numerical approach. The reasons for this failure are the difficulty to fit a function with a sum of four exponential functions, and the lack of data. Although, this kind of multiexponential function fitting consideration can be improved with additional optimisation method. However we did not investigated further this direction, this might be a perspective of our work. Consequently, instead of trying to fit sum of exponential functions, we build TACs from different transfer coefficients, and fit them with the TACs obtained by the preceding step.

This last step allowed us to find transfer parameters by combining exploration and optimisation steps. The optimisation was performed with a simplex algorithm. We finally obtain a set of transfer parameters that fit relatively well with the observed phenomenon.

The numerical resolution has been possible thanks to several simplification of the model toward a classical model (two-compartment system). Although, the solution that has been found is relevant for the system. In order to better match with the biological functional units, one should go back to a more complex model. Then, another kind of approach might be considered for the numerical resolution since there will be more transfer parameters to determine. Indeed, the dimension of space of values to explore will increase by 1 for each new transfer parameter to find. Consequently, the exploration of the space of values will be more complex and the time of computation will increase.

6.5.5 Evaluation of the method

We did not conduct complete evaluation of the robustness and adequacy of our method, however, our first results are satisfying because the method allows us to compute transfer parameter, and the computation seems relatively stable. Indeed, first experiments where we tried to perturbate the solution or to find other optimums for the transfer coefficients led us to similar coefficients (same order of magnitude). We can thus conclude for the moment that this analysis proved the feasibility of the study, and that our methodology is appropriate. However, further developments and probably refinement of the methodology, will be necessary to improve the robustness of the results and the precision

of the stomach model we propose. It is also necessary to validate and exploit our results in terms of biological interpretation.

6.5.6 Future works

The rest of this section will detail the further developments that are, to my mind, necessary to overcome the main limitations of our approach and to improve our method and results.

6.5.6.1 Mixing coefficient describing the composition of each layer

In a first step, we estimated from observation of the IHC images the mixing coefficients. We consider this first estimation as satisfactory as it leads to reasonable results and shows the feasibility of our study. However, we wonder if this estimation from a single observation of a single IHC image is relevant. Investigations are conducted on the reconstruction of a three (spatial) dimensions (3D) image of the murine stomach from a set IHC images[2]. This 3D image will be considered as an atlas for the stomach and will be registered to the SPECT images. It will provide information on the spatial distribution of the different functional units that have been considered. Considering the number of approximations that will be performed such as the resampling required for the IHC, the final atlas should not be used as a ground truth. The resulting 3D stomach atlas could be used to assess the mixing coefficients that have been determined in Section 6.3.2.2.

6.5.6.2 Robustness of the estimation of transfer parameters k_{ij}

While we checked that small variations of the starting values for the transfer parameters led to similar results, we did not perform any systematic robustness test on our obtained results. Here are some steps that we plan to do in the future in order to demonstrate the robustness and reproducibility of the estimation of the transfer parameters.

- **Exploration of the parameter space**. We started from 5 values for each of the 5 parameters. While extending much this step costs a lot of computation time due to the combinatorial explosion of the explored space, as the current exploration is performed in a few minutes, we could slightly extend the range of parameters investigated.
- **Direct comparison with L (observed layer TACs) instead of $\hat{C}$ (approximated compartment TACs)**. At the moment, we approximate the TACs of the compartments from the ones of the layers,

[2]Thanks a lot to Audrey Lamit, Julien Guglielmi and Philippe Pognonec for their time, help, support and involvement in the planning, experimental and acquisition process.

and optimise the difference between the TACs obtained from the layers and the ones obtained from the compartmental analysis (i.e. from the transfer parameters). Instead, we could apply the mixing coefficients on the TACs obtained from the compartmental analysis and obtain approximated TACs for all the layers; then we would directly optimise the difference between the observed and the estimated TACs for the layers. In other words, this approach consists in optimising directly the last two columns of Table 6.2. A first experiment seems to provide similar results with the two methods, but this should be further investigated.

- **Modification of the initialisation of the two execution of downhill simplex algorithm**. Several alternative ways of choosing the initial points of the downhill simplex and of perturbing this initial points should also be investigated.

  Among these investigations, one promising direction is to run the second execution of the downhill simplex on a large number of perturbated initial set of parameters in order to have statistics (average/standard deviation...) and then check the reproducibility of our results.

- **Increase the precision of the downhill simplex algorithm**. This consists in reducing the stopping condition ε, and increasing the maximal number of iterations. This requires more computation time and will not change much the results, but it should give us results with an improved precision.

- **Improve the speed the convergence** To improve the speed of convergence of the simplex algorithm, we could try to minimise the difference of normalised compartment or layer TACs, instead of the simple difference.

- **Constrain transfer parameter search to positive values** For the moment, we also explore the negative values for the transfer parameters while the biological significance of such a negative value is not clear. We could reduce the exploration space to positive values for transfer parameters, but this could perturbate the efficiency of the simplex algorithm. Though it could prevent us from detecting unreasonable results, especially if the negative value is not close to zero. In our experiments, we have reached a negative value for one transfer parameter, in the last iteration, but this value is quite small. Consequently, constraining transfer parameter search to positive values might not provide a significant gain.

6.5.6.3 Extending the dataset

At the moment, this work has been conducted on only one animal and one sequence of SPECT images. In order to fully validate the approach, it would

be interesting to perform a group study. The first outcome of such additional tests would be to know if the transfer parameters are really different, or if they are similar. Having parameters relatively similar for different animals would also convince us of the robustness of the results.

However, to use another set of data we need it to satisfy some constraints. These constraints are linked to the conditions of the imaging procedure. First, the image field of view should include the blood in order to be able to estimate the blood input function. Then the type of injection should be the same. Finally, the number of frames and the time lapse between each frame should be sufficient. In other words, the total sequence of acquisition should contain not less than 19 time frame acquired over at least 2 hours. Among the set of data available (see Table 5.1), only four sets match this prerequisites: the subject #0530 studied in this chapter and the subjects #0366, #0370, and #0371. However, on the remaining 4 sets, only the subject #0530 has the heart visible in the field of view.

6.5.6.4 Biological interpretation and validity

Last but not least, a first interpretation of the first result has been provided by the biologists. However, one result is not sufficient to conclude on the relevance of the approach and on the biological interpretation. Indeed, some transfer parameter values that have been determined do not reflect the biological reality. Consequently, it will be more relevant if we check first the robustness and reproducibility of the method, and if we increase the complexity of the compartmental model.

CONCLUSIONS

Chapter 7

Conclusions

Contents

In this thesis we address the study of longitudinal phenomena with application to small animal SPECT imaging. Among the wide range of processes that can be studied, we focus on two particular subjects with biological challenges that led to the development of dedicated methodologies. Overall, several challenges related to the work with animal imaging were addressed.

First, the elaboration of a relevant biological acquisition protocol is a demanding task which requires a lot of interaction with all the contributors (biologists, computer scientists), and a good understanding of all the variables that influence the biological and imaging outcome. The protocols had to deal with biological variability since the studied biological phenomena were not well known. For example, a new in vivo tumour model was considered for which the in vivo injection protocol was still on trial (cell lineage, animal lineage, sensitivity to radioactivity dose or Xray dose). The site of injection and the site of tumour fixation were also very sensitive to change, hard to predict and yield to a dataset with a lot of variability. The setting up of longitudinal acquisition also required organisation in order to estimate the speed and duration of evolution of the observed phenomenon. Indeed, the study of longitudinal phenomena suggests quantification and/or modelling of the phenomenon over time, and the time scale of a new phenomenon might be difficult to predict.

Second, both phenomena that are studied here are observed in the abdominal region, which lead us to two additional sub-challenges. The first one is the lack of imaging that would serve as detailed anatomical reference, indeed a simple computed tomography (CT) scan does not offer a good contrast in

the soft tissues. And the use of additional contrast agent without interference with the protocol is not guaranteed. One could consider approaches such as the ones presented in [MBC+10]. This method succeeds in extracting TAC from rodent PET images without the anatomical information.

The second one but not the least is the intrinsic motion of the considered area. Indeed, the subjects were anaesthetized mice, thus there were still breathing and their stomach and surrounding organs were moving. In both studies we thus had to take into account the movement of the organs.

7.1 Contributions

The major contributions were in terms of methodology. The first method addresses the problem of reconstruction of SPECT images without respiratory motion artefacts. The second method proposes a model for the kinetic of ^{99m}Tc-pertechnetate uptake in the murine stomach.

Simulated breath-hold reconstruction in micro-SPECT In order to avoid respiratory motion artefacts in SPECT images, we proposed a method that selects retrospectively and maximises the data used for a motionless reconstruction. This could be seen as a breath-hold like acquisition or a smart respiratory gated acquisition. This method guarantees a high signal-to-noise ratio (SNR) while eliminating respiratory motion artifacts. Moreover this method is adapted to breathing rhythms particular to anaesthetized animal (gasps) with high variability in terms of amplitude and length. This method is based on the extraction of intrinsic information; it is robust to the apparent asynchronism between the true motion in the images and the respiratory signal externally acquired. The quality and accuracy of reconstructed images are comparable to a non-gated reconstruction in terms of noise measure and SNR, and intermediary between gated and non-gated reconstruction for lesion measurements (SUV_{peak}, SUV_{mean} and lesion volume). Thanks to this method, new and more challenging studies concerning organs or tumour modelling in abdominal region can be addressed with SPECT imaging.

This contribution led to the development of a first version of a software implementing this method. This software with a graphical interface allows biologists to obtain a simulated breath-hold reconstruction from a SPECT acquisition.

Study of ^{99m}Tc-pertechnetate uptake in the stomach In order to help biologists to understand the process of iodide uptake and secretion in the stomach, we propose a method that permits us to build a first compartmental model describing the iodide analog ^{99m}Tc-pertechnetate uptake in the murine stomach. This conducted to the design of a compartmental model together

with a first estimation of hidden parameters, i.e., transfer parameters between compartments. The method relies on an original layer-based description of the stomach that permits us to obtain a relevant anatomical information of the stomach, and that makes up for the progressive ^{99m}Tc-pertechnetate uptake and irregularities in the stomach shape. Additionally, this layer description is robust to global stomach deformation such as contraction or relaxation. Still, several challenges had to be taken into account. A first challenge concerns the intensity-based stomach segmentation process without anatomical prior information. This segmentation step failed in the early time frame (just after activity injection) since the site of injection that was in the field of view, was segmented instead of the stomach. A second challenge was that each layer does not correspond to only one compartment. It is a mix of several compartment and in a certain sense, even if each compartment is supposed to be homogeneous, a layer is not. We thus considered the set of layers as a mix of compartment, each mixing coefficient being representative of the composition of each layer. A first determination of these mixing coefficients was proposed and yields really good results relatively to the method that was used to determine them. A few other challenges were only partially addressed, like the robustness of the method, or the non-uniform composition of each layer. Also, the method makes several simplifying hypotheses. For example, we do not take into account the local temporal stomach deformation that induces a slight layer mismatch between the outer layers. The first layer at a given instant might disappear in the next instant. Despite these points that can be improved, the method yields relevant results in terms of estimation of time-activity curves.

7.2 Future works and perspectives

The development of these two methods open a wide range of possibilities. First we present several direct improvements of our methods and results that could be envisioned. Then we propose a few longer term research directions.

7.2.1 Direct improvements of the contributions

Software for breath-hold like image reconstruction The software dedicated to the reconstruction of SPECT images without respiratory motion artefacts should be further developed. Although it has been developed for biologists, its current version is just a beta version and is not yet adapted to a routine use.

Validation of the breath-hold like reconstruction method on simulated data This validation step consists in simulating the SPECT imaging

of breathing mice in order to obtain a large set of data. These numerical mouse phantoms should include small lesions randomly located in the abdomen and a variable breathing rhythm. More precisely, one would have to animate a numerical mouse phantom with the same particular respiratory pattern that has been observed (gasps followed by a rest period). However, such a model has not been developed yet. For example, the MOBY phantom [STF+04] implemented a respiratory motion similar to humans, and would not be adequate.

Additionally, such a work requires the elaboration of a numerical model for our camera in order to simulate the acquisition and reconstruction processes. The disadvantage of this validation process is that it involves a set of data that will be perfectly produced by the simulation software without reflecting the reality of the manipulation and acquisition of living animals. However, such a simulation will provide a large set of data that will be valuable for the validation of our method.

Iodide uptake study in stomach Most of the future works related to this subject have been detailed in Section 6.5.6. Among them, the main points are the study of the robustness of the approach; the assessment of mixing coefficients from IHC slices; and the biological interpretation of the phenomenon.

7.2.2 Long term research directions

I present below a couple of longer term research objectives, they consist in improving the methods in the same direction of each approach I presented, but also in combining both approaches in order to study new research directions.

Abdominal tumour growth quantification and modelling Studying the abdominal tumours, and quantifying and modelling their growth was the initial goal of this thesis. However, this objective required preliminary works on the respiratory motion correction. This preliminary work turned to be more challenging than expected and has been addressed in Chapters 3, 4 and in Appendix A of this thesis. From this, the tracking and accurate quantification of tumours in the abdominal region will rely on strong basis. A tumour matching algorithm [WGR+01] should be developed in order to track the tumours along the time by taking into account their growth, the possible fusion of spatially close tumours, or the apparition of a new lesions. This kind of approach should include registration methods such as block matching [ORPA00]. Then, the tumour growth in the peritoneal cavity can be studied and will set up a computational model for tumour growth [KPCA08] in a deformable environment. Such a model should greatly help the biologists in the understanding of the growth of this kind of tumours.

Layer-based approach applied to the tumour heterogeneousness The original layer-based description of the stomach presented in Chapters 5 and 6 could be extended to other organs but also to tumours. Indeed, some tumours can be observed until a late stage. At late stage, the segmentation of tumours based on SPECT images reveals only the active part of the tumour, that is constituted by vascular cells. However, it does not reveal the necrosis part of the tumour. In the case of subcutaneous tumours, this can also be observed on CT imaging since the necrosis part sinks but not for other tumours.

First, in the case of NIS expressing tumorous cells, the necrosis of the tumour can be predicted by a decrease of the uptake in the internal layers of the tumour in a preceding imaging.

More generally, it has been also mentioned in [UTT+12] that the tumours interiors is never homogeneous, for the reasons mentioned above. In this article, authors presents the results of the first investigations done with high resolution SPECT imaging of small animal: they assess the heterogeneousness of tumours.

More interestingly, the idea of applying a layered-based approach to tumours is to better understand the structure and evolution of the tumour. Indeed, we could study the tumour not as an homogeneous system, where we calculate the average activity on the whole tumour. Instead, tumours could be studied as a set of subregions such as layers. We would calculate the average activity in each subregions. This would allow the identification of different parts of the tumour: necrosis, proliferating cells, but also some other intermediate parts. We hope that such an approach, with a region-based analysis of the tumour, would provide a much better understanding and modelling of the tumour growth.

List of publications

Most of my publications are available at http://www-sop.inria.fr/members/Marine.Breuilly/.

Article in peer-reviewed journal

[1] Marine Breuilly, Grégoire Malandain, Julien Guglielmi, Robert Marsault, Thierry Pourcher, Philippe R. Franken, and Jacques Darcourt. Amplitude-based data selection for optimal retrospective reconstruction in micro-SPECT. *Physics in Medicine and Biology*, 58(8):2657–2674, April 2013.

International conferences

[2] Marine Breuilly, Grégoire Malandain, Nicholas Ayache, Jacques Darcourt, Thierry Pourcher, and Philippe Franken. Simulated breath-hold reconstruction in micro-SPECT: Application to peritoneal metastases expressing NIS as reporter gene. *Journal of Nuclear Medicine Meeting Abstracts*, 53(1):2381, 2012. Poster.

[3] Marine Breuilly, Grégoire Malandain, Nicholas Ayache, Julien Guglielmi, Thierry Pourcher, Philippe R. Franken, and Jacques Darcourt. Image-based motion detection in 4D images and application to respiratory motion suppression. In *Proceedings of the 10th IEEE International Symposium on Biomedical Imaging 2013 (ISBI'13)*, San Francisco, USA, April 2013. IEEE. Poster.

National Conferences

[4] Marine Breuilly, Aymeric Histace, Christophe Portefaix, Bogdan Matuszewski, and Frederic Precioso. Segmentation des muscles oculomoteurs en irm cerebro-orbitaire pour l'aide au diagnostic de l'exophtalmie. In *22eme Colloque GRETSI 2009*, 2009. Oral.

[5] Marine Breuilly, Grégoire Malandain, Philippe Franken, Jacques Darcourt, and Thierry Pourcher. Prise en compte du mouvement respiratoire du

petit animal pour la reconstruction 3D TEMP synchronisée: application aux métastases péritonéales. 50ème Colloque de médecine nucléaire 2012, 2012. Poster.

[6] C. Portefaix, A. Histace, M. Breuilly, and B. Matuszewski. Segmentation semi-automatique en IRM3T des muscles oculomoteurs dans le suivi de la maladie de Grave-Basedow. In *Actes des Journées Françaises de Radiologie (JFR)*, Octobre 2009. Poster.

Miscellaneous

[7] Marine Breuilly. Investigation of medical active contour image segmentation techniques. Master's thesis, Université de Cergy-Pontoise, 2009.

[8] Marine Breuilly, Grégoire Malandain, Nicholas Ayache, Philippe Franken, Jacques Darcourt, and Thierry Pourcher. Definition of motionless phases for monitoring gated reconstruction of SPECT images in alive mice. ICVSS 2010, July 2010. Poster.

[9] Marine Breuilly, Grégoire Malandain, Nicholas Ayache, Philippe Franken, Jacques Darcourt, and Thierry Pourcher. Simulated breath-hold reconstruction in micro-SPECT: application to peritoneal metastases expressing NIS as reporter gene. 2ème colloque MIBO, 2012.

APPENDICES

Appendix A

Amplitude-based data selection for optimal retrospective reconstruction in micro-SPECT: Supplementary data

Contents

A.1 Introduction

In this appendix, we present complementary observations, investigations, and results to the published paper entitled "Amplitude-based data selection for optimal retrospective reconstruction in micro-SPECT" presented in Chapter 4. The overall aim of this appendix is twofold.

First, we explain the reasons that led us to the approach presented in Chapter 4. We present preliminary observations that led us to deeply investigate the reasons of respiratory motion variations, and that initiated the proposed method for motionless three (spatial) dimensions (3D) single photon emission computed tomography (SPECT) reconstruction. Some variability of the respiratory rhythm (length and amplitude of pressure cycles) of animal are naturally observed during the acquisition procedures. The operator had to concentrate his/her attention in order to prevent high rhythmic variation by manually adjusting the rate of anaesthetic gas. However, this was not sufficient to fully prevent variability of the respiratory rhythm. We have compared the average respiratory cycles extracted from the pressure sensor monitoring system for the set of acquisitions that we have and we tried to find some common similarity and trend. These characteristics will be described in Section A.2.1. Then, we wanted to check that the abdominal lesions were animated with the same motion as the one describe by the average respiratory signal. In practice, from the preliminary comparison between the temporal motion of the lesions centre of mass (COM) and the respiratory cycle, we observed a temporal shift of the peak of motion. This comparison of observed motion and respiratory signal will be detailed in Section A.2.2.

Second, the message given by these two observations justify a deep study of two phenomena. In a first time, we analysed the respiratory signal recorded by the monitoring system. In a second time, we studied the correlation between gating signals provided by the monitoring respiratory system and the one recorded by the camera (listmode). These investigations suggested to work exclusively with the gating signal (triggers) recorded in the listmode for post-acquisition reconstructions. Section A.3 deals with all investigations done on the gating signals.

Finally, in Section A.4, we provide additional results showing the efficiency of our approach. We show the performance of the successive improvement steps of our method for motionless 3D SPECT reconstruction. These improvements have been motivated by the investigations of the gating signal recorded in the listmode. In addition to the performance at each step, we show complementary results for the ultimate test of sensibility to the noise.

The results presented in the following were gathered in preliminary phases of our work and are intended to justify our approach.

A.2 Preliminary investigations on the respiratory signals

A.2.1 Study of the reproducibility of the respiratory signal

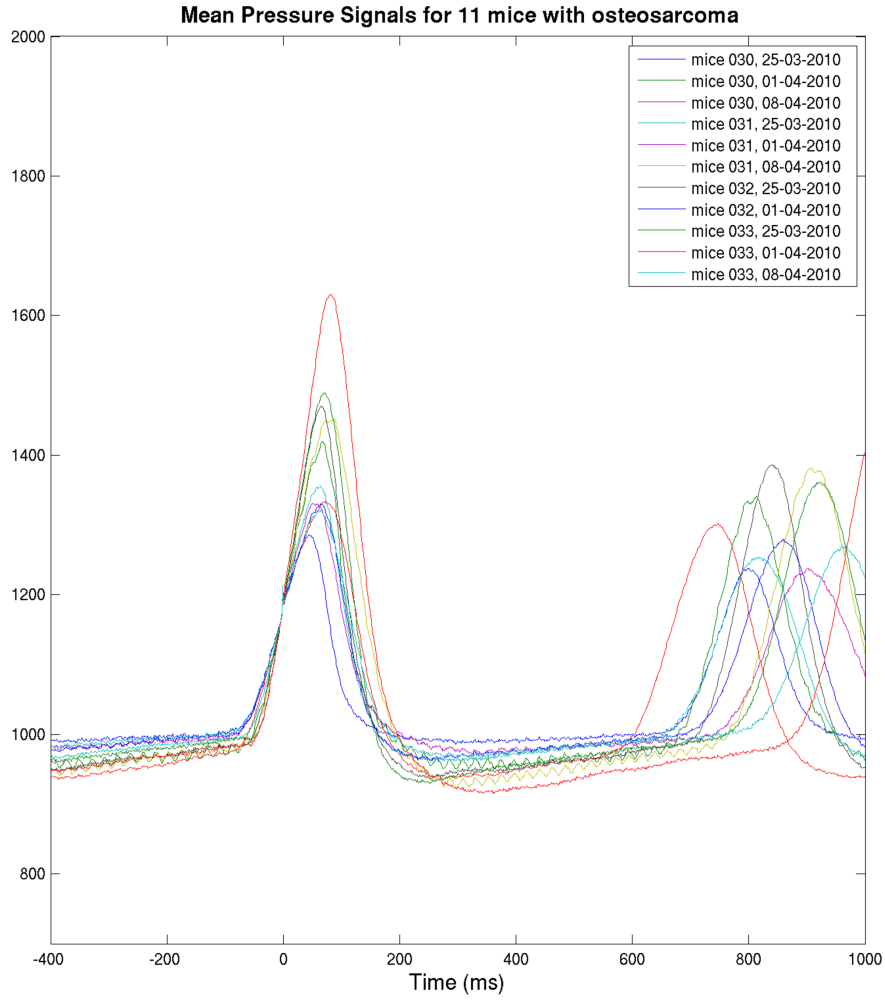

Figure A.1: Comparison of average respiratory cycle of four Balb/c mouse with osteosarcoma (K7M2 cells) at several days of acquisition

A preliminary simple test was the observation of the different average respiratory cycles according to different criteria: animal lineage, disease, subject,

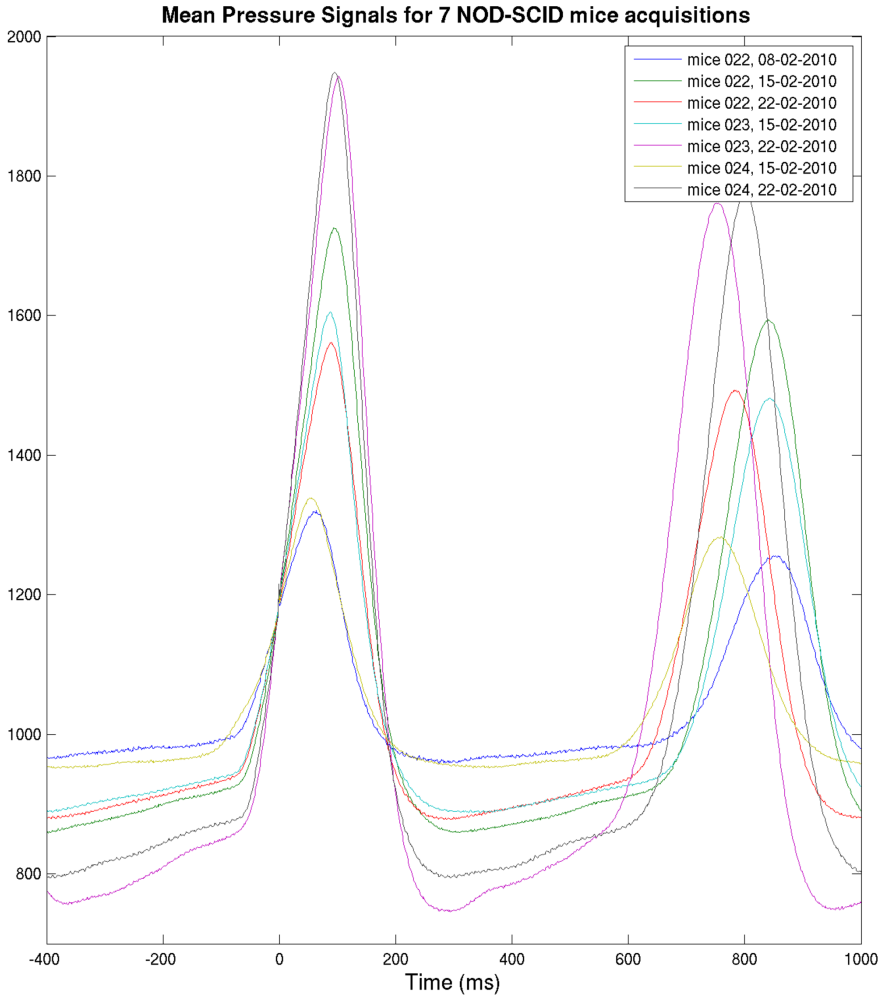

Figure A.2: Comparison of average respiratory cycle of three mouse of NOD-SCID lineage with IP injection of Prob-mNIS cells at several days of acquisition

in order to to see if there is a rule that describes the variability from one acquisition to another (Figure A.1, Figure A.2, Figure A.3, Figure A.4, Figure A.5, Figure A.6, and Figure A.7).

We conducted extensive experiments but we could not find a law expressing what the length or amplitude of breathing depends on. This could be expected from the initially observed high variability of the respiratory cycle, but it was crucial to try to find such a law because its existence would have helped the setting of the threshold during the acquisition, and could also have been

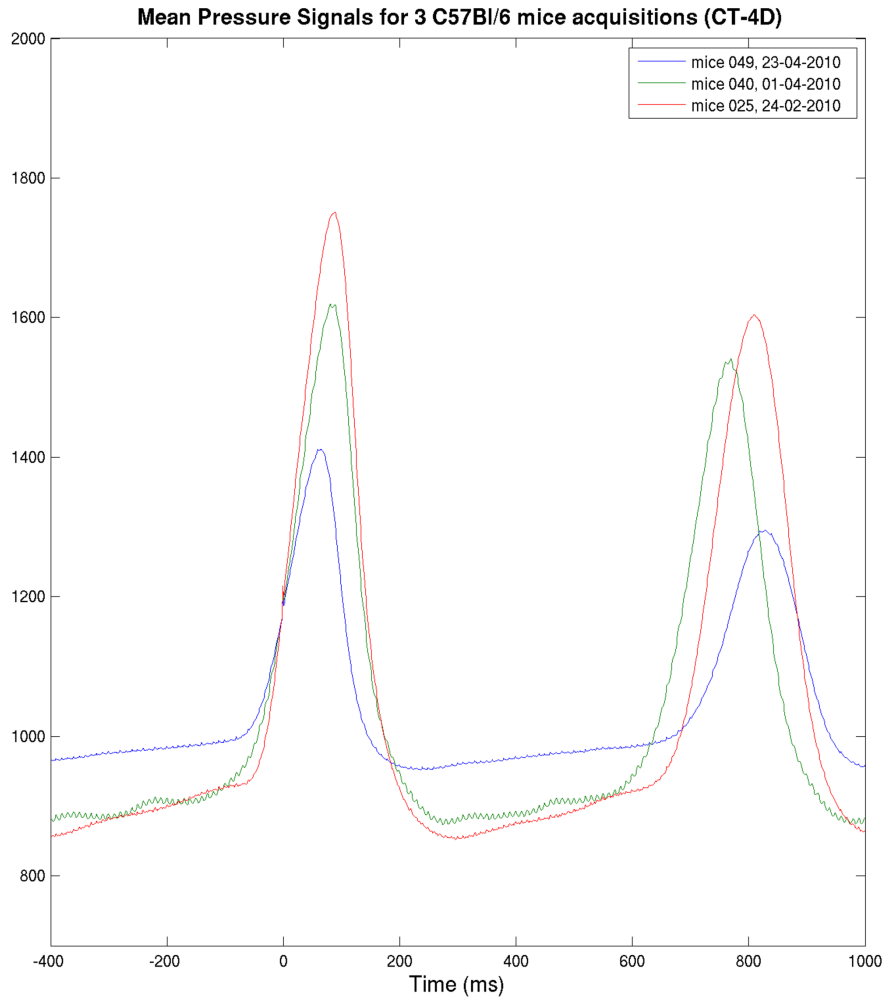

Figure A.3: Comparison of average respiratory cycle of three C57Bl/6 mice

exploited in our motion correction method. We tested:

- the inter individual variability on different days and on the same day of acquisition;
- the intra individual variability on follow-up acquisitions.

All these observations were done on a set of data acquired with the same respiratory monitoring constraints and recorded with the respiratory monitoring system. For all acquisitions, the operator adjusted the anaesthetic gas rate to keep the animal breathing at the same rhythm. An identical pressure threshold on rising edge was chosen for all acquisitions, this threshold

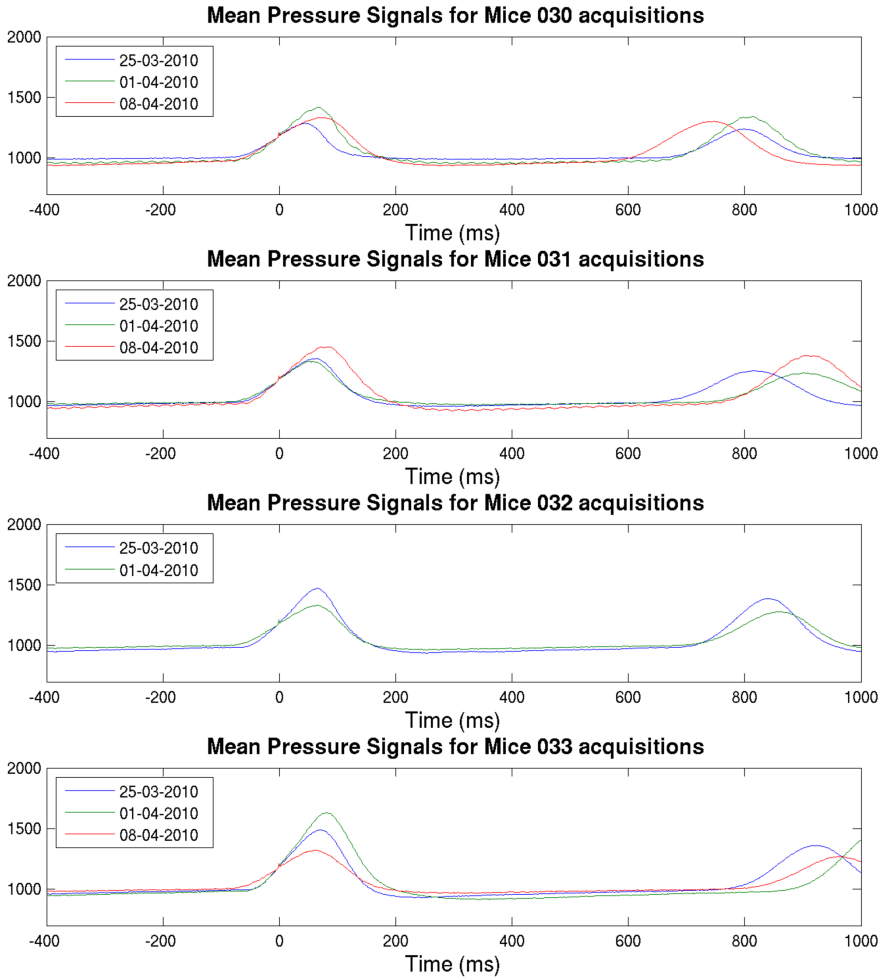

Figure A.4: Comparison of average pressure cycle obtained on repeated acquisitions of the same animal (C57Bl/6 lineage).

was used to delimit each cycle. An average respiratory cycle was computed from all cycles for each acquisition. At this preliminary stage, the average respiratory cycle is computed by summing up all the extracted cycles as they are (without resampling) and by dividing it by the number of cycles. As all the cycles were not of the same length we added to each cycle parts of the previous and next cycles in order to have all "cycles" length at 1400 ms: 400 ms before the beginning of each cycles and up to 400 ms after each cycles, so that all the intervals were of the same 1400 ms-length and could be summed up. Later, i.e. in all experiments shown in the following sections, each cycle

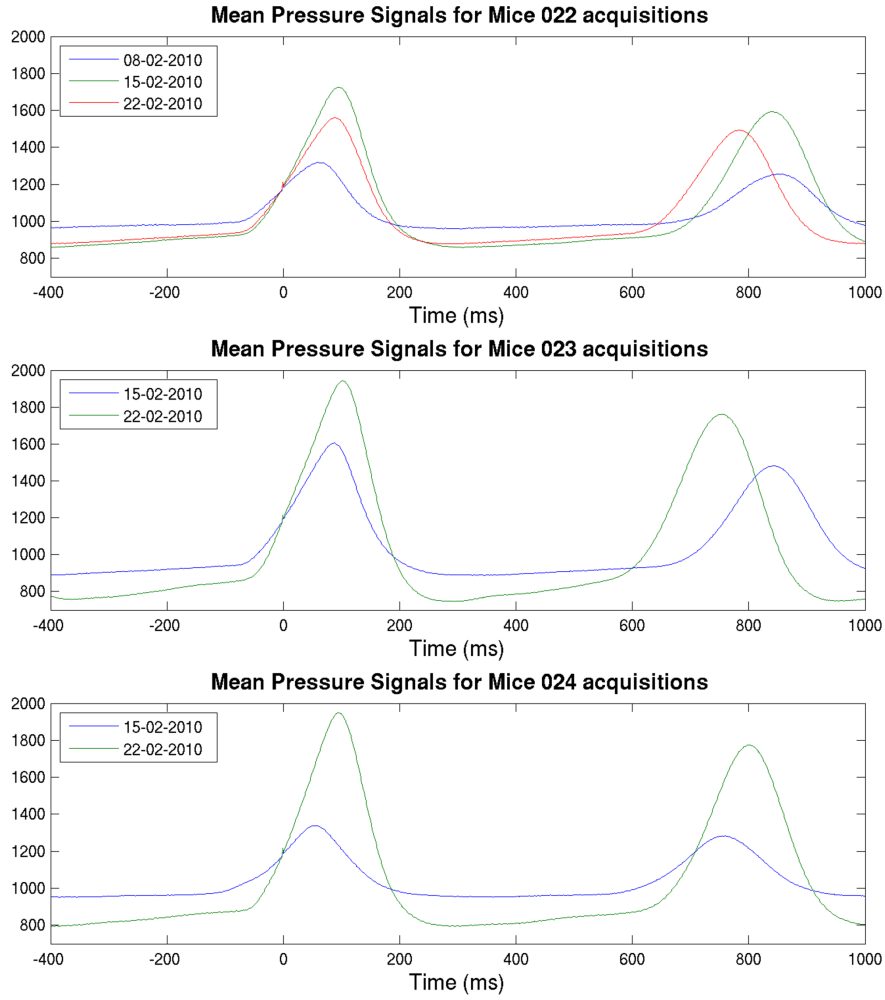

Figure A.5: Comparison of average pressure cycle obtained on repeated acquisitions of the same animal (NOD-SCID lineage).

will be resampled to the average cycle length before the summing since the variability of cycle length is high.

First, we compared the average cycle of different acquisitions according to the lineage of mice. Acquisitions were done on three different lineages: the Balb/c lineage in Figure A.1, the highly immunodeficient lineage NOD-SCID in Figure A.2, and the C57Bl/6 lineage in Figure A.3. The operator maintained the average respiratory rhythm in the same range, yielding the length of the average cycle to be in a range from 650 to 950 ms. However, the range of pressure variation from one acquisition to another is wider since it

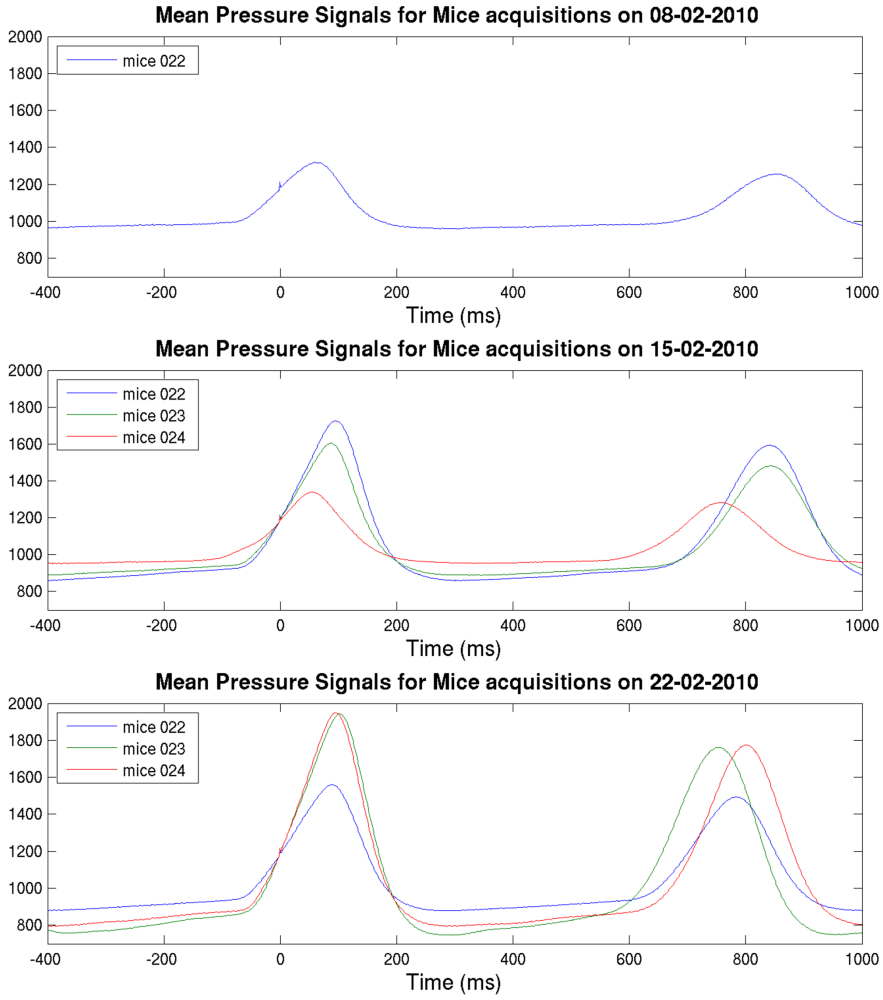

Figure A.6: Comparison of average pressure cycle according to the day of acquisition (NOD-SCID lineage).

could not be perfectly controlled. Only the acquisitions with the first lineage (Balb/c) were well aligned at the beginning of the cycle with respect to the range of amplitude, but with more variability with respect to the average length. For the two other lineages, the average signals are well aligned with respect to the length of cycle but the range of pressure variation can be double, depending on the acquisition. The hypothesis of a rule relating the respiratory rhythm or amplitude with the lineage does not hold since none of the observed characteristics (length and amplitude) is uniform at the same time for the three studied lineages.

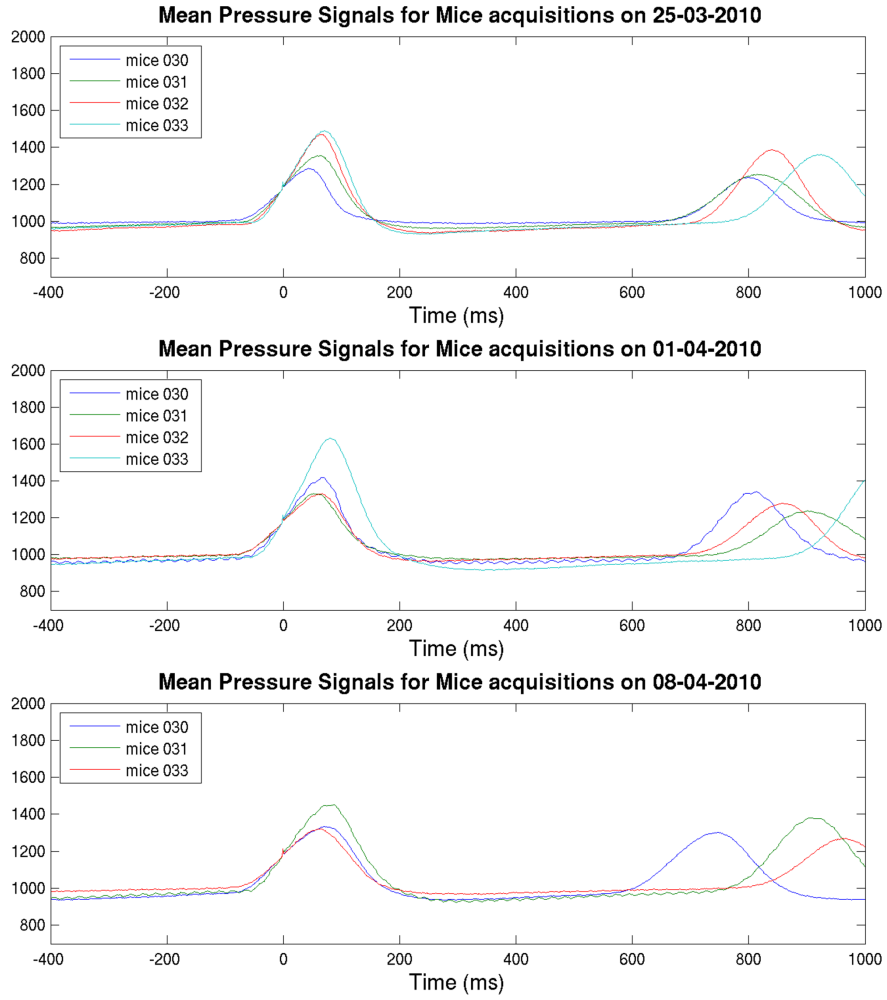

Figure A.7: Comparison of average pressure cycle according to the day of acquisition C57Bl/6 lineage.

Second, for the two first lineages (C57Bl/6 and NOD-SCID), each subject was imaged several times. As each animal has different characteristics, has a different weight, and is not affected similarly by the disease, we compared then the average cycle signal for each given subject. The observations for subject number 32 (see Figure A.4) exhibited the most two reproducible acquisitions, either with respect to the amplitude variation or the length of the average cycle. The observations for subjects number 30 and 31 exhibited relatively similar amplitude variation but less similar length of the average cycle. The observations for subject number 33 exhibited a similar trend but was less con-

vincing. However, the observations for subjects 22, 23 and 24 (see Figure A.5) exhibited neither uniformity in the amplitude range nor in the cycle length. To conclude, the hypothesis of a rule dependent to the subject does not hold either.

Third, for the same two first lineages (C57Bl/6 and NOD-SCID), the same animals were not only imaged several times but the acquisitions were done over two or three weeks. We compared then the average cycles with respect to the day of acquisition. Indeed, even if the same operator set up and controlled the animal for all the acquisitions, the placement of the animal in the bed and the positioning of the pressure sensor under the abdomen might be not exactly the same from one day to another. Moreover, the animal imaged on the same day were of the same lineage and age, and were injected with tumourous cells on the same day. We assume that the lesions were growing with the same speed and that the subject were affected by the lesions in a same manner. Thus, we considered that all animal imaged on the same day were in a similar state. For all separate days of acquisition, there were no reproducibility with respect to the length of the average cycle (see Figure A.6). We notice that the amplitude variations of the average signal were the most similar for the acquisitions on the day (08-04-2010), and by extension on the two previous days (25-03-2010 and 01-04-2010) (see Figure A.7). However, this similarity is too weak and not systematical; consequently, the day of acquisition is also not sufficient to characterize the average respiratory cycle.

A.2.2 Comparison between average pressure cycle and different intrinsic physiological signals

In this section, we investigate the similarity between the respiratory signal and the motion information intrinsic to the image. On the one hand, the average respiratory cycle is computed from the respiratory signal, as explained in the previous section. On the other hand, the motion information intrinsic to the image is related to the spatial motion of lesions, to the spatial motion of the diaphragmatic dome, or to the lung volume variation. These intrinsic information were extracted from three spatial + 1 temporal dimensions (4D) SPECT or 4D computed tomography (CT) images with algorithm based on intensity features. 4D SPECT images were reconstructed from the listmode as a set of fifteen 3D SPECT images, using the gating index recorded in the listmode as a delimitation of each cycle. 4D CT images were reconstructed from the gated projections.

SPECT intrinsic signal In 4D SPECT images, the motion signal is characterised by the lesion COM motion along each axis (coronal, sagittal and transverse). The lesions identified as hotspots in the abdomen, were seg-

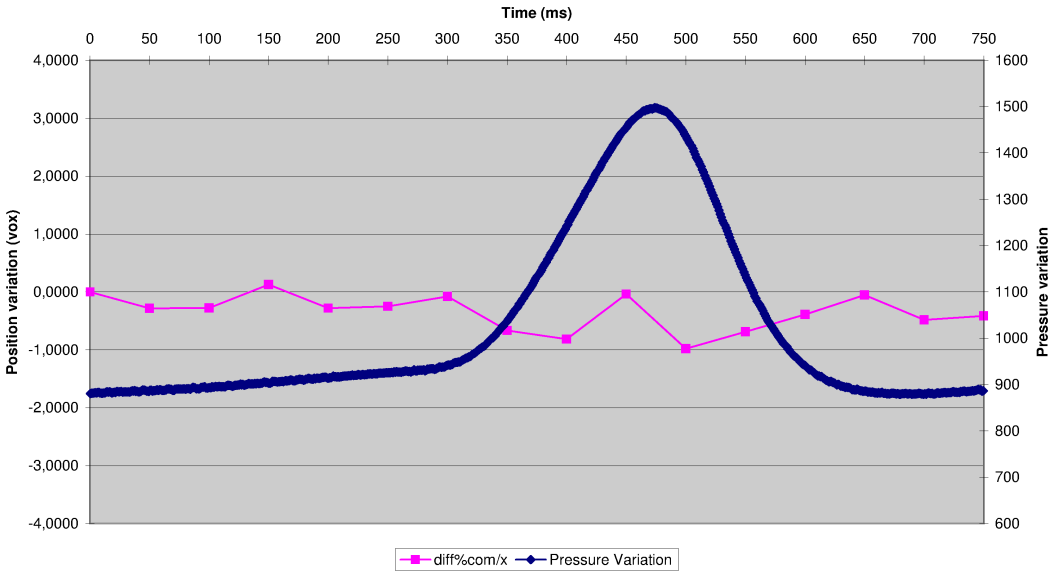

Figure A.8: **Comparison between center of mass motion along left-right axis and average respiratory cycle** for one lesion in mouse #022 and with respect to the first 50 ms phase.

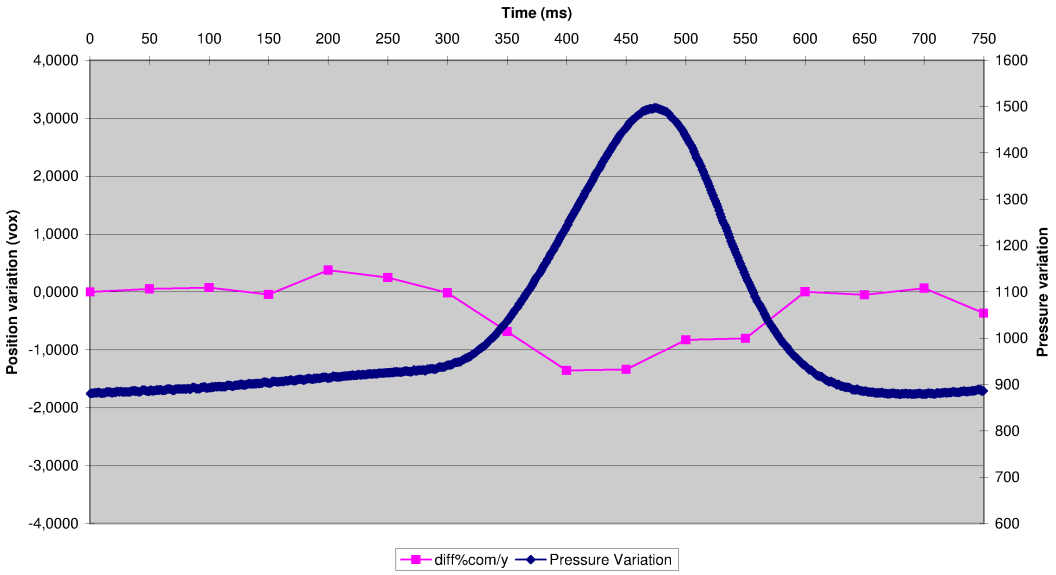

Figure A.9: **Comparison between center of mass motion along dorsoventral axis and average respiratory cycle** for one lesion in mouse #022 and with respect to the first 50 ms phase.

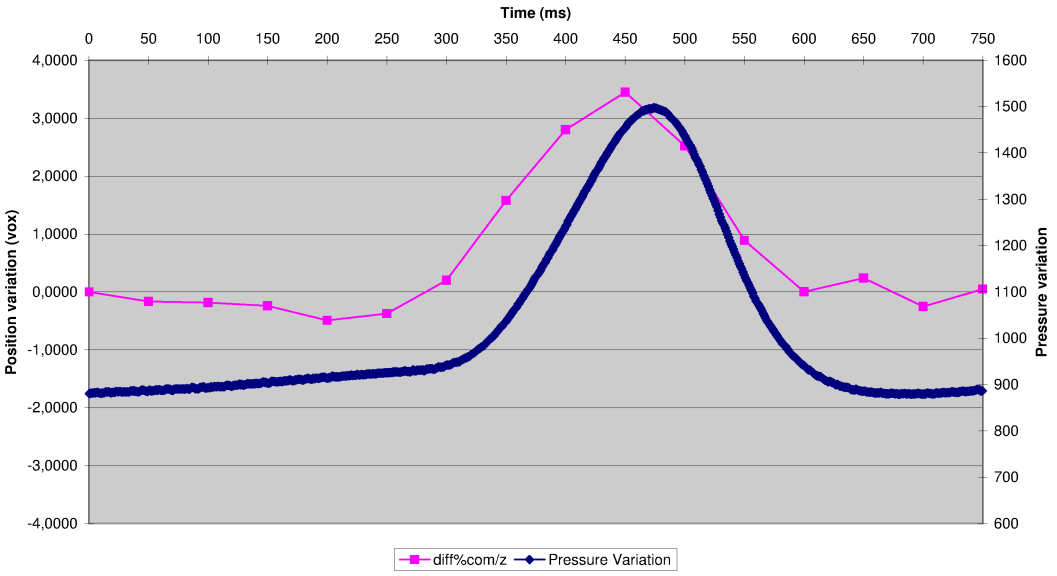

Figure A.10: **Comparison between center of mass motion along craniocaudal axis and average respiratory cycle** for one lesion in mouse #022 and with respect to the first 50 ms phase.

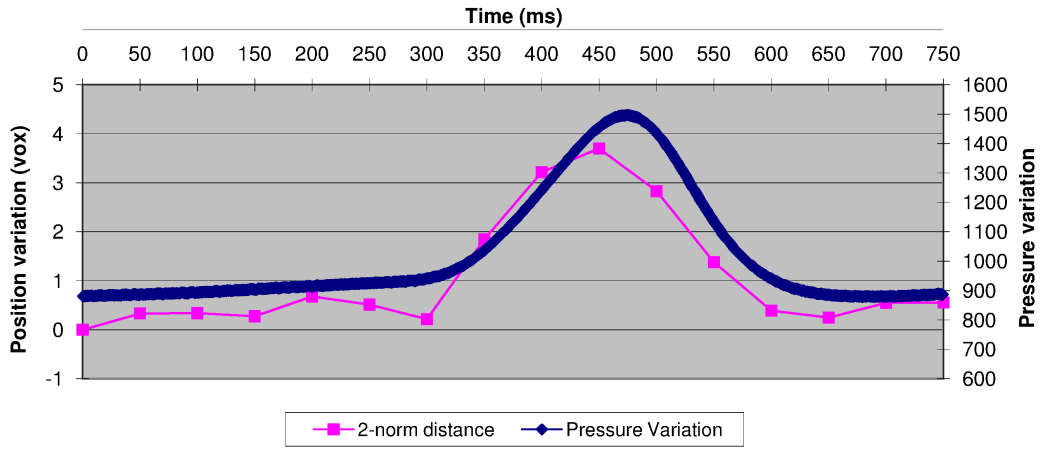

Figure A.11: **Comparison between euclidean distance of the lesion position shifting and the average respiratory cycle** for one lesion in mouse #022 and with respect to the first 50 ms phase.

mented along the time. An additional motion information was obtained from the Euclidean (or 2-norm) distance of the COM motion. The average respiratory cycles were compared to the COM lesion motions visually on graphics (see Figure A.8, Figure A.9, Figure A.10, Figure A.11, Figure A.12, Fig-

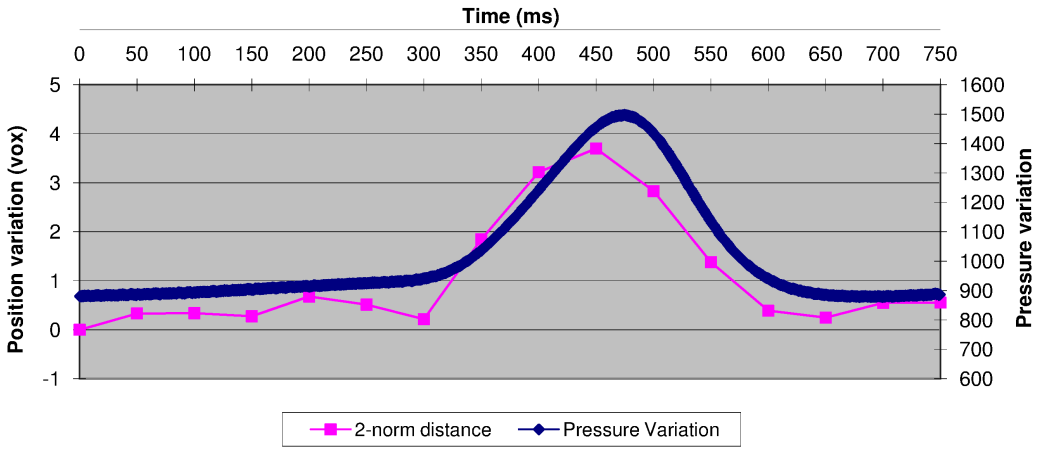

Figure A.12: Comparison between center of mass motion (Euclidean distance of the lesion position shifting) and average respiratory cycle for mouse #022 and metastase 4, with respect to the first 50 ms phase.

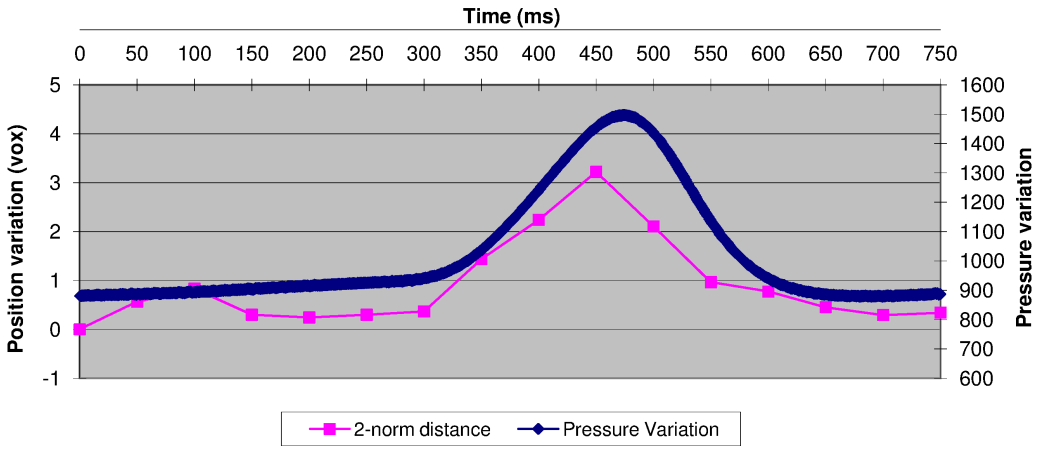

Figure A.13: Comparison between center of mass motion (Euclidean distance of the lesion position shifting) and average respiratory cycle for mouse #022 and metastase 5, with respect to the first 50 ms phase.

ure A.13, Figure A.14, and Figure A.15).

The graphics show that the lesion is not moving along the left-right axis (Figure A.8), while it is slightly moving along the dorsoventral axis (Figure A.9) with a shift above 1 voxel, and significantly moving along the craniocaudal axis (Figure A.10) with a cumulative shift above 4 voxels. The Euclidean distance of the lesion motion shows a shift of 4 voxels from the initial position (Figure A.11). Figure A.12, Figure A.13, Figure A.14, and Figure A.15 present the Euclidean distance illustrating the motion of several

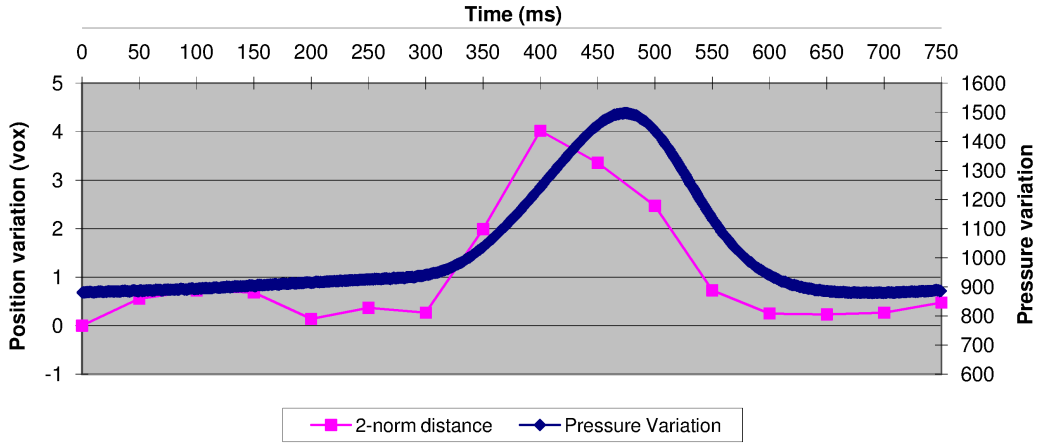

Figure A.14: Comparison between center of mass motion (Euclidean distance of the lesion position shifting) and average respiratory cycle for mouse #022 and metastase 6, with respect to the first 50 ms phase.

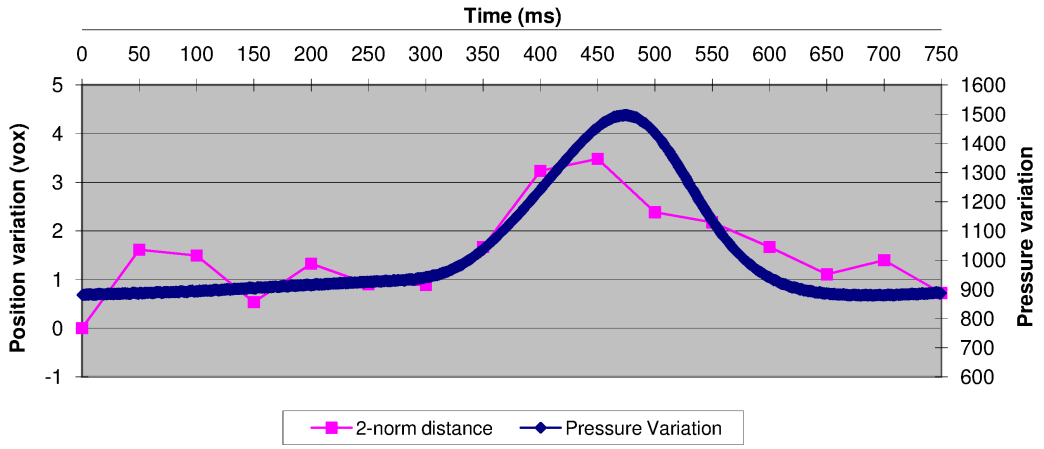

Figure A.15: Comparison between center of mass motion (Euclidean distance of the lesion position shifting) and average respiratory cycle for mouse #022 and metastase 7, with respect to the first 50 ms phase.

lesions. It suggests that all the lesions are animated by a similar motion, with a range of motion up to 4 voxels from the initial position. Two observations should be noted from these graphics.

First, the graphics suggest that the lesions are moving periodically, with the same frequency as the respiratory motion.

Second, the graphics show that the lesion motions are temporally shifted with respect to the moving phase of the average respiratory cycle. This suggests that there is a time shift between the lesion motion recorded in the

listmode acquisition and the respiratory signal recorded with the pressure sensor. However, in the introduction chapters, we made the assumption that the respiratory motion could be represented by the pressure signal that is recorded with the respiratory monitoring system. With this observation, it seems that this assumption should be considered with caution. The respiratory signal record, combined with a rising edge threshold detection, allows for a good cycle splitting since we observed that the movement of the lesion was following the same law as the average respiratory cycle concerning the length of the cycles. However, the respiratory signal can not be used to directly determine with accuracy the phase of the cycle in the listmode since we observed a slight time shift between the lesion motion and the signal variation that is smaller than the time shift observed in Figure A.16, Figure A.17, Figure A.18 between the respiratory signal and the intrinsic measure from 4D CT. We investigated the possibility that this time shift could be dependent on the imaging modality used; this is the reason why we also studied 4D CT images.

CT intrinsic signal In 4D CT images, the motion signal can be characterised either by the volume variation of the lungs or by the motion of some particular points of the lungs. The part of the lungs that is the most affected by the respiration in mice are the bases, just above the diaphragmatic dome. Here, both lung volume and diaphragmatic dome motion have been calculated. More precisely, two distinctive points of the lungs were localised, at the top and at the bottom of the diaphragmatic dome.

Figure A.16, Figure A.17, Figure A.18 present the average respiratory cycle, the lung volume variation, and the movement of the two points identified above for three distinctive acquisitions. First, the graphics show that the three intrinsic signals have a similar variation. This suggests that the lung volume variation is related to the diaphragm motion, and that the diaphragm motion only could be used as the intrinsic respiratory signal. Second, the intrinsic signals suggest a respiratory motion with the same frequency as the average respiratory signal. However, similarly to the case of SPECT, a temporal shift between extrinsic and intrinsic signal is perceptible. This shift is apparently not reproducible from one acquisition to another. The observations on the CT images strengthen the ones made on the SPECT images.

All together these observations suggest that it is crucial to study precisely the characteristics of both the extrinsic respiratory signal and the gating information recorded in the listmode of SPECT acquisitions, as well as the comparison between the two. Next section will present this study. One particular objective of the investigations on these signals is to know whether there is a law for characterising the time shift between respiratory signal and lesion motion or not.

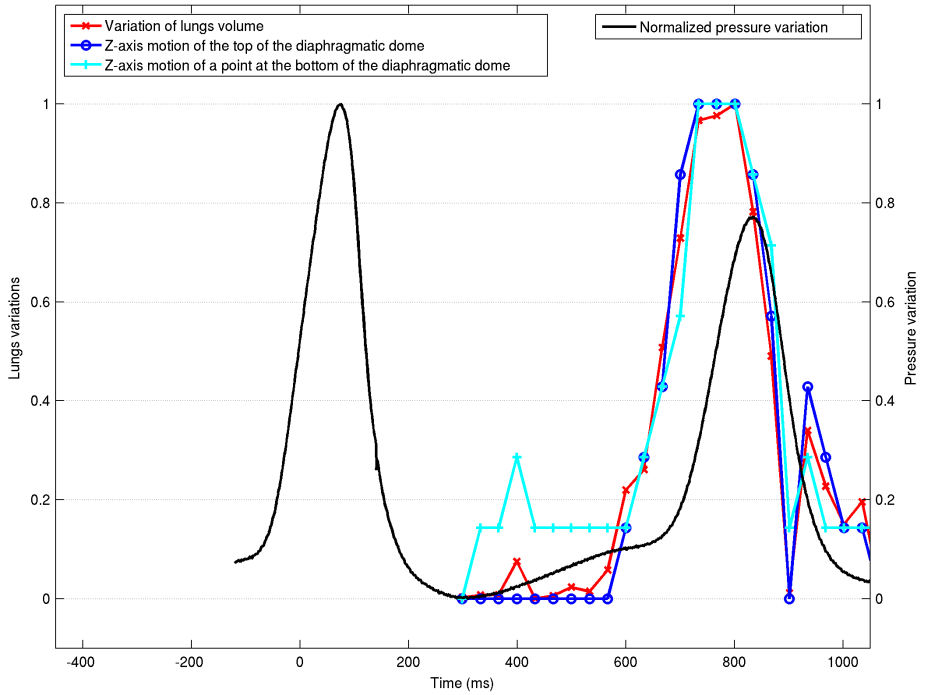

Figure A.16: **Comparison between the average pressure cycle (black curve) and intrinsic measures to 4D CT for acquisition #0283**: the lung volume variation (red curve with cross-shaped markers), the normalized z-axis motion of the top (dark blue curve with round-shaped markers) and the the normalized z-axis motion of base of the diaphragmatic dome (light blue curve with plus-shaped markers).

A.3 Intermediary investigations on the triggering signals

In this section, we investigate in more details the extrinsic respiratory signal and its associated triggering signal, the gating information recorded in the listmode of SPECT acquisitions. Another objective of this section is to compare the triggering signals in the extrinsic respiratory signal and in the listmode.

A.3.1 Respiratory cycles duration variations

First, we studied the variability of the length of the respiratory cycles within each of the eight acquisitions considered. As the breathing rhythm was definitely not stable during the whole acquisition, the first question concerned

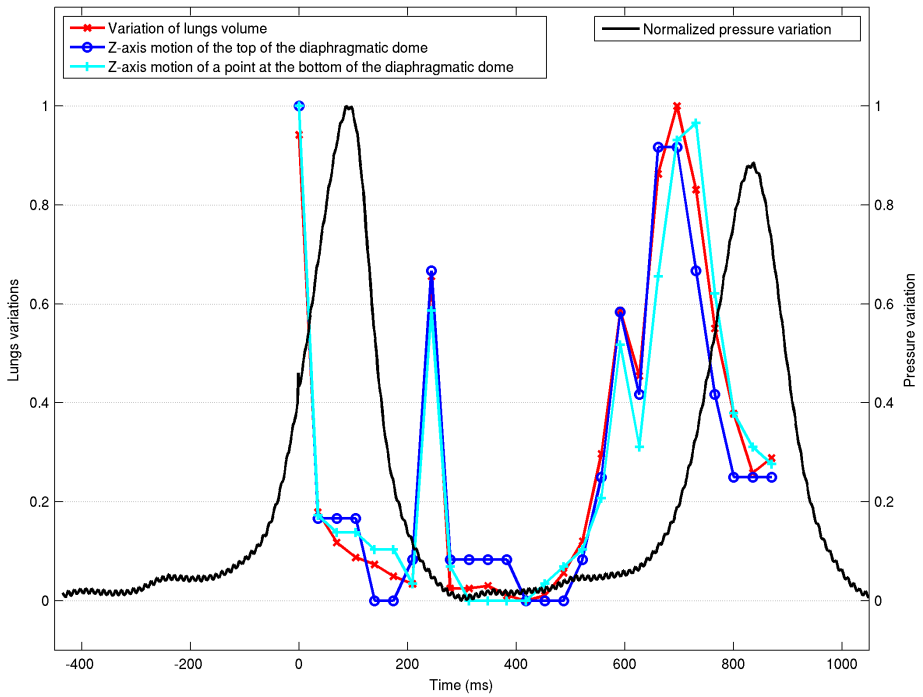

Figure A.17: **Comparison between the average pressure cycle (black curve) and intrinsic measures to 4D CT for acquisition #0340**: the lung volume variation (red curve with cross-shaped markers), the normalized z-axis motion of the top (dark blue curve with round-shaped markers) and the the normalized z-axis motion of base of the diaphragmatic dome (light blue curve with plus-shaped markers).

the distribution of the cycle length, and if this distribution was Gaussian or not.

We would like to suppress the data recorded during the outlier cycles (cycles that are much longer or shorter than the average) from the image reconstruction process. The reason for discarding these outlier cycles is that these much longer or shorter cycles suggest a default in the acquisition (missing data, bad detection of rising edge, ...). In addition, we would like to be able to estimate how much data will be discarded at the cycle selection step. If the distribution is Gaussian, we could fix the threshold at the same value (typically a multiple of the standard deviation) for all acquisitions. This threshold would have to be chosen in order to select only the cycles within a reasonable range and remove only the outlier cycles. Moreover, the number of discarded cycles could be estimated depending on the threshold that has been used.

Figure A.19 shows the variability in the distribution of cycle lengths for each acquisition together with the estimated Gaussian distribution law (es-

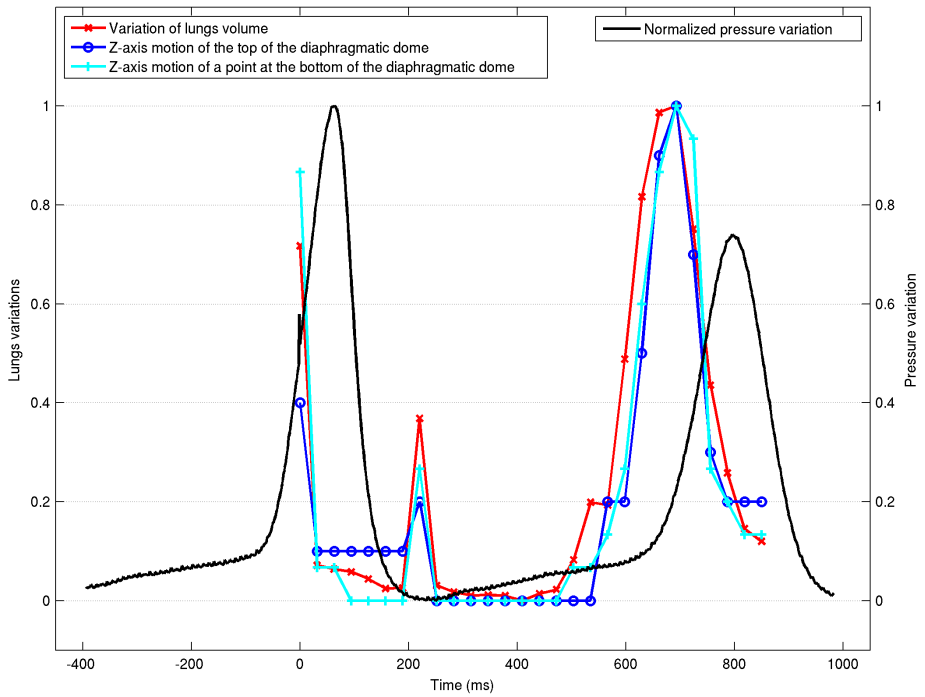

(a)

Figure A.18: **Comparison between the average pressure cycle (black curve) and intrinsic measures to 4D CT for acquisition #0375**: the lung volume variation (red curve with cross-shaped markers), the normalized z-axis motion of the top (dark blue curve with round-shaped markers) and the the normalized z-axis motion of base of the diaphragmatic dome (light blue curve with plus-shaped markers).

timated with three different methods). Some of the acquisitions present two modes in the distribution, meaning that the cycle lengths did vary during the acquisition around two different average lengths as we can see in Figure A.19(a), Figure A.19(b), and Figure A.19(c). For one acquisition in particular (Figure A.19(f)), the distribution of cycle length was particularly narrowed around the average. Concerning the other acquisitions, the distribution follows more or less a Gaussian distribution. Though the first estimate (red curves in figures) include the distributions more or less nicely. Additionally to this visual observation, the cycle length distributions were also numerically tested for their similarity with a Gaussian distribution. None of the acquisitions succeed at this test. The test consists in checking different criteria such as:

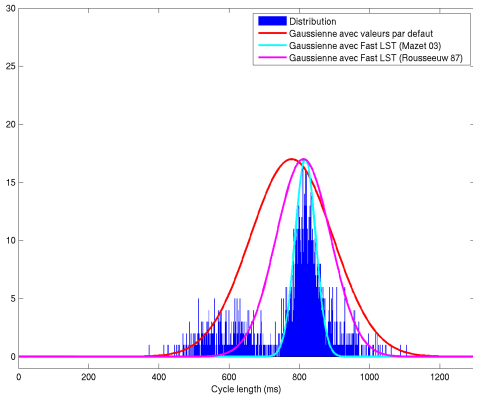

(a) Acquisition 0182

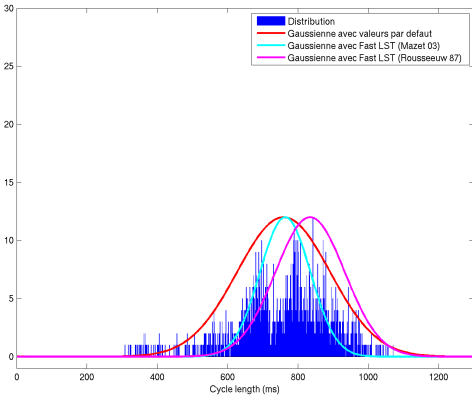

(b) Acquisition 0183

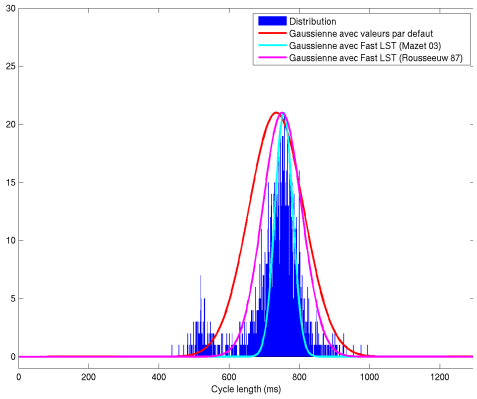

(c) Acquisition 0185

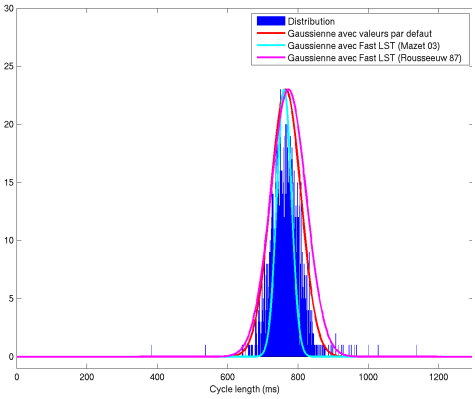

(d) Acquisition 0186

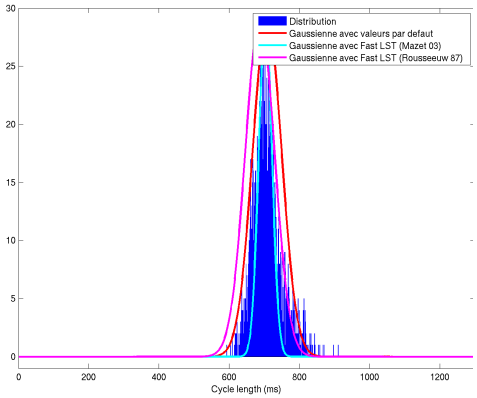

(e) Acquisition 0187

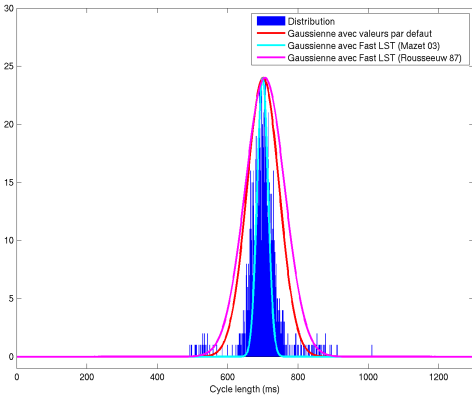

(f) Acquisition 0189

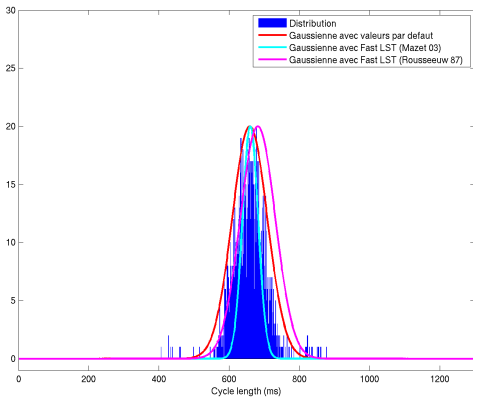

(g) Acquisition 0190

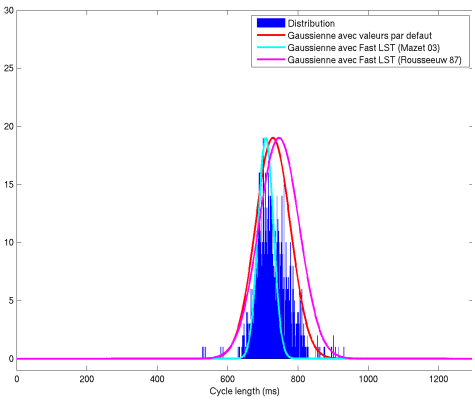

(h) Acquisition 0191

Figure A.19: Histogram of pressure cycle lengths (blue) with three Gaussian approximates: default (red), with Fast LST Mazet-method (light blue), with Fast LST Rousseeuw method (pink).

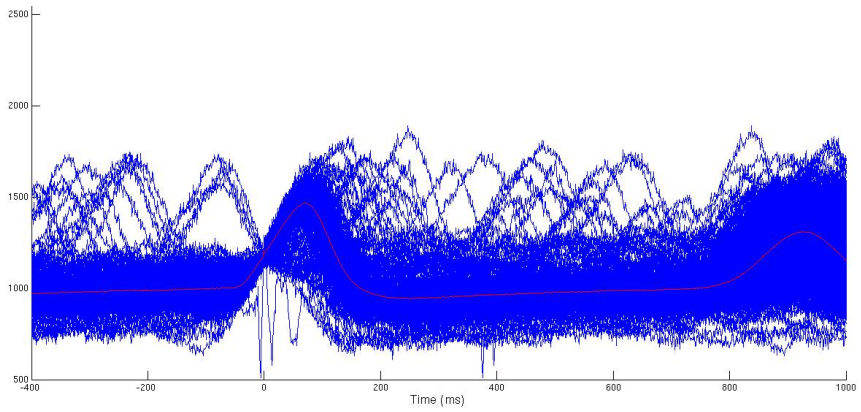

(a) All pressure cycles

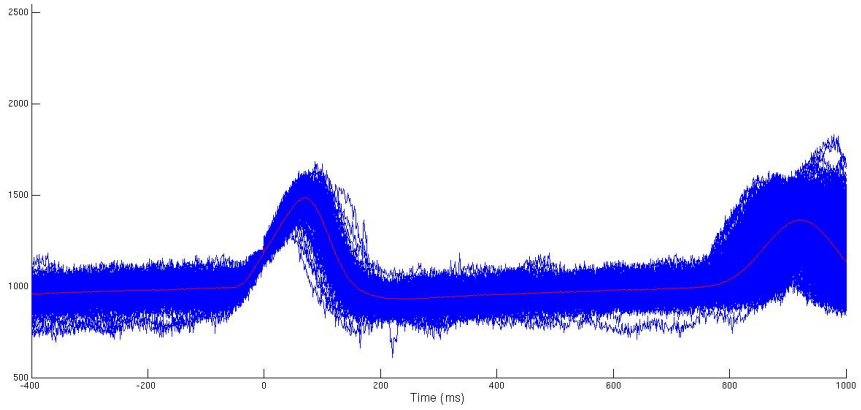

(b) Pressure cycles after rejection of outlier cycles: $[\mu - 3 * \sigma; \mu + 3 * \sigma]$

Figure A.20: Superposition of all pressure signal cycles (blue) from a signal acquired simultaneously to a SPECT acquisition (mouse #033). It shows the variability of amplitude and length of cycles. Cycles have been aligned according to the rising edge detection. The average pressure cycle appears in light red.

- 68% of the cycles should have a length range in the interval $[\mu-\sigma; \mu+\sigma]$ [1];
- 95% of the cycles should have a length range in the interval $[\mu - 2 * \sigma; \mu + 2 * \sigma]$;
- 99% of the cycles should have a length range in the interval $[\mu - 3 * \sigma; \mu + 3 * \sigma]$;

[1] μ refers to the average cycle length, σ refers to the standard deviation of length distribution

- the skewness: that is the symmetry of the distribution with respect to the average length;
- the kurtosis: that is the flattening of the distribution.

The visual examination of the figures already suggested that the cycle length distributions are not Gaussian although some of them look relatively close. The additional test described above confirmed that none of the acquisition could be safely approximated by a Gaussian distribution.

As our objective here is to discard the outlier cycles, i.e. the cycles that are longer or shorter than a given length range, we decided to perform a selection cycle step on the respiratory signal according to a cycle length. One needed to define the cycle length window that preserve the majority of the cycles. As we observed, according to the width of the length window, the ratio of remaining cycles after the selection outliers cannot be described by a general law. However, for all acquisitions, the length window $[\mu - 3 * \sigma; \mu + 3 * \sigma]$ includes most relevant cycles. Thus, this window has been used to initialise the cycle selection step of the reconstruction process.

Another observation can be done from Figure A.19. We wanted to find a law that describes nicely the distribution of cycle lengths, but actually, if the mice are breathing at the same rhythm at all times, the distribution should be an impulse function at a specific cycle length. On the contrary, the cycle lengths vary. In the previous paragraph, we suggested to perform a cycle selection step. However, the selected range ($\pm 3 * \sigma$) still leads to a relatively high variability. This can be explained visually with the observation of the respiratory signal. Each cycle is distinguished from the previous and next one by trigger indices. This trigger is recorded simultaneously in the respiratory signal and in the listmode. All the respiratory cycles can be superimposed on one figure per acquisition by aligning them according to the trigger indices at the beginning of cycles. Figure A.20 presents the superposition of all cycles before and after the cycle selection for one acquisition of the mouse #033. These figures show the variability of both cycle duration and amplitude. When all cycles (around 1400) are added, the resulting signal is very noisy due to cycles heterogeneity (Figure A.20(a)). After outlier cycles rejection, the resulting signal becomes much (Figure A.20(b)) To summarise, the benefit of the cycle selection step is illustrated by the fact that respiratory cycles vary similarly in the same window of amplitude. All breathing phases are positioned around the same instant at the beginning of the cycle with respect to the trigger.

A second improvement that is suggested by this variability is that all cycles should be resampled to the average cycle length. This cycle resampling step will increase the chance for a temporal window to correspond to the same phase in each cycle. We assume that the length of each respiratory cycle

phase is proportional to the cycle length. Resampling will then be an indirect manner to work with relative temporal window. However, the reconstruction system does not allow for the definition of temporal window proportional to the cycle length. The system only accepts absolute temporal window. As a consequence, a certain number of events are misused (see Table 4.2). These misused events justify a resampling step. In other words, cycle length resampling should be applied in order to assign each event to the right phase. This will guarantee that an equivalent number of event is used for the reconstruction of each frame of the 4D image. Indeed, if resampling is applied, then the instant corresponding to the beginning of the cycle plus N milliseconds will belong to the same phase in every cycle. On the contrary, in a non-resampled signal, the beginning of the cycle plus N milliseconds could be for example in the first half of a longer cycle and in the second half of a shorter cycle.

After this resampling step, we will notice a slight variability in the amplitude of the cycles. Indeed the variability in amplitude shown in Figure A.20(b) is unchanged when resampling relatively to cycle length. The triggers have been determined from an absolute threshold that has been fixed for the whole acquisition. It is not adapted to the amplitude variation. Consequently, each trigger does not correspond roughly to the same phase of the cycle; fixing the trigger at 20% of the amplitude variation between top and bottom amplitude of the cycle, if it was possible, would have given a more accurate result. In other words, we could have worked with a relative amplitude threshold. Unfortunately, setting a relative trigger is not possible with our system. Since both record (respiratory signal and listmode) are synchronised thanks to the common triggers, an additional improvement could be considered: the a posteriori redefinition of the rising edge detection threshold on the respiratory signal. Instead of a fixed value that is identical for all cycles, the threshold would be adapted to each cycle. This threshold would be a relative position on the excursion of pressure between inhalation and exhalation. Once redefined, a new triggering signal could be regenerated and modified in both respiratory signal record and listmode. However,the influence of the adjustment of the trigger according to the amplitude variability is quite low since the trigger will be shifted from only a few ms only. Considering the changes required to modify the triggering method and the low impact this aspect should have on the quality of the results, we kept the fixed trigger method for delimiting cycles.

A.3.2 Discrepancy between triggering signals

In this section, we investigate the discrepancy between the two triggering signals that are recorded during each acquisition. Triggering signals are simultaneously recorded in the respiratory signal and in the listmode. Even though, the acquisition of the two signals is done independently, we assume

Table A.1: Discrepancy between respiratory and listmode triggering signals with two different minimisation criteria: Least square minimisation on the cycle length difference, Minimisation of the number of outlier cycle (absolute difference between cycle length has to be greater than 1 ms).

Acquisition number	Number of shifted cycles at the beginning of respiratory signal after signal registration after two minimisation methods:		Number of cycles with difference between cycle length (respiratory signal - listmode) equal to:			
	LS minimisation	Outlier minimisation	-1	0	1	$\|diff\| > 1ms$
182	370	370	569	870	0	0
183	316	316	548	874	0	1
186	6	6	593	936	0	0
187	0	0	639	1138	0	2
189	498	498	446	810	0	0
190	57	57	485	970	0	3
191	337	337	427	723	0	3
1839	39	44	412	856	1	125
1839 (truncated)	*44*	*44*	*385*	*785*	*0*	*17*
1840	28	28	444	801	0	24
1841	28	28	398	847	2	160
1841 (truncated)	*28*	*28*	*378*	*804*	*0*	*18*
1842	48	48	447	658	0	19

that the two triggering signals are identical during the same temporal window. Indeed, the respiratory signal record usually starts short before, and finishes short after the listmode, thus the beginning of the listmode triggering signal should be slightly shifted with respect to the respiratory signal one and entirely included into it.

As we saw in the previous section, the cycles were not all of the same length before resampling. The sequence of cycle lengths in one acquisition can be seen as a pattern. This pattern is assumed to be identical in the two triggering signals. This pattern is used here to find the shift in cycle number (*cycle shift*) that registers the two triggering signals.

A first approach is based on the assumption that each cycle has the same length in both triggering signals. We naively expected that if we try all possible cycle shifts, there will be one for which each cycle fits the length of a cycle in the other. However none of the shifts succeeded in finding a null differ-

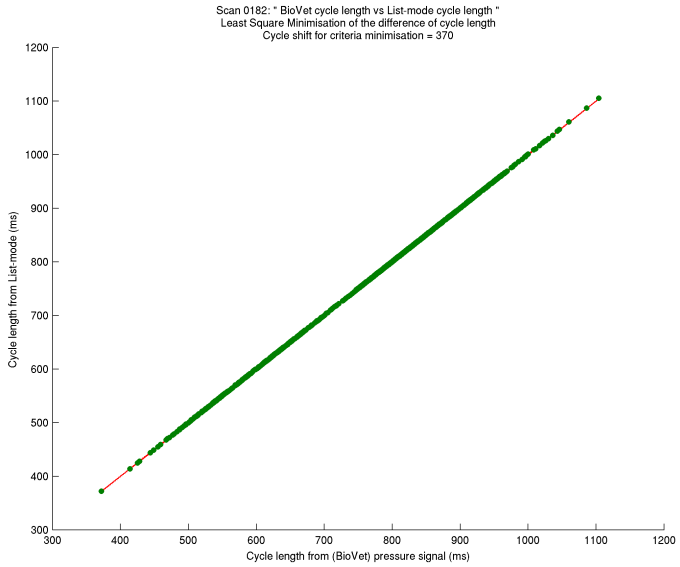

(a) Comparison of cycle length of matching cycles. Cycle shift has been determined with LS minimisation

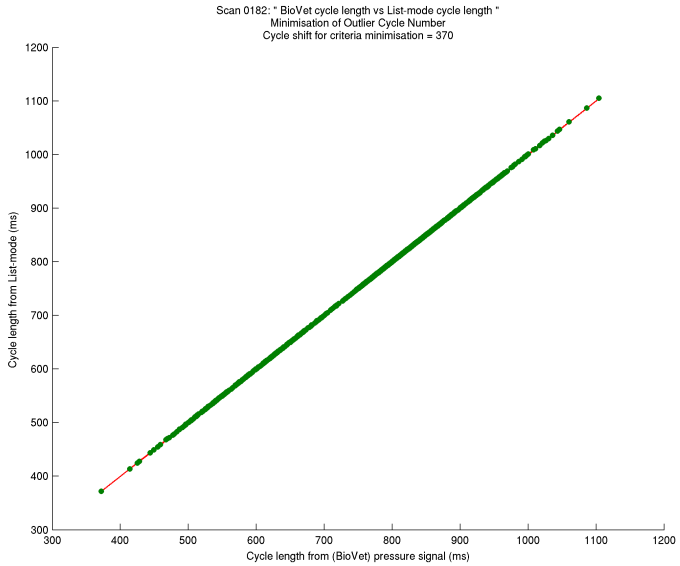

(b) Comparison of cycle length of matching cycles. Cycle shift has been determined with outlier minimisation

Figure A.21: Comparison between cycle lengths of triggering signals embedded in the respiratory signal and the listmode after cycle shifting, for acquisition #0182.

ence for all the cycles at the same time. The assumption that corresponding

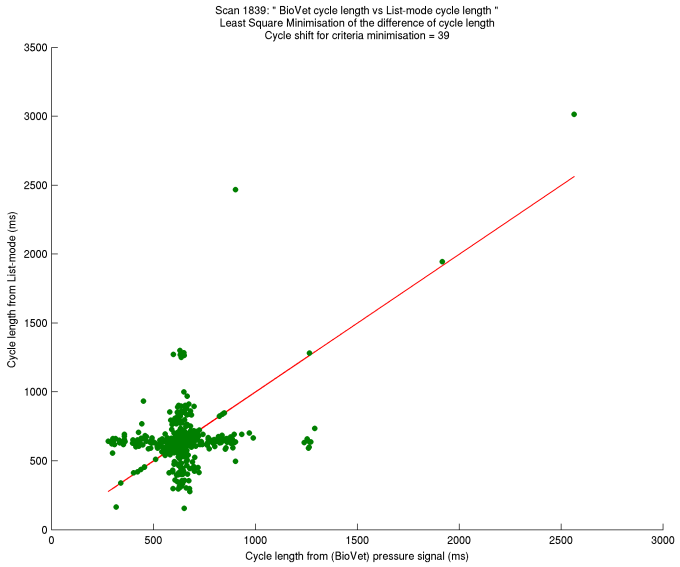

(a) Comparison of cycle length of matching cycles. Cycle shift has been determined with LS minimisation

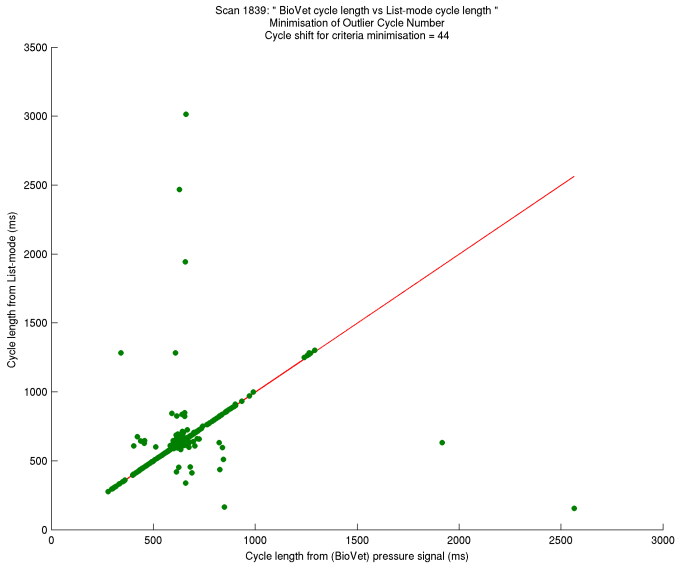

(b) Comparison of cycle length of matching cycles. Cycle shift has been determined with outlier minimisation

Figure A.22: Comparison between cycle lengths of triggering signals embedded in the respiratory signal and the listmode after cycle shifting, for acquisition #1839.

triggering signals are identical modulo a cycle shift is not true.

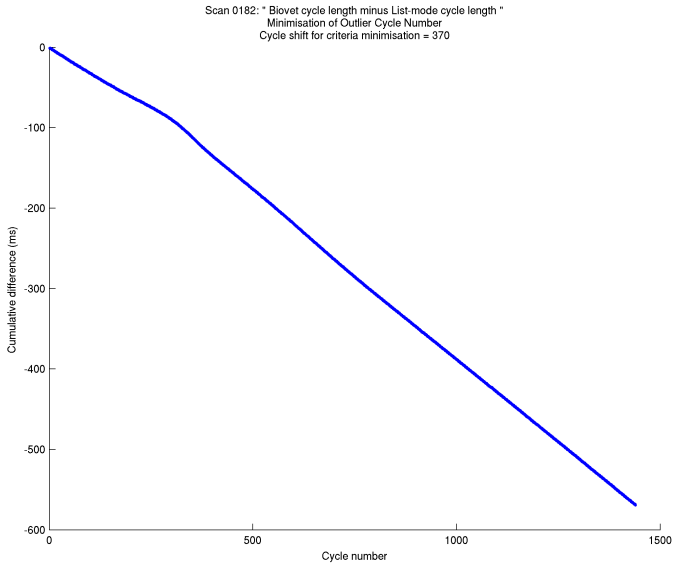

(a) Cumulative difference on cycle length between the two signals after cycle shifting

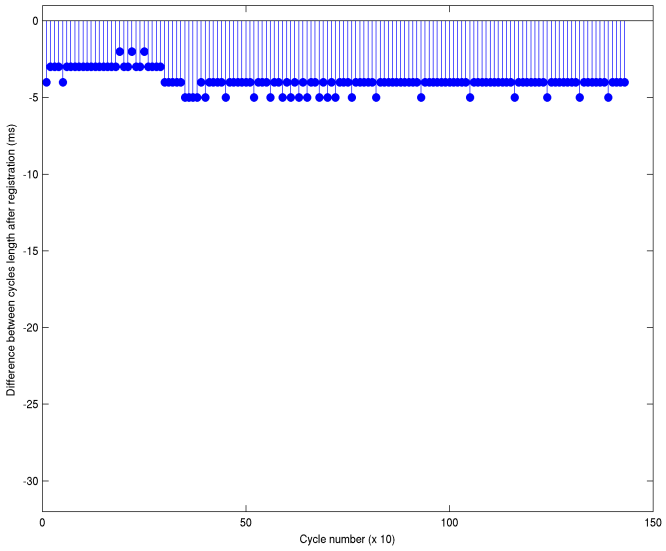

(b) Number of millisecond of difference between respiratory signal and listmode per 10 cycles after cycle shifting.

Figure A.23: Difference between cycle lengths after registration with outlier minimisation method of the triggering signals, for two acquisitions 0182

A second approach is based on the assumption that there is a cycle shift which minimise the difference of cycle length between the two signals. This

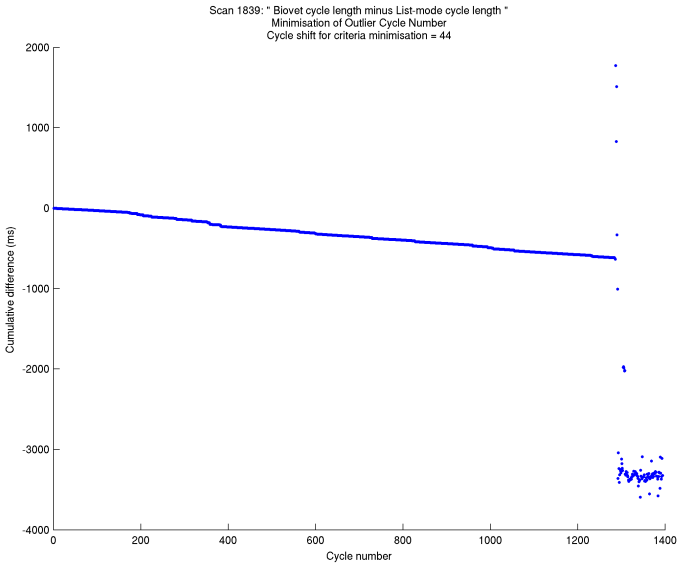

(a) Cumulative difference on cycle length between the two signals after cycle shifting

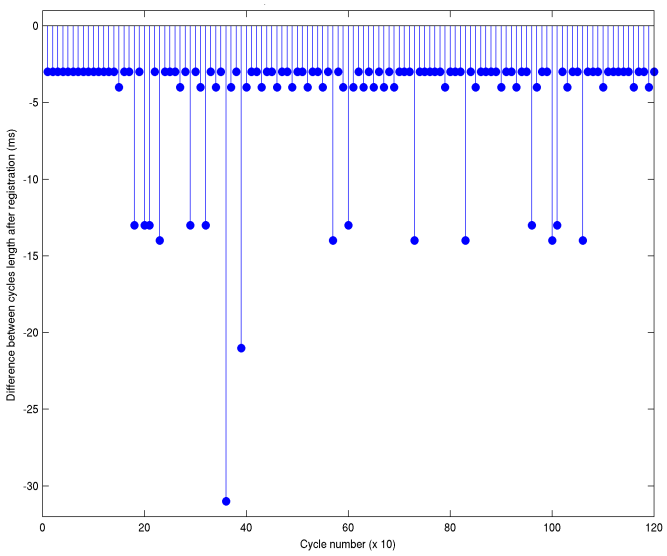

(b) Number of millisecond of difference between respiratory signal and listmode per 10 cycles after registration. Listmode triggering signal has been truncated after the 1200th cycle.

Figure A.24: Difference between cycle lengths after registration with outlier minimisation method of the triggering signals, for two acquisitions 1839

approach uses the least square method on the cycle lengths to determine the

cycle shift between the two triggering signals. This method permits to take into account small changes in some of the cycles: if cycles have the same length in average, they would realign nicely, with a low cumulative difference. The cycle shifts for the set of data between respiratory signal and listmode triggering signals are presented in Table A.1. We checked the correspondance between triggering signals by comparing pairwise the cycle lengths in the listmode with respect to the ones in the respiratory signal triggering signal (see Figure A.21(a) and Figure A.22(a)). The shift seems to be correct for some acquisitions (e.g. acquisition 182). However for the acquisition 1839, there are a lot of cycles with a large difference of length when trying to align one signal relatively to the other one(see the line highlighted in red).

We thus assumed that for some cycles the difference of length is so large that the least square minimisation failed. A new assumption is done which considered that most cycles have a 1 ms-difference in length but it might happen that few "outlier" cycles have a larger difference in length for unknown reasons. A third approach was tested based on the minimisation of the number of cycles that have a length difference greater than 1 ms in absolute value (see the third column of Table A.1). Cycle shifts identical to the second approach have been found for all acquisitions except for the acquisition 1839. A new shift was determined. Figure A.21(b) and Figure A.22(b) show the pairwise comparison of cycle length for the same two acquisitions, with the new shifts. For acquisition 1839, most cycle lengths now match. The cumulative pairwise difference (respiratory signal - listmode) for both acquisitions 0182 and 1839 is additionally presented in Figure A.23(a) and Figure A.24(a). This difference is decreasing over the cycles for both acquisitions. It suggests that a lot of cycles from the respiratory signal are missing some milliseconds. In total, this represents around 600 missing milliseconds for the acquisition 0182 and around 3500 missing milliseconds for the acquisition 1839. The two graphics show a cumulative difference between the cycle length (respiratory signal minus listmode) that reaches up to around two cycle lengths over the whole acquisition. The slope of the left hand figure suggests that the cumulative difference is more or less linear. However, the graphic for acquisition 1839 shows a high variation of this cumulative difference at the end of acquisition, after around 1300 cycles. Something strange happened during the record of either the respiratory motion or the listmode. This is why we also applied the method on a truncated signal of both acquisition 1839 and 1841, which leaded us to better results. As the cumulative difference seemed to be linear, we expected that the loss of milliseconds was regular. Figure A.23(b) and Figure A.24(b) show the sum of pairwise difference per sample of 10 cycles. Instead of remaining identical, the number of missing milliseconds randomly varies around 3 or 4 per 10 cycles, with some exceptions. For the acquisition 1839, we also observed the number of missing milliseconds but only on the first 1200 cycles (before the abnormal variations). This number also randomly

varies around 3 or 4 ms per 10 cycles and up to 31 ms of difference for one sample of 10 cycles. These observations can be completed by additional measures presented in the forth column of Table A.1. On the right column, the numbers of cycles that have a difference of -1 ms, 0 ms, 1 ms, and an absolute difference greater than 1 ms are given. For all the acquisitions, around 4 ms are lost every 10 cycles; this ratio seems to be relatively uniform. However according to Figure A.23(b) and Figure A.24(b), it is definitely not possible to find a law that will predict the frequency of missing instants in the respiratory signal.

These observations suggest that the respiratory signal record might be failing. It cannot be used easily to give additional information about the cycles (amplitude variation associated with respiratory phase). As a consequence, it has been decided to give importance only to the information that is directly provided by the listmode in terms of cycle length. Though the listmode does not contain directly the respiratory signal, a respiratory motion information can be extracted intrinsically from the data, before or after image reconstruction. In our case, we chose to extract an intrinsic respiratory signal from the 4D image, after reconstruction.

A.4 Performance at each step of the method for motionless 3D SPECT reconstruction

In this section, we will comment in more details the benefits of the proposed method with respect to the statistics at each step of its elaboration. This section complements the global results shown in Chapter 4 by giving the improvements provided in each intermediate phase, and by showing more results that justify the adequacy of our method.

A.4.1 Improvements with respect to the statistics on quantitative measurements

In this section, we present the improvement on quantitative measurements done on the images after the different reconstruction schemes. The measurements (noise, SUV_{peak}, SUV_{mean}, volume and SNR) are defined in Section 4.2.7. These results are presented in Table A.2, that complements Table 4.3 in Chapter 4. The comparison between G4D and NG3D was already done in Chapter 4. The differences on measurements of noise, standardized uptake values (SUVs), volume, and SNR were a consequence of the use of either a part or all the data. As only a fraction of all the data is used for each phase of the G4D image, the noise was increased by around 210% with respect to NG3D image. On the other hand, each phase represents only a fifteenth

Table A.2: Quantitative results on 76 lesions observed in eight subjects, for non gated 3D (NG3D), gated 4D, gated 4D after cycle selection (G4DS), gated 4D after cycle selection and resampling (G4DSR), and gated motionless 3D (G3DSR = BH3D) reconstruction methods: SUV_{peak}, SUV_{mean}, lesion volume (threshold at 40% of the SUV_{max} value), noise estimation in homogeneous liver area and signal-to-noise ratio (SNR). This table is a complement to Table 4.3. The information presented on the previous table is kept for the ease of comparison. The new information is written in **bold**. Values are presented as mean ± SD.

Parameters	NG3D	G4D [a] (15 phases)	G4DS [a]	G4DSR [a] (15 phases)	BH3D
Noise[b]	0.15± 0.04	0.47± 0.14	**0.48± 0.14**	**0.49± 0.14**	0.18± 0.05
SUV_{peak}	7.26± 5.32	8.18± 5.56	**8.22± 5.57**	**8.39± 5.66**	7.87± 5.47
SUV_{mean}	6.90± 5.26	8.63± 6.00	**8.72± 6.05**	**8.89± 6.09**	7.80± 5.65
Volume (mm^3)	2.14± 1.29	1.60± 0.87	**1.58± 0.87**	**1.53± 0.79**	1.79± 1.02
signal-to-noise ratio (SNR) (SUV_{mean}/Noise)	48.85±40.02	19.81±14.98	**19.60±13.77**	**19.50±13.36**	45.61±35.86

[a] G4D values are the average values of end-of-exhalation images corresponding to the motionless phases - i.e. 9 or 10 phases (respectively four) in the case of G4D with 15 phases (respectively 6 phases).

[b] Noise measure refers to the SD in a homogeneous liver area.

of the respiratory cycle. It means that it is short enough to be considered as without motion. Each phase was then reconstructed from counts that came from non moving regions for each temporal window. G4D images are characterised by an increase in SUV and a decrease on the volume of lesions. Indeed, the SUV_{peak} increased by 13%, the SUV_{mean} increased by 25%, while the volume was reduced by 25% with respect to NG3D image. The volume is the size of lesion defined at 40% of the maximum SUV. As a consequence of the large increase in noise and smaller increase in SUV in G4D, the SNR also decreased by 60% with respect to NG3D image.

Second, G4D images after cycle selection (G4DS) have a slightly higher level of noise than in G4D images: noise increased by 2% in comparison to G4D and G4DS. This is comprehensible since around 2% of data were discarded. The SUV measurements slightly increased comparing to G4D: SUV_{peak} by 0.4% and SUV_{mean} increased by 1%. The lesion volumes slightly decreased by 1.25%, with respect to G4D images.

Then, we perform a G4D reconstruction after cycle selection and resampling (G4DSR); we compare this G4DSR image to G4D and G4DS images. The measurements of SUVs and lesion volume were improved: SUV_{peak} and SUV_{mean} were both increased by 2% with respect to G4DS image, and were increased by respectively 2.5% and 3% with respect to G4D image. The lesion volumes were decreased by around 3% with respect to G4DS image and by around 4% with respect to G4D image. These results are assessing the improvements of image accuracy as expected since the cycle resampling step of the listmode aimed at re-affecting the counts to their corresponding phase of the dynamic image. However, the noise increased again by around 2% comparing to G4DS image, that makes a 4% increase with respect to G4D and a 226% increase with respect to NG3D. The SNR also decreased by 0.5% comparing to G4DS, that makes a 1.5% decrease with respect to G4D and a 60% decrease with respect to NG3D.

As a result the quantitative accuracy of the images was improved by the successive modifications of listmode (cycle selection and resampling) with respect to the lesions of interest. This suggests that each phase of the dynamic images were free of motion artifacts. However, the image quality was affected by the fact that less data were used for each phase image.

The modifications on the cycles (selection resampling) slightly improved the accuracy. Additional work is necessary to improve the quality with respect to the dynamic images. The idea is then to distinguish the phases in motion from the motionless phases intrinsically to the dynamic images. According to the results with respect to the image accuracy,to extract the intrisic motion signal, we use the G4DSR images rather than the G4D or the G4DS images. Working on the G4DSR images increases the chance of determining the consecutive phases that best correspond to the motionless phase of the respiratory signal. Finally, the motionless images are simply a gated images

reconstructed from data in the motionless phase according to the intrinsic motion signal. Motionless phase was determined during the study of intrinsic intensity variation along the time in region of interests (ROIs) of G4DSR images. It corresponds to two third of the respiratory cycle (around 10 phases over 15). These 10 phases were the one with the less variation in intensity with respect to time. Motionless images are also denoted as breath-hold like 3D image (BH3D). In quantitative terms, the BH3D images have a better quality than G4DSR images with both a lower level of noise (63% decrease with respect to G4DSR) and a higher SNR (134% increase with respect to G4DSR). BH3D images also have a better accuracy than NG3D image since BH3D images exhibit a 8% increase of the SUV_{peak}, a 13% increase of the SUV_{mean}, and a 16% decrease of the lesion volumes. Therefore, the improvement when compared to NG3D and G4D is mainly due to the motion correction with a minimal impact of cycle selection.

A.4.2 Sensibility of the image-based motion detection method with respect to noise

The test of sensibility to noise was described in Section 4.3.3 of Chapter 4. Figure A.25 presents the set of images which was tested for the motion detection method. Figure A.25(a) presents the original image that is a subimage of a G4DSR centered on one lesion. It is the image of the first phase of the dynamic image. The whole 4D subimage was considered for this test. The equivalent SNR in the lesion is 25. This lesion was chosen since it was located under the diaphragm and animated by the respiratory motion. This image was used as a basis to generate synthetic dynamic images of a moving lesion. Figure A.25(b) is the binary image obtained after thresholding the original image. This image has no noise thus the SNR is equivalent to infinity. Then, six noisy images were generated from the binary image with different level of additional Gaussian noise. The noise level was defined as the standard deviation (σ) of the Gaussian distribution: 256, 327, 422, 552, 731 and 979. Visually the noisy lesion starts to be hard to distinguish with a noise equal to 422, that corresponds to a SNR around 2.4.

Figure A.26 presents the results of the motion detection method on each synthetic image in comparison to the original image. They are presented as graphics that show the number of votes received per phase. The more vote received by a phase means the more this phase is susceptible to correspond to the motion phase. The method is considered as working as long as it is possible to distinguish a group of consecutive phases that received more votes than the others. From the observation of the graphics, it is confirmed that the motion detection method works well for both the original image (with SNR equal to 25) and the synthetic image without noise: the same phases received the more votes. The results on the images with SNR equal to 3.98 and 3.12

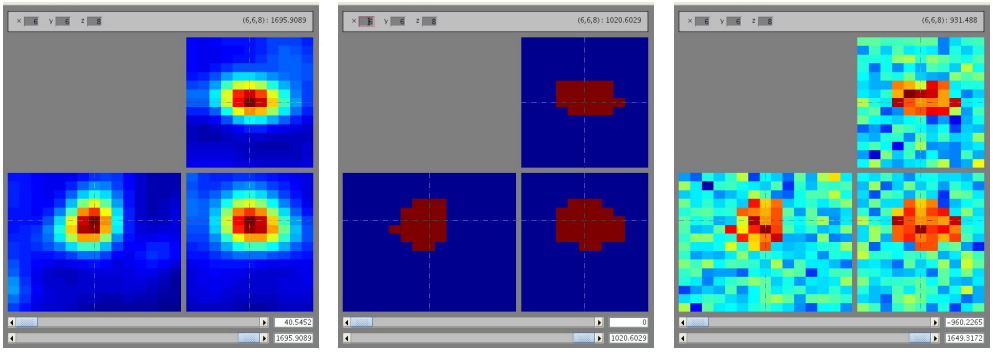

(a) SNR = 25 (b) SNR = ∞ (c) SNR = 3.98

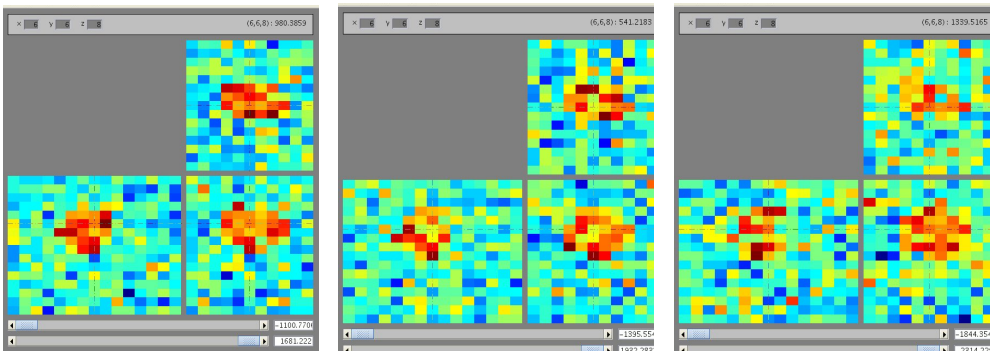

(d) SNR = 3.12 (e) SNR = 2.42 (f) SNR = 1.85

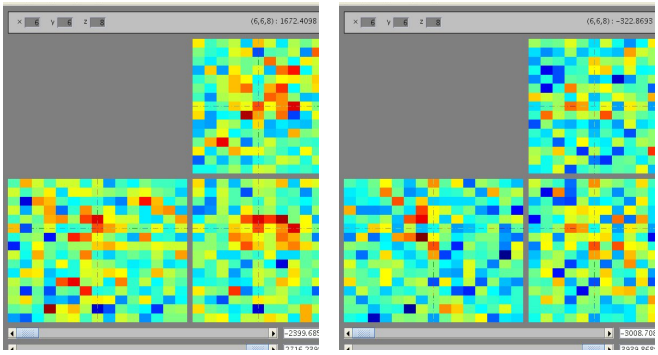

(g) SNR = 1.40 (h) SNR = 1.04

Figure A.25: Results of the sensibility to noise test. The figures present the first phase image of the lesion reference 4D image (a), the binary image after thresholding (b), and the set of synthetic image with increasing white Gaussian noise: σ=256 (c), 327 (d), 422 (e), 552 (f), 731 (g), 979 (h). The lesion is present along the three plane: the coronal plane (upper right), the sagittal plane (lower left) and the transverse plane (lower right).

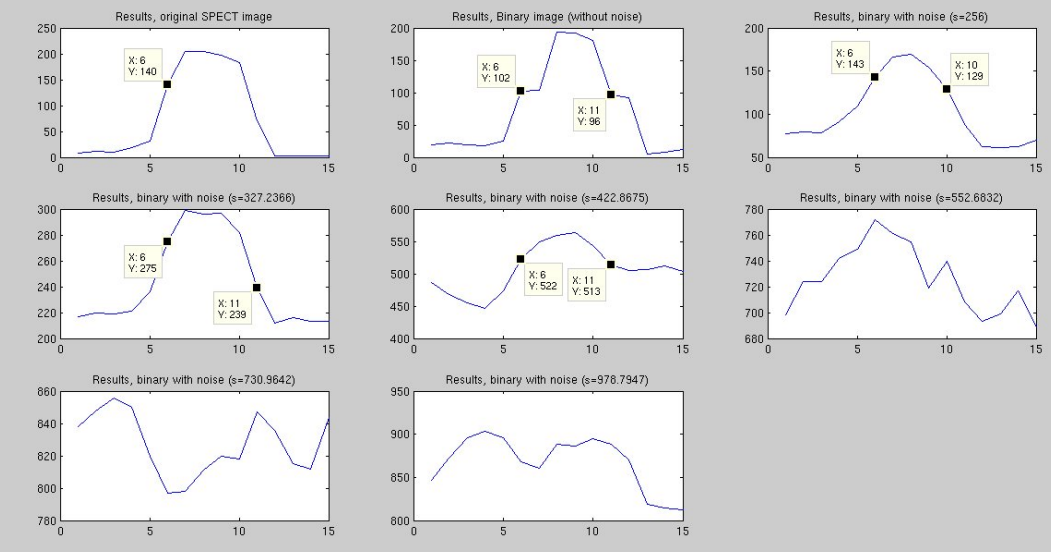

Figure A.26: Resulting graphics of votes from the motion detection method on the different images presented in Figure A.25: from top to bottom, first row: original, synthetic images without noise, with noise = 256; second row: synthetic image with noise = 327, noise = 422, noise = 553; third row: synthetic image with noise = 731, and with noise = 979.

were also coherent. However, the graphical result for the image with a SNR equal to 2.42 exhibits that the phases that have been detected as in motion received slightly more votes than the others. Though this is not sufficient for the automatic thresholding step to correctly distinguish the moving phases from the motionless phases. The graphical results on images with a lower SNR show that it is clearly not possible anymore to detect the motion phases with this method. It is not surprising since the lesion was barely visible on the images themselves and the method is based on the intensity variation of voxels along the time. A lower SNR means that the signal is drown in the noise and it makes it more difficult or impossible to distinguish the lesion from the background.

As a conclusion, the image-based motion detection method works on lesions with a minimal SNR of 3. Then, for images with SNR below, it will require additional constraints on the resulting histogram of votes to be able to automatically determine the motionless phases from the moving phases. The method is then appropriate for images as the ones we used in Chapter 4 since the average SNR in the lesions is around 20, and greater than the limit of 3.

A.4.3 Sensibility of the detection method to the edge detection

In this section, we discuss the motion detection method performance with respect to the choice of detecting rising edge instead of falling edge on the pressure variation during the acquisition. Figure A.27, Figure A.28, Figure A.29 and Figure A.30 present the results of the motion detection method on four different acquisitions. The difference between them is that the gating signal has been triggered either on the falling edge or on the rising edge, with or without an additional temporal delay. This additional delay is shifting the gating index in order to synchronise data in the middle of the motionless phase. A motion detection histogram was superimposed to the average respiratory cycle. Figures show that in any case, the phases that received the more votes were the same, with respect to the peak of respiratory motion. We should mentioned the fact that for the case of rising edge detection with a delay (see Figure A.30), the average respiratory cycle is slightly more noisy than for the other methods. This is due a higher variability of the breathing rhythm during this acquisition featured a higher variability. This result strengthen the wide application to this method. In practice, the rising edge detection of the motion, without delay, was chosen by default for the acquisition protocol. However, this choice does not affect the result of the motion detection method. Any other parameters could have been chosen.

A.5 Conclusion

In this appendix, we presented additional results, which both explain the reasons that leaded us to the method presented in Chapter 4, and show that this method is effective.

The first analyses we conducted leaded us to the conclusion that it is very difficult to obtain acquisitions with stable breathing either in frequency or in amplitude. Consequently our method must be able to deal with such highly variable breathing rhythms and amplitude.

Second, we observed that the movement recorded by the pressure balloon was indeed representing the respiratory motion of the mouse. However, we also observed a temporal shift between the balloon observations and the lesion movement in the images; this temporal shift is dependent on the position of the lesion and we were unable to find a systematic law for predicting the temporal shift. Overall, these observations make the detection of motionless phases more difficult because they imply that it is impossible to predict the characteristics of the breathing movement, neither for the movement observed by the pressure sensor, nor for the movement of the observed lesions when the pressure sensor movement is known. Consequently, it is necessary to design a

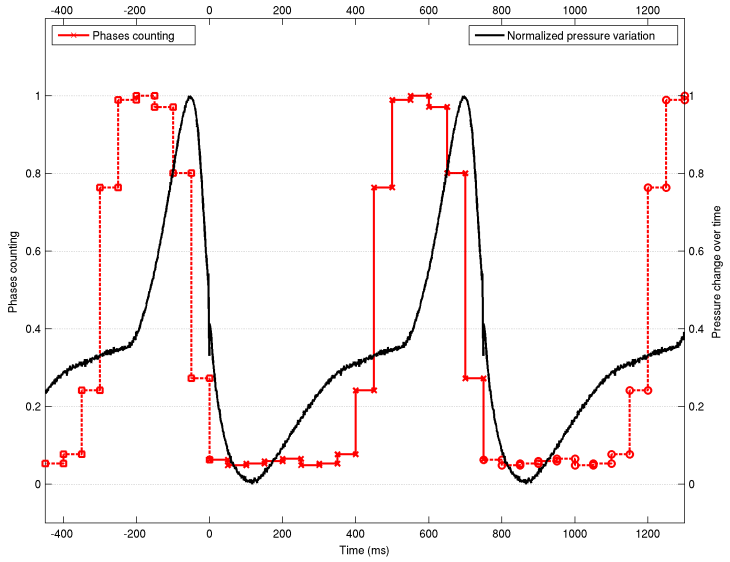

Figure A.27: Comparison between the average pressure cycle and motion detection (detailed method in Chapter 4 Section 4.2). The comparison was conducted on an acquisitions with gating on rising edge.

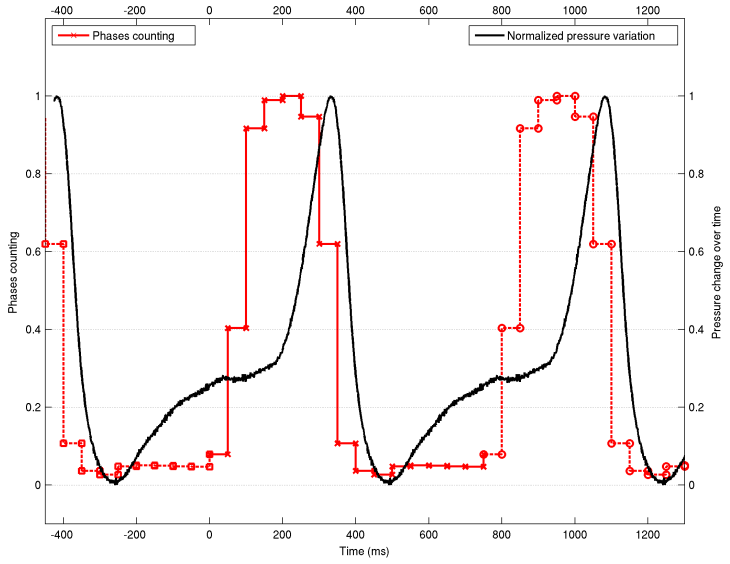

Figure A.28: Comparison between the average pressure cycle and motion detection (detailed method in Chapter 4 Section 4.2). The comparison was conducted on an acquisitions with gating on rising edge with a delay.

new method for detecting motionless phases only from the information contained in the listmode, and tolerating a high variability in the respiratory

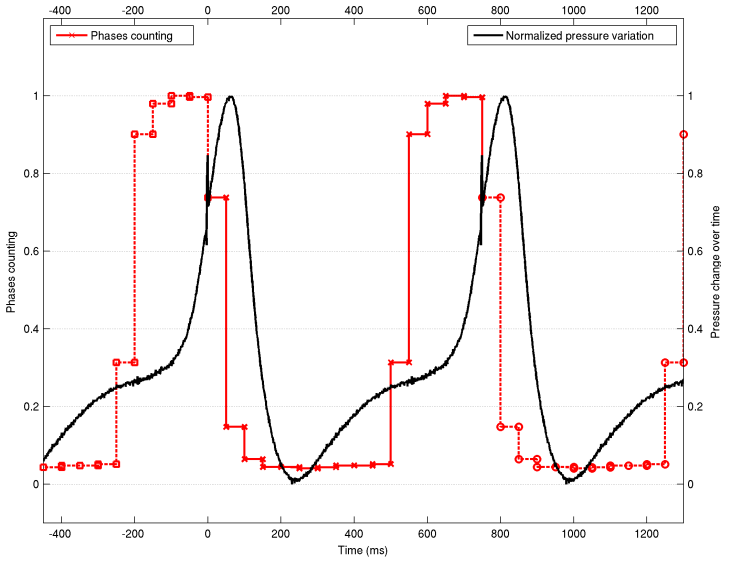

Figure A.29: Comparison between the average pressure cycle and motion detection (detailed method in Chapter 4 Section 4.2). The comparison was conducted on an acquisitions with gating on rising edge.

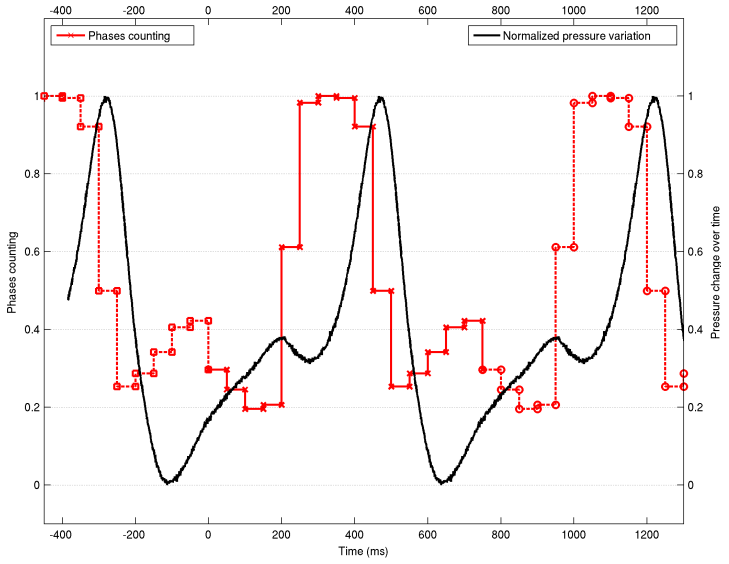

Figure A.30: Comparison between the average pressure cycle and motion detection (detailed method in Chapter 4 Section 4.2). The comparison was conducted on an acquisitions with gating on rising edge and with a delay.

rhythm. We also realised that there was no perfect match between the respiratory signal and the gating information stored in the listmode, which leaded

us to rely only on the information intrinsically available in the listmode.

Finally, this appendix also provides additional arguments to show the efficiency of our method, and to justify the different steps we designed for the reconstruction of a motionless 3D SPECT image. We showed that the lost events for the G4D reconstruction were coming from outlier cycles that were impairing the reconstruction because they were introducing a wrong count of events; some events being counted several times, and some other omitted. We also have shown in more details that our reconstruction methodology provides a much more reliable compromise between SNR and accuracy of the results that the existing classical methods (G4D and NG3D). We concluded this appendix by a short study on the sensitivity to noise; this study has shown that our algorithm is relatively reliable and that it is appropriate to use it for the kind of images provided by our camera.

Appendix B

Compartmental modelling

The work presented in Chapter 6 relies on compartmental analysis. Compartmental analysis can be used for a wide range of applications. It is a frequent approach used in pharmacology, biology and medicine for studying dynamic biodistribution of compounds since it is quite simple to use and to understand. In this section, we provide first a description of the bases of compartment analysis (for additional information please refer to [God83, Jac96]. The idea is to define all the elements required to build an appropriate and simple model for our problem.

B.1 Definitions

Some expression for compartmental analysis can be ambiguous, so we remind their definitions here. A *compartmental system* is a physiological or biochemical finite set of microscopic subunits located in an environment.

The *substance* is the studied material. Several substances can be studied simultaneously especially in pharmacology were substances react and yield to others.

The *compartment* is a macroscopic subunit of homogeneous and well-mixed substance. This means that in emission tomography (ET), the radioactivity concentration of the tracers is the same in the whole compartment (no gradient) or that the substance in this compartment is submitted to the same reaction or transformation function.

In ET, each *subunit* distinguishes from the others by different kinetic for the same substance. The interactions are characterised by the substance transfer or transport, or by substance transformation (between subunits or with the environment).

The *space* denotes the physical place where substances release or dilute. A compartment does not always match with a specific closed space. Several compartments can be physically mixed. When a compartmental model stud-

ies only one substance, each compartment refers to a different space; and the interactions between compartments are flow of substance. When two substances or more are studied, two compartments can overlap and occupy the same physical space. In that case, the interactions between compartments are transformations from a substance to another.

The *interactions* between compartments are described by ordinary differential equations (ODEs). The resolution of the ODEs will give the functions that describe the quantity or concentration of each substance in each compartment.

To summarise, the compartmental modelling implies the definition of the set of compartments based on physiological and anatomical information, and the determination and the resolution of ODEs.

B.2 Principles

The definition of a model requires a certain number of steps. First, we need to define the compartmental system by its elements and under some assumptions.

B.2.1 System definition

- State variable, $\mathbf{x}_i$, with $i \in 1..n$, and n the number of compartments,
- System inputs, $\mathbf{u}_i$ = external input on compartment i,
- System outputs, $\mathbf{y}$ = observation of compartment(s),
- Unknown parameters, parameters characterising the transfer functions between the different compartments, but also with the system inputs and outputs, they are represented by three matrices $\mathbf{A}$, $\mathbf{B}$, $\mathbf{C}$.

More precisely, each element k_{ij} of the matrix $\mathbf{A}$ represents the speed at which the substance transits from compartment j to compartment i. Similarly, each element b_{ij} of the matrix $\mathbf{B}$ represents the speed at which the substance transits from input j to compartment i. Overall, the derivative[1] of the concentration of the substance x in compartment i depends on the substance x_i in compartment i that flows to other compartments j with a factor k_{ji}, on the substance x_j in each compartment j that flows to compartment i with a factor k_{ij}, and of the input u_q that injects substance into the compartment i with a factor b_{iq}, more formally:

$$\dot{x_i} = \sum k_{ji} x_i + \sum k_{ij} x_j + \sum b_{iq} u_q$$

[1] We denote by $\dot{f}$ the derivative of f with respect to time.

The matrix $\mathbf{C}$ represents the relation between the system output functions y (e.g. observations) of each compartment i of the system and the substance concentration x in the different compartment. This represents the fact that the activity measures that are done on each compartment represent a fraction of the activity or a mix of the several compartment activity that is effectively there. Here, we consider that $\mathbf{C}$ is the identity matrix, more formally:

$$y_i = \sum c_{ij} x_j$$

All these elements can be summarised and represented analytically.

$$\mathbf{x} = \begin{bmatrix} x_1 \\ x_2 \\ \dots \\ x_n \end{bmatrix}, \ \mathbf{u} = \begin{bmatrix} u_1 \\ u_2 \\ \dots \\ u_n \end{bmatrix}, \ \mathbf{y} = \begin{bmatrix} y_1 \\ y_2 \\ \dots \\ y_n \end{bmatrix}, \ \dot{\mathbf{x}} = \mathbf{Ax} + \mathbf{Bu}, \ \mathbf{y} = \mathbf{Cx}$$

B.2.2 Assumptions

The assumptions are essential in compartmental analysis since they will yield to simplification of both the system and the resolution of the ODE. Those assumptions are:

- the transfer functions between any two compartments are constants, denoted $= k_{ji}$ (or $k_{j \leftarrow i}$) from compartment i to compartment j. This assumption is very frequent in a first time modelling; it is called the temporal invariance.
- the transfer equations between compartments are ODEs, which are linear and of first order.
- The system outputs are the state variables, in other words, we can observe the concentration of ^{99m}Tc-pertechnetate in each compartment, and use these observation as system outputs.

B.2.3 Resolution of the inverse problem

The inverse problem [BÅ70, RW71] consists in determining the transfer constants, k_{ji}, from the observations ($\mathbf{u}$ and $\mathbf{y}$). The transfer constants are the speed of transfer, transport or reaction between two compartments.

The resolution of ODEs usually yields to sum of two exponential functions if the input function of the system is an impulse. If the system is solved analytically, then we obtain a sum of exponential functions parameterised by the constants of the system. Thus, if we approximate the observations by multiexponential functions, this will allow us to deduce the value of the

constants. In [Fos70], authors made these assumptions. They show that it is possible to determine the transfer coefficients by approximating the discrete observations with sums of exponential functions.

The inverse problem can be solved analytically or numerically.

B.3 Example of a two-compartment system

For the sake of understanding the principles of compartmental analysis, we study below the case of a catenary two-compartment system. We assume that there is only one impulse input on compartment 1. The objective of this direct problem is to determine analytically $x_1(t)$ and $x_2(t)$, $t \geq 0$ for the system represented in Figure B.1.

We detail below the different steps and equations of such a study in this simple case. Indeed, we will see in Section 6.2 that the compartment model of the stomach can be modelled by a two-compartment system, with transfer functions. However in the case of the stomach, the input of the system will be more complex.

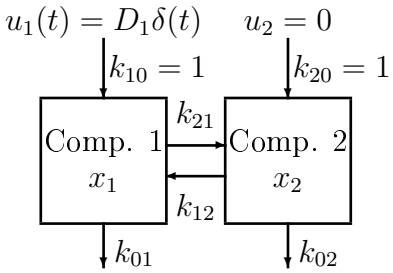

Figure B.1: Compartmental system representation of linear and time-invariant two-compartment system, with impulse input on compartment 1.

Here, we consider that (C) is the identity matrix. The system can be described by the following equations:

$$\begin{cases} \dot{x_1} &= -(k_{21}+k_{01})x_1 &+ k_{12}x_2 &+ u_1 \\ \dot{x_2} &= k_{21}x_1 &- (k_{12}+k_{02})x_2 & \\ y_1 &= x_1 & & \\ y_2 &= x_2 & & \end{cases} \tag{B.1}$$

Laplace transformation gives:

$$\begin{cases} \dot{\mathbf{x}} &= \mathbf{Ax}+\mathbf{Bu} &\xrightarrow{\mathcal{L}} & s\cdot\mathbf{X}(s) &= \mathbf{AX}(s)+\mathbf{BU}(s) \\ \mathbf{y} &= \mathbf{x} &\xrightarrow{\mathcal{L}} & \mathbf{Y}(s) &= (s\mathbf{I}-\mathbf{A})^{-1}\mathbf{BU}(s) \end{cases} \tag{B.2}$$

where the different matrices refer to:

$$\mathbf{X}(s) = \begin{bmatrix} X_1(s) \\ X_2(s) \end{bmatrix}, \ \mathbf{Y}(s) = \begin{bmatrix} Y_1(s) \\ Y_2(s) \end{bmatrix}, \ \mathbf{U}(s) = \begin{bmatrix} U_1(s) \\ U_2(s) \end{bmatrix} = \begin{bmatrix} D_1 \\ 0 \end{bmatrix} \tag{B.3}$$

$$\mathbf{A} = \begin{bmatrix} -(k_{21} + k_{01}) & k_{12} \\ k_{21} & -(k_{12} + k_{02}) \end{bmatrix} \tag{B.4}$$

In this case, we assume that:

$$\mathbf{B} = \begin{bmatrix} 1 & 0 \\ 0 & 1 \end{bmatrix} = \mathbf{I} \tag{B.5}$$

The observation matrix $\mathbf{Y}(s)$ can be also expressed as:

$$\mathbf{Y}(s) = \mathbf{G}(s)\mathbf{U}(s) \tag{B.6}$$

Since both $\mathbf{B}$ is assumed to be identity, we have:

$$\begin{aligned} \mathbf{G}(s) &= (s\mathbf{I} - \mathbf{A})^{-1}\mathbf{B} = (s\mathbf{I} - \mathbf{A})^{-1} \\ &= \begin{bmatrix} s + (k_{21} + k_{01}) & -k_{12} \\ -k_{21} & s + (k_{12} + k_{02}) \end{bmatrix}^{-1} \\ &= \tfrac{1}{\Delta(s)} \begin{bmatrix} s + (k_{12} + k_{02}) & k_{12} \\ k_{21} & s + (k_{21} + k_{01}) \end{bmatrix} \end{aligned} \tag{B.7}$$

$$\begin{aligned} \Delta(s) &= |s\mathbf{I} - \mathbf{A}| \\ &= \begin{vmatrix} s + (k_{21} + k_{01}) & -k_{12} \\ -k_{21} & s + (k_{12} + k_{02}) \end{vmatrix} \\ &= s^2 + (k_{21} + k_{01} + k_{12} + k_{02})s + (k_{21} + k_{01})(k_{12} + k_{02}) - k_{21}k_{12} \end{aligned} \tag{B.8}$$

It is possible to factorise the determinant $\Delta(s)$ as $(s-\lambda_1)(s-\lambda_2)$ where $\lambda_1\,\lambda_2$ are defined by:

$$\begin{aligned} \lambda_1, \lambda_2 &= \tfrac{1}{2}\Big(-(k_{21} + k_{01} + k_{12} + k_{02}) \\ &\qquad \pm\sqrt{(k_{21} + k_{01} + k_{12} + k_{02})^2 - 4(k_{21}k_{02} + k_{01}k_{12} + k_{01}k_{02})}\Big) \end{aligned} \tag{B.9}$$

At last, general expression for $\mathbf{G}(s)$ and $\mathbf{Y}(s)$ are given:

$$\mathbf{G}(s) = \begin{bmatrix} \frac{s+(k_{12}+k_{02})}{(s-\lambda_1)(s-\lambda_2)} & \frac{k_{12}}{(s-\lambda_1)(s-\lambda_2)} \\ \frac{k_{21}}{(s-\lambda_1)(s-\lambda_2)} & \frac{s+(k_{21}+k_{01})}{(s-\lambda_1)(s-\lambda_2)} \end{bmatrix} \tag{B.10}$$

$$\begin{aligned}
\mathbf{Y}(s) &= \mathbf{G}(s)\mathbf{U}(s) \\
&= \begin{bmatrix} \frac{(s+(k_{12}+k_{02}))}{(s-\lambda_1)(s-\lambda_2)} D_1 \\ \frac{k_{21}}{(s-\lambda_1)(s-\lambda_2)} D_1 \end{bmatrix} \\
&= \begin{bmatrix} D_1(\frac{\lambda_1+(k_{12}+k_{02})}{\lambda_1-\lambda_2}\frac{1}{s-\lambda_1} + \frac{\lambda_2+(k_{12}+k_{02})}{\lambda_2-\lambda_1}\frac{1}{s-\lambda_2}) \\ \frac{k_{21}D_1}{\lambda_1-\lambda_2}(\frac{1}{s-\lambda_1} - \frac{1}{(s-\lambda_2)}) \end{bmatrix}
\end{aligned} \tag{B.11}$$

Finally, it is possible to obtain back the output temporal functions $y_1(t)$ and $y_2(t)$ with the inverse Laplace ($\mathcal{L}^{-1}$).

$$\begin{cases}
y_1(t) &= D_1(\frac{\lambda_1+(k_{12}+k_{02})}{\lambda_1-\lambda_2}e^{\lambda_1 t} + \frac{\lambda_2+(k_{12}+k_{02})}{\lambda_2-\lambda_1}e^{\lambda_2 t}) \\
y_2(t) &= \frac{k_{21}D_1}{\lambda_1-\lambda_2}(e^{\lambda_1 t} - e^{\lambda_2 t})
\end{cases} \tag{B.12}$$

These equations give us the behaviour of the system made of two compartments and shown in Figure B.1 with an impulse input on the compartment 1.

To illustrate those equations, let us consider one example where the input function and constants are defined by:

$$\begin{cases}
u_1(t) &= 10\,\delta(t) \\
u_2(t) &= 0 \\
k_{10} &= 1 = k_{20} = k_{01} = k_{02} = k_{12} = k_{21}
\end{cases} \tag{B.13}$$

By replacing the known parameters in the equations, the eigen values and output functions can be easily deduced:

$$\begin{cases}
\{\lambda_1, \lambda_2\} &= \{-3, -1\} \\
y_1(t) &= 5(e^{-t} + e^{-3t}) \\
y_2(t) &= 5(e^{-t} - e^{-3t})
\end{cases} \tag{B.14}$$

Figure B.2 presents the different functions (inputs and outputs) for this example.

B.4 Related works: application of compartmental analysis to ET imaging

We review briefly below the application of compartmental analysis to determine the kinetic of a substance, based on ET imaging. Compartmental analysis has been used in the context of tomography, especially for its applications to pharmacology, biology or medicine.

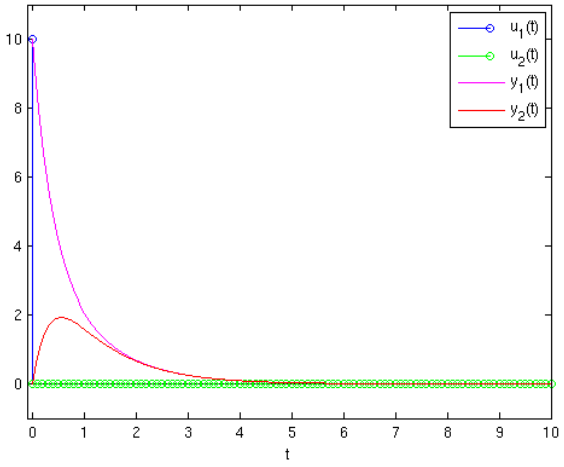

Figure B.2: Representation of input and output functions of the system with respect to the time: u_1 is an impulse, and y_1 and y_2 are the *output* functions. The output functions, also called *observations*, describe the substance variation in each compartment.

The analytic resolution has been frequently detailed in the literature according to the new imaging advances [BSW62, RW71, RD04, WIK+06, CK09].

Numerical resolution have been also done in order to study compound biodistribution and kinetic in different organs such as the thyroid, the brain or the heart. These studies aim at understanding or revealing physiological behaviour.

B.4.1 Thyroid

Among other organs, the thyroid has been subject to modelling studies for more than 50 years. The approaches for the study are mainly based on compartmental analysis, and the model has been updated in parallel to imaging advances. In [Hay78], thyroidal pertechnetate uptake was modeled with a simple three compartment model. The parameters of this model were obtained by using measurements of ^{99m}Tc-pertechnetate activity in the thyroid, in the surrounding neck (background) and in the blood. The input function of the system was obtained by approximating the blood radioactivity with a multiexponential function. Later a much more detailed and complex model was proposed in [DCH+08] where the compartments are not only spaces that contains inorganic iodide (such as blood, follicle cells and colloid), but also other organs that contains organic iodide. It also takes into account the dynamics of all biochemical that contribute or interact to iodide reactions. In [FGV+10], authors assessed the ^{99m}Tc-pertechnetate biodistribution in the whole body of mouse by planar SPECT imaging. Although, they do not propose a model.

B.4.2 Heart

Compartment analysis has been frequently used for the study of dynamic SPECT imaging of the heart [RGH98, HRZG98, RGH00, KG01, RGH02,

ZGK10, NYK12]. In particular, in [GRS+10], authors reviews all the bases for compartmental analysis applied on dynamic SPECT and their cardiac applications.

B.4.3 Brain

Some work have been also done using compartmental analysis on brain positron emission tomography (PET) imaging for application such as dynamic PET registration [JST+12] or the grading of brain tumours [NSG+13].

Appendix C

Pre-clinical image convention

Such as human radiological convention, there is a specific vertebrate radiological convention. This convention specifies anatomical directional terms and positioning convention. In general, the right and left sides are inverted that is the "real" left of the animal appears on the right of the image and the reverse. The axis going from head to tale is named "Craniocaudal axis", the axis going from left to right with respect to the spine is named "Left-right axis", and the axis going from spinal column to abdomen is named "Dorsoventral axis". Figure C.1 illustrated the orientation convention for vertebrates with a CT image of mouse chest.

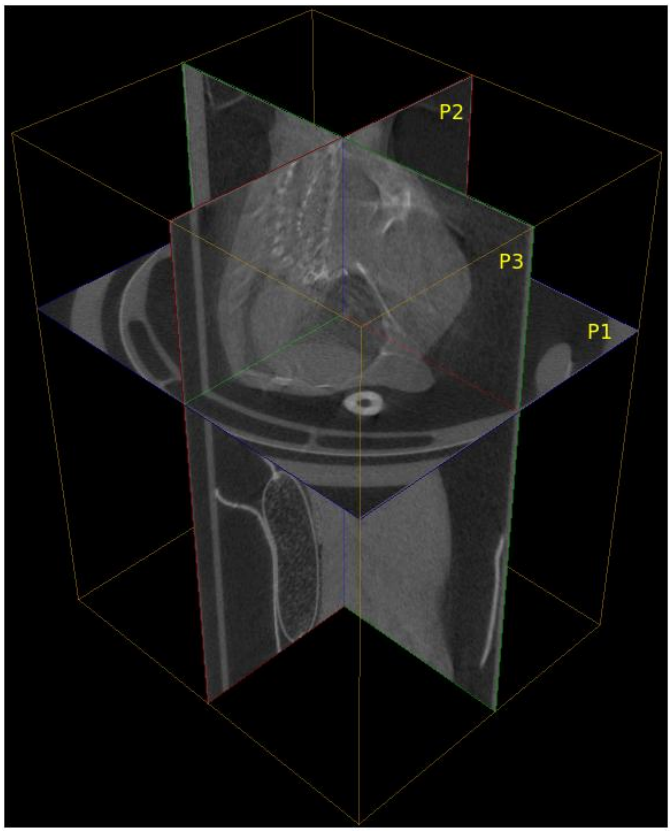

(a)

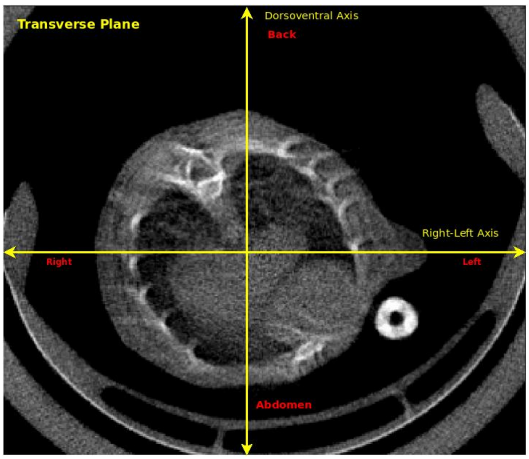

(b)

Figure C.1: 3D CT image of mouse chest (a), where P1 is the transverse plane (Figure C.1(b)), P2 is the sagittal plane (Figure C.2(a)) and P3 is the coronal plane (Figure C.2(b)).

(a)

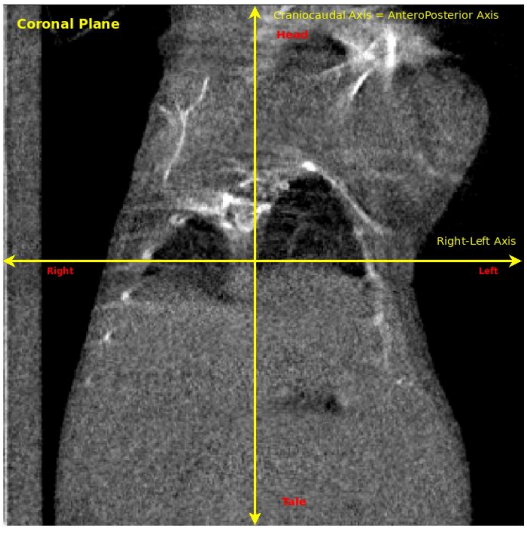

(b)

Figure C.2: Sagittal (a) and coronal (b) planes

Appendix D

CT acquisition sequences

Sequence	Fast Soft Tissue	Cardiac	Fast Scan
Imaging	CT120	CT120	CT120
Modality	Continuous	Gated	Continuous
Scanner technic	Short (180 °)	Short (180 °)	Short (180 °)
Angle view number/Sequence	220	220	220
Projections/angle	1	1/phase	1
Tube voltage (kV)	70,00	80,00	70,00
Tube current (mA)	50,00	32,00	32,00
Shooting time/angle (ms)	32	16	16
Total shooting time (ms)	7 040	3 520	3 520
Sensor sampling	2x2	4x4	4x4
Acquisition resolution (μm)	49,6	99,2	99,2
Reconstruction sampling for a 100 μm resolution	2x2	1x1	1x1
Average acquisition length for one field of view	2 min 30	~6 min/phase	1 min 27
Dose (mGy)	113	51	36
Noise (HU)	200	100	95
Gain	130	0	140
Offset	20	20	20

Sequence	InVitro High Resolution	InVivo Bone	Low Noise 50μm
Imaging	CT120	CT120	CT120
Modality	Step by step	Continuous	Step by step
Scanner technic	Full (360 °)	Full (360 °)	Full (360 °)
Angle view number/Sequence	1200	360	720
Projections/angle	1	1	2
Tube voltage (kV)	80,00	100,00	100,00
Tube current (mA)	32,00	50,00	50,00
Shooting time/angle (ms)	100 (125 ?)	20	20
Total shooting time (ms)	120 000	7 200	14 400
Sensor sampling	1x1	2x2	2x2
Acquisition resolution (μm)	24,8	49,6	49,6
Reconstruction sampling for a 100 μm resolution	4x4	2x2	2x2
Average acquisition length for one field of view	35 min	5 min	5 min (?)
Dose (mGy)	2400 (?)	250	
Noise (HU)	140 (?)	134	
Gain	25	25	25
Offset	20	20	20

Sequence	Soft Tissue	Step and Shoot
Imaging	CT120	CT120
Modality	Step by step	Step by step
Scanner technic	Short (180 °)	Full(360 °)
Angle view number/Sequence	220	360
Projections/angle	1	1
Tube voltage (kV)	80,00	80,00
Tube current (mA)	32,00	35,00
Shooting time/angle (ms)	16	100
Total shooting time (ms)	3 520	36 000
Sensor sampling	4x4	1x1
Acquisition resolution (μm)	99,2	24,8
Reconstruction sampling for a 100 μm resolution	1x1	4x4
Average acquisition length for one field of view	6 min	13 min (?)
Dose (mGy)	52	
Noise (HU)	100	
Gain	0	150
Offset	20	20

Appendix E

Introduction - version française

Contents

E.1 Contexte et Motivations: Etudes longitudinales et applications à l'imagerie du petit animal

Le contexte de cette thèse est l'étude de phénomènes longitudinaux. Notre but est d'utiliser l'imagerie afin de comprendre l'évolution de processus biologiques. Notre objectif est de fournir des outils pour réaliser des études longitudinales de ces processus.

Afin de suivre un phénomène au cours du temps, nous avons besoin de recueillir suffisamment d'information aussi précise que possible. Sachant que notre objectif dans cette thèse est de fournir aux biologistes des outils permettant d'extraire autant d'informations que possible à partir des données d'imagerie à disposition. Les techniques de traitement de l'image fournissent déjà des solutions à des problèmes complexes. Notre approche consiste ici à élaborer des méthodes simples, basées sur quelques-unes de ces techniques de traitement d'images. Les méthodes développées dans cette thèse sont consacrées à la résolution de problèmes biologiques précis.

Le contexte de cette thèse est aussi une collaboration entre deux équipes de recherche: l'équipe ASCLEPIOS à INRIA focalise ses recherches sur l'analyse d'images biomédicales et la modélisation de systèmes physiologiques entre

autres, et l'équipe TIRO au Commissariat à l'Energie Atomique et aux énergies alternatives (CEA)/Université de Nice Sophia Antipolis (UNS)/Centre de Lutte contre le cancer Antoine Lacassagne (CAL) qui se concentre sur l'étude du métabolisme de l'iodure: la fonction thyroïdienne, la radiotoxicologie, l'imagerie de gène rapporteur et les traitements en oncologie. Cette collaboration s'est concrétisée par l'achat d'une caméra innovante dédiée à l'imagerie du petit animal dans le cadre du contrat de projet État-Région (CPER), dossier Telius proposé par INRIA et ses collaborateurs.

Par conséquent, les problèmes biologiques que nous abordons dans cette thèse sont liés au suivi in vivo de l'absorption d'iodure dans les cellules à la tomographie d'émission monophotonique (TEMP) du petit animal, et notamment de souris. Il est particulièrement intéressant de rappeler que l'imagerie est vraiment importante pour les études longitudinales puisque cela permet d'éviter le sacrifice de nombreux animaux qui serait nécessaire sans imagerie.

Pour résumer, l'impact direct de cette thèse est de fournir des outils de précision afin de caractériser les phénomènes longitudinaux étudiés et observés sur des souris grâce à l'imagerie. La plupart des problèmes que nous avons rencontrés sont liés au mouvement du petit animal anesthésié. L'obtention de mesures précises à partir d'images en présence de tels mouvements figure parmi les principaux défis abordés dans cette thèse.

Dans cette thèse, nous montrons comment traiter les problèmes évolutifs avec deux contributions:

- Une méthode qui s'intéresse à la question du mouvement respiratoire pour l'imagerie des tumeurs. Nous proposons une procédure de reconstruction d'images TEMP sans mouvement avec un bon rapport signal sur bruit (RSB).

- Une représentation de l'estomac tolérante à ses déformations et aux mouvements de l'animal afin de comprendre le phénomène de prise de iodure. Nous proposons un moyen de mesurer cette prise dans l'estomac avec une approche basée sur une décomposition en couches de l'estomac, qui est beaucoup plus tolérante à la contraction et à la relaxation de l'estomac qu'une approche classique basée sur le suivi d'information au niveau des voxels.

E.2 Matériel et expériences

La caméra pré-clinique utilisée dans cette thèse permet l'acquisition d'images TEMP 4D. Les quatre dimensions se rapportent aux trois dimensions spatiales, plus une quatrième dimension temporelle. Cette dimension temporelle est caractérisée par le fait que plusieurs acquisitions sont obtenues en série, à intervalles temporels réguliers (minutes, jours ou semaines). Les

images TEMP permettent d'observer l'évolution de phénomènes biologiques au travers de la biodistribution d'un produit radiopharmaceutique injecté au préalable.

Dans le cas d'un intervalle temporel à l'échelle journalière ou hebdomadaire, la TEMP est dédiée à l'étude des processus tels que la croissance de la tumeur. Par exemple, les sites de prise d'activité dans les tumeurs peuvent être localisés et quantifiés et, par extension, la croissance des tumeurs peut être estimée.

Dans le cas d'un intervalle temporel court à l'échelle de quelques minutes ou heures, la TEMP permet l'observation des variations de biodistribution radiopharmaceutiques après injection.

E.3 Mouvement respiratoire

Le premier défi relevé dans cette thèse est la reconstruction d'images TEMP à fort contraste et quantitativement fiables de tumeurs péritonéales de souris. Parmi les différents phénomènes physiques induisant des artefacts, le mouvement respiratoire est le plus important [HFGH08].

Le mouvement respiratoire peut affecter la reconstruction d'images de tomographie par émission de positons (TEP) ou TEMP, ce qui va dégrader les mesures quantitatives qui seront effectuées par la suite dans la région supérieure de l'abdomen. La reconstruction synchronisée sur la phase d'un signal respiratoire corrige le problème de mouvement, mais détériore le RSB et d'autres mesures de qualité basées sur l'intensité. Dans cette thèse, nous proposons une méthode pour la reconstruction d'images TEMP 3D qui ne soient pas altérées par le mouvement respiratoire et qui conservent un fort RSB.

L'impact attendu de ce travail est de proposer un procédé qui garantit la reconstruction d'images sans artefact de mouvement permettant de mesurer précisement et de comprendre la croissance de tumeur. L'objectif biologique ici est d'être en mesure de suivre, de modéliser et, idéalement, de prédire l'évolution des tumeurs, afin de les traiter de façon plus efficace.

E.4 Distribution dynamique d'iodure dans l'estomac

Le deuxième défi s'intègre à l'étude du métabolisme de l'iodure de l'estomac murin. L'idée est de comprendre le cycle gastrique de l'iodure. Le premier objectif est donc de segmenter automatiquement un organe en couches dans un ensemble d'images TEMP 3D successives, où l'organe est animée d'un mouvement aléatoire. Le second objectif est de modéliser la distribution dynamique

de l'iodure à l'aide de l'analyse compartimentale, où chaque compartiment représente une unité fonctionnelle à l'échelle cellulaire.

Afin de comprendre le rôle physiologique de l'iodure, nous avons d'abord étudiŕ le processus de l'absorption de l'iodure. Ensuite, nous élaborons un modèle de l'estomac en utilisant une analyse compartimentale. Notre contribution concernant ce phénomène se situe plus au niveau de l'étude de faisabilité et de la méthodologie qu'au niveau de la caractérisation exacte du processus. Nos résultats peuvent être résumés comme suit.

- Nous réalisons une décomposition régionale en couches de l'estomac afin d'être tolérant à sa contraction et sa relaxation, et au mouvement de l'animal.
- Nous élaborons un modèle compartimental du transport de l'iodure dans l'estomac.
- Nous définissons les coefficients de mélange qui nous permettent de calculer l'activité dans chaque compartiment à partir de l'activité mesurée dans chaque couche.
- Nous mettons en place une méthodologie combinant des étapes de résolution analytiques et numériques permettant la caractérisation complète du cycle de prise de iodure.
- Enfin, nous calculons les coefficients de transfert pour notre modèle compartimental. Ces coefficients sont les paramètres du modèle compartimental. Les résultats sont très satisfaisants pour une première étude.

E.5 Organisation du manuscrit

Ce manuscrit s'articule autour de deux parties montrant les deux contributions principales:

1. La première partie traite du mouvement respiratoire et de la reconstruction d'images TEMP du petit animal sans artefact de mouvement.
2. La deuxième partie décrit la modélisation de la biodistribution de l'iodure dans l'estomac murin.

Le chapitre 2 décrit les contextes biologique et technique de cette thèse. Il décrit aussi les contraintes inhérentes au matériel et aux modèles animaux.

La partie I se concentre sur le mouvement respiratoire et se compose de deux chapitres. Le chapitre 3 présente un état de l'art sur les méthodes de correction du mouvement respiratoire. Le chapitre 4 reprend in extenso

l'article [BMG+13] dans lequel nous proposons un procédé dédié à la reconstruction optimale sans artefact de mouvement d'images TEMP 3D.

La partie II porte sur la biodistribution d'iodure dans l'estomac murin et se compose de deux chapitres. Dans le chapitre 5, nous décrivons de manière qualitative la biodistribution du pertechnétate de technétium ^{99m}Tc, analogue de l'iodure, dans l'estomac, à partir de l'observation d'images TEMP 4D. Dans le chapitre 6, nous caractérisons le phénomène d'absorption de l'iodure à l'aide d'un modèle compartimental simplifié.

Enfin, le chapitre 7 conclut cette thèse avec la liste des contributions et présente différentes perspectives possibles pour ce travail. Une liste des publications est fournie page 141.

Les annexes les plus utiles de cette thèse sont les suivantes. L'annexe A donne des résultats supplémentaires à propos du procédé de reconstruction d'images TEMP 3D sans mouvement. L'annexe B décrit les principes de l'analyse compartimentale.

Appendix F

Conclusion - version française

Contents

Dans cette thèse, nous abordons l'étude des phénomènes longitudinaux avec application à l'imagerie TEMP du petit animal à petite animaux imagerie. Parmi le large éventail de phénomènes qui peuvent être étudiés, nous nous concentrons sur deux sujets particuliers présentant des défis biologiques. Ceux-ci ont conduit à l'élaboration de méthodologies dédiées. Dans l'ensemble, plusieurs défis liés au travail avec l'imagerie animale ont été abordés.

Tout d'abord, l'élaboration d'un protocole d'acquisition biologique pertinent est une tâche exigeante qui nécessite beaucoup d'interactions avec tous les contributeurs (biologistes, informaticiens), et une bonne compréhension de toutes les variables qui influent sur le résultat en termes de biologie et d'imagerie. Pour cela, nous avons dû prendre en compte la variabilité biologique puisque les phénomènes biologiques étudiés ne sont pas bien connus. Par exemple, un nouveau modèle de tumeurs a été considéré pour lequel le protocole d'injection in vivo est toujours à l'essai (lignée cellulaire, lignée de souris, sensibilité à la dose de radioactivité ou à l'irradiation). Les sites d'injection et de fixation de la tumeur sont également très sensibles au changement, difficiles à prévoir. Cela engendre un ensemble de données avec beaucoup de variabilité. La mise en place d'acquisitions longitudinales a également requis de l'organisation afin d'estimer la vitesse et la durée de l'évolution du phénomène observé. En effet, l'étude des phénomènes longitudinaux signifie quantification et/ou modélisation du phénomène au cours du temps, et l'échelle de temps d'un nouveau phénomène peut être difficile à prédire.

Deuxièmement, les deux phénomènes qui sont étudiés ici sont observés dans la région abdominale, ce qui conduit à deux défis supplémentaires. Le premier est le manque d'imagerie qui devait servir de référence anatomique détaillée. En effet, une simple tomodensitométrie (TDM) n'offre pas un bon contraste dans les tissus mous. Et l'utilisation d'agent de contraste supplémentaire, sans interférence avec le protocole, n'est pas garanti. On pourrait envisager des approches telles que celle présentée dans [MBC+10]. Cette méthode réussit à extraire d'images TEMP de rongeurs, les courbes temps-activité (TAC), sans les informations anatomiques.

Le second phénomène, mais non le moindre, est le mouvement intrinsèque de la zone considérée. En effet, les sujets étaient des souris anesthésiées, donc qui respirent, et leur estomac et les organes environnants bougent. Dans ces deux études, nous avons donc dû prendre en compte le mouvement des organes.

F.1 Contributions

Les principales contributions étaient en termes de méthodologie. La première méthode traite la question de la reconstruction d'images TEMP sans artefacts de mouvement respiratoire. La deuxième méthode propose un modèle décrivant la cinétique de prise du pertechnétate de technétium ^{99m}Tc dans l'estomac murin.

Reconstruction d'images de micro-TEMP en quasi-apnée Afin d'éviter les artefacts de mouvement respiratoire dans les images TEMP, nous avons proposé une méthode qui sélectionne de manière rétrospective et maximise les données utilisées pour une reconstruction sans artefact de mouvement. Cela pourrait être considéré comme une acquisition en quasi-apnée ou synchronisée intelligemment sur la respiration. Cette méthode garantit un fort RSB tout en éliminant les artefacts de mouvement respiratoire. De plus, cette méthode est adaptée aux rythmes de respiration typique des souris sous anesthésie à l'isoflurane (respiration avec halètements). Les cycles respiratoires présentent une grande variabilité en termes d'amplitude et de longueur. Cette méthode est basée sur l'extraction d'information de manière intrinsèque. Elle est robuste à l'asynchronisme apparent entre le vrai mouvement observé dans les images et le signal respiratoire acquis extérieurement. La qualité et la précision des images reconstruites sont comparables à une reconstruction non synchronisée en termes de mesure de bruit et de RSB, et intermédiaires entre les reconstructions synchronisées et non synchronisées pour les mesures sur les lésions (SUV_{pic}, SUV_{moyen} et volume). Grâce à cette méthode, de nouvelles études plus complexes peuvent être envisagées avec l'imagerie micro-TEMP concernant par exemple d'autres organes ou modélisation de tumeurs dans la

région abdominale.

Cette contribution a conduit à l'élaboration d'une première version d'un logiciel mettant en oeuvre cette méthode. Ce logiciel avec interface graphique permet aux biologistes d'obtenir une reconstruction d'images TEMP en quasi apnée.

Etude de l'absorption du pertechnétate de technétium ^{99m}Tc dans l'estomac Afin d'aider les biologistes à mieux comprendre le processus d'absorption et la sécrétion de l'iodure dans l'estomac, nous proposons une méthode qui permet de construire un premier modèle compartimental décrivant le cycle de la prise de pertechnétate de technétium ^{99m}Tc, analogue du iodure, dans l'estomac murin. Ceci a conduit à la conception d'un modèle compartimental, avec une première estimation des coefficients de transfert entre les compartiments. La méthode repose sur une décomposition originale de l'estomac en couches qui nous permet d'obtenir une information anatomique pertinente de l'estomac, et qui compense l'absorption progressive du pertechnétate de technétium ^{99m}Tc et les irrégularités de forme de l'estomac. En outre, cette description en couches est robuste à la déformation générale de l'estomac. Néanmoins, plusieurs défis ont dû être résolus. Un premier défi concerne le processus de segmentation de l'estomac basée sur l'intensité a priori sans information anatomique. Cette étape de segmentation a échoué pour les images aux premiers instants (juste après injection d'activité) puisque le site d'injection, qui était dans le champ de vue de l'acquisition a été segmenté à la place de l'estomac. Un deuxième défi est que chaque couche ne correspond pas seulement à un compartiment. Chaque couche est un mélange de plusieurs compartiments, et même si chaque compartiment est supposé être homogène, une couche ne l'est pas. Nous avons donc considéré l'ensemble des couches comme un mélange de compartiments, chaque coefficient de mélange étant représentatif de la composition de chaque couche. Une première détermination de ces coefficients de mélange a été proposée. Cela a conduit à de très bons résultats au vu de la méthode utilisée pour les déterminer. Quelques autres défis n'ont été que partiellement résolus, comme la robustesse de la méthode, ou la composition non-uniforme de chaque couche. En outre, la méthode est basée sur plusieurs hypothèses simplificatrices. Par exemple, nous ne prenons pas en compte les déformations locales de l'estomac au cours du temps, ce qui engendre un léger décalage entre les couche externes. La première couche dans une image d'une séquence donnée peut disparaître dans l'image suivante de la même séquence. Malgré ces points qui peuvent être améliorés, la méthode donne des résultats pertinents en termes d'estimation des courbes temps-activité.

F.2 Travaux futurs et perspectives

Le développement de ces deux méthodes ouvre un large éventail de possibilités. Nous présentons d'abord plusieurs améliorations directes de nos méthodes et les résultats qui pourraient être envisagés. Ensuite, nous proposons quelques axes de recherche à long terme.

F.2.1 Améliorations directes des contributions

Logiciel pour la reconstruction d'image en quasi-apnée Le logiciel dédié à la reconstruction d'images TEMP sans artefact de mouvement respiratoire doit être davantage développé. Bien qu'il ait été développé pour les biologistes, sa version actuelle est juste une version bêta et n'est pas encore adaptée à une utilisation en routine.

Validation de la méthode de reconstruction d'images TEMP en quasi-apnée sur des données simulées Cette étape de validation consiste à simuler des images TEMP à partir d'un fantôme de souris incluant un modèle de la respiration, afin d'obtenir un plus grand nombre de données. Ces fantômes numériques de souris devraient présenter de petites lésions situées aléatoirement dans l'abdomen et un rythme de respiration variable. Plus précisément, il faudrait animer un fantôme numérique de la souris avec le même motif de la respiration que celui qui a été observée (halètements suivis d'une période d'apnée). Cependant, un tel modèle n'a pas encore été développé. Par exemple, le fantôme MOBY [STF+04] a été implémenté avec un mouvement respiratoire semblable à celui de l'homme, et ne serait pas suffisant.

En outre, un tel travail exige l'élaboration d'un modèle numérique de notre caméra afin de simuler les processus d'acquisition et de reconstruction. L'inconvénient de cette étape de validation est qu'elle implique un ensemble de données qui seront parfaitement produites par le logiciel de simulation sans refléter la réalité de la manipulation et de l'acquisition à partir d'animaux vivants. Cependant, une telle simulation offrira un vaste ensemble de données qui pourra être utile pour la validation de notre méthode.

Etude de l'absorption d'iodure dans l'estomac La plupart des travaux futurs liés à ce sujet ont été détaillées dans Section 6.5.6. Parmi eux, les points principaux sont l'étude de la robustesse de l'approche; l'évaluation des coefficients de mélange de coupes d'immunohistomchimie (IHC), et l'interprétation biologique du phénomène.

F.2.2 Directions de recherche à long terme

Je vous présente ci-dessous quelques objectifs de recherche à long terme. Ceux-ci consistent à améliorer les méthodes en suivant la même direction que chacune des contributions présentées, mais également en combinant les deux approches afin d'étudier de nouvelles directions de recherche.

Quantification et modélisation de la croissance de tumeurs abdominales L'étude des tumeurs abdominales, notamment la quantification et la modélisation de leur croissance a été le premier objectif de cette thèse. Cependant, cet objectif a nécessité des travaux préliminaires sur la correction du mouvement respiratoire. Ce travail préliminaire s'est avéré être plus difficile que prévu et a été abordé dans les chapitres 3, 4 et dans l'annexe A de cette thèse. Grâce à cela, le suivi et la quantification précise des tumeurs dans la région abdominale reposera sur des bases solides. Un algorithme d'appariement de la tumeur [WGR+01] pourrait être développé afin de suivre les tumeurs au cours du temps en prenant en compte leur croissance, la possibilité que des tumeurs proches fusionnent, ou l'apparition de nouvelles lésions. Ce type d'approche devrait inclure des méthodes de recalage basé sur des algorithme d'appariement de blocs [ORPA00]. Ensuite, la croissance de tumeur dans la cavité péritonéale peut être étudié et permettre la mise en place d'un modèle informatique de la croissance de tumeur [KPCA08] dans un environnement déformable. Un tel modèle devrait grandement aider les biologistes dans la compréhension de la croissance de ce type de tumeur.

Décomposition en couches appliquée à l'hétérogénéité des tumeurs La description originale de l'estomac présenté dans les chapitres 5 et 6 pourraient être étendue à d'autres organes, mais aussi à des tumeurs. En effet, certaines tumeurs ne peuvent être observées qu'à un stade avancé. A un stade tardif, la segmentation des tumeurs à partir d'images TEMP révèle seulement la partie active de la tumeur, constituée par des cellules vascularisées. Cependant, la segmentation ne permet pas de révéler la partie nécrosée de la tumeur. Dans le cas de tumeurs sous-cutanées, la partie nécrosée peut être observée avec l'imagerie TDM car celle-ci s'affaisse. Dans le cas de cellules tumorales exprimant la protéine NIS, la nécrose de la tumeur pourrait être prédite par une diminution de la prise de pertechnétate de technétium ^{99m}Tc dans les couches internes de la tumeur au cours du temps.

Plus généralement, il a été également mentionné dans [UTT+12] que l'intérieur des tumeurs n'est jamais homogène, pour les raisons mentionnées ci-dessus. Dans cet article, les auteurs présentent les résultats de premières enquêtes effectuées avec une imagerie TEMP à grande résolution du petit animal: ils évaluent l'hétérogénéité des tumeurs.

Plus intéressant encore, l'idée d'appliquer une décomposition en couches

sur des tumeurs permettrait d'améliorer la compréhension de la structure et de l'évolution de la tumeur. En effet, nous pourrions étudier la tumeur non pas comme un système homogène, où l'activité moyenne est calculée sur la totalité de la tumeur. Au lieu de cela, les tumeurs pourraient être étudiées comme un ensemble de sous-régions telles que des couches. Nous aimerions calculer l'activité moyenne dans chacune des sous-régions. Cela permettrait l'identification des différentes parties de la tumeur: nécrose, cellules proliférantes, mais aussi d'autres parties intermédiaires. Nous espérons qu'une telle approche, avec une décomposition en couches de la tumeur, permettrait une meilleure compréhension et la modélisation de la croissance de la tumeur.

List of Acronyms

COM	centre of mass
CT	computed tomography
muCT	μ-CT
ET	emission tomography
ECG	electrocardiogram
FOV	field of view
IHC	immunohistochemistry
IP	intraperitoneal
MRI	magnetic resonance imaging
NIS	sodium/iodide symporter
ODE	ordinary differential equation
PET	positron emission tomography
ROI	region of interest
RPM	real-time position management
RT	radiotherapy
SD	standard deviations
SNR	signal-to-noise ratio
SPECT	single photon emission computed tomography
SUV	standardized uptake value
VOI	volume of interest
TAC	time-activity curve
3D	three (spatial) dimensions
4D	three spatial + 1 temporal dimensions

List of Figures

List of Tables

References

[Act90] Forman S Acton. *Numerical methods that usually work*. MAA, 1990. 118

[BÅ70] R Bellman and KJ Åström. On structural identifiability. *Math. Biosci.*, 7:329–39, 1970. 100, 185

[Bar] 33

[BB09] W Bai and M Brady. Regularized B-spline deformable registration for respiratory motion correction in PET images. *Physics in Medicine and Biology*, 54(9):2719–36, May 2009. 28, 36

[BB11] W Bai and M Brady. Motion correction and attenuation correction for respiratory gated PET images. *IEEE Transactions on Medical Imaging*, 30(2):351–65, February 2011. 17, 18, 28, 29, 34, 36

[BDF09] Irène Buvat, Jacques Darcourt, and Philippe Franken. Single Photon Emission Computed Tomography. In Pierre Grangeat, editor, *Tomography*, chapter 13. ISTE Ltd. et John Wiley & Sons Inc., 2009. 10, 11

[BDS+09] F Büther, M Dawood, L Stegger, F Wubbeling, Mi Schäfers, O Schober, and KP Schäfers. List mode-driven cardiac and respiratory gating in PET. *Journal of Nuclear Medicine*, 50(5):674–81, May 2009. 29, 30, 31, 33, 34

[BED+10] F Büther, I Ernst, M Dawood, P Kraxner, M Schäfers, O Schober, and KP Schäfers. Detection of respiratory tumour motion using intrinsic list mode-driven gating in positron emission tomography. *Eur J Nucl Med Mol Imaging*, 37(12):2315–27, December 2010. 29, 31, 33, 34, 41

[BKS10] SH Bartling, J Kuntz, and W Semmler. Gating in small-animal cardio-thoracic CT. *Methods*, 50(1):42–9, January 2010. 33

[BLW+12] Laurel M Burk, Yueh Z Lee, J Matthew Wait, Jianping Lu, and Otto Z Zhou. Non-contact respiration monitoring for in-vivo murine micro computed tomography: characterization and imaging applications. *Phys Med Biol*, 57(18):5749–63, September 2012. 41, 57

[BMG+13] Marine Breuilly, Grégoire Malandain, Julien Guglielmi, Robert Marsault, Thierry Pourcher, Philippe R Franken, and Jacques Darcourt. Amplitude-based data selection for optimal retrospective reconstruction in micro-SPECT. *Physics in Medicine and Biology*, 58(8):2657–74, April 2013. 6, 201

[BMME+08] RA Bundschuh, A Martinez-Moller, M Essler, SG Nekolla, SI Ziegler, and M Schwaiger. Local motion correction for lung tumours in PET/CT: first results. *Eur J Nucl Med Mol Imaging*, 35(11):1981–8, November 2008. 29, 35, 41, 58

[Bor86] Gunilla Borgefors. Distance transformations in digital images. *Computer Vision, Graphics, and Image Processing*, 34(3):344–71, 1986. 76, 77

[BPD+10] V Bettinardi, M Picchio, N Di Muzio, L Gianolli, MC Gilardi, and C Messa. Detection and compensation of organ/lesion motion using 4D-PET/CT respiratory gated acquisition techniques. *Radiother Oncol*, 96(3):311–6, September 2010. 18, 29, 31, 41

[BRG+08] A Bitarafan, H Rajabi, B Gruy, F Rustgou, AA Sharafi, H Firoozabady, N Yaghoobi, H Malek, C Pirich, W Langesteger, and M Beheshti. Respiratory motion detection and correction in ECG-gated SPECT: a new approach. *Korean Journal of Radiology*, 9(6):490–7, Nov-Dec 2008. 17, 32

[BRG09] V Bettinardi, E Rapisarda, and M C Gilardi. Number of partitions (gates) needed to obtain motion-free images in a respiratory gated 4D-PET/CT study as a function of the lesion size and motion displacement. *Medical Physics*, 36(12):5547–58, December 2009. 28

[BSW62] Mones Berman, Ezra Shahn, and Marjory F. Weiss. The routine fitting of kinetic data to models: A mathematical formalism for digital computers. *Biophysical Journal*, 2(3):275–87, 1962. 189

[BVMA04] C Blondel, R Vaillant, G Malandain, and N Ayache. 3D tomographic reconstruction of coronary arteries using a precomputed 4D motion field. *Phys Med Biol*, 49(11):2197–208, 2004. 41

[CCP+10] G Chang, T Chang, T Pan, JW Clark, and OR Mawlawi. Implementation of an automated respiratory amplitude gating technique for PET/CT: clinical evaluation. *J Nucl Med*, 51(1):16–24, January 2010. 18, 29, 41

[CJP+04] D Cavanaugh, E Johnson, RE Price, J Kurie, EL Travis, and DD Cody. In vivo respiratory-gated micro-CT imaging in small animal oncology models. *Mol Imaging*, 3(1):55–62, January 2004. 17, 18, 31, 32, 46, 57

[CK09] Eric Clarkson and MA Kupinski. Global compartmental pharmacokinetic models for spatiotemporal SPECT and PET imaging. *SIAM journal on imaging sciences*, 2(1):203–225, 2009. 189

[Coo65] Margaret J Cook. *The anatomy of the laboratory mouse.* London (& New York): Academic Press., 1965. 71

[CVS+08] C Chavarrías, J J Vaquero, a Sisniega, a Rodríguez:Ruano, M L Soto:Montenegro, P García:Barreno, and M Desco. Extraction of the respiratory signal from small-animal CT projections for a retrospective gating method. *Physics in Medicine and Biology*, 53(17):4683–95, September 2008. 17

[DBJS08] Mohammad Dawood, F Buther, Xiaoyi Jiang, and Klaus P Schäfers. Respiratory motion correction in 3-D PET data with advanced optical flow algorithms. *IEEE Transactions on Medical Imaging*, 27(8):1164–1175, 2008. 36

[DBL+07] M Dawood, F Büther, N Lang, O Schober, and KP Schäfers. Respiratory gating in positron emission tomography: a quantitative comparison of different gating schemes. *Medical Physics*, 34(7):3067–76, 2007. 33

[DCH+08] M Degon, SR Chipkin, CV Hollot, RT Zoeller, and Y Chait. A computational model of the human thyroid. *Math Biosci*, 212(1):22–53, March 2008. 100, 189

[DCMW+04] NM De Clerck, K Meurrens, H Weiler, D Van Dyck, G Van Houtte, P Terpstra, and AA Postnov. High-resolution X-ray microtomography for the detection of lung tumors in living mice. *Neoplasia*, 6(4):374–9, Jul-Aug 2004. 16, 28

[DDlVP+03] Orsolya Dohan, Antonio De la Vieja, Viktoriya Paroder, Claudia Riedel, Mona Artani, Mia Reed, Christopher S Ginter, and Nancy Carrasco. The sodium/iodide Symporter (NIS): characterization, regulation, and medical significance. *Endocr Rev*, 24(1):48–77, February 2003. 70

[DFBM09] J Daouk, L Fin, P Bailly, and M-E Meyer. Respiratory-gated positron emission tomography and breathhold computed tomography coupling to reduce the influence of respiratory motion: methodology and feasibility. *Acta radiologica (Stockholm, Sweden : 1987)*, 50(2):144–55, March 2009. 18, 29

[DKF+08] Mohammad Dawood, Thomas Kösters, Michael Fieseler, Florian Büther, Xiaoyi Jiang, Frank Wübbeling, and Klaus P Schäfers. Motion correction in respiratory gated cardiac PET/CT using multi-scale optical flow. *Medical Image Computing and Computer-Assisted Intervention*, 11(Pt 2):155–62, January 2008. 36

[DLJS06] M Dawood, N Lang, X Jiang, and KP Schäfers. Lung motion correction on respiratory gated 3-D PET/CT images. *IEEE Trans Med Imaging*, 25(4):476–85, April 2006. 29, 31, 36, 41, 59

[FAMH08] BL Franc, PD Acton, C Mari, and BH Hasegawa. Small-animal SPECT and SPECT/CT: important tools for preclinical investigation. *J Nucl Med*, 49(10):1651–63, October 2008. 40

[FBDP89] Frederique Frouin, Jean-Pierre Bazin, and Robert Di Paola. Image Sequence Processing Using Factor Analysis And Compartmental Modelling. volume 1137, pages 37–45, 1989. 127

[FGV+10] Philippe R Franken, Julien Guglielmi, Christian Vanhove, Malick Koulibaly, Michel Defrise, Jacques Darcourt, and Thierry Pourcher. Distribution and Dynamics of 99m Tc-Pertechnetate Uptake in the Thyroid and Other Organs Assessed by Single-Photon Emission Computed Tomography in Living Mice. *Thyroid*, 20(5):519–26, 2010. 100, 189

[FJ86] JL Fresen and JM Juritz. A note on Foss's method of obtaining initial estimates for exponential curve fitting by numerical integration. *Biometrics*, 42(4):821–827, 1986. 108, 117

[Fos70] SD Foss. A method of exponential curve fitting by numerical integration. *Biometrics*, 26(4):815–821, 1970. 108, 186

[FWHD07] NL Ford, AR Wheatley, DW Holdsworth, and M Drangova. Optimization of a retrospective technique for respiratory-gated high speed micro-CT of free-breathing rodents. *Physics in Medicine and Biology*, 52(19):5749–69, October 2007. 30

[GJQ+11] X Guo, SM Johnston, Y Qi, GA Johnson, and CT Badea. 4D micro:CT using fast prospective gating. *Phys Med Biol*, 57(1):257–271, December 2011. 18, 41

[God83] K. Godfrey. *Compartmental models and their application*. Academic Press, 1983. 100, 183

[GRS+09] N Grotus, a J Reader, S Stute, J C Rosenwald, P Giraud, and I Buvat. Fully 4D list-mode reconstruction applied to respiratory-gated PET scans. *Phys Med Biol*, 54(6):1705–21, March 2009. 17, 29, 41

[GRS+10] Grant T Gullberg, Bryan W Reutter, Arkadiusz Sitek, Jonathan S Maltz, and Thomas F Budinger. Dynamic single photon emission computed tomography-basic principles and cardiac applications. *Physics in Medicine and Biology*, 55(20):R111–91, October 2010. 100, 107, 190

[Hay78] MT Hays. Kinetics of the human thyroid trap: a compartmental model. *Journal of Nuclear Medicine*, 19(7):789–95, July 1978. 100, 104, 189

[HFGH08] AB Hwang, BL Franc, GT Gullberg, and BH Hasegawa. Assessment of the sources of error affecting the quantitative accuracy of SPECT imaging in small animals. *Phys Med Biol*, 53(9):2233–52, May 2008. 5, 40, 199

[HL94] H Malcolm Hudson and Richard S Larkin. Ordered Subsets of Projection Data. 13(4):601–609, 1994. 11, 43

[HMW+12] Mathieu Hatt, Amandine Le Maitre, Daphné Wallach, Hadi Fayad, and Dimitris Visvikis. Comparison of different methods of incorporating respiratory motion for lung cancer tumor volume delineation on PET images: a simulation study. *Physics in Medicine and Biology*, 57(22):7409–30, November 2012. 36

[Hof67] NG Hofmeyr. Stomach scanning after intravenous 99mTc administration. A preliminary report. *South African medical journal/Suid-Afrikaanse tydskrif vir geneeskunde*, 41(23):572, 1967. 101

[HRZG98] R H Huesman, B W Reutter, G L Zeng, and G T Gullberg. Kinetic parameter estimation from SPECT cone-beam projection measurements. *Physics in Medicine and Biology*, 43(4):973–82, April 1998. 100, 190

[HSO+95] Joseph V Hajnal, Nadeem Saeed, Angela Oatridge, Elaine J Williams, Ian R Young, and Graeme M Bydder. Detection of subtle brain changes using subvoxel registration and subtraction of serial mr images. *Journal of Computer Assisted Tomography*, 19(5):677–691, 1995. 37

[HTM+08] Y Hori, N Takasuka, M Mutoh, T Kitahashi, S Kojima, K Imaida, M Suzuki, K Kohara, S Yamamoto, N Moriyama, T Sugimura, and K Wakabayashi. Periodic analysis of urethane-induced pulmonary tumors in living A/J mice by respiration-gated X-ray microcomputed tomography. *Cancer science*, 99(9):1774–7, September 2008. 32

[Jac96] J.A. Jacquez. *Compartmental analysis in biology and medicine*. BioMedware, 1996. 100, 183

[JPK+08] EM Johnson, RE Price, JM Kurie, BS Rivera, and DD Cody. A new method for respiratory gating during microcomputed tomography of lung in mice. *J Am Assoc Lab Anim Sci*, 47(4):46–56, July 2008. 18

[JST+12] J Jiao, GE Searle, AC Tziortzi, CA Salinas, RN Gunn, and JA Schnabel. Spatial-temporal pharmacokinetic model based registration of 4d brain pet data. In Stanley Durrleman, Tom Fletcher, Guido Gerig, and Marc Niethammer, editors, *Spatio-temporal Image Analysis for Longitudinal and Time-Series Image Data*, volume 7570 of *Lecture Notes in Computer Science*, pages 100–12. Springer Berlin Heidelberg, 2012. 100, 190

[Kar95] TT. Kararli. Comparison of the gastrointestinal anatomy, physiology, and biochemistry of humans and commonly used laboratory animals. *Biopharmaceutics & Drug Disposition*, 16(5):351–380, 1995. 71

[KC08] JH Kang and J-K Chung. Molecular-genetic imaging based on reporter gene expression. *J Nucl Med*, 49 Suppl 2:164, June 2008. 40

[KDZ+10] J Kuntz, J Dinkel, S Zwick, T Bauerle, M Grasruck, F Kiessling, R Gupta, W Semmler, and SH Bartling. Fully automated intrinsic respiratory and cardiac gating for small animal CT. *Phys Med Biol*, 55(7):2069–85, April 2010. 33, 34, 41

[KG01] DJ Kadrmas and GT Gullberg. 4D maximum a posteriori reconstruction in dynamic SPECT using a compartmental model-

based prior. *Physics in Medicine and Biology*, 46(5):1553–1574, 2001. 100, 190

[KIK+07] G Kovalski, O Israel, Z Keidar, A Frenkel, J Sachs, and H Azhari. Correction of Heart Motion Due to Respiration in Clinical Myocardial Perfusion SPECT Scans Using Respiratory Gating. *J Nucl Med*, 48(4):630–636, April 2007. 18, 41

[KM11] E Kyriakou and DR McKenzie. Dynamic modeling of lung tumor motion during respiration. *Phys Med Biol*, 56(10):2999–3013, May 2011. 41

[KPCA08] Ender Konukoglu, Xavier Pennec, Olivier Clatz, and Nicholas Ayache. Tumor growth modeling in oncological image analysis. In I. Bankman, editor, *Handbook of Medical Image Processing and Analysis - New edition*, chapter 18, pages 297–307. Academic Press, December 2008. 138, 207

[KRK11] Sabine Krueger, Albert Roessner, and Doerthe Kuester. Murine models of H. pylori-induced gastritis and gastric adenocarcinoma. *Pathology, research and practice*, 207(10):599–607, October 2011. 68, 211

[LCS+07] F Lamare, T Cresson, J Savean, C Cheze Le Rest, AJ Reader, and D Visvikis. Respiratory motion correction for PET oncology applications using affine transformation of list mode data. *Physics in Medicine and Biology*, 52(1):121–40, January 2007. 34

[LG03] AM Loening and SS Gambhir. AMIDE: a free software tool for multimodality medical image analysis. *Mol Imaging*, 2(3):131–7, July 2003. 50

[LH72] KA Lathrop and PV Harper. Biologic behavior of 99m Tc from 99m Tc-pertechnetate ion. *Progress in nuclear medicine*, 1:145, 1972. 101, 104, 212

[LLC+07] F Lamare, MJ Ledesma Carbayo, T Cresson, G Kontaxakis, A Santos, C Cheze Le Rest, AJ Reader, and D Visvikis. List-mode-based reconstruction for respiratory motion correction in PET using non-rigid body transformations. *Phys Med Biol*, 52(17):5187–204, September 2007. 34, 41

[LRS+06] L Livieratos, K Rajappan, L Stegger, K Schäfers, DL Bailey, and PG Camici. Respiratory gating of cardiac PET data in list-mode acquisition. *Eur J Nucl Med Mol Imaging*, 33(5):584–8, May 2006. 18, 29, 41

[LRWW98] JC Lagarias, JA Reeds, MH Wright, and PE Wright. Convergence Properties of the Nelder–Mead Simplex Method in Low Dimensions. *SIAM Journal on Optimization*, 9(1):112–147, January 1998. 116

[Luc09] G Lucignani. Respiratory and cardiac motion correction with 4D PET imaging: shooting at moving targets. *Eur J Nucl Med Mol Imaging*, 36(2):315–9, February 2009. 41

[MAB94] M Menke, MS Atkins, and KR Buckley. Compensation methods for head motion detected during PET imaging. In *Nuclear Science Symposium and Medical Imaging Conference*, pages 1638–1642, 1994. 25

[MBC+10] R Maroy, R Boisgard, C Comtat, B Jego, Y Fontyn, S Jan, A Dubois, R Trébossen, and B Tavitian. Quantitative organ time activity curve extraction from rodent PET images without anatomical prior. *Medical Physics*, 37(4):1507–17, 2010. 136, 204

[MDB+11] P Mancosu, M Danna, V Bettinardi, MA Aquilina, F Lobefalo, L Cozzi, A Fogliata, and M Scorsetti. Semiautomatic method to identify the best phase for gated RT in lung region by 4D-PET/CT acquisitions. *Medical Physics*, (1):354–62, January 2011. 17, 29, 30, 31

[MMZM85] GB Moody, RG Mark, Andrea Zoccola, and S Mantero. Derivation of respiratory signals from multi-lead ECGs. *Computers in cardiology*, c:1–9, 1985. 18

[MSL+10] L Martiniova, D Schimel, EW Lai, A Limpuangthip, R Kvetnansky, and K Pacak. In vivo micro-CT imaging of liver lesions in small animal models. *Methods*, 50(1):20–5, January 2010. 16, 30, 41

[NE08] SA Nehmeh and YE Erdi. Respiratory motion in positron emission tomography/computed tomography: a review. *Semin Nucl Med*, 38(3):167–76, May 2008. 18, 41

[NER+03] SA Nehmeh, YE Erdi, KE Rosenzweig, H Schoder, SM Larson, OD Squire, and JL Humm. Reduction of respiratory motion artifacts in PET imaging of lung cancer by respiratory correlated dynamic PET: methodology and comparison with respiratory gated PET. *Journal of Nuclear Medicine*, 44(10):1644–8, October 2003. 27, 31, 34

[NHAQ+11] SA Nehmeh, AA Haj-Ali, C Qing, C Stearns, H Kalaigian, S Kohlmyer, H Schoder, AY Ho, SM Larson, and JL Humm. A novel respiratory tracking system for smart-gated PET acquisition. *Med Phys*, 38(1):531–8, January 2011. 17, 29, 41

[NM65] J. A. Nelder and R Mead. A Simplex Method for Function Minimization. *The Computer Journal*, 7(4):308–313, January 1965. 116, 120

[NSG+13] Christophe Nioche, Marine Soret, Eric Gontier, Marion Lahutte, Guillaume Dutertre, Renaud Dulou, L Capelle, R Guillevin, H Foehrenbach, and Irène Buvat. Evaluation of quantitative criteria for glioma grading with static and dynamic 18F-FDopa PET/CT. *Clinical nuclear medicine*, 38(2):81–7, 2013. 100, 190

[NYK12] Xiaofeng Niu, Yongyi Yang, and Michael a King. Comparison study of temporal regularization methods for fully 5D reconstruction of cardiac gated dynamic SPECT. *Physics in Medicine and Biology*, 57(17):5523–42, September 2012. 100, 190

[ORPA00] S. Ourselin, A. Roche, S. Prima, and N. Ayache. Block Matching: A General Framework to Improve Robustness of Rigid Registration of Medical Images. In A.M. DiGioia and S. Delp, editors, *Third International Conference on Medical Robotics, Imaging And Computer Assisted Surgery (MICCAI 2000)*, volume 1935 of *Lectures Notes in Computer Science*, pages 557–566, Pittsburgh, Penn, USA, octobre 11-14 2000. Springer. 138, 207

[Ots79] N Otsu. A Threshold Selection Method from Gray-Level Histograms. *IEEE Trans Syst Man Cyb*, 9(1):62–66, 1979. 48, 75

[Pen55] R Penrose. A generalized inverse for matrices. *Proc. Cambridge Philos. Soc*, 51(July):406–413, 1955. 111

[PGW10] MA Pysz, SS Gambhir, and JK Willmann. Molecular imaging: current status and emerging strategies. *Clin Radiol*, 65(7):500–16, July 2010. 40

[PTVF92] WH Press, SA Teukolsky, WT Vetterling, and BP Flannery. *Downhill Simplex Method in Multidimensions*, chapter Numerical recipes in C: the art of scientific computing, pages 402–412. Cambridge University Press, Cambridge, UK, 2nd edition, oct 1992. 116, 120

[RD04] Dmitri Y Riabkov and Edward V R Di Bella. Blind identification of the kinetic parameters in three-compartment models. *Physics in Medicine and Biology*, 49(5):639–64, March 2004. 189

[Rey05] M Reyes. *Respiratory Motion Compensation in Emission Tomography*. PhD thesis, 2005. 34

[RGH98] B W Reutter, G T Gullberg, and R H Huesman. Kinetic parameter estimation from attenuated SPECT projection measurements. *IEEE Transactions on Nuclear Science*, 45(6):3007–3013, 1998. 100, 190

[RGH00] B W Reutter, G T Gullberg, and R H Huesman. Direct least-squares estimation of spatiotemporal distributions from dynamic SPECT projections using a spatial segmentation and temporal B-splines. 19(5):434–50, May 2000. 100, 190

[RGH02] BW Reutter, GT Gullberg, and R H Huesman. Effects of temporal modelling on the statistical uncertainty of spatiotemporal distributions estimated directly from dynamic SPECT projections. *Physics in Medicine and Biology*, 47(15):2673–2683, 2002. 100, 190

[RMK+07] M Reyes, G Malandain, P M Koulibaly, M A Gonzalez-Ballester, and J Darcourt. Model-based respiratory motion compensation for emission tomography image reconstruction. *Phys Med Biol*, 52(12):3579–600, June 2007. 27, 34, 41, 59

[RVHK11] P Ritt, H Vija, J Hornegger, and T Kuwert. Absolute quantification in SPECT. *Eur J Nucl Med Mol Imaging*, 38 Suppl 1:S69–77, May 2011. 40

[RW71] SI Rubinow and Alice Winzer. Compartment analysis: an inverse problem. *Math. Biosci.*, 11:203–247, 1971. 100, 107, 185, 189

[SDP+03] Piotr J. Slomka, Damini Dey, Christian Przetak, Usaf E. Aladl, and Richard P. Baum. Automated 3-Dimensional Registration of Stand-Alone 18F-FDG Whole-Body PET with CT. *Journal of Nuclear Medicine*, 44(7):1156–67, 2003. 20

[SOBM09] Paul J Schleyer, Michael J O'Doherty, Sally F Barrington, and Paul K Marsden. Retrospective data-driven respiratory gating for PET/CT. *Phys Med Biol*, 54(7):1935–50, April 2009. 41, 58

[SOM11] PJ Schleyer, MJ O'Doherty, and PK Marsden. Extension of a data-driven gating technique to 3D, whole body PET studies. *Phys Med Biol*, 56(13):3953–65, July 2011. 17, 29

[Son86] Dieter Sondermann. Stalistische Hefte Statistical Papers Best approximate solutions to matrix equations under rank restrictions. *Statistische Hefte*, 27:57–66, 1986. 111

[SRK+06] Nikolas Sakellios, JL Rubio, Nicolas Karakatsanis, G Kontaxakis, G Loudos, A Santos, K Nikita, and S Majewski. GATE simulations for small animal SPECT/PET using voxelized phantoms and rotating-head detectors. In *Nuclear Science Symposium Conference Record, 2006. IEEE*, volume 4, pages 2000–2003. IEEE, 2006. 60

[STF+04] WP Segars, BMW Tsui, EC Frey, GA Johnson, and SS Berr. Development of a 4-D digital mouse phantom for molecular imaging research. *Mol Imaging*, 6(3):149–59, 2004. 60, 138, 206

[SZI00] L a Schwarte, C J Zuurbier, and C Ince. Mechanical ventilation of mice. *Basic research in cardiology*, 95(6):510–20, December 2000. 16

[TLDF98] A Travaglini, C Lamberti, J DeBie, and M Ferri. Respiratory signal derived from eight-lead ECG. *Computers in Cardiology*, 25:65–68, 1998. 18

[TVD12] Piper M. Treuting, Mark A. Valasek, and Suzanne M. Dintzis. Chap 11 : Upper gastrointestinal tract. In Piper M. Treuting, Suzanne Dintzis, Denny Liggitt, and Charles W. Frevert, editors, *Comparative Anatomy and Histology*, pages 155–75. Academic Press, San Diego, 2012. 71

[UTT+12] IO Umeda, Kotaro Tani, Keisuke Tsuda, Masamitsu Kobayashi, Mayumi Ogata, Sadaaki Kimura, Mitsuyoshi Yoshimoto, Shuji Kojima, Kunikazu Moribe, Keiji Yamamoto, Noriyuki Moriyama, and Hirofumi Fujii. High resolution SPECT imaging for visualization of intratumoral heterogeneity using a SPECT/CT scanner dedicated for small animal imaging. *Annals of Nuclear Medicine*, 26(1):67–76, 2012. 139, 207

[vHJ+11] W van Elmpt, J Hamill, J Jones, D De Ruysscher, P Lambin, and M Ollers. Optimal gating compared to 3D and 4D PET reconstruction for characterization of lung tumours. *Eur J Nucl Med Mol Imaging*, 38(5):843–55, January 2011. 18, 29, 31, 32, 41

[VLB+07] D Visvikis, F Lamare, P Bruyant, A Turzo, Y Bizais, and C Cheze Le Rest. Correction de mouvement respiratoire en

TEP/TDM. *Médecine Nucléaire*, 31(4):153–159, 2007. 9è Conférence Internationale de l'ACOMEN : L'instrumentation en Médecine Nucléaire. 27, 29, 31, 35

[WGR+01] D Welti, G Gerig, EW Radü, L Kappos, and G Székely. Spatio-Temporal Segmentation of Active Multiple Sclerosis Lesions in Serial MRI Data. In *Information Processing in Medical Imaging*, pages 438–45. Springer, 2001. 138, 207

[WIK+06] Hiroshi Watabe, Yoko Ikoma, Yuichi Kimura, Mika Naganawa, and Miho Shidahara. PET kinetic analysis-compartmental model. 20(9):583–8, November 2006. 189

[WLKV11] D Wallach, F Lamare, G Kontaxakis, and D Visvikis. Super:resolution in respiratory synchronized positron emission tomography. *IEEE Transactions on Medical Imaging*, (c):1–12, October 2011. 17, 36

[XYY11] Quansheng Xu, Kehong Yuan, and Datian Ye. Respiratory motion blur identification and reduction in ungated thoracic PET imaging. *Physics in medicine and biology*, 56(14):4481–98, July 2011. 36

[ZGK10] Gengsheng L Zeng, Grant T Gullberg, and Dan J Kadrmas. Closed-form kinetic parameter estimation solution to the truncated data problem. *Physics in Medicine and Biology*, 55(24):7453–68, December 2010. 100, 190

[ZJL+04] Yufeng Zang, Tianzi Jiang, Yingli Lu, Yong He, and Lixia Tian. Regional homogeneity approach to fMRI data analysis. *NeuroImage*, 22(1):394–400, May 2004. 126